Black, Lauren Elaine (2024) *Investigation of the pathological mechanisms in canine degenerative myelopathy and the potential involvement of extracellular vesicles in disease progression.* PhD thesis.

http://theses.gla.ac.uk/84053/

Copyright and moral rights for this work are retained by the author

A copy can be downloaded for personal non-commercial research or study, without prior permission or charge

This work cannot be reproduced or quoted extensively from without first obtaining permission in writing from the author

The content must not be changed in any way or sold commercially in any format or medium without the formal permission of the author

When referring to this work, full bibliographic details including the author, title, awarding institution and date of the thesis must be given

Enlighten: Theses
https://theses.gla.ac.uk/
research-enlighten@glasgow.ac.uk

Investigation of the pathological mechanisms in canine degenerative myelopathy and the potential involvement of extracellular vesicles in disease progression

Lauren Elaine Black

M. Sci. Veterinary Biosciences

Submitted in fulfilment of the requirements for the Degree of

Doctor of Philosophy

School of Biodiversity, One Health and Veterinary Medicine

College of Medical, Veterinary and Life Sciences

University of Glasgow

August 2023

© Lauren Elaine Black 2023

Abstract

Canine degenerative myelopathy (DM) is a progressive and lethal adult-onset neurodegenerative disease with nonspecific clinical signs that can end in tetraplegia and respiratory dysfunction. It is frequently identified in German shepherd dogs (GSD) but has been described in other breeds. A definitive diagnosis is reached after histopathological examination of the spinal cord where axon degeneration and demyelination are characterised. Mutations in the gene encoding superoxide dismutase 1 (SOD1) are thought to have a pathological role in the disease and genotyping of the *Sod*1 gene can be used with clinical signs and histology to diagnose DM. The genetics, clinical signs and histology of DM suggests it may be a good naturally occurring large animal model for some forms of the human motor neurone disease, amyotrophic lateral sclerosis (ALS). This study aimed to 1) establish if defective cellular clearance pathways play a role in the aggregation of SOD1 and 2) if these defects contribute to the secretion of SOD1 positive extracellular vesicles (EVs) that 3) can spread mutant protein in a prion-like manner. Finally, 4) was to validate these findings with spinal cord tissue from DM cases using proteomics and biochemistry.

In vitro studies using a neuroblastoma derived cell line (SK-N-SH) were conducted to assess the effect of disrupting various cell clearance and toxicity pathways on wildtype (WT) and mutant SOD1 aggregation and EV production. The reducing agent dithiothreitol increased the propensity of WT- and DM-SOD1 to aggregate ($p \leq 0.01$) but did not have a statistically significant impact on the production of SOD1 positive EVs from cells. The autophagy inhibitor chloroquine increased the percentage of cells with DM-SOD1 aggregates ($p \leq 0.01$), but not WT-SOD1 aggregates. EV secretion was not statistically significantly affected by chloroquine treatment in cells with DM-SOD1, but there was a significant increase in the EV marker flotillin-1 from cells containing WT-SOD1 ($p \leq 0.01$). The proteasome inhibitor MG312 significantly increased the number of cells with WT- and DM-SOD1 aggregates ($p < 0.0001$), but they were higher in DM-SOD1 transfected cells ($p \leq 0.05$). Flotillin-1 showed a downward trend from treated cells however this was only statistically supported with EVs from WT-SOD1 containing cells ($p \leq 0.01$). WT- and DM-SOD1 showed an upwards trend in the EV fraction, but only reached significance in EVs from the cells containing DM-SOD1 ($p \leq 0.01$). Overall, disruption to the main protein processing pathways caused the induction of nontypical clearance pathways and some of these appear to be less effective in the presence of the DM associated *Sod*1 mutation. Further, mutant SOD1 may have an impact on the stabilisation of the cell membrane as indicated by changes to associated proteins and this could have subsequent effects on protein clearance, particularly at the level of the endosome pathway and EVs. Further studies indicated there is a potential for EVs to spread WT- and DM-SOD1 to other cells in culture which suggests EVs could be recruited in DM for the spread of mutant SOD1 to other cells and may contribute to the progression of DM throughout the thoracic spinal cord and to the cervical and lumbar regions.

Biochemical and proteomics analysis of spinal cords from control and DM dogs suggested axon and myelin integrity was disrupted and astrocytes were activated at early stages of DM. Evidence suggested these changes were the consequence of altered cellular metabolism, intracellular structure and protein processing. The *Sod*1 mutation caused an apparent reduction in SOD1 enzyme activity further suggesting the mutation is a contributor to the pathogenesis and progression of DM. Changes to plasma membrane organisation were also highlighted in the *ex vivo* study and may indicate perturbations to protein and lipid turnover.

Ultimately the findings presented in this thesis contribute to the understanding of DM pathogenesis and will aid the search for DM biomarkers to enable earlier diagnosis, monitor disease progression and identify treatment targets.

Table of Contents

Abstract 1

List of Tables 10

List of Figures 11

Acknowledgements 15

Author's Declaration 16

Abbreviations 17

1 Introduction 24

1.1 Canine degenerative myelopathy 24

1.1.1 Etymology of canine degenerative myelopathy 24

1.1.2 Signalment of DM 25

1.1.3 Clinical signs of DM 25

1.1.4 Histopathology 28

1.1.5 Diagnosis and prognosis of DM 32

1.2 Human amyotrophic lateral sclerosis 34

1.2.1 Clinical signs of ALS and phenotypic variations 35

1.2.2 Typical histopathology of ALS 36

1.2.3 ALS diagnosis and prognosis 37

1.2.4 Methods for investigating ALS 38

1.3 Potential risk factors for DM and ALS 39

1.3.1 Non-genetic risk factors 40

1.3.2 Genetic risk factors 40

1.4 Many pathological mechanisms may contribute to DM 44

1.4.1 The SOD1 protein 47

1.4.2 Heat shock protein response 52

1.4.3 ER associated degradation and the ubiquitin proteasome system 53

1.4.4 Autophagy 54

1.4.5 ER stress and the unfolded protein response 55

1.4.6 Cell death mechanisms 57

1.4.7 Cell metabolism 58

1.4.8 Inflammation 59

1.5 Extracellular vesicles may be involved in DM progression 60

1.5.1 Extracellular vesicles are a heterogenous population 60

1.5.2 Extracellular vesicles in disease 63

1.6 Hypothesis, aims and objectives 63

2 General materials and methods 65

2.1 Overview 65

2.1.1 *In vitro* study 65

2.1.2 *Ex vivo* study 65

2.2 Cell culture 66

2.2.1 Cell line and culture maintenance 66

2.2.2 Expression of proteins of interest in cell culture 67

2.3 Visualising cells, aggregates and EVs 69

2.3.1 Assessing cell viability by morphology 69

2.3.2 Lysosome stain 69

2.3.3 Cell fixation and nuclei staining 69

2.3.4 Visualisation of fluorescent proteins and stains 70

2.4 Analysis of proteins 70

2.4.1 Protein sample generation from *in vitro* cell culture 70

2.4.2 Protein sample generation from *ex vivo* tissues 72

2.4.3 Total protein measurement 72

2.4.4 Protein denaturation and loading 73

2.4.5 Separation of proteins within samples 74

2.4.6 Gel staining 75
2.4.7 Western Blot 77
2.4.8 Proteomic analysis 79
2.5 Analysis of nucleic acids 79
2.5.1 Sample preparation 79
2.5.2 Quantification and quality assessment of nucleic acids 81
2.5.3 Generation of cDNA from RNA 81
2.5.4 Polymerase chain reaction 83
2.5.5 PCR product purification 85
2.5.6 Restriction Fragment Length Polymorphism (RFLP) reaction 86
2.6 Statistical analysis 87

3 Optimisation of *in vitro* methods used for investigating SOD1 88
3.1 Background 88
3.2 Aims 90
3.3 Materials and Methods 90
3.3.1 Cell culture and transfection 90
3.3.2 Treatment optimisation 92
3.3.3 Statistical analysis 94
3.4 Results 94
3.4.1 Plasmid characterisation 94
3.4.2 Automatic cell counting was not sufficient 96
3.4.3 Growth media comparison 97
3.4.4 The optimal dose of DTT is 10 mM 98
3.4.5 The optimal dose of CQ is 40 µM 99
3.4.6 The optimal dose of MG132 is 5 µM 103
3.5 Discussion 105
3.5.1 Manual cell counting was selected for future work 105

3.5.2 GFP fusion proteins may influence cellular processes..................106
3.5.3 DTT dose and treatment duration affect cell survival..................108
3.5.4 Components of autophagy accumulate within CQ treated cells 108
3.5.5 Components of the UPS accumulate in MG132 treated cells 109

4 Characterisation of extracellular vesicles and their association with SOD1 *in vitro* 111
4.1 Background...111
4.2 Hypothesis and aims 113
4.3 Materials and Methods...114
4.3.1 Cell culture and transfection...114
4.3.2 Optimisation of EV isolation..114
4.3.3 EV transfer studies..116
4.3.4 Statistical analysis 117
4.4 Results 117
4.4.1 Three centrifugation steps may enrich NT EV fraction.................117
4.4.2 Total protein profiles of NT and transfected EVs are similar.........118
4.4.3 Characterisation of EVs 119
4.4.4 Analysis of endogenous and fusion SOD1 in EVs 122
4.4.5 Association between SOD1-EGFP and flotillin-1 124
4.4.6 EV transfer pilot study 126
4.4.7 Additional centrifugation steps reduced fluorescence transfer.......127
4.5 Discussion 130
4.5.1 Characterisation of EVs 130
4.5.2 Assessment of differential ultracentrifugation 131
4.5.3 Transfection procedure may influence EV production 133
4.5.4 SOD1 is found in the EV fraction from cell culture media 134
4.5.5 Transfer of WT and mutant SOD1 is possible *in vitro*...................135
4.6 Conclusions..137

5 *In vitro* investigation of protein processing, SOD1 aggregation and extracellular vesicles 138

5.1 Background 138

5.1.1 Summary of protein processing pathways 138

5.1.2 Extracellular vesicles (EVs) 139

5.1.3 Crosstalk between protein processing pathways 140

5.2 Hypothesis and aims 141

5.3 Materials and Methods 142

5.3.1 Cell culture, transfection and treatment 142

5.3.2 EV isolation 143

5.3.3 Protein analysis 144

5.3.4 RNA analysis 144

5.3.5 SOD1 aggregate visualisation 146

5.3.6 Statistical analysis 146

5.4 Results 146

5.4.1 Impact of the reducing agent DTT on protein processing 146

5.4.2 Impact of autophagy disruption by CQ treatment 155

5.4.3 Impact of proteasome inhibition by MG132 165

5.4.4 SOD1 aggregation in control cells 173

5.4.5 Evidence of crosstalk between protein processing pathways 173

5.4.6 The effect of three centrifugation steps on EVs 176

5.5 Discussion 180

5.5.1 Effect of autophagy inhibition on SOD1-EGFP processing 180

5.5.2 Widespread protein misfolding, ER stress and protein processing 186

5.5.3 Considerations and future work 188

5.6 Conclusions 190

6 *Ex vivo* assessment of DM spinal cord proteins 192

6.1 Background..192

6.1.1 The proteome 193

6.1.2 Summary of common omics techniques 193

6.1.3 Cell specific markers 194

6.2 Hypothesis and aims 196

6.3 Materials and Methods..197

6.3.1 Case recruitment, diagnosis and collection..............................197

6.3.2 Nucleic acid analysis...202

6.3.3 Protein analysis 204

6.3.4 Data and statistical analysis...209

6.4 Results 209

6.4.1 Diagnosis of DM...209

6.4.2 Nucleic acid analysis...212

6.4.3 Protein overview in spinal cord samples 213

6.4.4 Analysis of specific protein markers 220

6.4.5 Additional proteins were selected for biochemical validation 241

6.5 Discussion 243

6.5.1 Analysis of gene expression using mRNA..................................243

6.5.2 Methodological considerations for protein assessment.................243

6.5.3 Investigation of cell specific proteins.......................................245

6.5.4 Investigation of housekeeping proteins....................................250

6.5.5 Markers of neurodegeneration found in DM cord........................251

6.5.6 Cell clearance/toxicity pathway investigation 254

6.5.7 EV protein investigation...258

6.5.8 Proteomics suggest cellular metabolism changes in DM................259

6.6 Conclusions..262

7 General discussion and future direction.. 264

7.1 Discussion and updated hypotheses 264

7.1.1 Summary of CNS findings 264

7.1.2 Potential implications for specific cell types 266

7.1.3 Suggested hypothesis for regional differences in the spinal cord 269

7.2 Limitations and future work 270

7.2.1 *In vitro* and *ex vivo* sample sizes 270

7.2.2 Development of primary cell cultures and expansion of the *in vitro* model 270

7.2.3 Further assessment of biological samples 273

7.3 Conclusions and the impact of this study.....................................277

8 Appendices 279

8.1 COVID-19 impact statement 279

8.2 Supplementary materials and methods 280

8.2.1 Cell culture 280

8.2.2 Nucleic acid analysis...283

8.2.3 Protein analysis 283

8.2.4 Image processing with ImageJ 290

8.2.5 Case collection and processing 293

8.3 Supplementary results...296

8.3.1 Analysis of cell culture derived RNA 296

8.3.2 Analysis of tissue derived RNA 300

8.3.3 Analysis of proteins derived from cell culture...........................301

8.3.4 Analysis of proteins from tissue derived samples 307

List of references... 312

List of Tables

Table 1-1: Main clinical signs defining the different stages of DM. 26

Table 2-1: List of plasmids used in this study. 67

Table 2-2: List of antibodies used for WB... 78

Table 2-3: Incubation steps in generation of cDNA using SSIII™ and SSIV™. 82

Table 2-4: List of primers used in this study. 84

Table 3-1: Plasmid concentrations for transfection................................. 91

Table 5-1: Summary of the effect of treatment in cell culture. 191

Table 6-1: List of cases used in this study. 200

Table 6-2: Differentially expressed proteins in the cervical spinal cord. 216

Table 6-3: Differentially expressed proteins in the thoracic spinal cord. 217

Table 6-4: Proteins significantly different in spinal cord regions of DM dogs. ..263

Table 8-1: Poly-L-lysine working solution..281

Table 8-2: Primers pairs for the amplification of WT and DM *Sod*1 plasmids....282

Table 8-3: Example transfection reagent quantities per well. 282

Table 8-4: 100 bp DNA ladder working solution.....................................283

Table 8-5: Lysis buffer composition. 283

Table 8-6: Sample denaturation buffer. 284

Table 8-7: 2X loading buffer for native gel samples. 284

Table 8-8: Coomassie blue stain and de-stain.......................................285

Table 8-9: Silver stain solutions...285

Table 8-10: Acrylamide native gel recipe...286

Table 8-11: 100 mM phosphate buffer..286

Table 8-12: Riboflavin mixture recipe...287

Table 8-13: 10X T-TBS stock. 287

Table 8-14: Antibody validation information for use with canine tissue. 288

List of Figures

Figure 1-1: Many pathological mechanisms are involved in DM and ALS. 46

Figure 1-2: Summary of SOD1 activity and aggregation. 49

Figure 1-3: Overview of exosome formation and release............................ 62

Figure 1-4: Hypothesis tested in this PhD project. 64

Figure 2-1: Summary of centrifugation steps used throughout the study. 71

Figure 2-2: PCR thermocycler cycles for RT-PCR of cDNA and gDNA. 85

Figure 3-1: Characterisation of SOD1 plasmids used in this study.................. 95

Figure 3-2: Comparison of automatic and manual cell counting. 97

Figure 3-3: Assessment of pSOD1-EGFP transfected cells in NGM or EDM......... 98

Figure 3-4: Optimisation of dose and duration of DTT treatment.................. 99

Figure 3-5: Autophagy was inhibited by CQ and was visualised *in vitro*..........101

Figure 3-6: Understanding the effect of CQ at different cell densities. 102

Figure 3-7: MG132 dose optimisation..104

Figure 4-1: EV fraction may be enriched after two ultracentrifugation steps...118

Figure 4-2: Total protein profiles for cells and media associated fractions. 119

Figure 4-3: Flotillin-1 and actin in CLs and media associated fractions.........121

Figure 4-4: SOD1 in CLs and media associated fractions. 123

Figure 4-5: SOD activity in CLs and media associated fractions...................124

Figure 4-6: SOD1-EGFP and flotillin-1 in media associated fractions............125

Figure 4-7: EVs may spread WT- and DM-SOD1-EGFP to recipient cells. 127

Figure 4-8: Further studies confirm EVs may spread WT- and DM-SOD1-EGFP. .129

Figure 5-1: Summarised workflow for treatment studies..........................142

Figure 5-2: Analysis of RNA from DTT treated cells. 147

Figure 5-3: Representative total protein profiles for DTT treatment. 148

Figure 5-4: DTT treatment effect on CLs and EVs. 150

Figure 5-5: DTT treatment affects SOD activity. 151

Figure 5-6: DTT treatment affects the LC3BII/LC3BI ratio in transfected cells. 152

Figure 5-7: Cytology of DTT treated cells. 154

Figure 5-8: Analysis of RNA derived from control and CQ treated cells. 155

Figure 5-9: Representative total protein profiles for CQ treated cells. 156

Figure 5-10: Comparison of LC3B ratios between treatment groups in CLs......158

Figure 5-11: The effect of CQ treatment on CLs and EVs. 160

Figure 5-12: The effect of CQ on LC3B subtypes associated with EVs. 162

Figure 5-13: The effect of CQ treatment on SOD activity in CLs and EVs. 163

Figure 5-14: Cytology of cells treated with CQ. 164

Figure 5-15: Analysis of gene expression after MG132 treatment. 165

Figure 5-16: Total protein profiles of CLs and EVs in MG132 study. 166

Figure 5-17: MG132 treatment effect on ubiquitination within CLs and EVs. ...167

Figure 5-18: The effect of MG132 treatment on CLs and EVs. 169

Figure 5-19: The effect of MG132 treatment on SOD activity in CLs. 170

Figure 5-20: Cytology of cells treated with MG132. 172

Figure 5-21: CQ treatment may upregulate pathways including the UPS. 174

Figure 5-22: MG132 treatment effect on LC3B in CLs and EVs. 176

Figure 5-23: Comparison of SOD1-EGFP and flotillin-1 in CLs after CQ or MG132 treatment. 177

Figure 5-24: Comparison of SOD1-EGFP and flotillin-1 in EVs isolated using three centrifugation steps after CQ or MG132 treatment of cells. 179

Figure 6-1: *Sod*1 genotyping for all dogs used in this study. 210

Figure 6-2: Examples of normal and DM spinal cord histology. 212

Figure 6-3: Comparison of RNA markers in canine spinal cord segments. 213

Figure 6-4: Total protein profile for control and DM spinal cord regions. 214

Figure 6-5: Volcano plot assessment of TMT proteomics data. 215

Figure 6-6: KEGG pathway and GO analysis of the spinal cord. 220

Figure 6-7: Neurone associated proteins in canine spinal cord. 222

Figure 6-8: Myelin associated proteins in canine spinal cord. 224

Figure 6-9: Biochemical investigation of myelin PLP and DM20. 225

Figure 6-10: Glia associated proteins in canine spinal cord. 227

Figure 6-11: Housekeeping proteins in canine spinal cord. 229

Figure 6-12: Proteins associated with cellular clearance and toxicity pathways in canine spinal cord. 232

Figure 6-13: Biochemical investigation of autophagy and the proteasome. 234

Figure 6-14: Proteins associated with neurodegenerative diseases in canine spinal cord. 236

Figure 6-15: SOD1 protein and SOD activity in canine spinal cord regions. 238

Figure 6-16: EV associated proteins in canine spinal cord. 240

Figure 6-17: Additional proteins selected for validation with biochemistry. 242

Figure 7-1: Suggested schematic for updated hypotheses. 268

Figure 8-1: WB profiles for antibodies used in this study. 289

Figure 8-2: Quantifying proteins and nucleic acids using ImageJ. 290

Figure 8-3: Creating a coloured image with ImageJ using one filter. 291

Figure 8-4: Creating a coloured image in ImageJ using multiple filters. 291

Figure 8-5: Manually counting cells using ImageJ. 292

Figure 8-6: Counting cells automatically with Image J. 292

Figure 8-7: RNA integrity gels for DTT and CQ studies. 297

Figure 8-8: RNA integrity gel for control and MG132 treated cells. 298

Figure 8-9: Characterisation of primers for RT-PCR. 299

Figure 8-10: Spinal cord RNA integrity gels and characterisation of primers. ...300

Figure 8-11: Ponceau S staining of representative EV blots from Chapter 4. ...301

Figure 8-12: Ponceau S staining of representative EV blots for Chapter 5. 302

Figure 8-13: All total protein profiles from DTT studies. 303

Figure 8-14: All total protein profiles from the CQ study. 304

Figure 8-15: All total protein profiles from the MG132 study. 305

Figure 8-16: Full WBs for DTT studies. 305

Figure 8-17: Full WBs used for CQ EVs. 306

Figure 8-18: Full WBs used for MG132 EVs. 306

Figure 8-19: Full WBs for EVs from multiple steps. 307

Figure 8-20: Optimisation of the protein extraction method from tissue. 309

Figure 8-21: Ponceau S staining of tissue blots from Chapter 6. 310

Figure 8-22: Full WBs for tissue samples. 310

Figure 8-23: BLAST results for MBP isoform 1 and 4. 311

Figure 8-24: BLAST results for LDHA and LDHB. 311

Acknowledgements

Thank you to my supervisors Mark McLaughlin, Catherine Stalin, Richard Burchmore and Jim Anderson for sharing their support, encouragement and expertise, without which this project would not have been possible. During the COVID-19 pandemic, Mark, as my primary supervisor, went above and beyond to ensure this project was completed with me in one piece. I will be forever grateful for the patience that was shown by all, and I hope to implement this myself throughout my career and life. Thank you to the University of Glasgow (UoG) Veterinary Fund PGR Scheme who funded this project and many thanks to the annual reviewers and PGR convenors who have supported the progression of this work, namely Monika Mihm Carmichael, Collette Britton, Michelle Bellingham, Peter Hastie and Jo-Anne Murray.

Technical support was provided by numerous people over the last four years. Thank you to Ana Monteiro, Lynne Fleming and Marie Ward for sharing their expertise and taking the time to answer so many of my questions with a smile. To Jennifer Barrie and Roua Abulkassim, thank you for your training and advice in the early stages of this project and to Paul Montague for methodological assistance. Thank you to Ruben Riosa and Caroline Hutchinson for providing feedback on the case recruitment poster. Many thanks to the neurology staff and residents at the UoG Small Animal Hospital who helped me with the clinical side of things. Thank you to the owners who donated their animals to the study. Thank you to those within the Veterinary Diagnostic Service, particularly Frazer Bell and Lynn Oxford for their advice on tissue processing and histology, Veronica Patton, Gail Chapman, Angelika Rupp and Pamela Johnston for sharing their knowledge of pathology and for contributing to the review of this thesis (Pamela). Thank you to the Glasgow Polyomics team who helped to produce and assess the data presented in Chapter 6. A special thank you to Suzanne McGill who provided further training and guidance on proteomics.

Finally, working within the Physiology and Welfare group has been a joy and I have met so many lovely people at different stages of their career who have inspired me and whom I shall not forget; thank you!

Author's Declaration

I, Lauren Elaine Black, declare that the work presented in this thesis was carried out by myself, or with due acknowledgement, and has not been presented for the award of another degree at the University of Glasgow or any other university.

Signed:

Printed: LAUREN ELAINE BLACK

Abbreviations

%	percent
°C	degree Celsius
≥	greater than or equal to
≤	less than or equal to
μg	microgram
μl	microlitre
μm	micrometre
μM	micromolar
xg	relative centrifugal force
52A>T	alanine to thymine substitution at nucleotide 52
118G>A	guanine to alanine substitution at nucleotide 118
A4V	alanine to valine substitution at 4th codon (SOD1)
ABC	ammonium bicarbonate
AC	Akita cross dog
ACN	acetonitrile
ALIX	programmed cell death 6-interacting protein
ALS	amyotrophic lateral sclerosis
ANXA1	annexin A1
ApoE	apolipoprotein E
APS	ammonium persulphate
ASK1	apoptosis signal-regulating kinase 1
ATF3	activating transcription factor 3
ATF6	activating transcription factor 6
ATP	adenosine triphosphate
AU	arbitrary units
bps	base pairs
Bad	Bcl2-associated death promotor
BBB	blood-brain barrier
BCA	bicinchoninic acid
Bcl2	B-cell lymphoma 2 protein
BiP	immunoglobulin-binding protein
BMD	Bernese Mountain dog

BSA	bovine serum albumin
BXR	Boxer dog
C*n*	cervical spinal cord segment number *n*
C9orf72	chromosome 9 open reading frame 72 gene
Ca^{2+}	calcium ion
Caspr	contactin-associated protein 1
cDNA	complementary deoxyribonucleic acid
CHOP	CCAAT/enhancer binding protein homologous protein
CL	cell lysate
CNP	2′,3′-cyclic-nucleotide 3′-phosphodiesterase
CNS	central nervous system
CNX	calnexin
CO_2	carbon dioxide
CQ	chloroquine
CSF	cerebrospinal fluid
CSP	Cocker Spaniel
CTSD	cathepsin D
Cu^{2+}	cupric ion
Cu^{+}	cuprous ion
CuZnSOD	copper zinc superoxide dismutase
CV	cervical
Cyc	cyclophilin
D90A	aspartic acid to alanine substitution at 90th codon (SOD1)
DAPI	4′,6-diamidino-2-phenylindole
DM	degenerative myelopathy
DMEM	Dulbecco's Modified Eagle Medium
DMSO	dimethyl sulfoxide
DNA	deoxyribonucleic acid
DPBS	Dulbecco’s PBS
DTT	dithiothreitol
E40K	glutamate to lysine substitution at 40th codon (SOD1)
EAAT	excitatory amino acid transporter
ECL	enhanced chemiluminescence
ECSOD	extracellular superoxide dismutase

EDM	exosome-depleted medium
EDTA	ethylenediaminetetraacetic acid
EGFP	enhanced green fluorescent protein
EM	electron microscopy
ER	endoplasmic reticulum
EV	extracellular vesicle
fALS	familial amyotrophic lateral sclerosis
FBS	foetal bovine serum
FC	fold change
FTD	frontotemporal dementia
FUS	fused in sarcoma gene
g	gram
GAPDH	glyceraldehyde-3-phosphate dehydrogenase
gDNA	genomic deoxyribonucleic acid
GFAP	glial fibrillary acidic protein
GLAST	glutamate/aspartate transporter
GLT-1	glutamate transporter 1
GO	gene ontology
GP	Glasgow Polyomics
GSD	German shepherd dog
Hz	Hertz
H_2O_2	hydrogen peroxide
HCl	hydrochloric acid
HE	haematoxylin and eosin
HRP	horseradish peroxidase
HSP	heat shock protein
*Hyp*AV	restriction enzyme site present in WT *Sod*1
Iba-1	ionised calcium binding adaptor molecule 1
IHC	immunohistochemistry
ILV	intraluminal vesicle
iNOS	inducible nitric oxide synthase
IRE1	inositol-requiring enzyme 1
ISEV	International Society for Extracellular Vesicles
IVDD	intervertebral disc disease
kDa	kilodalton

KEGG	Kyoto Encyclopaedia of Genes and Genomes
L*n*	lumbar spinal cord segment number *n*
LC3	microtubule-associated protein light chain 3
LC	liquid chromatography
LC-MS	liquid chromatography-mass spectrometry
LC-MS/MS	liquid chromatography tandem mass spectrometry
LDELS	LC3-dependent EV loading and secretion
LDH	lactate dehydrogenase
LDHA	lactate dehydrogenase A chain
LDHB	lactate dehydrogenase B chain
LDS	lithium dodecyl sulfate
LMN	lower motor neurone
LN	liquid nitrogen
mA	milliampere
ml	millilitre
mm	millimetre
mM	millimolar
M	molar
MAG	myelin-associated glycoprotein
MBP	myelin basic protein
MEM	minimal essential medium
MES	2-(N-morpholino) ethanesulfonic acid
miRNA	micro ribonucleic acid
MISEV	Minimal Information for Studies of Extracellular Vesicles
MN	motor neurone
MND	Motor Neurone Disease
MnSOD	manganese superoxide dismutase
MOG	myelin-oligodendrocyte glycoprotein
MQ	milli-Q
MRI	magnetic resonance imaging
mRNA	messenger ribonucleic acid
MS	mass spectrometry
MSCs	mesenchymal stem cells
MV	microvesicle

MVB	microvesicular body
n	number of replicates
nm	nanometre
NaCl	sodium chloride
nLC-ESI-MS/MS	nanoflow high-performance liquid chromatography electrospray tandem mass spectrometry
NBT	nitro blue tetrazolium
NF	neurofascin
NfH	neurofilament heavy polypeptide
NfL	neurofilament light polypeptide
NfM	neurofilament medium polypeptide
NGM	normal growth medium
NO	nitric oxide
NSE	neurone specific enolase ***or*** γ-enolase
NTA	nanoparticle tracking analysis
ORF	open reading frame
O_2	molecular oxygen
O_2^-	superoxide free radical
p	*p*-value
PB	phosphate buffer
PBD	Pitbull dog
PBM	Pitbull Mastiff mix dog
PBS	phosphate buffered saline
PCR	polymerase chain reaction
PDI	protein disulfide isomerase
pDM-SOD1-EGFP	fluorescent-tagged DM *Sod*1 expression vector
pEGFP-C3	fluorescent-tagged expression vector
PERK	protein kinase R-like ER kinase
PFA	paraformaldehyde
pmol	picomole
PLP	proteolipid protein
PLS	primary lateral sclerosis
PMSF	phenylmethylsulfonyl fluoride
PNS	peripheral nervous system
PSMA1	proteasome subunit α type 1

Pst1	restriction enzyme site present in unspliced *XBP1*
PTM	post translational modification
PWC	Pembroke Welsh Corgi
pWT-SOD1-EGFP	fluorescent-tagged WT *Sod*1 expression vector
RFLP	restriction fragment length polymorphism
RNA	ribonucleic acid
ROS	reactive oxygen species
rRNA	ribosomal ribonucleic acid
RT-PCR	reverse transcription polymerase chain reaction
S100ß	S100 calcium binding protein ß
sALS	sporadic amyotrophic lateral sclerosis
SBT	Staffordshire Bull Terrier
SD	standard deviation; σ in equation
SDS	sodium dodecyl sulfate
SDS-PAGE	SDS-polyacrylamide gel electrophoresis
SEM	standard error of the mean
SN	supernatant
SNP	single nucleotide polymorphism
SOD1	superoxide dismutase 1 (protein)
*SOD*1	superoxide dismutase 1 gene (human)
*Sod*1	superoxide dismutase 1 gene (animal)
SOD2	superoxide dismutase 2
SOD3	superoxide dismutase 3
SOP	standard operating procedure
SP110	SP110 nuclear body protein gene
SSIII	SuperScript III Reverse Transcriptase
SSIV	SuperScript IV Reverse Transcriptase
SSPCA	Scottish Society for Prevention of Cruelty to Animals
STWS	Scott’s tap water substitute
T18S	threonine to serine substitution at 18th codon (SOD1)
TARDBP	Tar DNA-binding protein gene
TBE	Tris-borate-EDTA
TCA	Trichloroacetic acid
TDP43	Tar DNA-binding protein 43
TEMED	tetramethylethylenediamine

TFA	trifluoracetic acid
TM	total media
TMT	tandem mass tag
T*n*	thoracic spinal cord segment number *n*
TH	thoracic
tRNA	transfer ribonucleic acid
TSG101	Tumour suppressor gene 101
T-TBS	Tris-buffered saline with Tween 20
UK	United Kingdom
UKN	unknown
UMN	upper motor neurone
UoGSAH	University of Glasgow Small Animal Hospital
UPR	unfolded protein response
UPS	ubiquitin-proteasome system
USA	United States of America
UV	ultraviolet
V	volts
VDS	Veterinary Diagnostic Services
WB	Western blot
WT	wildtype
XBP1	X-box binding protein 1
XBP1s	X-box binding protein 1 spliced nucleic acid
XBP1t	X-box binding protein 1 total nucleic acid
XBP1u	X-box binding protein 1 unspliced nucleic acid

1 Introduction

1.1 Canine degenerative myelopathy

1.1.1 Etymology of canine degenerative myelopathy

Canine degenerative myelopathy (DM) was first reported in the early 1970s (Averill, 1973), however there have been several names introduced over the decades. Chronic ossifying pachymeningitis, chronic degenerative radiculomyelopathy (Griffiths and Duncan, 1975), German shepherd dog myelopathy (Braund and Vandevelde, 1978) and progressive myelopathy (Waxman *et al.*, 1980) have all been used to varying extents. Initial descriptions of the clinical signs centred around the progressive weakness, ataxia and proprioceptive deficits in the pelvic limbs of adult dogs, primarily belonging to large breeds (Griffiths and Duncan, 1975). Chronic ossifying pachymeningitis was disregarded early on as it implied bone plaques found in the spinal dura influenced the development of DM, a finding not supported by Averill (1973) or Griffiths and Duncan (1975). It is now widely accepted that these bone plaques (technically known as dural ossification or ossifying pachymeningitis) are normal, incidental findings common in older dogs that rarely associate with a particular disease (Miller, 2013). Chronic degenerative radiculomyelopathy, until fairly recently, was believed to be a particular subgroup of degenerative myelopathy where the lack of reflexes in the pelvic limbs was observed due to the involvement of nerve roots (Coates *et al.*, 2007). It is now generally considered that hyporeflexia of the pelvic limbs may or may not be present in DM dogs and there is no differentiation into subgroups. In the historical reports, DM was predominantly studied in the German shepherd dog (GSD), but it was suspected to affect other large breeds (Braund and Vandevelde, 1978) and has since been found in many breeds, large and small (Coates and Wininger, 2010). Now, (canine) degenerative myelopathy is the most frequently used term for the disease.

1.1.2 Signalment of DM

1.1.2.1 Breed distribution

DM has been histopathologically confirmed in over 24 breeds including the Bernese Mountain dog (BMD), Boxer (BXR), GSD, Golden Retriever, Miniature Poodle, Pembroke Welsh Corgi (PWC), Rough Collie and Siberian Huskey. Mixed breeds, large and small, have also had a confirmed DM diagnosis. DM has been presumptively diagnosed in nine other breeds including the Great Dane and Labrador Retriever (Coates and Wininger, 2010; Ivansson *et al.*, 2016; Kohyama *et al.*, 2017). The susceptibility of developing DM appears to vary between breeds (Zeng *et al.*, 2014) with the GSD, PWC, BXR, Rhodesian ridgeback and Chesapeake Bay retriever being diagnosed most frequently (Awano *et al.*, 2009). The GSD is known to be particularly susceptible to DM and it is the main cause of premature death in the breed (Holder *et al.*, 2014). In a study of dogs presented to American veterinary teaching hospitals in the 1990s, the overall prevalence of DM was 0.19%. DM was most prevalent in GSDs at 2.01% then the Cardigan Welsh Corgi at 1.51%. In the same study, DM was thought to have a prevalence of 0.58% in the PWC (Coates *et al.*, 2007), a possibly out of date finding given the number of publications studying DM in the breed.

1.1.2.2 Age and sex of affected dogs

Dogs are usually at least eight years old when diagnosed with DM (Coates and Wininger, 2010). In larger breeds, the mean age of onset is nine years old and in smaller breeds, for example the PWC, the mean age is eleven years old (Story *et al.*, 2020). There have been no reports of a predisposition to DM based on sex or neuter status so far (Coates and Wininger, 2010).

1.1.3 Clinical signs of DM

The clinical signs observed in DM can be separated into four main stages that represent early and late phases of the disease (Coates and Wininger, 2010). The characteristic symptoms that define each stage are summarised in Table 1-1 along with the type of motor neurones (MNs) affected.

Table 1-1: Main clinical signs defining the different stages of DM.

DM stage	DM phase	Months post-onset	Limb group(s) affected	Prominent clinical observations
1	Early	6 to 12	Pelvic	Asymmetric UMN spastic paraparesis and general proprioceptive ataxia of pelvic limb(s)
2	Early	9 to 18	Pelvic	LMN paraparesis progressing to paraplegia in pelvic limbs
3	Late	14 to 24	Pelvic and thoracic	LMN flaccid paraplegia and muscle atrophy in pelvic limbs with the development of weakness in thoracic limbs
4	Late	>36	Pelvic and thoracic	LMN flaccid tetraplegia, severe widespread muscle atrophy and difficulties swallowing or moving tongue indicating brain stem involvement

Listed in the table are the 4 main stages of DM, the defining clinical signs for each stage and when, post-onset, they are frequently observed. Stages 1 and 2 make up the early phase of DM while stages 3 and 4 are assigned to the late phase. Stage 4 is also known as the endpoint of the disease. Based on information from Coates and Wininger (2010). UMN= upper motor neurone; LMN= lower motor neurone.

1.1.3.1 Early DM

The earliest clinical signs of DM are general proprioceptive ataxia and mild spastic paresis of the pelvic limbs. Upon examination, paws have worn nails and abrasive lesions due to proprioceptive defects in the pelvic limbs which is often asymmetrical. Eventually, this stage ends when non-ambulatory paraparesis occurs and is often the stage when euthanasia is elected because dogs cannot weight bear in their pelvic limbs (Coates and Wininger, 2010). Various reflexes may be affected, for example, spinal reflexes are often abnormal and are consistent with signs of UMN lesions in the T3 to L3 region of the spinal cord. The patellar stretch (myotatic) reflex may be normal or abnormal. An abnormal patellar reflex in this case is exaggerated or clonic, where there is repeated involuntary contractions and relaxations from a muscle group, or there is hyporeflexia. The latter could be due to inhibition of afferent sensory signals along the femoral nerve, or it could be an artefact of normal age-related changes in older dogs. Lastly, the flexor (withdrawal) reflex is usually normal or there is evidence of cross extension, where extension of the limb opposite the flexing limb occurs. This can suggest chronic UMN dysfunction as there is no inhibition of extension in the opposite limb (Coates and Wininger, 2010).

1.1.3.2 Late DM

If the disease is allowed to progress to the later stage, paraplegia due to LMN involvement ensues and signs spread to the thoracic limbs. Hyporeflexia of the patellar and flexor (withdrawal) reflexes occurs which is indicative of LMN involvement. Eventually in advanced disease, flaccid tetraplegia occurs with a more symmetrical distribution. Muscles atrophy first in the pelvic limbs when they are no longer able to weight bear, then in all limbs, primarily due to disuse. In late DM there is severe loss of muscle from limbs and it has been suggested that this occurs because of denervation of the muscles (Coates and Wininger, 2010). Urinary and faecal continence is usually maintained until paraplegia and the former appears to be more commonly affected in some studies. Kobatake *et al.* (2021) found urinary and faecal incontinence in 77.5% and 42.5% of DM cases respectively and suggest the lower percentage for the latter is due to increased autonomic nervous system control in the process. Urination and defecation are controlled by neurones in the peripheral autonomic system, spinal cord and the brainstem. In the same study, there was further evidence of brainstem involvement when a small percentage of dogs developed symptoms including dysphagia (swallowing problems), dysphonia (vocal problems), tongue spasms and paralysis of cranial nerves (Kobatake *et al.*, 2021).

Failure in the respiratory system is the natural endpoint for the disease and it has been suggested that due to problems with the intercostal muscles, efficient thoracic expansion is compromised, leading to hypoventilation and hypoxemia. In these later stages, there may be an increase in abdominal respiration as the diaphragm compensates for reduced thoracic expansion (Oyake *et al.*, 2016). The onset of respiratory dysfunction can be correlated with disease duration. It is also possible that respiratory dysfunction contributes to dysphonia observed in some cases (Kobatake *et al.*, 2021).

1.1.4 Histopathology

DM has been described as a primary central axonopathy restricted to the spinal cord but it has been suggested that this description be expanded to a multisystem, diffuse, central and peripheral axonopathy (Coates and Wininger, 2010). Pathological changes have been noted at varying frequencies in the brain, spinal cord, peripheral nerves and muscles.

1.1.4.1 General lesions observed in DM

Characteristic lesions include the degeneration of axons and myelin in the spinal cord and may be visualised as myelin sheath dilation (March *et al.*, 2009), axon cylinder vacuolisation, dropout and swelling (spheroid bodies) and digestion chambers (Wininger *et al.*, 2011). Lost axons and myelin may be replaced by astrogliosis and these areas can be large, and macrophages may be present to fragment and phagocytose myelin and axon debris. This is thought to be a secondary response to the neurodegenerative processes occurring, so DM is generally not considered an inflammatory disease. Chromatolysis has been recorded in the grey matter of the spinal cord (Coates and Wininger, 2010; Ogawa *et al.*, 2014). There are varying reports regarding the sparing or loss of neurones in DM (Coates and Wininger, 2010) and this may reflect the disease progression to the terminal phase of disease (Morgan *et al.*, 2014).

1.1.4.2 Distribution of lesions in the spinal cord

The most severely affected area of the spinal cord is the mid to caudal region of the thoracic segment, particularly T12 (March *et al.*, 2009), but the general longitudinal distribution of lesions along the spinal cord changes as the disease progresses. Pathology spreads cranially to the cervical segments and caudally to the lumbar segments. There are a range of hypotheses explaining why the thoracic cord is most affected, one suggesting there is reduced perfusion of this segment, potentially leaving the thoracic cord more susceptible to ischemic processes such as oxidative stress and excitotoxicity (Coates and Wininger, 2010).

From early descriptions, DM has been identified as a degenerative disease affecting both motor and sensory tracts and dorsal nerve roots (Griffiths and Duncan, 1975). Lesions can be observed in all funiculi encompassing general proprioceptive sensory, somatosensory and motor tracts. Lesions may be more severe in the dorsal portion of the lateral funiculus which houses several ascending and descending tracts including the descending lateral corticospinal tract, descending medullary reticulospinal tract, descending rubrospinal tract and ascending dorsal spinocerebellar tract. Of note, the latter tract ultimately takes information from muscle spindles of the pelvic limbs to the cerebellum via the spinal ganglia. Lesions may also be observed in the dorsal funiculus, particularly in the fasciculus gracilis. Here the fibres ascend to the medulla of the brain and synapse in the nucleus gracilis. This tract therefore communicates signals regarding touch, pressure and joint proprioception from the pelvic region to the brain. Combined, increased lesion severity in these areas would explain the clinical signs of dysfunctional general proprioception and paraparesis. In addition, spread of lesions along the ascending general proprioceptive and descending UMN pathways in the cervical regions of the spinal cord would explain the tetraparesis and ataxia. Urinary and faecal incontinence is observed in some dogs and may be due to lesions in the dorsal funiculus in the thoracic, lumbar or sacral regions of the spinal cord, regions that contain the sensory pathways informing the brain of colorectal or bladder distension, but urinary incontinence may also indicate LMN involvement (Coates and Wininger, 2010).

Evidence of sensory involvement was provided by Morgan *et al.* (2014) who found an approximate 20% reduction in dorsal root axons of a thoracic segment in late stage DM PWCs and dorsal root ganglion neurones had pyknotic nuclei and condensed cytoplasm (Morgan *et al.*, 2014). In the ventral aspect of the spinal cord, where efferent signals are sent to the muscles through LMNs, ventral horn neurones generally appear normal or may have some axon loss. In some studies, a reduction in the number of neurones in the ventral horns of cervical, thoracic and lumber segments has been found in addition to the presence of chromatolysis and lipofuscin in neurones, although the lipofuscin may be an age-related change. In one study, there was an approximate 50% reduction in neuronal synapses, particularly in the ventral horns and astrocytes and microglia could be found throughout the white and grey matter (Ogawa *et al.*, 2014).

Loss of MNs from the thoracic cord and lesions in the ventral roots have been observed in studies where samples are acquired from terminal cases of DM (Ogawa *et al.*, 2014). The terminal stage is where respiratory function is compromised, causing mortality, and is only really seen in some cultures where euthanasia is not a commonly elected practice (Morgan *et al.*, 2014).

There is some variation in the lesion severity and funicular distribution between breeds (March *et al.*, 2009). In GSDs, there are discontinuous, multifocal areas of axon degeneration and myelin loss. In PWCs, lesions are more continuous and are present in more defined funicular areas. The difference between breeds may be down to the fact that smaller breeds are generally able to be kept alive for longer, allowing lesions to become more severe (Coates and Wininger, 2010).

1.1.4.3 Lesions observed in the brain and brainstem

This area of DM research has not been extensively investigated and findings vary between studies. Some report no changes in the brain while others have noted changes in the brainstem and cerebellum. Specifically, the nucleus gracilis (Griffiths and Duncan, 1975), red and lateral vestibular nuclei of the brainstem and the dentate and fastigial nuclei of the cerebellum (Coates and Wininger, 2010; Johnston *et al.*, 2000) have shown evidence of neurone degeneration and loss accompanied by gliosis (Johnston *et al.*, 2000).

1.1.4.4 Distribution of lesions in peripheral nerves and muscles

As previously noted, LMN signs occur later in disease suggesting a progression of DM pathology to the peripheral nervous system (PNS). Studies of peripheral pelvic nerves and muscles have demonstrated a progressive deterioration of the PNS and muscle atrophy in BXRs and PWC. Due to axonal degeneration in both breeds, demyelination in PWCs, and alterations to the muscle fibres, it is thought atrophy occurs by denervation due to defective LMNs (Shelton *et al.*, 2012). A later study investigating intercostal muscles in the same breeds found there is evidence of muscle atrophy, fibrosis and changes in muscle fibre morphology in the late stages of DM, although this may differ between breeds, but there was no apparent loss of UMNs from the thoracic cord or detachment of

LMN terminals from the muscle fibres. This implies the muscle pathology is not caused by physical denervation but functional deficits in MNs (Morgan *et al.*, 2013) which can include problems with axon transport and mitochondrial function (Morgan *et al.*, 2014). As the pelvic limbs are affected much earlier in the disease than the respiratory muscles, it is possible that these findings merely represent an earlier stage of the muscle atrophy process (Morgan *et al.*, 2013). As the study by Morgan *et al.* (2014) was conducted on cases before they reached the terminal stage, it could be concluded that muscle atrophy comes before MN loss in intercostal muscles, but it is difficult to make this assumption for other muscles, especially the pelvic limbs as they are usually in the advanced stage of disease when dogs are euthanised. It is also possible for mitochondria in muscles themselves to become compromised and contribute to secondary MN dysfunction (Corti *et al.*, 2009).

1.1.4.5 Discussion surrounding MN degeneration

Pathologically, axon and myelin degeneration and astrogliosis were noted early in the dorsal and dorsolateral columns, fasciculus gracilis and nucleus gracilis of the brainstem. It was described as a “dying-back” disease because the distal portion of the longest and largest diameter afferent nerves showed degeneration in the direction towards the neurone cell body. This is also why it was considered to primarily affect larger breeds (Griffiths and Duncan, 1975). In studies investigating DM in GSDs, this dying-back theory and the presence of Wallerian degeneration is generally supported (Johnston *et al.*, 2000), however in studies looking at DM in PWCs, opinions vary (Coates and Wininger, 2010).

Pathology in the brain reported in GSD DM supports the dying-back theory with Wallerian degeneration. Johnston *et al.* (2000) suggested there is an unknown deficit in the neurone cell body which may affect axonal transport of components to the distal portion of the axon, resulting in degeneration. As the disease progresses, neuronal cell bodies may also deteriorate. As significant brain pathology has not been identified in PWC DM, the dying-back theory of degeneration does not account for all pathology observed in the breed as the brainstem and cerebellum are the areas where many proprioceptive tracts terminate. Compared to the multifocal and discontinuous nature of GSD DM, PWC DM may have a more continuous distribution of lesions throughout the spinal cord tracts meaning segmental degeneration may play a larger role than Wallerian degeneration. This may imply that supporting cells like oligodendrocytes or astrocytes are defective in DM or that both anterograde and retrograde axonal transport is disrupted (Coates and Wininger, 2010; March *et al.*, 2009). Coates and Wininger (2010) state that spheroid bodies are not frequently observed in DM, however this may be the case for PWC as opposed to GSD DM, where they could be considered a hallmark (Johnston *et al.*, 2000).

1.1.5 Diagnosis and prognosis of DM

1.1.5.1 Diagnosis

DM may account for 1-5% of referrals to neurologists (Miller *et al.*, 2009) and is presumptively diagnosed by a process of elimination of other diseases causing the same clinical signs. These diseases include, but are not limited to, spinal cord neoplasia, intervertebral disc disease (IVDD), degenerative joint diseases, neuromuscular diseases and meningitis. As DM is associated with older dogs and aging is associated with neurological and orthopaedic diseases, these factors could impede the proper interpretation of clinical signs. One way to distinguish orthopaedic disease from neurological disease is to test the proprioceptive positioning of a dog’s paw. In orthopaedic disease, this reflex will be normal as there is no weight bearing involved with the test (Coates and Wininger, 2010). Definitive diagnosis can only be provided after post-mortem examination of spinal cord histopathology (Story *et al.*, 2020).

Magnetic resonance imaging (MRI) and myelography can rule out compressive myelopathies including IVDD but these can be concurrent with DM. MRI can also identify neoplasia. Electromyography abnormalities are not often detected in early stages of DM but do occur in later stages and indicate LMN involvement in disease. Changes include multifocal spontaneous activity in distal limb muscles and in the tibial and ulnar nerves there is reduced M wave amplitude and reduced conduction velocity in MNs when compared to normal reference ranges. The M wave amplitude reduction indicates there is denervation and motor axonopathy and reduced MN conduction velocity indicates there is peripheral demyelination (Awano *et al.*, 2009; Coates and Wininger, 2010).

Cerebrospinal fluid (CSF) and blood can be tested to rule out meningitis and ensure there are no other biochemical changes that could be causing the clinical signs (Coates and Wininger, 2010). A study in 2009 identified a mutation in the *Sod*1 gene, located on chromosome 31 (CFA31) which can be strongly associated with DM (Awano *et al.*, 2009) and a later study suggested another mutation in the same gene may influence development of DM in BMDs (Wininger *et al.*, 2011). This provided the opportunity for genetic testing for mutations in the *Sod*1 gene to identify the risk of developing DM, but unfortunately it cannot diagnose the disease by itself (Story *et al.*, 2020). Specific biomarkers for DM have not been fully characterised, however potential candidates have been identified (Shafie *et al.*, 2014).

1.1.5.2 DM progression and management

The progression of DM in smaller breeds may be slower than in larger breeds and the pathology noted varies within and between breeds, suggesting there may be different phenotypes of DM (Coates and Wininger, 2010; Story *et al.*, 2020). The mean period of disease duration is six months for larger breeds which generally coincides with the election of euthanasia. This is because, within six to nine months of initial clinical symptoms, even though dogs can still move their pelvic limbs, they can no longer support their weight in the pelvic limbs (non-ambulatory paraparesis), therefore requiring walking assistance. In smaller breeds, it is easier to support dogs at this stage and so disease duration tends to be longer. Generally, in the PWC, the average disease duration is 19 months (Coates and Wininger, 2010), but in some studies, particularly in countries where cultural norms view euthanasia less favourably (Sugita and Irimajiri, 2016), it can be as long as 36 months on average (Kobatake *et al.*, 2021). If euthanasia is chosen in these breeds, thoracic limbs will often also display clinical signs (Coates and Wininger, 2010). If euthanasia is not selected, respiratory failure is more likely to develop (Oyake *et al.*, 2016). DM can last for over three years if symptoms are managed (Awano *et al.*, 2009).

Currently, DM treatment strategies aim to improve quality of life. Various drugs, immunotherapies and nutritional supplements have been tested but they have little to no effect on DM disease progression. Preliminary investigations studying intensive physiotherapy have found that it can slow the progression of DM as patients live significantly longer than those with moderate or no physiotherapy. As DM can present in many different ways, it is likely that a multidisciplinary approach to treatment will be most effective (Coates and Wininger, 2010).

1.2 Human amyotrophic lateral sclerosis

Links were made between the pathologies observed in DM and the human motor neurone disease (MND) amyotrophic lateral sclerosis (ALS; also Lou Gehrig disease) as far back as 1975 by Griffiths and Duncan. The involvement of *Sod*1 mutations in DM, coupled with other clinical and histological similarities, led to the speculation that DM may be similar to some forms of human ALS (Awano *et al.*, 2009; Coates and Wininger, 2010).

MND is an umbrella term that includes several diseases that affect somatic MNs (Gois *et al.*, 2020). MND is often thought of as a spectrum and ALS is the most common form (Leighton *et al.*, 2019). There are two main branches of ALS: sporadic (sALS) and familial (fALS). The former accounts for 90% to 95% of cases (Chen *et al.*, 2019). There are no obvious differences in clinical symptoms between sALS and fALS, suggesting there may be similarities in the pathological mechanisms (Hanspal *et al.*, 2017). The age at onset with sALS is frequently between 58 and 63 years old, and fALS between 47 and 52 years old (Kiernan *et al.*, 2011). The estimated median prevalence is 5.4 cases per 100,000 people (Hosaka *et al.*, 2019). In Scotland between 2015 and 2017, the incidence was 3.8 per 100,000 person-years. The prevalence of ALS has increased in the last 25 years and is thought to be due to better diagnostic criteria and identification of the disease due to more genes being associated and could also be a reflection of increased survival rates for other age-related diseases including heart disease (Leighton *et al.*, 2019). Different geographical regions may have different rates of disease and this may be contributed to by the reduced presence of ALS associated genes in different populations (Longinetti and Fang, 2019).

1.2.1 Clinical signs of ALS and phenotypic variations

Characteristic signs early in disease are muscle weakness, twitching and cramping (Story *et al.*, 2020). Symptoms at onset are representative of a local pathology but as the disease progresses throughout the CNS, signs become more widespread (Hanspal *et al.*, 2017; Urushitani *et al.*, 2006). In all cases, as disease progresses, dysphagia (swallowing difficulties) and dyspnoea (laboured breathing) become more apparent if they were not initially present (Story *et al.*, 2020) and complete paralysis and respiratory failure are observed (Berdyński *et al.*, 2022). It is thought respiratory failure is the result of MN denervation of the diaphragm and muscles of the chest (Kobatake *et al.*, 2021). In ALS, some patients experience sensory clinical signs including numbness in the legs (Morgan *et al.*, 2014). Cognitive impairments can be observed; around 30% of ALS patients also develop frontotemporal dementia (FTD) and around 15% of patients with FTD also develop ALS, indicating there is an overlap between the two diseases and suggesting they are comorbidities. Disease duration can differ by over a year when patients have the comorbidity or ALS alone (Ravits *et al.*, 2013). ALS is a multisystem disease (Chen *et al.*, 2019) and non-MN specific signs can be observed including weight loss, hypermetabolism and hyperlipidaemia. These signs suggest there are problems with energy metabolism in ALS patients, possibly due to the involvement of non-motor brain regions, for example the hypothalamus, and/or because ALS is not just a nervous system disease (Ravits *et al.*, 2013).

ALS can be further grouped into phenotypic variants based on the location of symptoms at onset and the dominating group of MNs affected. ALS is often thought of as a spectrum; each case will have different levels of UMN and LMN involvement and it will affect some regions of the body more than others, potentially influencing progression. Typical ALS is defined by the involvement of both UMN and LMN dysfunction causing weakness. It can be further divided into bulbar-onset and limb-onset ALS, depending on the location where clinical signs first appeared. Some cases of ALS have predominantly UMN or LMN involvement and are differentiated with specific names: primary lateral sclerosis (PLS) and progressive muscular atrophy respectively. It is not yet clear if typical ALS is a spectrum, or if it consists of separate, distinct diseases; currently, they all fall under the ALS umbrella. While the location of pathology may vary between the phenotypes, the actual pathology or mechanisms involved appear to be similar (Ravits *et al.*, 2013). Phenotypic variations can occur within families with the same causal genetic mutation suggesting there are additional modifying genes or mechanisms involved in ALS development and progression (Van Damme, Robberecht and Van Den Bosch, 2017).

1.2.2 Typical histopathology of ALS

The name of the disease itself indicates some of the common clinical and histopathological features; “amyotrophic” refers to the muscle atrophy observed due to denervation as a result of neuronal degeneration and “lateral sclerosis” refers to the “hardening” of the lateral and posterior spinal cord tracts due to gliosis (Story *et al.*, 2020). Selective MN death occurs in the spinal cord, brainstem and cortex of patients (Lee *et al.*, 2016) leading to MN loss (Otake, Kamiguchi and Hirozane, 2019). Wallerian and axonal degeneration can occur in UMNs and LMNs and occur in pathways that are projected out from the MNs. UMN pathways in the corticospinal tract of the lateral spinal cord thin and harden while anterior root and peripheral nerve axons degenerate, causing muscle denervation (Ravits *et al.*, 2013). In PLS, it is mainly the corticospinal and corticopontine MNs that are affected and in bulbar- and pseudobulbar-onset ALS, changes can be associated with specific cranial nerves or the UMNs associated with these nerves (Story *et al.*, 2020). Muscle weakness and wasting are often not identified until at least 30% of the anterior horn neurones have degenerated (Hosaka *et al.*, 2019). There is a neuroinflammatory process that is activated when MNs die; astrocytes, microglia and oligodendrocytes proliferate (Story *et al.*, 2020). One of the pathological hallmarks of fALS in particular is the accumulation and aggregation of mutant protein in the cytoplasm of MNs and other CNS cells (Lee *et al.*, 2016; Story *et al.*, 2020). As cognitive and behavioural changes are present in some ALS patients, it suggests that MNs are not the only cell type affected and not the only factor contributing to disease (Ravits *et al.*, 2013).

1.2.3 ALS diagnosis and prognosis

The current diagnostic criteria are not too dissimilar from DM; diagnosis is by elimination of diseases that produce similar clinical signs. Clinical findings, genetic testing and electrophysiological examination are major players as there is a lack of specific biomarkers. Unfortunately, there is often a delay in diagnosis which may not be given until six to eighteen months after initial presentation (Hosaka *et al.*, 2019; Story *et al.*, 2020). ALS is diagnosed when there are UMN and LMN signs that progressively worsen over time. UMN signs used for ALS diagnosis include hyperreflexia, increased muscle tone and slowing down of movement, while LMN signs include involuntary muscle contractions (fasciculations) and muscle wasting (Van Damme, Robberecht and Van Den Bosch, 2017).

ALS usually causes death within three to five years of initial onset (Chen *et al.*, 2019), but in around 50% of cases, patients can die within three years of initial onset (Kiernan *et al.*, 2011). Around 10% of ALS cases are slow to progress and can extend disease duration to over a decade (Longinetti and Fang, 2019). There is no prevention or cure for ALS and treatment requires a multidisciplinary approach which includes medicinal, nutritional and respiratory support in addition to the management of associated symptoms (Van Damme, Robberecht and Van Den Bosch, 2017). The number of licensed drugs available for ALS globally are limited and only increase survival by a matter of months (Miller, Mitchell and Moore, 2012). Approximately fifty randomised controlled trials for ALS disease modifying treatments have failed in the same number or years. The lack of a biomarker for the pathological mechanisms involved could be an integral part of this statistic due to the inability to efficiently track disease progression (Otake, Kamiguchi and Hirozane, 2019).

1.2.4 Methods for investigating ALS

There are many ways to study ALS *in vitro* and this can include the manipulation of genes in yeast, the study of different pathways in rodent MN primary cell culture and the culture of induced pluripotent stem cells from ALS patients (Bonifacino *et al.*, 2021; Van Damme, Robberecht and Van Den Bosch, 2017). *In vitro* cell cultures are relatively easy to maintain in the laboratory and reduce the use of animals in research. They allow investigation of specific cell or tissue mechanisms and single body systems in a controlled environment. Also, the genes of cells in culture can be easily manipulated (Gois *et al.*, 2020). One disadvantage of cell culture models is the difficulty to recreate the complex interactions that occur during disease in the human body (Van Damme, Robberecht and Van Den Bosch, 2017). Also, genes often need to be overexpressed, meaning the protein levels are above physiological norms (Crisp *et al.*, 2013).

Many small animal and rodent models are used in ALS research and they are beneficial for unbiased genetic screenings of ALS causal genes and proof-of-concept studies. Small animal models, including *Drosophila melanogaster*, *Caenorhabditis elegans* and *Danio rerio* are often used to generate hypotheses which can be validated with larger models including rodents, pigs and nonhuman primates, which have a more complex body system more akin to the human (Van Damme, Robberecht and Van Den Bosch, 2017). All animal models have their advantages and disadvantages including ethical considerations. Another limitation with these models is translating results into the clinical setting for human ALS patients (Van Damme, Robberecht and Van Den Bosch, 2017). For example, overexpressing genes, mutant or WT, leads to non-physiological levels of proteins (Crisp *et al.*, 2013), potentially resulting in cell toxicity (Van Damme, Robberecht and Van Den Bosch, 2017).

Canines are often predisposed to the same morbidities affecting humans (Ivansson *et al.*, 2016). Dogs share the same environment as their owners and are thus exposed to the same environmental risks. They have access to clinics that are often as robust as human clinics, making the canine an alluring model for some human diseases. Dogs have a brain and spinal cord that shadows the size, volume and complexity of the human brain and spinal cord relatively well. Cognition in dogs is also more akin to that of a human. The genome is relatively similar between the two species and dogs, compared to laboratory mice, are well outbred. Dogs also have a longer lifespan compared to mice, allowing a greater temporal analysis of disease (Coates and Wininger, 2010; Story *et al.*, 2020). Additionally, in ALS, tissue samples are usually collected post-mortem when patients have reached the endpoint of the disease, but in DM, dogs may be euthanised at various stages, allowing for better analysis of disease progression (Morgan *et al.*, 2013). In terms of drug development, the body size, body weight, metabolism and pharmacodynamics of a dog's system opens the possibility for more reliable surgical directions and therapeutic testing. The use of dogs as an animal model has already led to the development of several therapies in humans and other animals for various diseases, including those of oncogenic (Crisp *et al.*, 2013), neurodegenerative and musculoskeletal nature (Story *et al.*, 2020).

It is hoped that DM dogs can help to better understand ALS pathogenesis and identify modifier loci and environmental factors that may influence the development of the disease (Awano *et al.*, 2009). Additionally, the veterinary field can benefit from the intense research conducted on ALS. There are some differences however between ALS and DM; ALS primarily affects the motor tracts and have evidence of neurone cell body degeneration and loss at the anterior horn, whereas DM predominantly affects proprioceptive pathways and UMN tracts (Wininger *et al.*, 2011). When clinical and histopathological findings are considered together, DM is most similar to PLS fALS (Story *et al.*, 2020).

1.3 Potential risk factors for DM and ALS

DM is thought to be a multifactorial disease as vascular, immunologic, metabolic, nutritional, genetic, excitotoxic and oxidative stress factors have been implicated (Coates and Wininger, 2010; March *et al.*, 2009; Story *et al.*, 2020). Some of the contributing factors have also been found in ALS meaning there could be value in exploring many of the areas in DM.

1.3.1 Non-genetic risk factors

Age is considered one of the biggest risk factors for ALS (Hosaka *et al.*, 2019) and DM (Draper *et al.*, 2020) development. There are many environmental risk factors that have been attributed to ALS development including exposure to heavy metals, pesticides, fertilizers, radiation and other pollutants found in the atmosphere. Lifestyle choices, such as cigarette smoking, can increase risk of ALS as well as previous military service, trauma and general physical activity (Gois *et al.*, 2020; Story *et al.*, 2020). As dogs share the same environment as humans, it would be interesting to see if the same nongenetic risk factors affect predisposition to DM.

1.3.2 Genetic risk factors

1.3.2.1 *Sod*1 mutations in DM

As previously introduced, two mutations in the *Sod*1 gene have been found to be strongly associated with development of DM (Awano *et al.*, 2009; Wininger *et al.*, 2011). There have been reports of familial DM in some breeds including the PWC and Siberian Huskey, further suggesting a role of genetics. The late onset of DM makes it difficult to fully explore the heritability of the disease as parents and siblings may not be available to test (Coates and Wininger, 2010).

The main *Sod*1 mutation strongly associated with DM consists of a single nucleotide transition from guanine to adenine at nucleotide 118 (*Sod1:c.118G>A*). This corresponds to a missense mutation in the amino acid sequence E40K, where the glutamate (E) at position 40 becomes lysine (K) (Awano *et al.*, 2009). This mutation has been found in at least 124 breeds but has only been associated with DM in a few breeds including the BXR, GSD and PWC (Coates and Wininger, 2010; Ivansson *et al.*, 2016; Zeng *et al.*, 2014). Homozygosity for this mutation does not always result in DM but it puts dogs at greater risk of developing it. *Sod1:c.118G>A* DM is often described as autosomal recessive with age related incomplete penetrance because of the abundance of homozygotes affected (Awano *et al.*, 2009; Draper *et al.*, 2020; Qi *et al.*, 2019). Dogs heterozygous for the mutation or homozygous for the WT gene are less likely to develop DM (Coates and Wininger, 2010). Some asymptomatic heterozygotes have histological changes associated with DM suggesting that in these animals, DM progresses too slowly to present itself with symptoms (Awano *et al.*, 2009). As both homozygotes and heterozygotes can develop DM, genetic tests for *Sod*1 mutations can only estimate the risk of DM development (Coates and Wininger, 2010). Heterozygotes are carriers of the mutation meaning the mutation may be passed on to offspring while WT homozygotes are able to pass on a protective WT allele to their offspring (Coates and Wininger, 2010).

Other genes may be responsible for causing DM in Labrador Retrievers and Golden Retrievers as the *Sod*1*:c.118*A mutation has not yet been identified in these breeds (Broeckx *et al.*, 2013). A breed specific *Sod*1 mutation has been associated with DM in BMDs and it may be associated with slower progressing disease. It consists of an adenine to thymine transversion at nucleotide 52 (*Sod1:c.52A>T*) which predicts an amino acid substitution, T18S, of a threonine (T) at position 18 to a serine (S) (Wininger *et al.*, 2011). Some BMDs are compound heterozygotes where they are heterozygous for both the *Sod1:c.118A* and *Sod1:c.52T* allele but only a minority of these dogs develop DM. Homozygosity for both mutations is rare suggesting there is compound heterozygosity rather than a haplotype between the two nucleotides (Zeng *et al.*, 2014). This mutation will not be discussed further due to limited presence in the canine population.

1.3.2.2 Distribution of the *Sod1:c.118A* allele in the canine population

The overall prevalence of DM in GSDs is suspected to be around 0.37 (Shaffer *et al.*, 2017). In the UK, the *Sod1:c.118A* allele is considered to have a relatively high prevalence of 0.38 in GSDs (Holder *et al.*, 2014), while in Japan, the mutant allele frequency in GSDs has been found to be significantly lower than the UK and the USA at 0.22. A study in Brazil was unable to identify the mutant allele in GSDs (Maki *et al.*, 2022). The *Sod1:c.118A* allele frequency is higher in PWCs compared to GSDs in the USA (Holder *et al.*, 2014) and Japan (Maki *et al.*, 2022). BXRs also have a higher frequency of the allele compared to GSDs in the USA (Holder *et al.*, 2014). In Japan’s case, there is a large number of DM affected PWCs, partially due to the high prevalence of the mutation in the breed, the large population of PWCs in the country and the fact they are easier to care for than larger breeds with DM (Kobatake *et al.*, 2021). While there is a large number of DM PWCs, most mutant homozygotes or heterozygotes do not develop the disease, indicating there may be other contributors (Ogawa *et al.*, 2015) including the involvement of other genes and mutations, or it could be due to the adult onset (Chang *et al.*, 2013). Studies have also found differences in the histopathology between breeds, suggesting the mutation may result in different disease characteristics between breeds, but this could also be influenced by the size of an animal and their nerves (Shelton *et al.*, 2012).

There is variance in the age of onset of DM in mutant homozygotes within and between breeds. For example, some studies have shown that most BXRs with histopathological changes and homozygosity for the *Sod*1 mutation show signs of DM before the age of 11 years old, while PWCs can reach 15 years old before displaying signs. Further, there is often variation within the PWC as some can display early onset between seven and nine years old. These differences in DM onset suggest there are additional genetic factors such as modifier loci (Ivansson *et al.*, 2016).

1.3.2.3 Other genetic associations in DM

The pathogenesis of a disease where a protein is involved may be caused directly by the expression of the protein, or it may be due to the association of the protein with other genetic or environmental influencers. DM may show incomplete penetrance because there are other influential factors including the presence of modified loci, environmental factors and age or they may die of other causes before clinical signs develop (Awano *et al.*, 2009; Draper *et al.*, 2020). The involvement of a modifier locus in the SP110 nuclear body protein (*SP110*) gene, found on chromosome 25 (CFA25) was first proposed by Ivansson *et al.*, (2016). The authors conducted a genome study of PWC dogs homozygous for the *Sod1:c.118G>A* mutation and found a haplotype of single nucleotide polymorphisms (SNPs) within the *SP110* gene that appeared to increase the probability of DM development and at a younger age. Usually only one copy of the *SP110* haplotype was required showing it had a dominant effect. In other breeds, this haplotype was not a risk factor, but it could contribute to the predisposition to DM nevertheless. Further studies are required to understand how the *SP110* haplotype influences the DM phenotypes and to identify other modifier loci that may contribute to DM (Ivansson *et al.*, 2016).

1.3.2.4 A summary of genetic risk factors in ALS

The exact aetiology of ALS is not known but at least 25 genes have been identified as having a role in sALS, fALS or both (Story *et al.*, 2020). Genetic mutations are found in approximately 80% of fALS cases and 5 to 10% of sALS cases (Van Damme, Robberecht and Van Den Bosch, 2017). Protein products from these genes have been linked to RNA metabolism, vesicle trafficking and the proteasome (Bozzo, Mirra and Carri, 2017). The genes associated most with ALS are *C9orf72* (chromosome 9 open reading frame 72; 5 to 10% all cases), *SOD*1 (2% all cases), *TARDBP* (TAR DNA-binding protein; 0.9% all cases) and *FUS* (fused in sarcoma; 0.7% all cases) (Van Damme, Robberecht and Van Den Bosch, 2017). Mutations in *C9orf72* and *SOD*1 account for 50% to 60% of fALS cases (Story *et al.*, 2020) and around 20% of the fALS cases are attributed to mutations in the *SOD*1 gene (Hanspal *et al.*, 2017). In sALS, *SOD*1 mutations are identified in 2% to 7% of cases (Hosaka *et al.*, 2019). In Scotland, one *SOD*1 variant is associated with 4% of fALS and sALS cases while mutations in *C9orf72* are present in 11% of cases (Leighton *et al.*, 2019). Mutations are usually autosomal dominant in ALS but autosomal recessive have also been noted as a result of compound heterogenicity (Hosaka *et al.*, 2019; Story *et al.*, 2020) meaning that in some fALS cases, it is possible to have mutations in more than one of the associated genes (van Blitterswijk *et al.*, 2012). Mutations do not associate with specific phenotypes of ALS; the clinical signs observed in fALS can vary as much as they do in sALS, and one mutation can cause a range of phenotypes (Ravits *et al.*, 2013).

The *SOD*1 gene is found on chromosome 21 and over 200 mutations in the gene have been associated with ALS (ALSoD, 2023) and can occur anywhere in the protein (Berdyński *et al.*, 2022). According to the ALSoD database (2023), *SOD*1 mutations are mostly associated with spinal ALS versus bulbar ALS. Variants can influence the duration and progression of ALS (Berdyński *et al.*, 2022). *SOD*1 mutations are predominantly dominantly inherited but recessive inheritance is also possible (Van Damme, Robberecht and Van Den Bosch, 2017). The D90A (aspartate to alanine) amino acid substitution is autosomal recessive in some families and autosomal dominant in others. Those with the recessive form have deficits in their lower limbs at onset and ALS progresses slowly, similar to DM. Those with the dominant form, particularly homozygotes, have an earlier disease onset (Awano *et al.*, 2009). It is not entirely clear how *SOD*1 mutations contribute to ALS, however it is likely mutations result in a gain of toxic protein function, but loss of SOD1 function has been reported in various studies. This is proposed to be a result of structural changes and abnormal interactions and can induce oxidative stress in a significant number of patients (Berdyński *et al.*, 2022).

1.4 Many pathological mechanisms may contribute to DM

Multiple pathological mechanisms have been implicated in DM and ALS (summarised in Figure 1-1), so it is likely that a combination of pathways are involved and may interact (Hosaka *et al.*, 2019). To maintain healthy cells, protein generation, folding and degradation need to be intricately controlled and adapted to environmental conditions. This protein homeostasis, specifically proteostasis, can be disrupted by multiple intrinsic and extrinsic factors including, but not limited to, genetic mutations, oxidative stress, proteasome dysfunction and aging (Laskowska, Kuczyńska-Wiśnik and Lipińska, 2019).

Proteins are synthesised from mRNA at ribosomes which are organelles found free in the cytoplasm or bound to the endoplasmic reticulum (ER). When ribosomes bind to the ER, these regions become termed the rough ER while regions without ribosomes are termed the smooth ER. Initial formation of polypeptide chains starts at free ribosomes in the cytoplasm but the presence of specific sequences results in translocation of the developing polypeptide chain and the corresponding ribosome(s) to the ER. Transmembrane and water-soluble proteins are synthesised and folded at the ER and are translocated to the relevant location, for example the plasma membrane or extracellular environment respectively, upon completion (Alberts *et al.*, 2002). Proteins exiting the ER are folded by chaperones, for example calnexin, and foldase enzymes including protein disulfide isomerase (PDI) (Chang *et al.*, 2019; Prell, Lautenschläger and Grosskreutz, 2013). The ER is important for the synthesis of proteins and lipids which are involved with most cellular organelles including, but not limited to, the plasma membrane, endosomes, lysosomes and secretory vesicles. The ER also synthesises the majority of lipids required by mitochondria. If proteins are not required to be synthesised at the ER, they are synthesised and folded in the cytoplasm (Alberts *et al.*, 2002).

Cells have several quality control pathways that work in concert to refold misfolded proteins, alter the synthesis of proteins, and ensure they fold correctly. Chaperones, including heat shock proteins (HSPs), promote the rectification of misfolded proteins, prevent spontaneous interactions between aberrant proteins to prevent formation of cytotoxic aggregates and shuttle these proteins to degradation pathways. In the case of obsolete or irreparably damaged or misfolded proteins, degradation systems including the ubiquitin proteasome system (UPS) are recruited. Proteins and other dysfunctional organelles can be moved through the autophagy pathway which ends in the lysosomal degradation of the aforementioned components. As the UPS and autophagy are the two main protein degradation systems, cross talk occurs between the pathways which ensures the upregulation of one when the other is dysfunctional. This cooperation can reduce the cytotoxic effects of protein misfolding and aggregation and ensures amino acids from degradation are recycled (Laskowska, Kuczyńska-Wiśnik and Lipińska, 2019). The accumulation of misfolded proteins can result in the initiation of ER stress which triggers a cascade of mechanisms, called the unfolded protein response (UPR), which upregulate different molecules to moderate pathways involved in protein synthesis, refolding and degradation. If this response does not rectify ER stress, cell death can occur by apoptosis or programmed cell death II (Ogawa *et al.*, 2015; Yokota *et al.*, 2018).

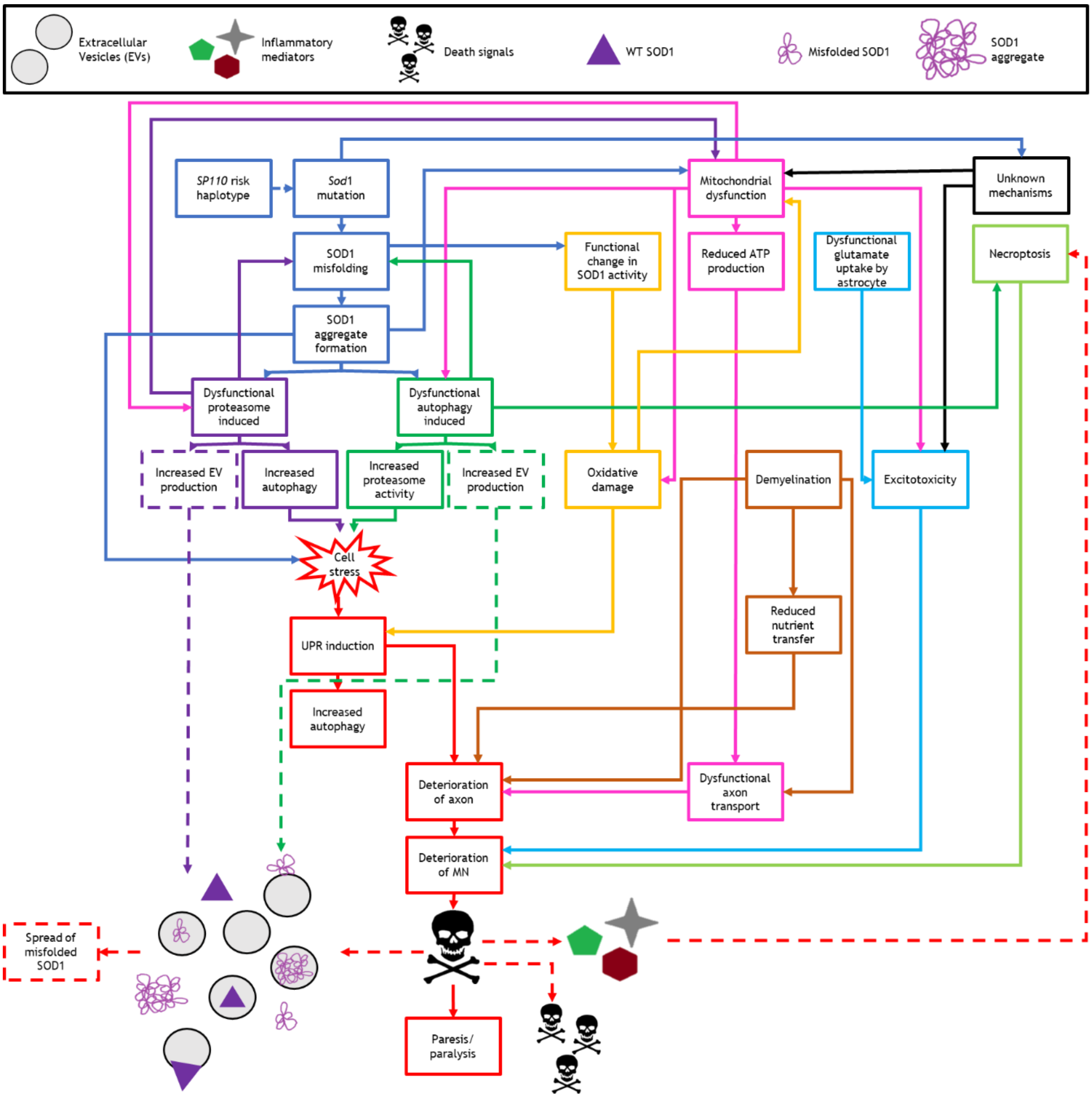
Extracellular Vesicles (EVs)
Inflammatory mediators
Death signals
WT SOD1
Misfolded SOD1
SOD1 aggregate
SP110 risk haplotype
Sod1 mutation
Mitochondrial dysfunction
Unknown mechanisms
SOD1 misfolding
Functional change in SOD1 activity
Reduced ATP production
Dysfunctional glutamate uptake by astrocyte
Necroptosis
SOD1 aggregate formation
Dysfunctional proteasome induced
Dysfunctional autophagy induced
Increased EV production
Increased autophagy
Increased proteasome activity
Increased EV production
Oxidative damage
Demyelination
Excitotoxicity
Cell stress
Reduced nutrient transfer
UPR induction
Increased autophagy
Deterioration of axon
Dysfunctional axon transport
Deterioration of MN
Spread of misfolded SOD1
Paresis/ paralysis

Figure 1-1: Many pathological mechanisms are involved in DM and ALS. Oxidative stress and excitotoxicity are considered the primary causes of MN loss in ALS. Ogawa *et al.*, (2014) proposed excitotoxicity and subsequent neurone deterioration in DM may be due to a reduction in astrocytic excitatory amino acid transporters, which causes a defect in the reuptake of glutamate. They believe this down regulation occurs as the disease progresses and is an exacerbating factor for neurodegeneration. Crisp *et al.*, (2013) suggest the SOD1 mutation induces a toxic gain of function but many believe that SOD1's ability to protect cells against oxidative damage is hindered in DM. In ALS research, there is evidence supporting an element of oxidative stress in pathogenesis. Although there are many sources of reactive oxygen species (ROS), the majority come from mitochondria. Oxidative stress may lead to the aggregation of unfolded proteins in ALS if they are not removed due to defective protein degradation and autophagy pathways (Bozzo, Mirra and Carri, 2017; Corti *et al.*, 2009). It has been suggested that selective autophagy for dysfunctional mitochondria may be defective which could explain mitochondrial deficits (Nardone *et al.*, 2016). Also, mitochondria may have a role in regulating necroptosis (Choi *et al.*, 2019). Dysfunction of the proteasome pathway and autophagy can lead to ER stress and subsequent activation of the UPR. Most genes associated with ER stress show increased expression in DM spinal cord (Yokota *et al.*, 2018) and mutations in genes associated with the UPR have been implicated in DM and ALS, including *PDI*. Stress may also result in the production of extracellular vesicles (EVs). If normal cell homeostasis is not met, this can lead to cell death and the production of EVs, inflammatory and death signals and free and aggregated WT and mutant SOD1 (Chang *et al.*, 2019; Lovett *et al.*, 2014; Silverman *et al.*, 2019; Yokota *et al.*, 2018). The disruption of multiple pathways results in axon, MN and myelin degeneration culminating in paresis first in the pelvic limbs, then in the thoracic limbs.

1.4.1 The SOD1 protein

SOD1 (also CuZnSOD) is a metalloenzyme found in eukaryotic cells and is present at high concentrations in the CNS (Coates and Wininger, 2010; Green *et al.*, 2002). The protein is primarily located in the cytoplasm of cells but has also been reported in other organelles including the nucleus (Hanspal *et al.*, 2017) and mitochondria (Tiwari and Hayward, 2005). The main role of SOD1 (Figure 1-2A) is to scavenge and catalyse the neutralisation of superoxide free radicals (O_2^-) to hydrogen peroxide (H_2O_2) and oxygen (O_2) (Awano *et al.*, 2009; Crisp *et al.*, 2013). One free radical molecule is oxidised at the copper binding site within SOD1 and another is subsequently reduced to provide O_2 and H_2O_2 (Rakhit and Chakrabartty, 2006). Other SODs include SOD2 (also manganese SOD; MnSOD) and SOD3 (also extracellular SOD; ECSOD) which are important antioxidants (Green *et al.*, 2002; Zelko, Mariani and Folz, 2002) found primarily in mitochondria and the extracellular space respectively. SOD3 also has copper and zinc ions in the enzyme active site while SOD2 has manganese ions. All three SODs have roles in CNS diseases when ablated or mutated (Zelko, Mariani and Folz, 2002).

Canine and human SOD1 are likely to be similar in structure as the 153 amino acid sequences are around 80% similar between the two species (Wakayama *et al.*, 2022). SOD1 is a homodimer that is approximately 32 kDa in total (Green *et al.*, 2002) and the subunits interact with disulphide bonds at cysteine residues 57 and 146 (Wakayama *et al.*, 2022). Each subunit consists of a ß-barrel composed of eight ß-sheets. The eight ß-sheets localise into two groups that are connected and stabilised by a Greek key connecting loop (Awano *et al.*, 2009). Also within each subunit is a copper ion for catalytic activity and a zinc ion which is important for SOD1 structure. The region at one end of the SOD1 ß-barrel is known as the ß-barrel plug and is thought to be important for maintaining the stability of the protein as it protects the edges and hydrophobic regions of the protein which are more susceptible to interacting with other cellular components (Wakayama *et al.*, 2022). The DM associated mutation, E40K, is found within the ß-barrel plug region and prevents the formation of the native salt bridge between E40 and K91 of the same subunit (Kimura *et al.*, 2020; Wakayama *et al.*, 2022). In humans, 40 amino acids within this region contribute to a cluster of ALS associated missense mutations (Awano *et al.*, 2009). Mutations in this region are thought to cause steric hinderance whereby aberrant interactions or repulsions between amino acid side chains may result in disruption of the ß-barrel plug. A consequence of this is the exposure of the now unprotected hydrophobic core of the ß-barrel (Draper *et al.*, 2020) and potential destabilisation of the zinc binding domain (Kimura *et al.*, 2020).

E40K mutant SOD1 has a lower net negative charge (-2.0) compared to WT SOD1 (-4.5) (Kimura *et al.*, 2020) in physiological conditions and this can reduce the repulsive forces of the protein and/or increase electrostatic interactions between anionic surfaces and other unfolded proteins (Awano *et al.*, 2009; Kimura *et al.*, 2020). Equine SOD1, which shares 75% amino acid similarity to canine SOD1, is stable despite the amino acid at the 40th codon being lysine (K). This is thought to be because the residue at the 91st codon is glutamate, therefore maintaining the salt bridge. In *in vitro* studies with canine SOD1 E40K and K91E double mutants, the salt bridge was returned, the overall structural stability and solubility improved and aggregation reduced compared to the E40K mutant (Draper *et al.*, 2020; Hashimoto *et al.*, 2023; Wakayama *et al.*, 2022). The E40K mutation has not been identified as an ALS associated mutation, but it has been investigated *in vitro* to better understand how the mutation affects SOD1 structure. The E40K mutation does not increase the propensity of human SOD1 to aggregate, so it is believed there must be other residues surrounding the 40th and 91st codons that interact in equine and human SOD1 to compensate for the loss of the salt bridge and/or there may be other mutations that contribute to aggregation in canine SOD1 (Draper *et al.*, 2020). Hashimoto *et al.*, (2023) suggested that the methionine (M) residue at 117 in canine SOD1 may contribute to the inherent instability of SOD1 in the species. In human SOD1, the 117th codon is leucine (L) and introducing the M117L mutation into canine E40K mutants improved the stability of the protein. The 117th codon is present within the hydrophobic core of the ß-barrel and appears to contribute to the packing of amino acids within the core. Leucine is more hydrophobic than methionine, so it is believed this amino acid improves the packing of the ß-barrel core resulting in more electrostatic interactions between amino acids in the area. In canine WT SOD1, this compactness may be missing which could make the protein less stable and ablation of the ß-barrel plug because of the E40K mutation allows increased solvent access to the hydrophobic region, increasing the chance of aberrant interactions (Hashimoto *et al.*, 2023).

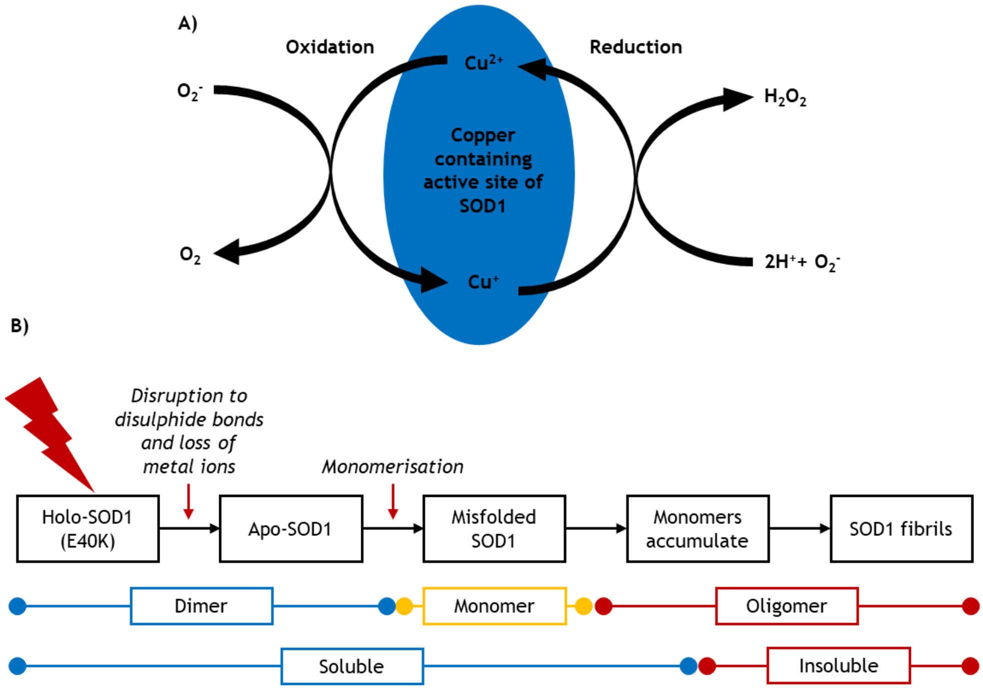
A)
Oxidation
Reduction
O_2^-
O_2
Cu^{2+}
Cu^+
Copper containing active site of SOD1
H_2O_2
$2H^+ + O_2^-$
B)
Disruption to disulphide bonds and loss of metal ions
Monomerisation
Holo-SOD1 (E40K)
Apo-SOD1
Misfolded SOD1
Monomers accumulate
SOD1 fibrils
Dimer
Monomer
Oligomer
Soluble
Insoluble

Figure 1-2: Summary of SOD1 activity and aggregation. The schematic in **A)** demonstrates the oxidation and reduction of superoxide, O_2^-, to O_2 and H_2O_2 which is catalysed by the copper active binding site on SOD1. Schematic based on the image from Rakhit and Chakrabartty (2006). **B)** summarises the current hypothesis for the formation of SOD1 aggregates as described by several researchers in the DM and ALS fields (Hanspal *et al.*, 2017; Hashimoto *et al.*, 2023; Kimura *et al.*, 2020; Tiwari and Hayward, 2005; Wakayama *et al.*, 2022).

In physiological conditions, SOD1 is found in immature and mature states (Kimura *et al.*, 2020). The apoenzyme state is the immature form of SOD1 where the copper and zinc metal ions have not yet bound to the structure. The binding of these metal ions produces the mature and active species of the protein, holo-SOD1 (Hanspal *et al.*, 2017; Kimura *et al.*, 2020). In physiological conditions, WT and E40K holo-SOD1 is active and does not aggregate. In the same conditions, WT and E40K apo-SOD1 is less stable and less active than holo-SOD1 but only E40K apo-SOD1 develops aggregates. Protein aggregation typically develops after the formation of an unstable intermediate, so these findings suggested that apo-SOD1 may not just be an immature SOD1 species, but also potentially a pathological, unstable intermediate (Kimura *et al.*, 2020).

The canine E40K mutation and multiple human ALS associated mutants are considered to be “wildtype-like” mutations whereby mutations do not directly affect the copper or zinc binding regions and result in only a minor change to the backbone folding, thus mainly maintaining the native WT conformation (Hashimoto *et al.*, 2023; Tiwari and Hayward, 2005). In physiological conditions, the intermolecular disulphide bond is more susceptible to perturbations in the WT-like mutants compared to true WT SOD1. When stressors are added (Figure 1-2B), this can affect metal binding as a consequence of the mutation resulting in the formation of apo-SOD1. Further, as the disulphide bond between the two protein subunits is less stable in the mutant, this is also likely to be disrupted (Hashimoto *et al.*, 2023) and can further contribute to the loss of metal ions as well as introducing protein misfolding and monomerisation. Partially folded or fully unfolded SOD1 will be produced in this process and these species are more likely to form aberrant interactions with other SOD1 species or cellular components (Tiwari and Hayward, 2005). Various protein species exist in equilibrium in the cellular environment, including the less stable apo-SOD1. This suggests even in physiological conditions, there will be low levels of SOD1 misfolding. When the E40K mutation is considered, this is likely to increase the concentration of misfolded proteins as it is less stable than WT apo-SOD1. This increase in misfolded proteins is likely to lead to the formation of soluble oligomers which eventually become insoluble oligomers/fibrils (Wakayama *et al.*, 2022).

At a gross level, SOD1 aggregates can be found in the neurones and glia of DM and ALS patients when techniques such as immunohistochemistry (IHC) are used. SOD1 aggregates are often reported in homozygous mutants and can be observed in heterozygotes. In WT homozygotes, labelling is usually indicative of an absence of SOD1 aggregates as it is faint or cannot be differentiated from background labelling. On some occasions, SOD1 aggregates can be observed in mutant homozygote and heterozygous spinal cords by IHC, but the dogs do not present with clinical signs. These dogs may not have reached an age where clinical signs developed (Awano *et al.*, 2009). Further assessment of the E40K mutation with a canine specific SOD1 antibody (antibodies raised against human SOD1 most frequently used), only homozygous mutants display aggregates in neurones but both mutant homozygotes and heterozygotes have aggregates in astrocytes showing DM is non-cell autonomous (Nakamae *et al.*, 2015). SOD1 aggregation can also be investigated with biochemical techniques by comparing the levels of detergent soluble and insoluble SOD1 to give an indication of disease severity (Figure 1-2B). In DM, detergent insoluble SOD1 increases as the disease progresses while soluble SOD1 is comparable between unaffected and affected dogs. Age related changes can cause the aggregation of WT-SOD1 but levels do not reach the level of insoluble aggregates observed in early DM (Grade 1; Table 1-1) (Crisp *et al.*, 2013).

It is not yet clear exactly how the *Sod*1 mutation contributes to DM, however it is thought there is a toxic gain of function where mutants have an increased propensity to aggregate (Crisp *et al.*, 2013; Nakamae *et al.*, 2015) and insoluble aggregates alter intracellular functions (Coates and Wininger, 2010). Insoluble SOD1 aggregates appear in the later stages of disease so it is proposed that there are soluble oligomers that are pathogenic earlier in disease (Draper *et al.*, 2020; Tiwari and Hayward, 2005). SOD1 has been shown to play various roles in pathological changes in MNDs including changes to oxidative conditions, disruption to chaperone functions and clearance mechanisms, mitochondrial dysfunction, changes to axon transport and many more. Small amounts of misfolded SOD1 have been attributed to changes and it is not clear if toxicity exerted by SOD1 is due to direct interactions between SOD1 and other cellular constituents, the requirement for constant turnover or changes to SOD1 activity (Tiwari and Hayward, 2005).

Activity in the canine E40K SOD1 mutant has been shown to be retained in *in vitro* studies (Crisp *et al.*, 2013; Kimura *et al.*, 2020; Qi *et al.*, 2019) however the impact on endogenous SOD1 has not been assessed. Function is suspected to be retained as the mutation does not directly affect the metal binding region (Crisp *et al.*, 2013). A study by Draper *et al.*, (2020) reported significantly more superoxide ions in samples containing the canine mutant SOD1 compared to WT SOD1 and studies from human SOD1 ALS have identified changes, even when mutations are not present at the active site (Saccon *et al.*, 2013). It has been suggested that changes to SOD1 structure and interactions may contribute to defective activity in some ALS cases (Berdyński *et al.*, 2022). *In vivo* studies of DM SOD1 function are required.

Generally, in DM and ALS, patients with SOD1 mutations do not normally develop clinical signs until later in life when normal cellular changes associated with aging occur. Cells normally employ adaptive mechanisms that enable the refolding, degradation or sequestration of misfolded proteins, but these mechanisms (to be discussed in this section) may become less efficient with age. Further, oxidative stress is thought to be one of the potential triggers for the SOD1 aggregation cascade. The brain and spinal cord appear to have a predilection for the accumulation of mutant SOD1 and aggregates compared to other organs (Tiwari and Hayward, 2005). There is a hypothesis in the ALS field suggesting that select neuronal populations may be more susceptible to insults than other populations in the CNS which may result in the accumulation of stressors and eventual misfolding and aggregation of SOD1. Furthermore, stress signals or pathogenic proteins may enable other less vulnerable areas of the CNS to produce pathologic levels of misfolded SOD1 (Hanspal *et al.*, 2017).

1.4.2 Heat shock protein response

HSPs, including HSP70 and HSP90 families, are chaperones involved in the maintenance of proteostasis by promoting the adenosine triphosphate (ATP) dependent refolding of misfolded proteins when bound. During stress conditions, HSPs, including HSP70-1 and HSP70-2, become upregulated in the cytoplasm and nucleus. Another member of the HSP70 family, HSP70-5, alternatively known as binding-immunoglobulin protein (BiP), interacts with proteins at the ER membrane or those that are secreted from the organelle. Generally, HSP70s can prevent the interaction between misfolded proteins to prevent aggregation, enable the refolding of proteins and can solubilise protein aggregates for subsequent refolding. HSP90 is an important chaperone involved in protein folding, degradation and apoptosis in addition to roles in control of the cell cycle, signalling and cell differentiation. This chaperone works downstream of HSP70 and can interact with HSP70 to maintain/regain proteostasis (Laskowska, Kuczyńska-Wiśnik and Lipińska, 2019).

1.4.3 ER associated degradation and the ubiquitin proteasome system

The UPS is one of the primary intracellular protein degradation pathways (Ogawa *et al.*, 2015) which selectively removes unfolded, damaged or obsolete proteins from cells to maintain homeostatic protein turnover (Cheroni *et al.*, 2009). Proteins due to be degraded by the proteasome are first labelled by the ubiquitin protein after a cascade of enzymatic activity by E1 (ubiquitin-activating enzyme), E2 (ubiquitin-conjugating enzyme) and E3 (ubiquitin ligase). More ubiquitin protein can be added to the protein to form a polyubiquitin tail, and the number and structural orientation of the tail determines the outcome for the protein. Some polyubiquitinated proteins are degraded by the 26S proteasome which, in mammals, consists of two particles, the 19S particle and the 20S particle. The polyubiquitinated protein is recognised by the regulatory 19S particle which then removes ubiquitin and unfolds the protein. The 20S particle contains multiple protease subunits, including proteasome subunit α type-1 (PSMA1), that degrade proteins in the presence of ATP and produce peptides which can be recycled (Laskowska, Kuczyńska-Wiśnik and Lipińska, 2019).

Studies of DM have found alterations in the proteasome pathway (Nakamae *et al.*, 2015). Ubiquitin granules have been observed in the neuropile and glia of DM spinal cords, however some have not found granules in healthy neurones, only degenerated neurones and associated neuropil. Several studies have not been able to colocalise SOD1 and ubiquitin suggesting other misfolded proteins, or a defect in the UPS or autophagy, may be involved in disease aetiology (Nakata *et al.*, 2021; Ogawa *et al.*, 2011; Ogawa *et al.*, 2014). A study of regulatory microRNA (miRNA) in DM found that miRNA dysregulation may prevent the ubiquitination of mutant SOD1 in neurones, causing evasion of the UPS and aggregation of mutant SOD1 (Nakata *et al.*, 2021).

1.4.4 Autophagy

Macroautophagy (referred to as autophagy hereon) is another key intracellular protein degradation pathway and it can be further categorised into basal autophagy and inducible autophagy. Basal autophagy is responsible for the homeostatic turnover of cytosolic constituents including denatured proteins (Ogawa *et al.*, 2015), protein aggregates, damaged organelles (Xu, Camfield and Gorski, 2018) and lipofuscin. Inducible autophagy is upregulated in response to stimuli including nutrient starvation, hypoxia, oxidative stress and excitotoxicity (Ogawa *et al.*, 2015). Degradation products including amino acids, lipids and sugars are recycled to maintain homeostasis and sustain cell survival during periods of stress (Xu, Camfield and Gorski, 2018). When autophagy is irreparably dysfunctional, it results in type II programmed cell death. Basal autophagy has been associated with neurodegenerative disease, including ALS and DM, when dysfunctional (Ogawa *et al.*, 2015; Onesto *et al.*, 2011).

Autophagy involves the formation of autophagosomes which are vesicles with a double membrane that are randomly formed after expansion of the phagophore in the cytoplasm (Renna *et al.*, 2010). When autophagy is induced, a complex forms which generates the early phagophore (Xu, Camfield and Gorski, 2018) and the phagophore is expanded by another complex formation. Microtubule-associated protein 1 light chain 3 (LC3) is modified to LC3I after post-translational modification in the cytoplasm and when autophagy is induced, LC3I is converted to LC3II, the autophagosome associated form of the protein, by conjugation with phosphatidylethanolamine (Ogawa *et al.*, 2015; Xu, Camfield and Gorski, 2018). As the autophagosome forms, it engulfs cytoplasmic components associated with adaptor proteins including p62 (Ogawa *et al.*, 2015). Using microtubules in the dynein transport system, autophagosomes are moved to the microtubule-organising centre (Renna *et al.*, 2010) and fuse with lysosomes to form an autolysosome. One protein involved in the fusion process is Annexin A1 (ANXA1) which is believed to promote the degradation of autolysosomal contents (Kang *et al.*, 2011; Xi, Ju and Wang, 2020). The lysosome contains many acid hydrolases, including the proteolytic cathepsin D (CTSD), which degrade the contents of the original autophagosome (Ogawa *et al.*, 2015; Renna *et al.*, 2010; Wootz *et al.*, 2006; Xu, Camfield and Gorski, 2018). LC3 is the only mammalian protein currently known to be specifically associated with the autophagosome membrane (Renna *et al.*, 2010) and can be used as a marker of the autophagosome and autolysosome (Ogawa *et al.*, 2015).

Polyubiquitinated misfolded proteins can be degraded in the autophagy pathway and tend to be those resistant to the UPS. Chaperones, including HSP70 and HSP90 can be associated with lysosomal degradation in a process called chaperone mediated autophagy which is distinct from the autophagy just discussed (Laskowska, Kuczyńska-Wiśnik and Lipińska, 2019).

Dysfunctional autophagy is hypothesised to be a cause and consequence of DM. Several autophagy markers have been investigated in PWCs with DM and an increase in LC3 puncta in DM spinal cord neurites in grey matter compared to control groups has been observed. LC3 did not colocalise with a lysosome marker, suggesting there is a disruption to the fusion of the autophagosome and lysosome. This would lead to stress due to an increase in autophagosomes. Another autophagy component, p62, was found to colocalise with ubiquitin in DM spinal cords of the same study. This showed that selective autophagy is a compensatory pathway utilised by cells when the UPS is overwhelmed by ubiquitinated proteins and therefore accumulations of both proteins in the cord may suggest both pathways are defective. These two observations suggested there is a disturbance in the balance between formation and degradation of autophagosomes, known as autophagy flux, which may contribute to DM pathology and lead to programmed cell death of MNs (Ogawa *et al.*, 2015).

1.4.5 ER stress and the unfolded protein response

In DM, CSF has been shown to have increased levels of clusterin, a protein with many functional roles including the protection of cells against ER stress mediated apoptosis (Yokota *et al.*, 2018), the protection against oxidative stress and it is a chaperone involved in protein aggregation (Shafie *et al.*, 2014). Increases in this protein could suggest ER stress is present in DM CNS (Yokota *et al.*, 2018) and it is in fact thought to be one of the main pathophysiological contributors in DM and ALS. It is proposed that mutant SOD1 accumulates in the ER and cytoplasm in DM, inducing ER stress and the UPR (Yokota *et al.*, 2018).

In the absence of stress, BiP is bound to the UPR sensors inositol-requiring enzyme 1 (IRE1), activating transcription factor 6 (ATF6) and protein kinase R-like ER kinase (PERK). Upon accumulation of misfolded proteins in the ER, BiP detaches from the sensors (Prell, Lautenschläger and Grosskreutz, 2013) which in turn promote death signals such as CCAAT/enhancer binding protein homologous protein (CHOP) and X-box binding protein 1 (XBP1) to induce apoptosis. ER chaperones including PDI (Chang *et al.*, 2019) and calnexin (Prell, Lautenschläger and Grosskreutz, 2013) also become upregulated. The response is initially a protective mechanism to prevent further ER stress caused by the build-up of abnormal proteins, but when it is chronically activated, it induces widespread cell death signals and subsequent apoptosis, ultimately contributing to MN degeneration (Chang *et al.*, 2019).

A few studies have indicated that ER stress may be induced in the spinal cord of DM dogs. This was evidenced by an increase in PDI and CHOP in the DM spinal cord compared to controls and colocalization of PDI with SOD1 in MNs of DM samples only. Furthermore, a similar trend in PDI upregulation has been reported in ALS studies (Chang *et al.*, 2019). Another study reported increased expression of BiP in astrocytes and microglia. Further transcript analysis identified upregulation of apoptosis signal-regulating kinase 1 (*ASK1*) and spliced *XBP1*, both indicators of the UPR. The authors suggest the UPR may be related to the deterioration of white matter (Yokota *et al.*, 2018).

Activating transcription factor 3 (ATF3) is a transcription factor that can be activated by ER stress. In healthy cells, ATF3 is found at low levels but expression is increased by numerous exogenous and endogenous stressors. Depending on the cellular conditions and which promotor interacts with the ATF3 protein, ATF3 may be inhibitory or stimulatory and is thought to have a role in metabolic and immunologic regulation (Ku and Cheng, 2020).

1.4.6 Cell death mechanisms

Generally, the cooperation between the UPS and autophagy can restore homeostasis in a cell, however other factors, including ageing or disease, can make the pathways less effective resulting in protein aggregates which are resistant to refolding and degradation (Laskowska, Kuczyńska-Wiśnik and Lipińska, 2019). Eventually, programmed cell death type I (apoptosis), type II (autophagic) or type III (necroptosis) can be induced depending on the cascades initiated. Programmed cell death is important for homeostasis and is used to dispose of obsolete or surplus cells, or those that have the potential to exert negative effects on other cells. Programmed cell death type II is induced by the autophagy pathway and was discussed earlier (Deiss *et al.*, 1996).

As there are several causes of ER stress, there are different ways in which apoptosis can be initiated. CTSD is a glycoprotein that can play a role in initiation of apoptosis and at several other stages of the cascade when found in the cytoplasm. CTSD has been found to play a role in neurodegeneration and can contribute to cytoskeleton degradation in some disease states (Deiss *et al.*, 1996). As previously mentioned, BiP can also be involved in the initiation of apoptosis. In addition to being bound to ER stress sensors, BiP is also bound to a calcium (Ca^{2+}) channel. When bound, the channel is inactivated so upon BiP release in ER stress, the channel becomes activated and transports Ca^{2+} from the ER to the cytoplasm which can subsequently cause apoptosis by initiation of the caspase-3 pathway (Prell, Lautenschläger and Grosskreutz, 2013). Another initiator of the same caspase dependent apoptotic pathway is ANXA1, which increases the Ca^{2+} in the cytoplasm by dephosphorylating Bcl2-associated death promotor (Bad) at mitochondrial membranes, particularly in phagocytic cells including monocytes (Sheikh and Solito, 2018).

Necroptosis is similar to, but distinct from apoptosis. Caspase independent cascades instigate necroptosis and a main feature is the deterioration of cellular membranes which allow cellular proteins to escape the cell, subsequently inducing an inflammatory response. Research in relation to DM and ALS is limited, but some groups have identified necroptosis in neurones and glia in some fALS and sALS models (Morrice, Gregory-Evans and Shaw, 2017).

1.4.7 Cell metabolism

1.4.7.1 Mitochondria and oxidative stress

In the CNS, ANXA1 has been found in neurones, astrocytes, microglia and endothelial cells and is thought to be important for maintaining the integrity of the blood-brain barrier (BBB) to ensure delivery of essential components for CNS metabolism. The protein decreases with age which is thought to disrupt the BBB by increasing its permeability which can help with the progression of neurodegenerative diseases, including Alzheimer's disease (Sheikh and Solito, 2018).

Reactive oxygen species (ROS, also termed free radicals) are generated by normal metabolic cellular processes, including oxidative phosphorylation in mitochondria, but can have deleterious effects on cells if they are not tightly regulated (Bozzo, Mirra and Carri, 2017). Oxidative stress is the term used to describe any pathological changes to cells due to the presence of ROS, excitatory amino acids and more (Coates *et al.*, 2007) and it is thought to contribute to many neurodegenerative diseases, including ALS (Ogawa *et al.*, 2011). Evidence of oxidative damage has been found in ALS patient tissues affecting proteins, lipids and DNA and oxidative stress is thought to contribute to protein aggregation (Bozzo, Mirra and Carri, 2017). In ALS, oxidative stress may be caused by an increase in nitric oxide (NO) production. Limited studies have been conducted to assess the contribution of oxidative stress in DM, but preliminary findings suggest inducible nitric oxide synthase (iNOS), indicative of NO production, is increasingly expressed in glia of DM cords (Ogawa *et al.*, 2011) in a similar way to ALS cases (Sasaki *et al.*, 2000).

Other ROS include superoxide ions (O_2^-) which are highly reactive and damaging to lipid membranes and DNA (Draper *et al.*, 2020). An increase in cellular O_2^- has been recorded in SOD1 related ALS. In a study by Draper *et al.*, (2020) where cells in a DM *in vitro* model expressed WT and mutant SOD1 protein, more O_2^- were found in cells expressing mutant SOD1 despite there being no statistically significant differences between mitochondrial physiology recorded. Mitochondria were mostly morphologically similar, however the cells expressing mutant SOD1 also had increased branching within the mitochondria. The authors suggested several explanations for increased O_2^- including changes to SOD1 enzymatic activity (Draper *et al.*, 2020) which has also been suggested by others in the ALS field (Corti *et al.*, 2009). Changes to mitochondrial morphology and functions can negatively impact energy availability, calcium pathways and cellular viability and can make cells more susceptible to apoptosis due to the mitochondrial relationship with apoptotic pathways (Bozzo, Mirra and Carri, 2017). Mutant SOD1 has been found to be associated with mitochondria in ALS to varying extents in the CNS and muscle. On occasion, SOD1 can become misfolded and form aggregates within mitochondria which may cause functional changes to the organelle including deficient ATP generation (Corti *et al.*, 2009).

1.4.7.2 Excitotoxicity

An important function of astrocytes is to remove the excitatory neurotransmitter glutamate from the extracellular environment to prevent excitotoxicity in neurones due to high concentrations or prolonged exposure to glutamate (Duan *et al.*, 1999). Using excitatory amino acid transporter 1 (EAAT1; also glutamate/aspartate transporter, GLAST) and EAAT2 (also astrocytic glutamate transporter 1, GLT-1) at the cell membrane, glutamate is escorted into the astrocyte and converted into glutamine. It has been found that EAAT2 is downregulated in the DM spinal cord and this could be one of the contributing factors to neuronal degeneration as it will encourage excitotoxicity (Ogawa *et al.*, 2014).

1.4.8 Inflammation

Microglia are the resident immune cells of the CNS and can be identified by the ionised calcium binding adaptor molecule 1 (Iba-1) protein. This cell type has been implicated in ALS progression in murine and human studies and it has been suggested that early in the disease, they have neuroprotective functions, but later, they become neurotoxic. In DM, it has been found that microglia expressing neuroprotective phenotypes decreased as DM progressed while microglia expressing neurotoxic markers were not statistically different from age matched controls (Toedebusch *et al.*, 2018).

It is possible that ER stress is induced at some stage in DM astrocytes and microglia which may increase inflammation in the spinal cord. It has been postulated that ER stress occurs first in astrocytes which causes the production of inflammatory cytokines and chemokines. Production of these molecules may lead to microglial migration and accumulation which might then impact the health of MNs (Yokota *et al.*, 2018).

1.5 Extracellular vesicles may be involved in DM progression

1.5.1 Extracellular vesicles are a heterogenous population

Extracellular vesicles (EVs) are imperative for tissue homeostasis and can be produced from all CNS cells. EVs can interact with other cells and share their contents (Hosaka *et al.*, 2019; Silverman *et al.*, 2019), and an example includes the shuttling of neurotransmitters at synapses (Hosaka *et al.*, 2019). EVs are found in most biological fluids and cell culture media (Haraszti *et al.*, 2016). There are several subgroups of EVs including exosomes, microvesicles (MVs), apoptotic bodies and RNA binding proteins, that can be separated by size and other properties (Hosaka *et al.*, 2019). Knowing the type of EV isolated from fluids or media can give an indication of their biochemical properties and biological function in the system. EVs can be separated into subgroups using various laboratory methods including, but not limited to, immunoaffinity, flotation velocity, sucrose density gradient, ultrafiltration and differential centrifugation. Unfortunately, there is currently no method that is able to fully separate each EV group as some physical properties, for example size, overlap EV groups. Additionally, non-EV contaminants including extracellular proteins and lipoprotein particles can be found in the isolate (Haraszti *et al.*, 2016).

1.5.1.1 Large EVs

MVs are found with diameters ranging from 100 nm to 1 µm and are formed by budding of the plasma membrane. They are involved in cellular communication and can transport transmembrane proteins between microglia and astrocytes for example (Hosaka *et al.*, 2019). They can be separated from other EVs by centrifugation at 15,000 *xg* (Silverman *et al.*, 2019). Apoptotic bodies are between 500 nm and 2 µm in diameter and are released from apoptotic cells by blebbing of the plasma membrane. They can contain organelles and nucleotides from apoptotic cells. RNA binding proteins can bind RNA found in the extracellular environment (Hosaka *et al.*, 2019).

1.5.1.2 Small EVs

Exosomes are between 30 nm and 200 nm in diameter (Chen *et al.*, 2019; Hosaka *et al.*, 2019; Otake, Kamiguchi and Hirozane, 2019) and originate from the endocytic pathway (Xu, Camfield and Gorski, 2018) and endosome system (Hosaka *et al.*, 2019). The formation of exosomes is summarised in Figure 1-3. Firstly, the plasma membrane invaginates and may endocytose fluids, macromolecules, receptors and membranes. The resulting intracellular vesicle formed when the invaginated membrane pinches off from the plasma membrane merges with early endosomes where the contents is organised. The early endosome matures into the late endosome, also termed the multivesicular body (MVB), then undergoes one of many processes including direct fusion with lysosomes, fusion with new autophagosomes before fusing with lysosomes, or further invagination of the MVB membrane to produce smaller vesicles called intraluminal vesicles (ILVs). When ILVs are formed, the MVB fuses with the plasma membrane then releases the ILVs from the cell which become exosomes in the extracellular environment (Xu, Camfield and Gorski, 2018; Hosaka et al., 2019). Endosome sorting complexes required for transport are involved in the formation of ILVs and exosomes along with associated accessory proteins. If any of the components of this system are silenced, it results in the production of exosomes with altered size, protein composition and overall quantity. Ceramide, a lipid molecule, is also involved in the generation of exosomes in some cell types (Xu, Camfield and Gorski, 2018).

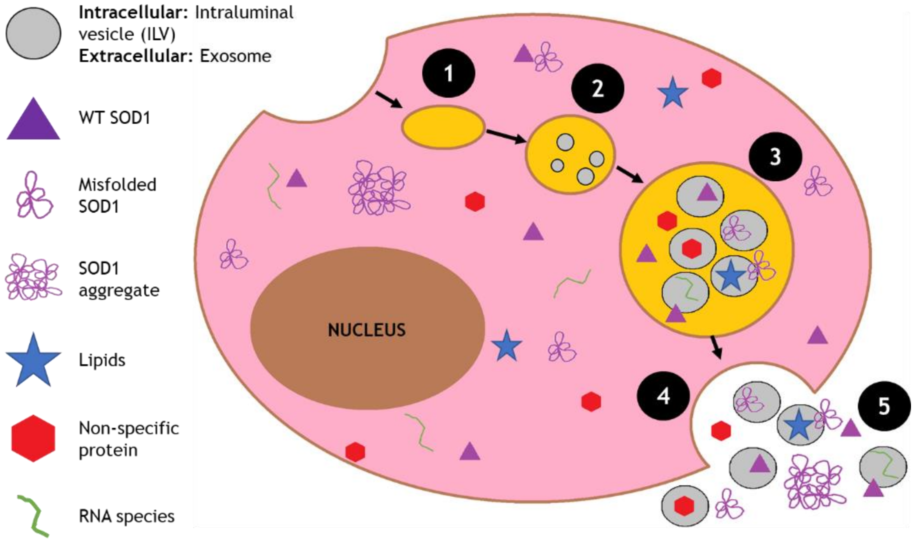

Figure 1-3: Overview of exosome formation and release. 1) Formation of the endosome from the plasma membrane. **2)** Invagination of the endosomal membrane to form ILVs. **3)** Formation of the late endosome, or MVB containing ILVs and proteins, lipids and RNA. **4)** MVB fuses with plasma membrane. **5)** Release of MVB contents including exosomes. Various cellular components incorporated into exosomes include RNA, lipids and proteins such as WT and mutant SOD1.

Exosomes can be secreted from almost all cell types and consist of a lipid bilayer that encloses proteins, lipids and RNA (Chen *et al.*, 2019). It was thought that the main function of exosomes was for the excretion of waste products from cells however it was later discovered that they are mediators of cellular communication (Hosaka *et al.*, 2019; Otake, Kamiguchi and Hirozane, 2019) and can be selectively loaded depending on the cell type and stimuli present (including ubiquitination). Exosomes are enriched in multiple proteins, and these can be specific for the cell they were produced from (Chen *et al.*, 2019; Hayashi *et al.*, 2019; Otake, Kamiguchi and Hirozane, 2019; Thompson *et al.*, 2020). These proteins have an array of functions including structural support and protection from circulating phagocytic cells (Xu, Camfield and Gorski, 2018). Components found in exosomes tend to be of cytoplasmic or plasma membrane origin and normally lack most proteins from the nucleus, mitochondria and ER (Gomes *et al.*, 2007).

Exosomes can be taken into cells by autocrine (exosome taken in by the cell that secreted it), paracrine (exosome taken in by cells near the secreting cell) or endocrine (exosome travels to other areas of the body using vessels) systems (Xu, Camfield and Gorski, 2018). The ability of exosomes to move in the extracellular space, which includes body fluids, allows them to transport their contents from cell to cell (Chen *et al.*, 2019). The uptake process may include membrane receptor-mediated endocytosis, phagocytosis or macropinocytosis but this list is not exhaustive (Xu, Camfield and Gorski, 2018). Exosomes can cross the BBB and can be isolated from most biological fluids (Chen *et al.*, 2019; Lee *et al.*, 2016) and they can be enriched by sequential centrifugation (Silverman *et al.*, 2019).

1.5.2 Extracellular vesicles in disease

EVs have been implicated in various neurodegenerative diseases and are believed to behave similarly to prion proteins as pathogenic proteins can be seeded and spread in association with EVs. This has been suggested in Alzheimer's disease and Lewy-body dementia where tau and α-synuclein proteins respectively play major roles in disease pathology. This area is gaining more ground in ALS research where more studies are finding this mechanism could aid spread of ALS pathology (Silverman *et al.*, 2019). Also, it is believed that EVs can give an indication of the status of protein disposal and intercellular transport mechanisms (Thompson *et al.*, 2020). Exosomes found in the CSF are considered to provide an insight into the condition of the CNS cells due to their intimate association (Otake, Kamiguchi and Hirozane, 2019) and are being investigated as potential biomarkers for neurodegenerative diseases including ALS (Otake, Kamiguchi and Hirozane, 2019) and DM (Pfeiffer *et al.*, 2023).

1.6 Hypothesis, aims and objectives

The overarching aim of this project was to use a multistrand approach to understand the aetiology and progression of DM. The working hypothesis for this PhD project is as follows and is summarised in Figure 1-4.

- Misfolded SOD1 caused by the DM associated *Sod*1 mutation may disrupt cell clearance and toxicity pathways within cells of the spinal cord.
- The consequences of this are increased SOD1 aggregation and defective protein and lipid processing which may have detrimental effects on cellular metabolism and structure, culminating in the associated axonal degeneration and demyelination observed in histopathology.

- Disruption to alternative pathways involving the release of extracellular vesicles is also suspected and could be associated with the spread of misfolded SOD1 to other cells in the spinal cord.
- It is likely that these pathological changes act in concert to cause the clinical signs that progress from the pelvic limbs to the thoracic limbs.

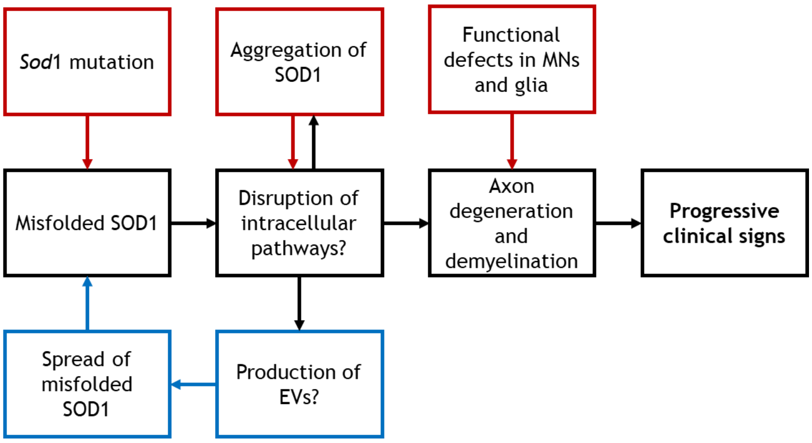
Sod1 mutation
Aggregation of SOD1
Functional defects in MNs and glia
Misfolded SOD1
Disruption of intracellular pathways?
Axon degeneration and demyelination
Progressive clinical signs
Spread of misfolded SOD1
Production of EVs?

Figure 1-4: Hypothesis tested in this PhD project. Schematic representation of the hypothesis tested in this project that shows how each part may fit together.

We tested this hypothesis using the following objectives:

1. An *in vitro* approach was used to establish if defective cellular clearance and toxicity pathways play a role in SOD1 aggregation.
2. The contribution of these defects in the secretion of SOD1 positive EVs and the potential for EVs to spread mutant protein in a prion-like manner was assessed using cell culture experiments and biochemistry.
3. Proteomic and biochemical techniques were used to validate potential toxic pathways and identify novel pathological mechanisms in DM using tissues collected from positive cases.

Completion of these objectives will help to establish how the genetic anomaly, protein processing pathways and the general CNS proteome interact to cause the pathology and subsequent clinical presentation of DM.

2 General materials and methods

2.1 Overview

2.1.1 *In vitro* study

The human neuroblastoma SK-N-SH cell line was used to investigate cell clearance and toxicity pathways and EVs *in vitro*. Cells were transfected with WT or mutant (DM) SOD1 tagged with enhanced green fluorescent protein (EGFP), then treated with chemicals that disrupt several cellular clearance and toxicity pathways. Chemicals used were the reducing agent dithiothreitol (DTT) which induces ER stress, chloroquine (CQ), which inhibits autophagy and MG132 which inhibits the proteasome. The expression of various markers of these pathways and SOD1 were analysed using reverse transcription polymerase chain reaction (RT-PCR) and Western blotting (WB) techniques. SOD1 aggregation was also monitored using fluorescence microscopy. In parallel, the production of EVs after chemical treatment was analysed using WB. EV isolation was optimised and EVs were characterised using WB. To verify if EVs may contribute to the spread of mutant SOD1, conditioned medium experiments were performed by transferring donor EVs to recipient cells.

2.1.2 *Ex vivo* study

Running in tandem with *in vitro* studies, DM and control cases were recruited to the study with clinicians at the University of Glasgow Small Animal Hospital (UoGSAH) and the Scottish Society for Prevention of Cruelty to Animals (SSPCA). To diagnose DM, diagnostic services included neurological examination, MRI and blood biochemistry to rule out other diseases that may cause the same clinical signs. Genotyping at the level of the *Sod*1 gene was outsourced (Laboklin, UK) and confirmed by an inhouse assay. Dogs that showed neurological signs and were homozygous for the *Sod*1:c.118G>A mutation were included in the study. Owner consent was imperative for any involvement in the study and ethical approval from The School of Veterinary Medicine Ethics and Welfare Committee was granted (application number EA10/20). After euthanasia or death, various tissues were collected to generate material for *ex vivo* work, and to generate a canine tissue repository at the University of Glasgow. Tissues, including brain and spinal cord, were collected as per a Standard Operating Procedure (SOP) developed for the study. Samples were snap-frozen for biochemical and proteomic studies or fixed in formalin for histology. Biochemistry included WB and RT-PCR for cell toxicity markers identified in *in vitro* studies and investigation of EVs and SOD1. Histology was assessed by members of the pathology team to definitively diagnose DM.

2.2 Cell culture

2.2.1 Cell line and culture maintenance

The immortalised human SK-N-SH cell line (gifted by Dr Paul Montague, University of Glasgow) were broken out of storage, passaged and frozen using the methods described in Appendix 8.2.1. Cells were maintained in Dulbecco's Modified Eagle Medium (DMEM) high glucose medium (Invitrogen, UK) with 10% heat-inactivated foetal bovine serum (FBS; Gibco, UK), 1% penicillin-streptomycin (Gibco, UK) and 0.5% amphotericin B (Gibco, UK). This will be referred to as normal growth medium (NGM). For EV experiments, DMEM was supplemented with 10% exosome-depleted FBS (Gibco, UK) instead of normal FBS. Exosome-depleted FBS was used to provide important nutrients for cell growth, but with ≥90% depletion of circulating bovine exosomes. The cells were incubated in humidified conditions at 37°C (to mimic human body temperature) with 5% CO_2 for a maximum of 20 passages. Limiting the passage number is important as the genotype and phenotype of a culture can change due to exposure to culture conditions and genetic instability (ECACC (2020)).

The SK-N-SH cell line was originally isolated from a bone marrow neuroblastoma metastasis in the 1970s and maintained for research (Biedler, Helson and Spengler, 1973). Components in the growth media provide growth factors, energy sources and more to facilitate cell growth, adhesion, maintain the pH at physiological levels in combination with incubator CO_2 levels and prevent microbial contamination (Price, 2017).

For experiments, cells were seeded onto cell culture flasks, 4-well plates with poly-L-lysine treated coverslips (Appendix 8.2.1.1), and 6-well plates at the appropriate density (defined in specific chapters) using the trypan blue exclusion counting method (Appendix 8.2.1.2). The seeding density of cells is dependent on the surface area of the vessel they are being transferred to, the cell lineage and purpose of experiment (Appendix 8.2.1.2 for calculation).

2.2.2 Expression of proteins of interest in cell culture

2.2.2.1 Generation of plasmids

Plasmids used in this study are summarised in Table 2-1 and were purchased, gifted or constructed previously.

Table 2-1: List of plasmids used in this study.

Plasmid	**Source**	**Working concentration (ng/µl)**
pGFP	Gifted by Dr Paul Montague (PM)	154
pEGFP	Gifted by PM	244
pmaxGFP	Lonza, Switzerland	615
pWT-*Sod*1-EGFP	Described in Qi *et al.*, (2016) and Qi *et al.* (2019), generated by PM	200-300
pDM-*Sod*1-EGFP	Described in Qi *et al.*, (2016) and Qi *et al.* (2019), generated by PM	200-300
pLC3-GFP	Gifted by Dr Yoshimori, Osaka University	300

The pLC3-GFP recombinant was gifted and engineered as outlined in Kabeya *et al.*, (2000). Generation of the *Sod*1 plasmids used a range of standard molecular cloning techniques including ligation and transformation of *Escherichia coli* competent cells, Topoisomerase T/A cloning, recombinant screening, plasmid growth and purification (Qiagen, Germany), as detailed in Qi *et al.*, (2016) and Qi *et al.* (2019). In summary, RNA was extracted (Amsbio, UK) from the T12 region of the spinal cord from DM and control dogs harbouring *Sod*1 118G>A and WT 118G respectively and converted to complementary DNA (cDNA; Thermo

Fisher, UK). Primers corresponding to the first 24 and last 24 mRNA nucleotides incorporating the initiation and stop codons respectively (Appendix 8.2.1.3) were used to generate WT and mutant *Sod*1 amplicons encoding a 157 amino acid open reading frame (ORF). The forward and reverse primers were anchored with the restriction sites, *Xho*I or *Hind*III respectively. To minimize copying errors during the PCR amplification process, the WT and mutant *Sod*1 amplicons were synthesized using the high fidelity proofreading EasyA Polymerase (Stratagene, USA) and cloned into the topoisomerase 1 based T/A cloning vector pSC-A (Stratagene, USA). The *Sod*1 pSC-A plasmids were digested with *Xho*I and *Hind*III to release the restriction fragments. The column purified (Qiagen, Germany) *Sod*1 fragments were covalently linked in-frame at the corresponding *Xho*I and *Hind*III sites in the multiple cloning sites of the fluorescent tagged expression vectors pEGFP-C3 (Clontech, USA) allowing the detection of the 48 kDa fluorescent SOD1-EGFP fusion protein in transiently transfected neuronal cell types. The purified recombinant plasmids were quantified and diluted to a standardised working concentration of 200-300 ng/µl for transfection studies.

2.2.2.2 Transfection procedure

Cells were transfected with plasmids using Opti-MEM Reduced-Serum Minimal Essential Medium (Opti-MEM; Gibco, UK) and Lipofectamine™ 3000 Transfection reagent (Invitrogen, UK) using the manufacturers recommendations as a guide. Based on the recommended reagent ratios (Appendix 8.2.1.4), a typical reaction would contain 200-300 ng/µl of DNA for 4-well plates and double this for 6-well plates. Transfection mixtures were incubated at room temperature (RT) for 5 minutes, the mixtures containing pWT-*Sod*1-EGFP or pDM-*Sod*1-EGFP were added equally to the NGM already in each well based on the experimental design. The plates were incubated in humidified conditions at 37°C with CO_2. In the presence of the plasmid and Lipofectamine™ 3000 reagents, condensed nucleic acid-cationic lipid complexes form spontaneously. Cells exposed to this complex appear to endocytose the complex before the DNA contents is released into the cell cytoplasm and eventually translocated to the nucleus and expressed.

2.3 Visualising cells, aggregates and EVs

2.3.1 Assessing cell viability by morphology

The morphology of cells can indicate how viable cells are. If cells shrink, become more rounded and their nuclei become more condensed (pyknotic), this indicates they are in the early phase of apoptosis. When the plasma membrane starts to “bleb” and apoptotic bodies form in addition to fragmentation of the nucleus (karyorrhexis), this indicates cells are undergoing apoptotic cell death (Elmore, 2007).

2.3.2 Lysosome stain

To assess the distribution of lysosomes in treated cells (Chapter 3), NGM media in 4-well plates was replenished after treatment, then LysoTracker™ Red DND-99 (Invitrogen, UK) was applied to each well at a 50 nM concentration and plates incubated for 30 minutes at 37°C. Media was replaced with PBS for visualisation under the microscope to minimise background interference from the pink media. Lysosomes were stained without cell fixation or permeabilisation as fluorescence was lost after the procedure.

2.3.3 Cell fixation and nuclei staining

When cells were ready to be assessed, growth medium was removed and cells were washed with PBS, three times. To fix cells, formaldehyde (4%; PFA) was applied and cells were incubated at RT for 10 minutes. Cells were washed three times in PBS then chilled absolute methanol was applied to permeabilise cell which were incubated at -20°C for 5 minutes. Methanol was aspirated off, one well at a time, then PBS was immediately added to the same well. A further 2 PBS washes were performed before 4′,6-diamidino-2-phenylindole (DAPI) stain (10 ng/µl in PBS; Sigma-Aldrich, UK) was applied and cells incubated for 1 minute at RT. DAPI is a synthetic fluorescent dye that binds to the adenosine and thymine base pairs in DNA, allowing visualisation of nuclei (Abramowitz and Davidson, 2020). After another three washes with PBS, coverslips were removed and placed cell-face down onto a drop of Citifluor mountant solution on a glass microscope slide. Coverslips were sealed with nail varnish to prevent the cells from drying out, then stored at 4°C until visualised.

2.3.4 Visualisation of fluorescent proteins and stains

Cells were visualised under a fluorescent microscope (Olympus IX70) using the violet filter (350 nm) for blue DAPI stained nuclei, the green filter (550 nm) for red stained lysosomes and the blue filter (450 nm) for (E)GFP tagged proteins. EGFP tagged proteins have an excitation wavelength range of 489-511 nm, DAPI a range of 350-470 nm and LysoTracker™ a range of 577-590 nm.

To assess SOD1-EGFP aggregation, images captured from three random fields, using Image Pro Plus (v.6, Media Cybernetics), were selected from each sample using the DAPI stained nuclei so that personal bias to select aggregated SOD1 was minimised. Nuclei, transfected cells and SOD1 aggregates were counted using ImageJ (Rasband, 1997) and the Cell Counter plugin (De Vos, 2001). Different workflows were used for each count type and are found in Appendix 8.2.4.

2.4 Analysis of proteins

2.4.1 Protein sample generation from *in vitro* cell culture

2.4.1.1 Isolation of small EVs and purification of exosomes

Different methods have been described in the literature for EV isolation (Section 1.5.1). In this study, a classical centrifugation approach was employed based on the protocol described in Momen-Heravi (2017) and theory in Théry *et al.*, (2018). Early in the study, a basic two step centrifugation method was used (Figure 2-1A), but this was later optimised to three steps (as explained in Chapter 4; Figure 2-1B). Generally, for both methods, EDM was collected from wells and pooled with media from the same genotype and conditions within each experiment resulting in a total volume of approximately 4.5 ml. Media was centrifuged at 110 *xg* (later increased to 800 *xg*) for 5 minutes at RT to pellet dead cells. Of the supernatant (SN), 4 ml was transferred to a centrifuge tube and the remaining SN was collected and stored at -20°C. After balancing the tubes with EDM as appropriate, the SN was centrifuged in a Type 50.4 Ti Fixed-Angle Titanium rotor (Beckman Coulter) at 110,858 *xg* for 2 hours or 10,000 *xg* for 30 minutes at 4°C. The SN from the 10,000 *xg* spin was transferred to another centrifuge tube, balanced, and centrifuged at 110,858 *xg* for 2 hours at 4°C. The SNs from the 110,858 *xg* spins were discarded and pellets from each step were resuspended in 50 µl of lysis buffer (Appendices 8.2.3.1) then processed for protein quantification (Section 2.4.3). Lysis buffer contains buffers, detergents and various enzyme inhibitors to allow the recovery of intracellular/intra-EV and membrane proteins without degradation of these proteins. Samples were stored at -20°C until required.

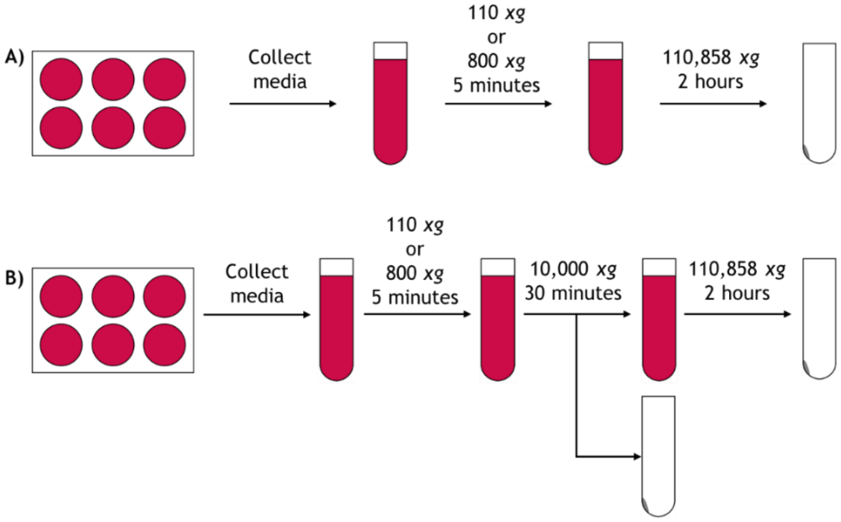

Figure 2-1: Summary of centrifugation steps used throughout the study. The main centrifugation steps used to isolate EVs from media are shown in **A)** and **B)**. Once collected, media was centrifuged at 110 *xg* or 800 *xg* (speed used stated in each section). In **A)**, the SN was further centrifuged at 110,000 *xg* for 2 hours then the SN was removed, and the pellet resuspended in the appropriate buffer. In **B)**, the SN was centrifuged at 10,000 *xg* for 30 minutes before a final centrifugation at 110,858 *xg* for 2 hours. The SN was removed, and the pellet resuspended in the appropriate buffer.

2.4.1.2 TCA precipitation for generation of total media fraction

Proteins from EDM left over after the 110 *xg* (800 *xg* after optimisation) centrifugation step were precipitated with 50% TCA then incubated on ice for 30 minutes. Samples were centrifuged at 2516 *xg* (5000 rpm on Biofuge Fresco, Heraeus Instruments) for 10 minutes at 4°C. The SN was discarded, and the pellet was resuspended in 5 µl of 1 M Tris-base and 75 µl of lysis buffer, then vortexed before total protein was measured.

2.4.1.3 Harvesting cells

When cells were ready to be assessed, media was removed and cells were washed two times with phosphate buffered saline (PBS) then 100 µl lysis buffer was applied. Cells were dislodged from the bottom of each well using a cell scraper and collected. Samples were rotated for 30 minutes at 4°C then centrifuged at 2516 *xg* (5000 rpm on Biofuge Fresco) for 10 minutes at 4°C. The SN (containing cell lysates (CLs)), and pellet (containing membranous components) were separated then either stored at -20°C or immediately processed for protein quantification.

2.4.2 Protein sample generation from *ex vivo* tissues

Spinal cord tissues were collected from control and DM cases and proteins were extracted as described in Section 6.3.3. Briefly, samples were snap frozen in liquid nitrogen (LN) and stored at -70°C until required. Tissue sections were powdered in LN using a mortar and pestle then 50 mg aliquots were made. Aliquots were homogenised using a ball mill (Retsch Mixer Mill MM 400, Germany) in a buffer containing 2% SDS and 100 mM Tris-HCl (pH 7.4) and were subjected to low-speed centrifugation to remove large debris. Samples were incubated on ice then centrifuged at a high speed to remove insoluble components.

2.4.3 Total protein measurement

The copper-based Pierce™ BCA (bicinchoninic acid) Protein Assay Kit (Thermo Scientific, UK) was used following the manufacturer's protocol to determine the concentration of protein in samples. In alkaline conditions, cupric ions (Cu^{2+}) present in Reagent B (4% cupric acid) are reduced to cuprous ions (Cu^{+}) when they form a chelate complex with peptides consisting of at least 3 amino acids. At this stage, known as the biuret reaction, there is a light blue colour. When BCA in Reagent A is added, it chelates with Cu^{+} and forms a purple complex. The absorbance of the complex at 562 nm increases as protein concentrations increase. Protein assays were carried out in 96-well plates using MQ as blanks and bovine serum albumin (BSA) diluted to a standard range between 0.05 and 0.80 mg/ml for a protein reference range. Reactions consisted of 250 µl of BCA working solution and either 25 µl of standard or 2.5 µl of sample. The plate was agitated on a plate shaker at high speed for 10 to 20 seconds before being incubated for 30 minutes at 37°C. Absorbances for standards and samples were recorded (LT-4500 Absorbance Microplate Reader, Labtech International Limited, UK) and, using the absorbances for the BSA standards, a standard curve was plotted (absorbance against concentration in mg/ml). The protein concentration of each sample was calculated from the standard curve and corrected for the dilution factor. Protein concentrations were used to determine the volume of sample required for downstream applications including gel electrophoresis.

2.4.4 Protein denaturation and loading

Samples used in gels for Coomassie Blue staining, Silver staining and WB were made up to the loading volume of the gel with MQ water and sample denaturation buffer (Appendix 8.2.3.2) at a ratio of two parts sample and MQ, to one part sample buffer. Samples were placed onto a block heater for 4 minutes at ~95°C. The sample buffer contains the detergent lithium dodecyl sulphate (LDS) which denatures proteins and gives them an overall negative charge which facilitates the separation of proteins by size in gel electrophoresis. DTT is added to reduce the disulphide bonds between cysteine amino acids so that proteins lose tertiary or quaternary structure and become linear. This means that proteins will be separated only by size, not charge and three-dimensional structure (GE Healthcare Bio-Sciences AB, 2018).

Where the native structure of proteins was important for downstream applications, proteins were separated in non-reducing conditions therefore LDS/SDS was not included in the sample buffer. Native gels separate proteins and complexes based on the charge and hydrodynamic size of the native quaternary structure of the protein (GE Healthcare Bio-Sciences AB, 2018). Samples to be used in native gels were made up to the loading volume with MQ water and a non-reducing 2x loading buffer (Appendix 8.2.3.3) was added at a 1:1 ratio.

2.4.5 Separation of proteins within samples

2.4.5.1 One dimensional polyacrylamide gel electrophoresis (SDS-PAGE)

Proteins can be separated based on size and charge when they are run through a porous gel by an electric current. Polyacrylamide gels have a cross-linked structure which creates pores that are similar in size to many proteins; the size of pore is determined by the concentration of acrylamide and the chemical cross-linking agent. When an electric current is applied, large proteins smaller than the pores move slowly through the gel while small molecules move faster. It may be beneficial to use gels that contain an increasing concentration of acrylamide towards the positive anode, for example 4-12%, to allow optimal recovery of proteins ranging in molecular weights from approximately 14,000 to 205,000 $M_{r.}$ Larger proteins are separated in the lower concentration and smaller proteins will be better separated in the more concentrated area. Buffers containing counter ions, such as Bis-Tris, are an important constituent of gels and function to maintain a consistent pH at both electrodes to ensure constant charge and mobility of proteins (GE Healthcare Bio-Sciences AB, 2018).

For SDS-PAGE in this study, large gels (18 or 26 well 1mm thick precast polyacrylamide 4-12% Bis-Tris gels; Criterion™ XT, Bio-Rad Laboratories Ltd., UK) were used in a Criterion™ electrophoresis cell (Bio-Rad Laboratories Ltd., UK) with 1X XT MES (2-(N-morpholino) ethanesulfonic acid) running buffer (Bio-Rad Laboratories Ltd, UK). Small gels (10 or 12 well 1 mm thick precast polyacrylamide 4-12% Bis-Tris mini gels; NuPAGE™ Novex™, Invitrogen, UK) were also used in a XCell SureLock™ Mini-Cell (Invitrogen, UK) with 1X NuPAGE™ MES SDS running buffer (Invitrogen, UK). Samples were loaded into wells alongside the SeeBlue™ Plus2 Pre-stained Protein Standard (4-250 kDa; Invitrogen, UK) and proteins were routinely separated at 150 V for 1 hour.

2.4.5.2 Native gels

Proteins/complexes are separated based on charge and hydrodynamic size in native gels. Proteins that have a larger conformation have reduced mobility and smaller, more compactly folded proteins/complexes travel faster.

Proteins/complexes can be recovered in their native state from the gels (GE Healthcare Bio-Sciences AB, 2018) so it can be used to analyse the native conformation of SOD1 in samples and subsequently, its activity (Section 2.4.6.3).

A 10% acrylamide resolving gel with a 4% acrylamide stacking layer (Appendix 8.2.3.6) was positioned in a gel rig (packed on the outside with ice) with Tris-glycine running buffer (25 mM Tris, 200 mM glycine at pH 8.3) before samples were loaded into the gel. The proteins/complexes were separated by an electric current at a 40 mA for 30 minutes to allow proteins to enter the gel, then 50 mA for 80 to 100 minutes.

2.4.6 Gel staining

2.4.6.1 Coomassie Blue stain

Coomassie Blue staining was used to produce total protein profiles of CLs and tissue samples that were separated by SDS-PAGE. Gels were submerged in Coomassie Blue stain (Appendix 8.2.3.3) on a plate shaker for at least three hours then washed in de-stain (Appendix 8.2.3.3) and rehydrated in MQ before visualisation with a BioRad Gel Doc Imaging System. Coomassie Blue binds to the majority of proteins and any stain that does not bind to protein is washed away using de-stain, resulting in the clear visualisation of protein bands (GE Healthcare Bio-Sciences AB, 2018).

2.4.6.2 Silver stain

Silver staining was used to produce total protein profiles of samples with low protein quantities, particularly EVs, that were separated using SDS-PAGE. Silver staining is a sensitive technique that can detect low concentrations (ng) of protein and is based on the reduction of silver ions to metallic silver in the presence of protein. The gel is saturated with silver ions before being developed by formaldehyde which, in the presence of protein, reduces the silver ions to metallic silver. The latter stage forms a brown precipitate that can be visualised (GE Healthcare Bio-Sciences AB, 2018).

The SilverXpress™ silver staining kit (Invitrogen, UK) and protocol was with slight adjustments. Gels were covered in MQ water for a few minutes on a plate shaker. Fixing solution was applied for at least 10 minutes for protein fixation. This solution was replaced with Sensitising solution, which was applied for 30 minutes before the gel was washed for 10 minutes, twice with MQ water. The gel was incubated with Staining solution for 15 minutes then washed for 5 minutes, twice with MQ water. The gel was immersed in Developing solution until the bands were visible then the reaction was stopped with Stopping solution for 10 minutes. A final MQ water wash cycle of 3, 10-minute rounds was carried out before imaging with the Gel Doc Imaging System. Details regarding the composition of solutions used are presented in Appendix 8.2.3.5.

2.4.6.3 Nitroblue Tetrazolium (NBT) stain

NBT staining was used to assess SOD1 activity in gels containing natively folded proteins. All steps in the NBT staining protocol were carried out on a plate shaker at RT. After removal from the rig, gels were washed for several minutes in MQ water. The rest of the steps were carried out in a light-tight container with a lid to prevent premature activation of the staining reagents. The staining reagents were made in 100 mM phosphate buffer (PB; pH 7.8; Appendix 8.2.3.7). After the first wash, NBT (1 mg/ml in PB) was applied to the gel for 15 minutes. The gels were washed again for several minutes before a riboflavin mixture containing TEMED (Appendix 8.2.3.8) was added for a further 15 minutes. The gels were finally washed in MQ water for several minutes before being exposed to light for 10 to 15 minutes. Gels were visualised on a light box, then scanned into a computer with an Epson Perfection V300 Photo scanner.

The NBT staining assay is used to determine the activity of manganese SOD (MnSOD; 88kDa) and CuZnSOD (32 kDa). NBT competes with SOD for free radicals which are generated by riboflavin and TEMED in the assay (Rakhit and Chakrabartty, 2006; Weydert and Cullen, 2010). Free radicals reduce tetrazolium within NBT from a yellow colour to a blue precipitate. Where active SOD is present, achromatic bands are produced in the gel, indicating the activity of the enzyme.

2.4.7 Western Blot

2.4.7.1 Transfer of proteins from polyacrylamide gels to nitrocellulose membrane

After gel electrophoresis, gels were trimmed to remove wells and placed onto nitrocellulose sheets in the dry blotting system iBlot™ Transfer Stack (Invitrogen, UK) for the iBlot™ Gel Transfer Device (Invitrogen, UK) and 20 V was passed through for 7 minutes to allow transfer of proteins from the gel onto the membrane. The nitrocellulose membrane was stained with 0.1% Ponceau S in 5% acetic acid to assess gel loading and protein transfer. Ponceau S is negatively charged so binds to positively charged amino acids in proteins and also binds to non-polar areas of proteins by forming non-covalent bonds (Sigma, 1998).

2.4.7.2 Probing of blots with antibodies

All steps in this section were performed on a plate shaker. Nitrocellulose membranes were washed in MQ water twice and once with 1X Tris-buffered saline (1X T-TBS; Appendix 8.2.3.9) for 5 to 10 minutes to remove Ponceau S. To block non-specific binding sites, a 5% dried milk powder in 1X T-TBS solution was applied for 1 hour at RT. This step minimises non-specific binding sites of antibodies that may otherwise bind to the matrix, producing artefactual background.

All antibodies were prepared in 5% dried milk powder in 1X T-TBS. Primary antibodies were made to the appropriate dilution (Table 2-2) then applied to nitrocellulose membranes, after removal of the block, overnight at 4°C. The next day, the blot was washed for 10 minutes, 3 times with 1X T-TBS to remove excess antibodies and limit background contamination. The relevant secondary antibody linked to the enzyme horseradish peroxidase (HRP) was made to the appropriate dilution (Table 2-2) and applied to the blot for at least 90 minutes at RT. The blot was washed 3 times for 10 minutes with 1X T-TBS. For antibody validation and profiles, see Appendix 8.2.3.10.

Table 2-2: List of antibodies used for WB.

Primary antibody	Dilution	Secondary antibody	Dilution
Mouse monoclonal anti-actin (Sigma-Aldrich, UK; #A5441)	1:200,000	Goat anti-mouse IgG HRP-linked antibody (Abcam, UK; #ab205719)	1:5000
Rabbit polyclonal anti-CuZnSOD (Enzo Life Sciences, US; #ADI-SOD1-100)	1:2000	Goat anti-rabbit IgG HRP-linked antibody (Abcam, UK; #ab6721)	1:5000
Mouse monoclonal anti-flotillin-1 (BD Transduction Laboratories, USA; #610821)	1:2000	Goat anti-mouse IgG HRP-linked antibody (Abcam, UK; #ab205719)	1:5000
Goat polyclonal anti-GFP (Abcam, UK; #ab6673)	1:2000, 1:5000 or 1:25,000	Mouse anti-goat IgG HRP-linked antibody (Abcam, UK; #ab157532) or rabbit anti-sheep IgG HRP-linked antibody (Abcam, UK; #ab6747)	1:10,000 or 1:5000
Rabbit polyclonal anti-HSP70 (Cell Signalling Technology, US; #4876)	1:2000	Goat anti-rabbit IgG HRP-linked antibody (Cell Signalling Technology, US; #7074)	1:5000
Rabbit polyclonal anti-LC3 (Cell Signalling Technology, US; #2775)	1:1000	Goat anti-rabbit IgG HRP-linked antibody (Abcam, UK; #ab6721) or donkey anti-rabbit IgG HRP-linked antibody (Abcam, UK; #ab205722)	1:5000
Rabbit polyclonal anti-ubiquitin (DAKO, US; #Z0458)	1:500 or 1:2000	Goat anti-rabbit IgG HRP-linked antibody (Cell Signalling Technology, US; #7074) or Goat anti-rabbit IgG HRP-linked antibody (Abcam, UK; #ab6721)	1:5000
Rabbit polyclonal anti-glial fibrillary acidic protein (DAKO, US; #Z0334)	1:10,000	Goat anti-rabbit IgG HRP-linked antibody (Abcam, UK; #ab6721)	1:5000
Rabbit polyclonal anti-lactate dehydrogenase (Abcam, UK; #ab130923)	1:5000	Goat anti-rabbit IgG HRP-linked antibody (Cell Signalling Technology, US; #7074)	1:5000
Mouse monoclonal anti-human neurone specific enolase (Agilent Dako, US; #M087301-2)	1:2000	Goat anti-mouse IgG HRP-linked antibody (Abcam, UK; #ab205719)	1:5000
Rabbit polyclonal anti-proteolipid protein (gifted by Prof. N.P. Groome)	1:20,000	Goat anti-rabbit IgG HRP-linked antibody (Abcam, UK; #ab6721)	1:10,000
Mouse monoclonal anti-vimentin (Sigma-Adrich, UK; #V6630)	1:5000	Goat anti-mouse IgG HRP-linked antibody (Abcam, UK; #ab205719)	1:5000

Shown in the table are the sources and dilutions of primary antibodies used for WB. The relevant secondary antibodies follow the primary antibody. Their source and dilution are also noted.

Generally, monoclonal antibodies bind to one specific epitope of a protein, however this reduces sensitivity, while polyclonal antibodies bind to several epitopes in a protein so are more sensitive, however less specific. Secondary antibodies are raised against the immunoglobulin constant region of the primary antibody in a separate species. Secondary antibodies can be tagged with HRP, to allow visualisation of the protein by enhanced chemiluminescence (ECL) (GE Healthcare Bio-Sciences AB, 2018).

2.4.7.3 ECL and signal quantification

Pierce™ ECL substrate (Thermo Scientific, UK) was used to visualise proteins tagged with HRP-linked antibodies. The blot was thoroughly coated with a working solution of ECL substrate (Detection Reagents 1 and 2 combined at a 1:1 ratio) for approximately 1 minute. Excess solution was removed before the blot was wrapped in clear plastic wrap and sealed. Membranes were exposed to x-ray film (GE Healthcare, UK or Thermo Fisher, UK) for varying time periods then processed in an x-ray processor. X-ray films were scanned (Epson Perfection V300 Photo scanner) and ImageJ (v1.52a,(Rasband, 1997)) was used to quantify the intensity of each band (Appendix 8.2.4.1 for workflow).

The ECL substrate contains luminol peroxide, which is oxidised to luminol, a process catalysed by HRP. This reaction results in the emission of light (428 nm) which is enhanced by other chemicals in the ECL reagents. The intensity of the light emitted is dependent on the number of enzyme molecules reacting, which is proportional to the amount of antibody and thus, protein present (GE Healthcare Bio-Sciences AB, 2018).

2.4.8 Proteomic analysis

After extraction of proteins (Section 2.4.2), samples were taken to Glasgow Polyomics (GP; https://www.polyomics.gla.ac.uk/proteomics.html) for nanoflow HPLC electrospray tandem mass spectrometry (nLC-ESI-MS/MS) analysis. Standard procedures were used by GP and are described in Chapter 6.

2.5 Analysis of nucleic acids

2.5.1 Sample preparation

2.5.1.1 RNA extraction from *in vitro* and *ex vivo* samples

RNA was extracted from cells and spinal cord tissue using TRIzol™ Reagent (Invitrogen, UK). The methods were slightly different for cells and tissue but were derived from the manufacturer's protocol. Details of RNA extraction from cells are found in Section 5.3.4 and from tissue, in Section 6.3.2.2.

Briefly, for RNA extraction from cells, media was removed then TRIzol™ Reagent was applied to lyse cells and a pipette was used to homogenise the sample before it was collected. For tissues, TRIzol™ was added to approximately 50 mg of powdered spinal cord, then samples were homogenised using a ball mill (Retsch Mixer Mill MM 400, Germany). As spinal cord has a high proportion of lipids, samples were centrifuged and the SNs were used for the rest of the procedure.

RNA, DNA and proteins in the cell and tissue samples were separated after the addition of chloroform, then, after an incubation period and centrifugation step, the top aqueous layer containing RNA was collected. Glycogen (1 mg/ml) was added to samples as a carrier to ensure the optimal quantity of RNA was isolated. RNA was precipitated using isopropanol and washed with 75% ethanol. These stages were accompanied by short incubation and centrifugation steps. The RNA pellet was resuspended in RNAse free water then samples were stored at -20°C until required. RNA was quantified and quality checked (section 2.5.2) before RNA integrity (Section 2.5.2) was analysed and cDNA generated (section 0).

2.5.1.2 Extraction of genomic DNA from *ex vivo* samples

Genomic DNA (gDNA) was extracted from whole blood samples using the DNeasy™ Blood and Tissue Kit (Qiagen, Germany) as per manufacturer's instructions. Details can be found in Section 6.3.2.1 but briefly, blood samples were lysed by proteinase K, then a buffer containing high concentrations of salt was added to ensure DNA in the sample specifically adsorbed onto the DNeasy silica membrane during centrifugation. Contaminants and enzymes in the sample were removed from the sample as they do not bind to the membrane and were washed out with various buffers and further centrifugation steps. DNA was ultimately eluted from the membrane, quantified and quality checked.

2.5.2 Quantification and quality assessment of nucleic acids

RNA was quantified using the *Nucleic Acid* RNA-40 program (ND-1000, V3.1.2) and DNA was quantified using the *Nucleic Acid* DNA-50 program with the NanoDrop 1000 Spectrophotometer (Thermo Scientific, UK; Nanodrop). The NanoDrop passes light through the sample to assess absorbance and calculates the concentration of nucleic acid using a modified version of the Beer-Lambert equation (Thermo Fisher Scientific Inc., 2010). The NanoDrop was also used to assess nucleic acid purity by recording the 260/280 ratio. This is calculated by expressing the absorbance of the sample at 260 nm and 280 nm as a ratio. An RNA or DNA sample is considered pure if the ratio is around 2.0 or 1.8 respectively. Deviations from these ratios suggest samples may be contaminated with protein or phenol from extraction for example (Thermo Fisher Scientific Inc., 2010).

To analyse the integrity of RNA, samples were prepared by calculating the volume of sample required for 500 ng (tissue derived RNA) or 1000 ng (cell derived) of RNA. Samples were combined with loading buffer (New England BioLabs, USA) and separated on a 1.5% agarose gel (UltraPure^{TM} Agarose, Invitrogen, UK) with 1X Tris-acetate-EDTA (TAE; Thermo Scientific, UK) and 1X SYBR Safe DNA stain (Invitrogen, UK). A 100 bp DNA ladder (Appendix 8.2.2.1) was also loaded so the size of the products could be assessed. Gels were run at 70 V for 40 minutes and bands were visualised using ultraviolet (UV) light (GeneFlash, Syngene, UK). Here, RNA (and DNA) bands are separated based on size.

2.5.3 Generation of cDNA from RNA

cDNA was generated based on the methods described in SuperScript^{TM} IV (SSIV) First Strand Synthesis System (Invitrogen, UK) and SuperScript^{TM} III (SSIII) Reverse Transcriptase (Invitrogen, UK). For generation of cDNA, the final reaction volume was 20 µl and concentrations of reagents at all steps relate to this volume. The first part of the reaction (13 µl) contained template RNA (1 mg final), random hexamers (2.5 ng/µl), dNTP mix (0.05 mM; Promega, US) and PCR water. The volume of RNA and PCR water was the same within each set of samples but varied between preparations due to the concentration of RNA extracted. Samples were mixed with a pipette tip and heated at 65°C for 5 minutes to denature RNA, then cooled rapidly to allow random hexamers to anneal to RNA by incubating on ice for 10 minutes. In the second step of the reaction, a master mix containing 1X SSIII™ First-Strand Buffer or SSIV™ buffer, DTT (5 mM DTT), RNAseOUT (2 U/µl) and SSIII™ or SSIV™ reverse transcriptase (200 U/µl) was added to make the final volume of 20 µl. Samples underwent several incubation periods to allow reverse transcriptase to bind to primers and to synthesise cDNA using the nucleotides present (dNTPs). These steps varied slightly depending on the kit used and are detailed in Chapter 5. The reaction was stopped by high temperature incubation to inhibit the RT enzymes, then cDNA was resuspended in MQ water. Most samples were resuspended in 230 µl, but samples with reduced starting RNA were resuspended in less. The quantity and purity of the resultant cDNA was recorded using the NanoDrop as per section 2.5.2.

Table 2-3: Incubation steps in generation of cDNA using SSIII™ and SSIV™.

Step	SSIII™ conditions	SSIV™ conditions
Binding of reverse transcriptase to primers	25°C for 5 minutes	23°C for 10 minutes
Synthesis of cDNA	50°C for 45 minutes	50°C for 10 minutes
Termination of reaction	70°C for 15 minutes	80°C for 10 minutes

Comparison of the temperatures and times used for each step using SSIII™ or SSIV™.

2.5.4 Polymerase chain reaction

For RNA derived cDNA (cells and tissue), cellular clearance and toxicity pathways were analysed while a specific *Sod*1 region was amplified from gDNA. Each sample represented a different reaction and each reaction contained REDTaq™ ReadyMix™ PCR Reaction Mix (Sigma-Aldrich, UK), forward and reverse primers (5 pmol per reaction). Samples were added to a thermocycler and different cycle parameters were used depending on the primer pairs. Only the blueprint for the RT-PCR reaction will be described here; details for cellular cDNA (Section 5.3.4), tissue cDNA (Section 6.3.2.4) and gDNA (Section 6.3.2.2) are found in the respective sections.

The final reaction volume for all PCRs was 25 µl, 50% of which was Ready Mix™ REDTaq® reaction mix with $mgcl_2$ (Sigma, UK) and 10% consisted of 1 mg of SK-N-SH cDNA or 500 ng of tissue cDNA or 100 ng gDNA. *Rumpshaker* (*rsh*) mouse RNA was used as a positive control when investigating cellular pathways as many of the associated pathways, including ER stress, were reported to be induced previously in Mark McLaughlin's (MM) laboratory (McLaughlin *et al.*, 2007). For *Sod*1 PCRs, previously tested gDNA were included as positive controls. MQ water included as a negative control in every reaction.

Each reaction contained 2 to 4 pmol of each primer (0.5 µl; Table 2-4) and were made up to the final volume with PCR water. All primers (Table 2-4), except *Sod*1, were made using murine sequences but BLAST searches against human and canine sequences were conducted to ensure compatibility with study samples. Primers were characterised before use on cellular cDNA (Section 8.3.1.3) and tissue cDNA (Section 8.3.2). *Sod*1 primers were developed from canine sequences and were only used on canine tissue (Section 6.3.2.2). *GAPDH* was used as the housekeeping primer for SK-N-SH studies while *cyclophilin* (*Cyc*) was used for tissue studies due to compatibility of primers and samples.

Table 2-4: List of primers used in this study.

Gene	Accession no.	Sequence	Product size (bps)
ATF3	BC064799.1	**F:** 5′-CAA CAT CCA GGC CAG GTC T-3′ **R:** 5′-CTC TGC AAC GTT CCT TCT TTT-3′	532
Bcl2	NM_177410.3	**F:** 5′-CTG GCA TCT TCT CCT TCC AGC-3′ **R:** 5′-ACC TAC CCA GCC TCC GTT ATC-3′	446
BiP	NM_001163434.1 and NM_022310.3	**F:** 5′-CTG GGT ACA TTT GAT CTG ACT GG-3′ **R:** 5′-GCA TCC TGG TGG CTT TCC AGC CAT TC-3′	398
CHOP	X67083.1	**F:** 5′-CAT ACA CCA CCA CAC CTG AAA G-3′ **R:** 5′-CCG TTT CCT AGT TCT TCC TTG C-3′	356
*Cyc**	NM_008907	**F:** 5′-ACC CCA CCG TGT TCT TCG AC-3′ **R:** 5′-CAT TTG CCA TGG ACA AGA TG-3′	300
GAPDH	NM_001289726.2, NM_008084.4, NM_001411840.1, NM_001411841.1, NM_001411842.1, NM_001411843.1, NM_001411844.1 and NM_001411845.1	**F:** 5′-CCA TGG AGA AGG CTG GGG-3′ **R:** 5′-CAA AGT TGT CAT GGA TGA CC-3′	195
XBP1	NM_013842.3 (*XBP1u*) And NM_001271730.1 (*XBP1s*)	**F:** 5′-AAA CAG AGT AGC AGC TCA GAC TGC-3′ **R:** 5′-TCC TTC TGG GTA GAC CTC TGG GA-3′	***XBP1u***: 480; ***XBP1s***: 454
Sod1	NC_006613.3	**F:** 5′-GCC TGT TGT GGT ATC AGG AAC CA-3′ **R:** 5′-AGA GTC AAA AAC CGG C TT TGT GGA-3′	236

Listed in the table are the details for each primer pair used in this study written from 5′ to 3′. **F**= forward, **R**= reverse. The primer pairs underlined were used only for tissue studies and *GAPDH* (in bold) was only used for *in vitro* studies. **Cyc* also known as peptidylprolyl isomerase A. All primers from Eurofins, Germany. *BiP*, *GAPDH* and *XBP1* primers target multiple transcript variants. *BiP* and *GAPDH* variants are the same size.

Samples were loaded into a T Personal thermocycler (Biometra, Germany) so specific DNA could be amplified. The PCR cycles for cDNA and gDNA were moderately different and are shown in Figure 2-2. PCR products of RNA origin were separated in 2% agarose gels (UltraPure$^{\text{TM}}$ Agarose, Invitrogen, UK) with 1X TAE and 1X SYBR Safe DNA stain while PCR products of gDNA origin were separated in 2.5% agarose gels (UltraPure$^{\text{TM}}$ Agarose) with 1X Tris-borate-EDTA (1X TBE; Thermo Scientific, UK) and 1X SYBR Safe DNA stain. A 100 bp DNA ladder (Appendix 8.2.2.1) was also loaded so the size of the products could be assessed. Gels were run at 70 V for 30 to 40 minutes and visualised with UV light (GeneFlash, Syngene, UK).

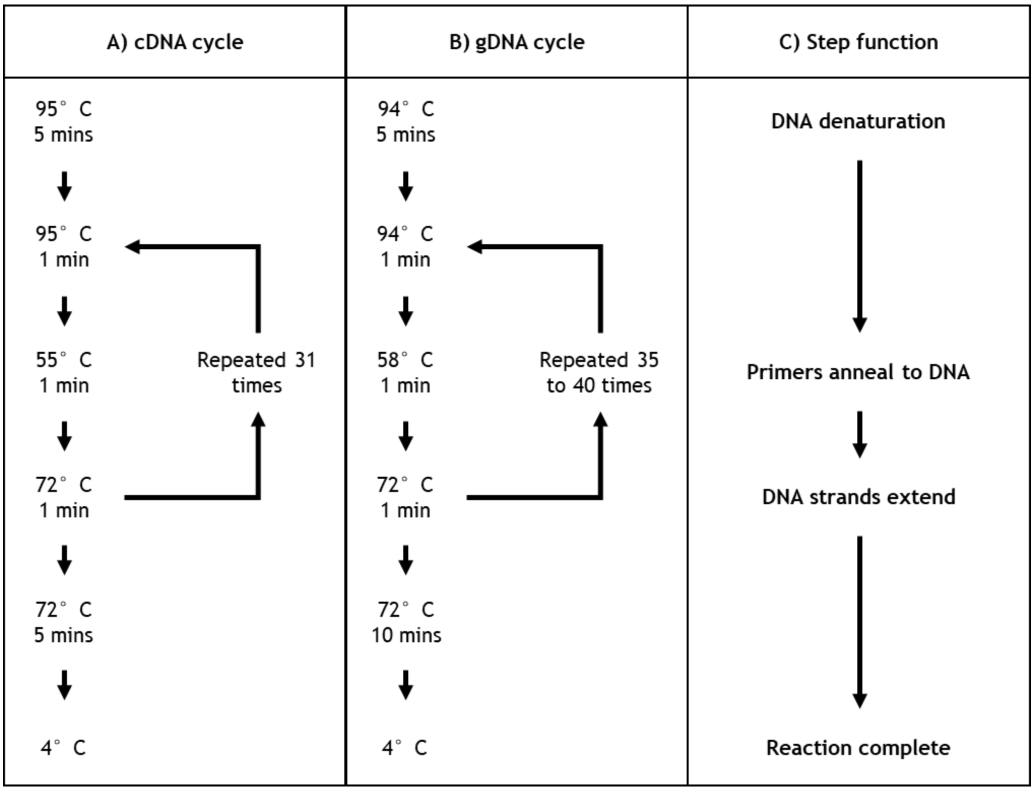
A) cDNA cycle
B) gDNA cycle
C) Step function
95° C
5 mins
95° C
1 min
55° C
1 min
Repeated 31 times
72° C
1 min
72° C
5 mins
4° C
94° C
5 mins
94° C
1 min
58° C
1 min
Repeated 35 to 40 times
72° C
1 min
72° C
10 mins
4° C
DNA denaturation
Primers anneal to DNA
DNA strands extend
Reaction complete

Figure 2-2: PCR thermocycler cycles for RT-PCR of cDNA and gDNA. The flowcharts above depict the cycles used to amplify cDNA **(A)** and gDNA **(B)** using a thermocycler. Each step has a specific role shown in **C)**. To summarise, double stranded cDNA is heated to 94 or 95°C to separate it into two single strands of DNA and denatured, then rapidly cooled to 55 or 58°C to allow primers to bind. Samples are heated again to 72°C so the enzyme Taq polymerase can bind to the primers and extend the DNA strand using nucleotides present in the REDTaq.

2.5.5 PCR product purification

PCR products were purified using the QIAquick™ PCR Purification Kit (Qiagen, Germany) as per manufacturer’s instructions when restriction fragment length polymorphism (RFLP) was required downstream. A buffer containing guanidine hydrochloride and isopropanol from the kit was added to PCR products and transferred into QIAquick columns that contain a silica membrane. The PCR products adsorb to the membrane when the tubes are subsequently centrifuged at 16,100 *xg* for 1 minute. This step allows the removal of primers and other contaminants, so the PCR products are purified. The PCR products were then washed with a buffer containing absolute ethanol and centrifuged at 16,100 *xg* for 1 minute. The column was spun again to remove residual buffer before an elution buffer (containing 10 mM Tris-hydrochloride (Tris-HCl), pH 8.5) was added and the columns centrifuged at 16,100 *xg* for 1 minute to elute the purified PCR products from the spin column membrane. The NanoDrop was used to quantify the concentration as described previously.

2.5.6 Restriction Fragment Length Polymorphism (RFLP) reaction

RFLP reactions were used in cell and tissue derived purified PCR products. Only the *Pst1-HF* RFLP reaction will be described here but details for RFLP conducted on gDNA derived PCR products, which follows similar methodological principles, are found in Section 6.3.2.2.

When a cell is under ER stress, *XBP1* is spliced and starts the UPR cascade. To investigate induction of the UPR, the enzyme *Pst1* can be used to cut *XBP1* (McLaughlin et al., 2007). If *XBP1* is not activated, it will not be spliced and will be digested by *Pst1*. If *XBP1* is activated because of ER stress, it will be spliced and remain undigested. This can be visualised when digested products are electrophoresed on a gel as there will be two or three bands present if unspliced (*XBP1u*) and only one intense band when spliced (*XBP1s*). *XBP1* RFLP was carried out using purified *XBP1* PCR products and the *Pst1*-HF enzyme. The purified products were made to a concentration of 150 ng in 10 µl of MQ, then 10 µl of a master mix containing 1X rCutSmart^{TM} Buffer (10X; New England BioLabs, UK) and *Pst1*-HF (20 U/µl; New England BioLabs, UK) made in MQ was added. Samples were incubated at 37°C for 15 minutes, then transferred onto ice. After adding 1X Loading buffer blue (6X; New England BioLabs, UK) to samples, they were loaded onto 2% agarose gels (Pulse Field Certified, Ultra Pure DNA Grade Agarose, BioRad, UK) with 1X TBE and 1X SYBR Safe DNA stain. A 100 bp DNA ladder (Appendix 8.2.2.1) was also loaded so the size of the products could be assessed. Gels were run at 70 V for 30 to 40 minutes and visualised with UV light (GeneFlash, Syngene, UK).

2.6 Statistical analysis

Most graphical and statistical analyses were carried out using GraphPad Prism 9 software (version 9). For proteomics data, Proteome Discoverer (version 2.4; Thermo Fisher Scientific, UK) was used. Data were plotted in graphs with the mean and standard deviation (SD) to give an indication of the variability of measurements around the mean. In cases where tables were used to summarise data, SD was calculated in Excel (Version 2306; Microsoft, USA) using the STDEV.S() formula. Standard error of the mean (SEM) was calculated for cell and aggregate counts in Excel using the following formula where σ represents SD: $SEM = \frac{\sigma}{\sqrt{n}}$. SEM was presented as mean ± SEM and was used to show the uncertainty in the estimate of the mean based on all observations within each group.

The Royston Shapiro-Wilk test was used to assess the distribution of residuals so the appropriate parametric or non-parametric test could be used. The specific tests are described in each chapter.

3 Optimisation of *in vitro* methods used for investigating SOD1

3.1 Background

WT and mutant SOD1 have been studied in many cell lines including the embryonic kidney cell line HEK293A, the hybrid murine MN like cell line NSC-34, the murine brain neuroblast Neuro2a cell line, the human neuroblastoma SK-N-SH cell line and subline SH-SY5Y. In these studies, SOD1 has been tagged with various constructs including the FLAG-tag, yellow fluorescent protein, green fluorescent protein (GFP) and Cherry (Crisp *et al.*, 2013; Draper *et al.*, 2020; Nakamae *et al.*, 2015; Qi *et al.*, 2019; Wakayama *et al.*, 2022). In DM cell culture models, *Sod*1 mutations result in a fairly low number of aggregates, with only 10-20% of transfected or transduced cells containing SOD1 aggregates 48 hours after transduction/transfection (Crisp *et al.*, 2013; Draper *et al.*, 2020). The addition of fluorescent tags allows the biochemical properties of SOD1, including aggregation, to be assessed under different conditions. In this chapter, conditions were altered to investigate different cellular pathways and processes.

As discussed extensively in Chapter 1 (Section 1.4, Figure 1-1), multiple pathways have been attributed to the generation of DM and ALS. Autophagy and the ubiquitin proteasome system (UPS) are the main clearance pathways for misfolded or defective proteins. Autophagy involves the formation of a membrane around waste components in a cell to form a vesicle (autophagosome) which fuses with lysosomes to be digested (autolysosome). As previously discussed (Section 0), LC3BI is converted to LC3BII when autophagy is induced. LC3BII is incorporated into the autophagosome membrane that forms around debris to be digested by lysosomes in cells. To complete autophagy, lysosomes and autophagosomes fuse to form autolysosomes and, if the conditions are correct, the autolysosome and its contents will be digested (Ogawa *et al.*, 2015; Renna *et al.*, 2010; Xu, Camfield and Gorski, 2018). Chloroquine (CQ) is a chemical agent used to inhibit autophagy in cell culture by changing the autolysosome pH which inhibits digestion (Schrezenmeier and Dörner, 2020). Conversely, autophagy can be induced by nutrient starvation so endogenous components/nutrients can be recycled (Xu, Camfield and Gorski, 2018). LC3 is the only mammalian protein currently known to be specifically associated with the autophagosome membrane (Renna *et al.*, 2010) and can be used as a marker of the autophagosome and autolysosome (Ogawa *et al.*, 2015).

When proteins misfold they can be degraded by proteasomes (Hetz, 2012). Ubiquitin is a chaperone protein that binds to misfolded proteins and transports them to the proteasome for digestion. Other chaperone proteins, including HSP70, have been implicated in both the UPS and autophagy to aid protein folding and degradation. The specific interactions between HSP70 and other chaperones determine the outcome for bound proteins. In some studies, HSP70 has been implicated in the inhibition of apoptosis (Fernández-Fernández *et al.*, 2017). As ubiquitin is essential for the UPS and HSP70 can direct proteins to the UPS, both proteins can be utilised as markers of proteasome function. MG132 can be used as a proteasome inhibitor as it binds to subunits within the 20S proteasome unit of the 26S proteasome (Guo and Peng, 2013).

Accumulation of misfolded proteins in the endoplasmic reticulum (ER) leads to ER stress and a cascade called the unfolded protein response (UPR) is activated for cell adaptation or death by apoptosis (Hetz, 2012). Dithiothreitol (DTT) is a reducing agent and non-specific ER stress inducer. It induces stress by preventing the formation of disulphide (cysteine to cysteine) bonds within proteins (Oslowski and Urano, 2011). There are several specific markers that will be discussed in Chapter 5, but for this chapter, cellular morphology and viability were the main indicators of ER stress induction. The most important morphological features were the loss of extended processes and overall rounding of cells, and the fragmentation of nuclei (karyorrhexis). These features indicate apoptotic processes are taking place (Elmore, 2007).

3.2 Aims

The overall aim of this chapter was to optimise the methods used throughout this thesis. Several smaller aims were generated as follows:

1. Optimise the cellular expression of WT- and DM-SOD1-EGFP plasmid constructs in the SK-N-SH cell line.
2. Scrutinise manual and automatic cell counting methods to ensure the most accurate evaluation of total cell and transfected cell counts of cultured SK-N-SH cells and assess their potential to count intracellular WT- and DM-SOD1-EGFP aggregates.
3. Examine if the presence or absence of exosomes in foetal bovine serum (FBS) affects WT- or DM-SOD1-EGFP aggregation within SK-N-SH cells or their transport between cells in culture.
4. Determine the optimal dose of DTT required to induce ER stress in non-transfected (NT), WT- or DM-SOD1-EGFP transfected SK-N-SH cells.
5. Establish the optimal dose of CQ required to inhibit the autophagy pathway in NT, WT- and DM-SOD1-EGFP transfected SK-N-SH cells.
6. Determine the optimal dose of MG132 required to inhibit the proteasome in NT, WT- and DM-SOD1-EGFP transfected SK-N-SH cells.

3.3 Materials and Methods

3.3.1 Cell culture and transfection

SK-N-SH cells were cultured and split into 4-well or 6-well plates as appropriate then transfected with plasmids as described in Section 2.2.

3.3.1.1 Plasmid characterisation

Using Lipofectamine™ 3000, cells were transfected with pGFP, pmaxGFP, pEGFP, pWT-SOD1-EGFP or pDM-SOD1-EGFP (Table 3-1).

Table 3-1: Plasmid concentrations for transfection.

Plasmid construct	ng/well (4-well)	ng/well (6-well)
pGFP	154	308
pEGFP	244	488
pmaxGFP	615	1230
pWT-SOD1-EGFP	300	600
pDM-SOD1-EGFP	300	600

Forty-eight hours after transfection, 4-well plates were fixed and DAPI stained (Section 2.3.3) and cells in the 6-well plates were lysed (Section 2.4.1). Protein was quantified (Section 2.4.3), then 10 µg of protein was electrophoresed and processed for WB (Section 2.4.7). CuZnSOD, GFP and actin antibodies were used to probe blots and bands were quantified. A native NBT stained gel was also carried out with 10 µg of protein (Section 2.4.5.2 and 2.4.6.3).

3.3.1.2 Manual versus automatic cell counting

Different parameters were tested to facilitate automatic counting of DAPI nuclei and SOD1-EGFP transfected cells. Coverslips contained cells transfected with WT- or DM-SOD1-EGFP, with or without the reducing agent DTT (described further in Chapter 5). Three fields were randomly captured at 200X magnification within each coverslip for three different preparations (*n*= 3). Using 8-bit images in Image J, the threshold was changed so that the background of the image was white and the cells were black. This threshold was adjusted to ensure as many cells were included as possible. Next, the particles were analysed which required the size and circularity to be set. The size setting determines what range of particles will be counted and this correlates to cell size. This had to be set to ignore small, non-cellular particles and include all cells. The circularity setting determined the shape that would be included. As cell nuclei and transfected cells have variation in their shape, this was kept broad. The same settings were used for all total cell counts and for transfected cell counts. From the same images, nuclei and transfected cells were manually counted using the Cell Counter plugin (De Vos, 2001-2021) for Image J. Flowcharts for automatic and manual cell counting are found in Appendices 8.2.4.4 and 8.2.4.5.

3.3.1.3 Growth media comparison

To study EVs, EDM must be used before isolation of EVs instead of NGM to ensure EVs come only from the cells being studied. A comparison of SOD1 aggregation in WT-SOD1-EGFP or DM-SOD1-EGFP transfected cells grown in NGM or EDM was carried out to determine if FBS with or without exosomes respectively influences the development of aggregates. A day after transfection, NGM was refreshed and cells cultured for six hours to mimic treatment, then the media was replaced with either NGM or EDM for 18-20 hours. Cells were fixed and DAPI stained as usual (Section 2.3.3).

3.3.2 Treatment optimisation

3.3.2.1 Determination of optimal DTT dose and treatment duration

The optimal dose of DTT was decided by comparing two doses: 10 mM and 50 mM. Cells were seeded into 6-well plates then left non-transfected (NT) or they were transfected using WT- or DM-SOD1-EGFP plasmids (Section 2.2.2.2). NT cells were untreated or treated with 10 mM or 50 mM DTT the day after seeding for 20 hours. The transfected cells were untreated or treated with 10 mM or 50 mM DTT for 6 hours the day after transfection. After the treatment periods, the morphology of cells and nuclei was assessed using phase-contrast and fluorescence microscopy (Section 2.3.4), then cells were lysed as described previously (Section 2.4.1.3). Protein recovery was determined by carrying out a BCA protein assay (Section 2.4.3).

3.3.2.2 Determination of optimal CQ dose

To study the effect of different doses of CQ on autophagy, cells were first transfected with pLC3-GFP (300 ng/µl). Twenty-four hours after transfection, media was changed to NGM or NGM without FBS. The latter was used to starve cells which induces autophagy. Additionally, one well of cells from each media group was left untreated or was treated with 10 μM or 40 μM CQ (filter sterilised) for 18 hours. After this, cells were lysed (Section 2.4.1.3) and processed for WB using 15 μg of protein (Section 2.4.7). LC3 antibodies were used as a marker of autophagy. To assess the distribution of lysosomes and nuclei within cells treated with CQ, LysoTracker™ Red DND-99 (50 mM; Invitrogen, UK) and DAPI staining were carried out on cells grown in 4-well plates (Section 2.3.2 and 2.3.3).

To further study CQ dose, the effect of media changes and seeding densities, cells were seeded onto a 96-well plate using a serial dilution of 0.125×10^4 to 2×10^4 cells/well. One row was left in NGM for five days before cells were washed and frozen. In another two rows, cells were treated with 10 μM or 40 μM filter sterilised CQ at day 3 for 24 hours. These two rows and the remaining row had their media changed from NGM to EDM on day 4, then cells were washed with PBS and frozen on day 5. Cells were thawed later and 50 μl of lysis buffer was applied for 30 minutes while the cells were being rocked at 4°C. Samples were drawn up and down a pipette tip to dislodge cells from the well surface, then they were collected and processed as normal (Section 2.4.1.3). Proteins were quantified (Section 2.4.3) then values were plotted against cell density as a measure of protein recovery.

3.3.2.3 Determination of optimal MG132 dose

Twenty-four hours after cells were seeded onto 4-well or 6-well plates, cells were treated with 0.5 μM, 1.0 μM, 5.0 μM, 10.0 μM and 50.0 μM MG132 made in DMSO and DMSO alone was added to one well as a control. After a further 24 hours, cells in the 6-well plate were lysed (Section 2.4.1.3), quantified and processed for WB using 10 μg of protein (Section 2.4.7). Ubiquitin, HSP70 and actin antibodies were used to probe blots and bands were quantified (Section 2.4.7.3) to produce a concentration-response curve. The 4-well plates were stained using 50 nM LysoTracker™ Red DND-99 (Section 2.3.2), imaged, fixed and DAPI stained (Section 2.3.3).

3.3.3 Statistical analysis

Statistical analysis was performed in GraphPad Prism for the comparison of manual and automatic cell counts (*n*= 3) and the comparison of SOD1 aggregates using different media (*n*= 4). For other experiments, the number of replicates were too low to perform statistics (*n*= 1 or *n*= 2). After carrying out Royston Shapiro-Wilk normality tests, a nonparametric test (Kruskal-Wallis with Dunn's multiple comparison test) was used for comparison of cell counts and a parametric test (ordinary one-way ANOVA with Bonferroni's multiple comparison test) was used for the comparison of SOD1 aggregates. All graphs were created using the same software.

3.4 Results

3.4.1 Plasmid characterisation

Fluorescence was not observed in NT cells and only endogenous SOD1 was found using WB (Figure 3-1). Green fluorescence was observed in the cells transfected with the three GFP only plasmids and the two SOD1-EGFP plasmids (Figure 3-1A). GFP was generally well distributed throughout cells of all GFP and SOD1-EGFP plasmids, but there were also areas with more intense fluorescence which may indicate the presence of aggregates.

Using an anti-GFP antibody (Figure 3-1B), the protein was observed at ~27 kDa when cells were transfected with pGFP and pEGFP and ~49 kDa in the cells transfected with pWT- and pDM-SOD1-EGFP. Further, when samples were probed for SOD1 (Figure 3-1C), a band was also observed at ~49 kDa in the pWT- and pDM-SOD1-EGFP CLs, corresponding to the fusion proteins. Endogenous SOD1 (~20 kDa) was observed in all CLs whether they were transfected or not. GFP protein was not observed in pmaxGFP CLs using the anti-GFP antibody. Both blots were reprobed with anti-actin to ensure samples were loaded into the gel equally (Figure 3-1B and C). As a result of using the same blots, SOD1-EGFP left over from the first probe can also be seen.

The NBT stained native gel showed endogenous SOD activity was present in NT and both pWT- and pDM-SOD1-EGFP transfected cells and two additional bands were found for the fusion proteins (Figure 3-1D). The distribution of the additional bands were different between the two plasmids as previously demonstrated by Qi *et al.* (2019).

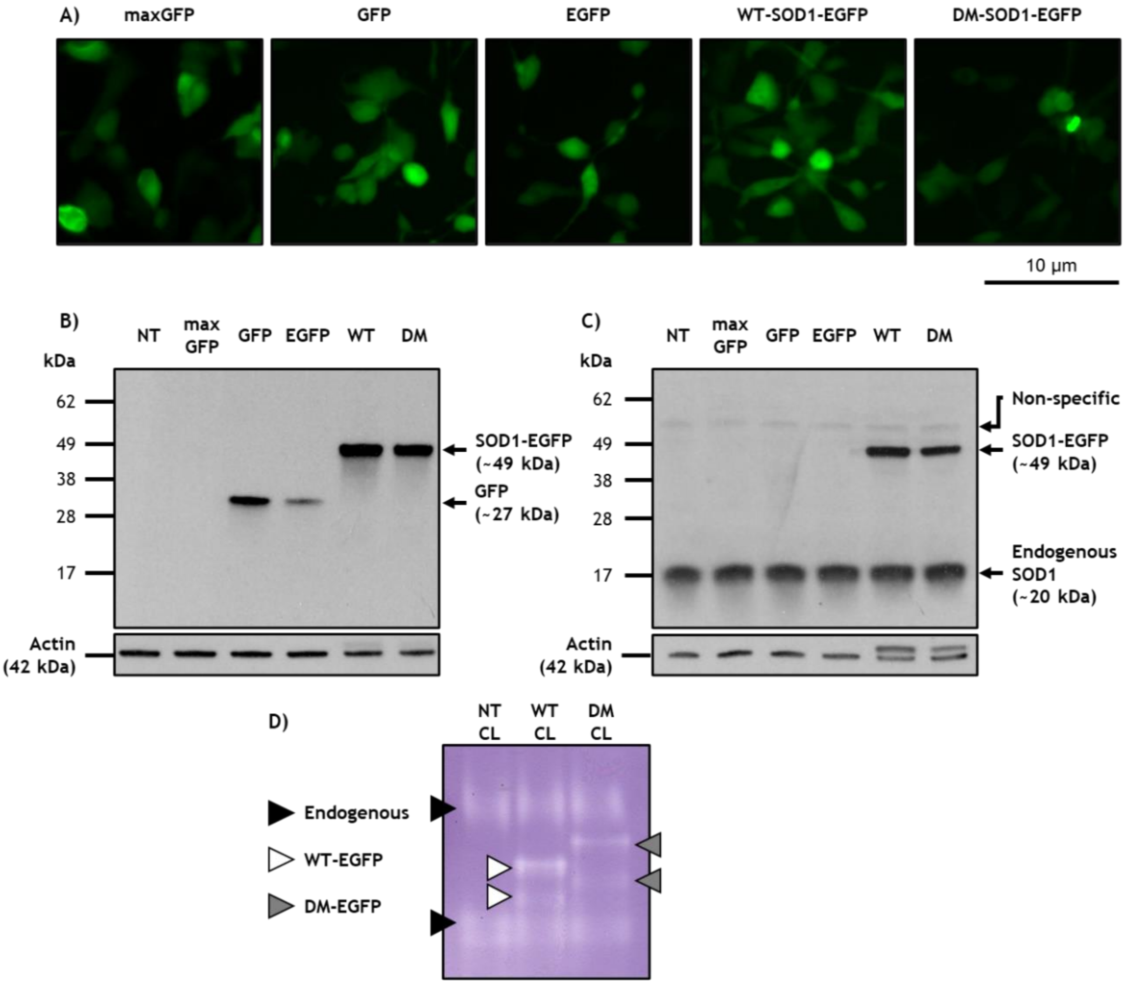
A)
maxGFP
GFP
EGFP
WT-SOD1-EGFP
DM-SOD1-EGFP
10 µm
B)
kDa
NT
max GFP
GFP
EGFP
WT
DM
62
49
38
28
17
SOD1-EGFP (~49 kDa)
GFP (~27 kDa)
Actin (42 kDa)
C)
kDa
NT
max GFP
GFP
EGFP
WT
DM
62
49
38
28
17
Non-specific
SOD1-EGFP (~49 kDa)
Endogenous SOD1 (~20 kDa)
Actin (42 kDa)
D)
NT CL
WT CL
DM CL
Endogenous
WT-EGFP
DM-EGFP

Figure 3-1: Characterisation of SOD1 plasmids used in this study. Cells were transfected with three different GFP plasmids: pmaxGFP, pGFP and pEGFP or one of two fusion proteins: pWT-SOD1-EGFP or pDM-SOD1-EGFP. **A)** Images were captured to understand the distribution of the different plasmids within cells. Scale bar= 10 µm. Proteins were also recovered from cells, separated in gels and probed with anti-GFP **(B)**, anti-CuZnSOD **(C)** and anti-actin antibodies. **B)** GFP was detected in cells transfected with pGFP and pEGFP while the fusion proteins were detected in the WT- and DM-SOD1-EGFP cells. pmaxGFP potentially did not produce a protein with the epitope that is recognised by the goat anti-GFP antibody used in this study. **C)** Endogenous SOD was present in all samples while fusion SOD1-EGFP was only found in the samples from pWT- or pDM-SOD1-EGFP transfected cells. Faint non-specific protein was found in all samples. The blots shown in **B)** and **C)** were reprobed with anti-actin and these are shown at the bottom of **B)** and **C)**. In the pWT- and pDM-SOD1-EGFP samples, there is an additional band at around 49 kDa which corresponds to the fusion proteins. **D)** pWT- and pDM-SOD1-EGFP can also be validated using NBT stained native gels which show enzymatic activity. Endogenous SOD was found in all samples (black arrows). The fusion proteins have distinctive banding: white arrows= pWT-SOD1-EGFP; grey arrows= pDM-SOD1-EGFP.

3.4.2 Automatic cell counting was not sufficient

The number of nuclei counted manually and automatically were compared by expressing the automatic cell counts as a percentage of the manually counted cells. From this, the percentage increase or decrease (difference) was calculated to determine how efficient the automatic process was for DAPI stained nuclei and SOD1-EGFP transfected cells (Figure 3-2). Both total cell and transfected cell counts failed the Shapiro-Wilk test for normality, so Kruskal-Wallis with Dunn's multiple comparison tests were used for each population. There were significantly more nuclei counted with the automatic method compared to the manual method for both untreated ($p \leq 0.05$) and treated cells ($p \leq 0.001$; Figure 3-2A). There was no difference between the treatment groups. For the counting of transfected cells, the automatic method resulted in significantly higher numbers of treated cells compared to the manual method ($p \leq 0.01$), but there was no significant difference between methods for the untreated cells. There was a significant difference between the treatment groups ($p \leq 0.01$; Figure 3-2B).

The percentage differences were moderately variable for untreated (mean ± SD; 5.0 ± 7.3%) and treated (8.7 ± 9.2%) total cell counts. For transfected cell counts, the differences were more variable for both groups (untreated -1.2 ± 23.1%; treated 30.1 ± 40.3%). As a result of these findings, manual cell counting was used for all other experiments.

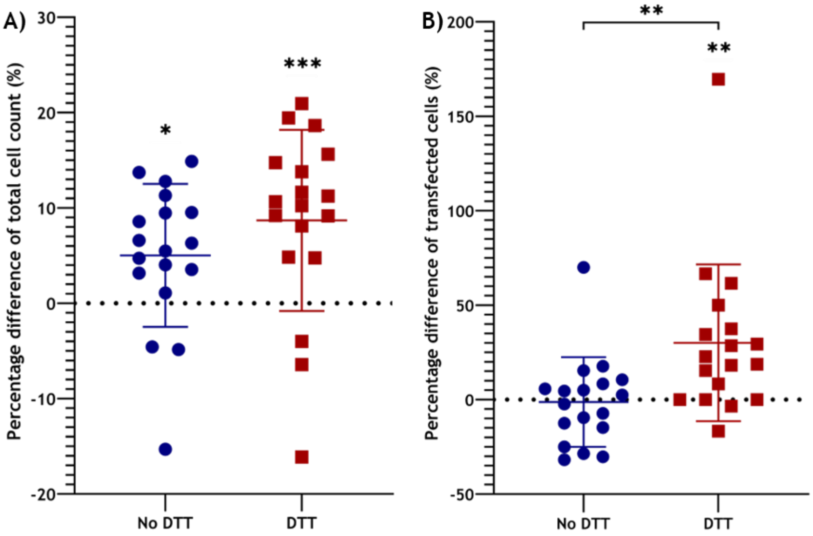

Figure 3-2: Comparison of automatic and manual cell counting. Three fields were used to count nuclei and transfected cells automatically or manually using the Cell Counter plugin in Image J in slides transfected with WT- or DM-SOD1-EGFP, with or without DTT. This was repeated for three preparations. **A)** Automatically counted cell nuclei were expressed as a percentage of manually counted cell nuclei then the percentage difference was plotted. **B)** Automatically counted transfected cells were expressed as a percentage of manually counted transfected cells then the percentage difference was plotted. Kruskal-Wallis with Dunn's multiple comparisons test was used in both cases. *$p \leq 0.05$; **$p \leq 0.01$; ***$p \leq 0.001$.

3.4.3 Growth media comparison

The transfection efficiency and SOD1 aggregate density were assessed in transfected cells grown in NGM or EDM using manual counting methods only. There were no differences in the transfection efficiency of pWT- or pDM-SOD1-EGFP when cells were grown in NGM or EDM (Figure 3-3A). Natively folded and aggregated SOD1-EGFP was found in all groups at varying densities (Figure 3-3B). When using an ordinary one-way ANOVA, there were no significant differences in the average percentage of aggregation within each plasmid when grown in NGM or EDM, but there was a significant increase in aggregation of DM-SOD1-EGFP compared to WT-SOD1-EGFP when cells were grown in NGM ($p \leq 0.05$; Figure 3-3C). There were no statistical differences between the fusion proteins when grown in EDM. Further statistical analysis was carried out to compare aggregation between genotypes within each media type separately using unpaired t-tests. It was found that DM-SOD1-EGFP caused significantly more aggregation compared to WT-SOD1-EGFP when cells were grown in NGM ($p \leq 0.05$) and EDM ($p \leq 0.05$).

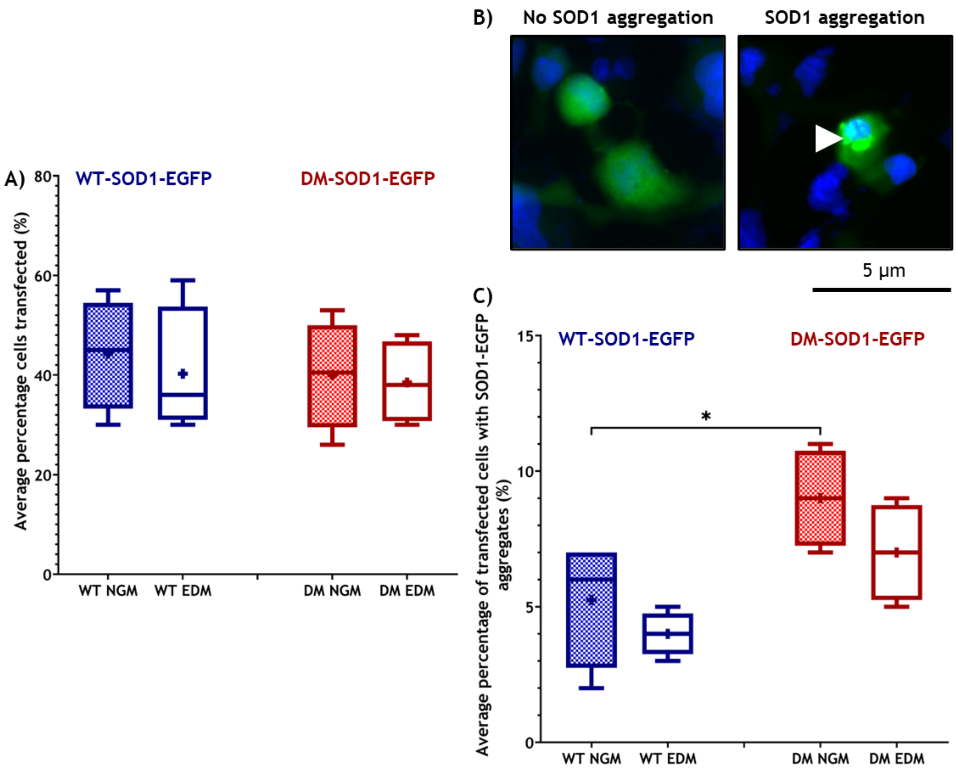

Figure 3-3: Assessment of pSOD1-EGFP transfected cells in NGM or EDM. WT- and DM-SOD1-EGFP transfected cells were grown in NGM or EDM to compare transfection efficiency and SOD1 aggregation within each media type (repeated four times). The transfection efficiency was found by expressing the number of cells transfected with either plasmid as a percentage of the total number of cells (number of DAPI stained cell nuclei). Results were plotted in graph **A)**. **B)** Normally folded and aggregated SOD1 (indicated by white arrowheads) were observed in both WT- and DM-SOD1-EGFP transfected cells of both media types. Scale bars= 5 µm. The percentage of transfected cells with SOD1 aggregates were recorded and plotted in graph **C)**. Ordinary one-way ANOVA with Bonferroni multiple comparisons tests were used to generate statistics in graphs **A)** and **C)**. $^*p \leq 0.05$. += mean.

3.4.4 The optimal dose of DTT is 10 mM

There was noticeable cell loss at 50 mM DTT while 10 mM caused a lower level of cell loss. When treated with DTT, cells presented with a morphology associated with apoptosis (rounded cells and karyorrhexis), suggesting cell stress had been initiated (images not available for this section, examples at 10 mM DTT shown in Figure 5-7).

The quantity (mg/ml) of protein present (protein recovery) in CLs was used to determine cell density in untreated and DTT treated cells. NT cells treated for approximately 20 hours showed that as the dose of DTT increased, protein recovery decreased, suggesting there was cell loss (Figure 3-4A). In transfected cells (Figure 3-4B) after six hours of treatment, protein recovery was similar between untreated CLs suggesting cell survival was not affected by plasmid genotype. At 10 mM and 50 mM DTT, there was a slight reduction in WT-SOD1-EGFP CLs compared to untreated CLs. At 10 mM DTT, DM-SOD1-EGFP CL protein recovery was similar to untreated CLs but there was a slight reduction at 50 mM DTT. The biggest reduction in protein recovery for both genotypes appeared to occur at 50 mM DTT, also suggesting there was more cell loss. As the number of replicates for this experiment is two, statistical analysis was not available.

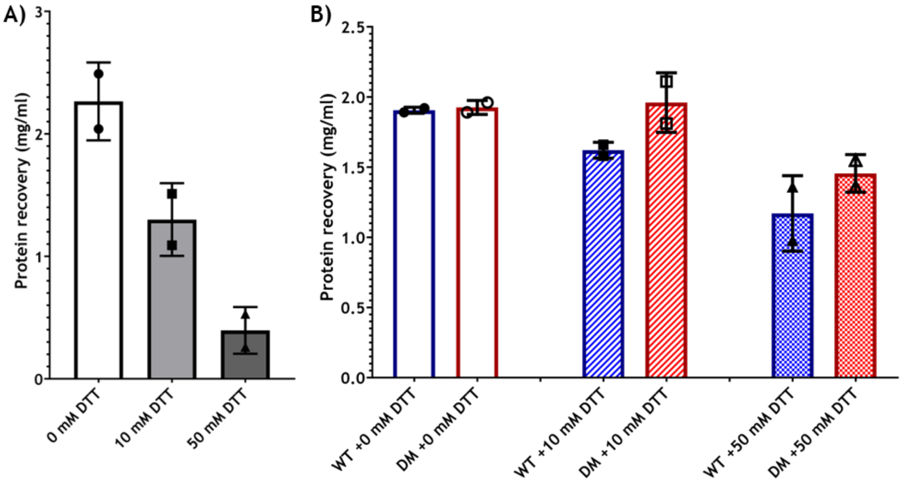

Figure 3-4: Optimisation of dose and duration of DTT treatment. Cells were lysed and a BCA protein assay carried out to determine protein recovery under the different conditions. As the duration of treatment was different for non-transfected and transfected cells, protein recovery was plotted in separate graphs for the groups: non-transfected protein recovery in **A)** and transfected protein recovery in **B)**. **A)** Non-transfected cells were untreated or treated with 10 mM or 50 mM DTT for approximately 20 hours. **B)** WT- and DM-SOD1-EGFP transfected cells were untreated or treated with 10 mM or 50 mM DTT for 6 hours. Error bars represent the SD from two preparations. Individual values are represented by the various shapes.

3.4.5 The optimal dose of CQ is 40 µM

To find the optimal dose of CQ for autophagy inhibition, several studies assessing cytology and specific or nonspecific protein quantities were carried out. In cytology, cells were transfected with the autophagosome marker pLC3B-GFP and grown in NGM with FBS or without FBS (to induce autophagy) before being left untreated or treated with 10 µM or 40 µM CQ. In untreated cells, LC3B-GFP was generally well distributed around the cytoplasm with few puncta. In the treated cells, there was cytoplasmic distribution of LC3B-GFP, but there were more puncta, and these appeared to be most abundant in the cells treated with 40 µM CQ. Further, the absence of FBS may have increased the number of puncta compared to cells grown with FBS (Figure 3-5A). There were no obvious differences in cell density between the treatment groups, however no quantitative assessments were made. The presence of LC3-GFP puncta suggests autophagosomes/autolysosomes were just forming or were not digested. To further assess the interaction between autophagosomes and lysosomes, the distribution of lysosomes was analysed, but only in cells grown in NGM with FBS. In the untreated cells, lysosomes were generally well distributed throughout the cells, but as the concentration of CQ was increased, lysosomes appeared to aggregate or accumulate more as shown by more intense areas of red (Figure 3-5B). DAPI stained nuclei showed the distribution of cells was similar between each group (Figure 3-5B).

For a quantitative investigation of optimal CQ dose, the same marker protein, LC3B-GFP, and the endogenous counterpart LC3, were assessed by WB. The CLs used for WB were the ones transfected with LC3-GFP, described and imaged in Figure 3-5A. Endogenous LC3BI and LC3BII were visible in most samples at varying quantities while LC3B-GFP was only found in transfected CLs (Figure 3-5C). Endogenous LC3BII was quantified, plotted (Figure 3-5D) and compared between NT and transfected groups because it gave the most robust signal and is related to the autophagosome membrane. LC3BII was highest in cells treated with 40 μM CQ regardless of transfection and FBS status suggesting it was inhibiting the most autophagy. LC3BII was highest in the transfected cells across all three CQ doses compared to NT cells. This is likely to be an effect of transfecting cells with the fusion protein which may induce autophagy itself, regardless of the presence or absence of FBS. Finally, LC3BII was generally higher in the NT and transfected CLs without FBS compared to those with FBS, except for NT cells given 10 μM CQ. This may reflect more autophagy being induced as a result of the FBS mitigation which was subsequently being inhibited because of the presence of CQ.

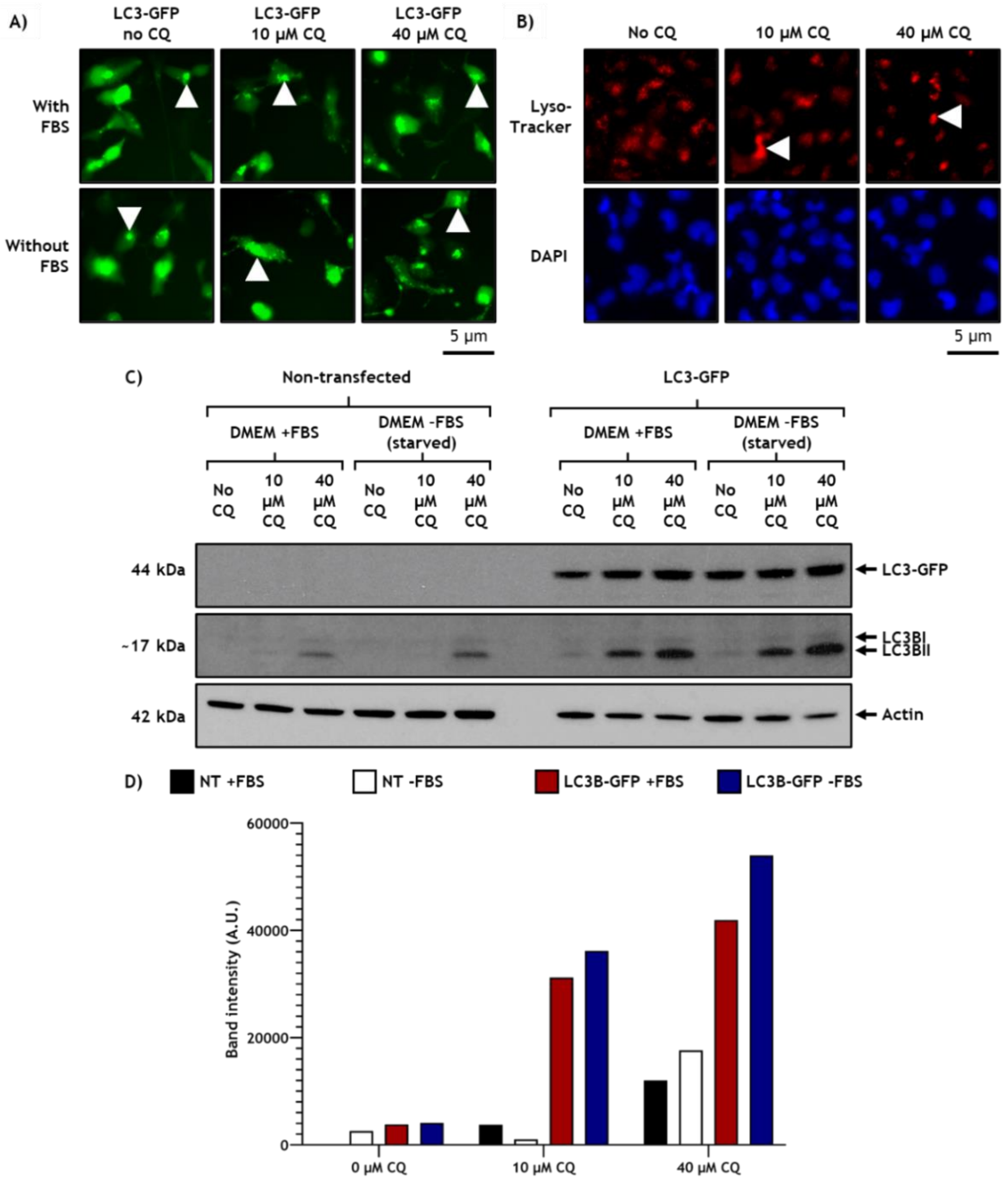
A)
LC3-GFP no CQ
LC3-GFP 10 µM CQ
LC3-GFP 40 µM CQ
With FBS
Without FBS
5 µm
B)
No CQ
10 µM CQ
40 µM CQ
Lyso-Tracker
DAPI
5 µm
C)
Non-transfected
LC3-GFP
DMEM +FBS
DMEM -FBS (starved)
DMEM +FBS
DMEM -FBS (starved)
No CQ
10 µM CQ
40 µM CQ
No CQ
10 µM CQ
40 µM CQ
No CQ
10 µM CQ
40 µM CQ
No CQ
10 µM CQ
40 µM CQ
44 kDa
~17 kDa
42 kDa
LC3-GFP
LC3BI
LC3BII
Actin
D)
NT +FBS
NT -FBS
LC3B-GFP +FBS
LC3B-GFP -FBS
Band intensity (A.U.)
60000
40000
20000
0
0 µM CQ
10 µM CQ
40 µM CQ

Figure 3-5: Autophagy was inhibited by CQ and was visualised *in vitro*. A) SK-N-SH cells were transfected with a green LC3-GFP plasmid and untreated or treated with 10 µM or 40 µM CQ. Top row= cells grown in NGM with FBS; bottom row= cells grown in NGM without FBS. Examples of LC3-GFP puncta are highlighted (white arrowheads). Scale bar= 5 µm. **B)** Cells in 4-well plates were stained with LysoTracker™ to assess the distribution of lysosomes within cells. At 40 µM CQ, there were multiple aggregates of LysoTracker™ but only one example has been highlighted (white arrowhead). Cells were fixed and DAPI stained to show nuclei density but LysoTracker™ staining was lost after fixation so DAPI images are not from the same field. Scale bar= 5 µm. **C)** WBs for NT or LC3-GFP transfected cells shown in **A)**. Top WB= LC3-GFP (~44 kDa); middle blot= endogenous LC3B I and LC3B II (~17 kDa) and bottom blot= actin (42 kDa). The autophagosome membrane associated protein LC3BII was quantified for each condition and plotted in the graph in **D)**.

Another experiment analysed the effect of media type and CQ dose on cell density and protein recovery from NT cells (Figure 3-6). Phase-contrast images showed that as the CQ concentration is increased, the cell density reduced. At 10 µM CQ, the cells started to become rounded but maintained most processes, while at 40 µM CQ, they were clearly rounded, and cells lost processes (Figure 3-6A). The rounded cell morphology is a sign that apoptotic processes were occurring in cells (Elmore, 2007). Figure 3-6B shows that 10 µM CQ did not have a great effect on the quantity of protein recovered in CLs at any cell plating density compared to untreated cells. When 40 µM of CQ was added, there was a more noticeable reduction in protein recovery compared to all other groups, especially at 2x10^4 cells/well. Protein recovery may have been elevated at 2x10^4 cells/well when cells were grown in EDM as this media replaced the older media at day 4, replenishing nutrients, while cells grown in NGM only would have reduced nutrients by the day of harvesting.

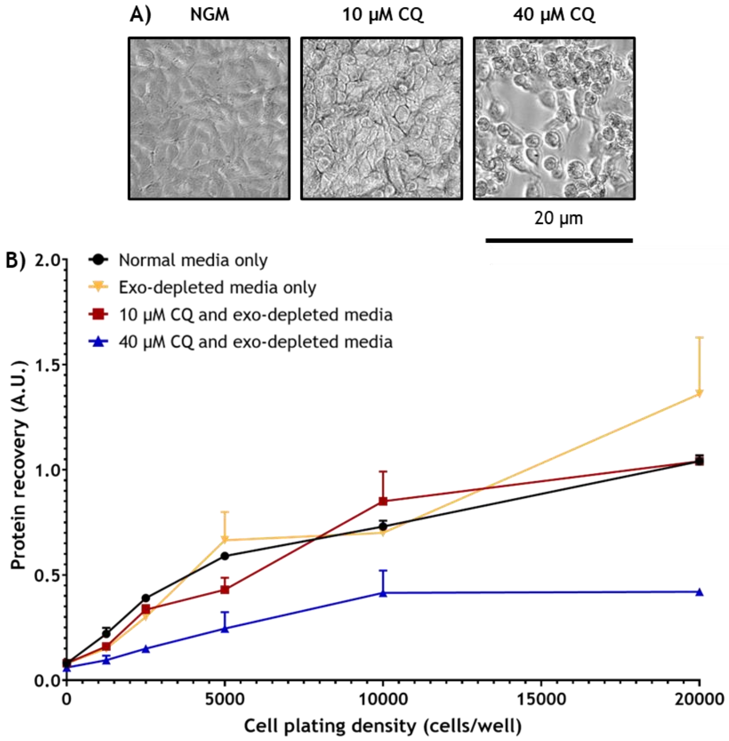

Figure 3-6: Understanding the effect of CQ at different cell densities. Cells were plated onto a 96-well plate at different densities in duplicate. Different rows received different treatments. **A)** The effect of treatment on cell density at 2x10^4 cells plated/well. Scale bar= 20 µm. **B)** Graph showing the protein recovery in different conditions with different plating densities of cells. **Black (circle):** NGM throughout the experiment, no changes. **Yellow (upside-down triangle):** NGM until day 4, where EDM was applied. **Red (square):** grown in NGM until day 4 where EDM was applied, also treated with 10 µM CQ on day 3. **Blue (up-right triangle):** grown in NGM until day 4 where EDM was applied, also treated with 40 µM CQ on day 3. Experiments for this section were carried out once (n=1).

It was concluded that 40 µM of CQ was the optimal dose and so was used for further experiments.

3.4.6 The optimal dose of MG132 is 5 µM

WB and cytology were used to assess the concentration-response effect of the proteasome inhibiter MG132. The cell density of different doses of MG132 was assessed (Figure 3-7A) and it was determined that as the dose increased, the cell density decreased. Additionally, the cells became more rounded, suggesting apoptosis had been initiated.

The cells shown in Figure 3-7A were harvested, and blots were probed for two markers associated with the UPS: ubiquitin and HSP70. Protein analysis showed that treatment at a low concentration, 0.5 µM, MG132 induced a marked increase in HSP70 and ubiquitin (Figure 3-7B). Concentration-response curves indicated 5 µM MG132 was the optimal dose (Figure 3-7C and D).

Lysosomes were also investigated at different concentrations of MG132 using LysoTracker™ (Figure 3-7). Generally, the lysosomes became less distributed around cells as the dose was increased and they started to accumulate and aggregate. There was also a reduced signal at higher doses which may reflect cell loss.

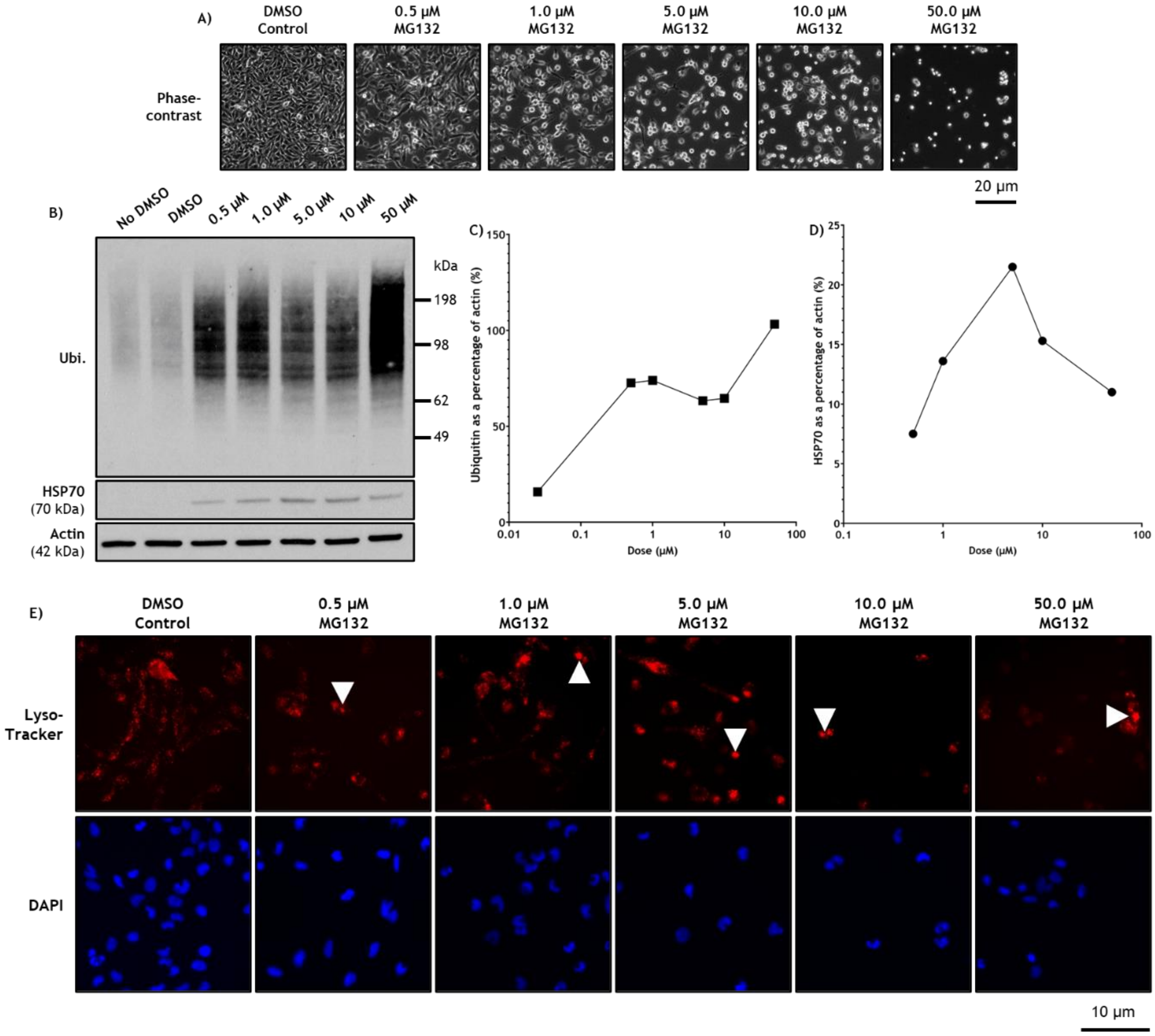
A)
DMSO Control
0.5 µM MG132
1.0 µM MG132
5.0 µM MG132
10.0 µM MG132
50.0 µM MG132
Phase-contrast
20 µm
B)
No DMSO
DMSO
0.5 µM
1.0 µM
5.0 µM
10 µM
50 µM
kDa
198
98
62
49
Ubi.
HSP70 (70 kDa)
Actin (42 kDa)
C)
Ubiquitin as a percentage of actin (%)
150
100
50
0
0.01
0.1
1
10
100
Dose (µM)
D)
HSP70 as a percentage of actin (%)
25
20
15
10
5
0
0.1
1
10
100
Dose (µM)
E)
DMSO Control
0.5 µM MG132
1.0 µM MG132
5.0 µM MG132
10.0 µM MG132
50.0 µM MG132
Lyso-Tracker
DAPI
10 µm

Figure 3-7: MG132 dose optimisation. A) Images captured from 6-well plate before harvesting cells for protein analysis by WB. Scale bar= 20 µm. **B)** WBs probed with Ubiquitin (Ubi.), HSP70 and actin antibodies. A NT control CL from a previous experiment was included to compare with the DMSO control. Bands in the WBs were quantified then values for ubiquitin and HSP70 were expressed as a percentage of actin and plotted to produce concentration-response curves for ubiquitin **(C)** and HSP70 **(D)**. Both graphs use a logarithmic scale (log10) for dose. As 0 is undefined on a logarithmic scale, a low value (0.025) was used so the response with ubiquitin with no MG132 could be plotted **(C)**. For **D),** the DMSO control was not plotted as there was no quantifiable band for HSP70. **E)** Cells in 4-well plates were stained with LysoTracker™ to assess the distribution of lysosomes within cells after treatment with MG132. Aggregates of LysoTracker™ developed when MG132 was added and numbers varied between doses. One example of an aggregate has been highlighted (white arrowhead) in each image so they are not obscured. Cells were fixed and DAPI stained to show nuclei but LysoTracker™ staining was lost so the DAPI images are not from the same fields. The DAPI stained nuclei give an indication of cell density. Scale bar= 10 µm.

3.5 Discussion

3.5.1 Manual cell counting was selected for future work

To reduce personal bias when selecting the images for cell and SOD1-EGFP aggregate counting, three random fields were selected using the DAPI channel, a method that has been reported by others (Tanaka *et al.*, 2021), so fields were not chosen based on the number of SOD1-EGFP aggregates. An automated cell counting method was assessed to further minimise personal bias in counting SOD1 aggregates and ensure consistency in total counts, however the first trial showed there was considerable variation of the counts compared to manual measurements. There were a few potential reasons for this, and in some instances, it could be linked to the presence or absence of DTT. The automated counter struggled to separate clusters of nuclei and would underestimate the number present. In cells treated with DTT, nuclei became fragmented (karyorrhexis) and resulted in small particles being formed which may have been missed or counted individually by the automated system. For transfected cells, it was difficult to set the threshold to a level that would count the number of transfected cells visible: adjusting the threshold would often show more cells than were visible to the naked eye. Additionally, when DTT was added, the cytoplasm could display a fragmented or blebbed appearance which caused problems for the automated system. It is important to ensure total and transfected counts are accurate so transfection efficiency and the percentage of cells with SOD1 aggregates can be calculated accurately.

Further adjustments were made to the method to improve accuracy of measurements and included the use of Watershed and Despeckle functions. These functions attempt to separate particles (cells) based on the distribution of pixels and reduce the number of small, non-cell particles respectively. Unfortunately, due to time constraints, it was decided to abandon the automatic method and utilise manual counting to ensure counts reflected the true values. There is value in streamlining the automated counting method in the future, particularly for transfected cells, as it would improve the consistency in transfected cells being counted. Manually, this can be difficult as transfected cell fluorescence often has different intensities within one field. Further, using the automated method was trialled for counting SOD1 aggregates, but this was particularly sensitive to the difference in fluorescence intensity. Another observation made in the trial was that at 200X magnification, it was difficult to find enough SOD1 aggregates within each field to generate meaningful conclusions. As a result of this, images were captured randomly at 100X magnification for all future studies.

3.5.2 GFP fusion proteins may influence cellular processes

3.5.2.1 General GFP fusion protein characteristics

It is possible that the addition of the (E)GFP tags to LC3B or SOD1 could affect the biochemical properties of the tagged protein, potentially because of their relatively large size. Several studies have suggested that the fusion protein does not significantly affect SOD1 aggregation or activity compared to the endogenous form (Draper *et al.*, 2020; Qi *et al.*, 2019). The results from this chapter however suggest that the larger fusion protein may influence the cellular response to some treatments. When cells were transfected with pLC3B-GFP, LC3BII levels were consistently higher regardless of CQ dose or the presence/absence of FBS compared to NT cells. This may indicate that the addition of the large fusion protein induces autophagy which is then inhibited by CQ. It is also possible that the use of Lipofectamine™ 3000 in the transfection procedure could influence the stimulation of cellular pathways, potentially increasing the effect of drugs compared to the effect seen in NT cells.

3.5.2.2 Activity profiles of WT- and DM-SOD1-EGFP fusion proteins are different

Using the in-gel activity assay, the activity profiles of WT- and DM-SOD1-EGFP fusion proteins differed from each other and from endogenous SOD1 as previously reported by Qi *et al.* (2019). The presence of activity suggested the covalent link between the fluorescent GFP-tag and mutant protein did not significantly change the SOD1 activity and Qi *et al.* (2019) hypothesised the banding pattern was due to the presence of SOD1 heteromers. Mutant SOD1 is less negative than WT SOD1 (Kimura *et al.*, 2020) so the difference in the migration of the fusion protein bands could reflect this. In non-native WBs, NT, WT- and DM-SOD1-EGFP were present at the same molecular weight when probed with anti-CuZnSOD (Figure 3-1C) indicating that when denatured, they all migrate similarly.

3.5.2.3 Aggregation density of WT- and DM-SOD1-EGFP fusion proteins are different

The number of SOD1-EGFP aggregates was compared between WT- and DM-SOD1-EGFP transfected cells. More aggregates were present in the cells transfected with pDM-SOD1-EGFP compared to pWT-SOD1-EGFP which is consistent with previous reports (Crisp *et al.*, 2013; Draper *et al.*, 2020; Nakamae *et al.*, 2015; Qi *et al.*, 2019; Wakayama *et al.*, 2022). SOD1 aggregation was present in WT-SOD1-EGFP cells as misfolding of proteins can occur in any cell. Factors that influence the misfolding of SOD1 will be investigated in Chapter 5.

In the current experiment, SOD1-EGFP aggregation in different culture mediums was investigated. There was a significant increase in DM-SOD1-EGFP aggregation compared to WT-SOD1-EGFP when grown in NGM (FBS containing endogenous exosomes; $p \leq 0.05$) but the difference in means for those grown in EDM (exosome depleted FBS) did not reach statistical significance. A potential reason for the difference in significance may be because of the depletion of exosomes in the FBS used to make EDM. EDM is essential when investigating EVs in cell culture so that endogenous exosomes found in FBS do not interfere with measurements. Results suggest that replacing NGM with EDM reduces the severity of SOD1 aggregation within cells. This would imply that EVs (specifically exosomes) may contribute to the spread of SOD1, a phenomenon that will be investigated further in Chapters 4 and 5 of this thesis. Only four replicates were completed in this study but using a larger sample size in the future may allow the use of more robust statistical tests which could demonstrate differences in both media types.

3.5.3 DTT dose and treatment duration affect cell survival

To assess the optimal dose and duration of treatment with DTT required to induce general ER stress, cell viability and total protein recovery in CLs were investigated. Treatment with 10 mM or 50 mM DTT for 20 hours caused a marked reduction in cell survival and the overall quantity of protein recovered from CLs so treatment duration was reduced. Treatment with 50 mM DTT for 6 hours continued to cause a marked reduction in cell density and protein recovery compared to treatment with 10 mM DTT. These observations suggest treatment with 10 mM DTT for 6 hours ensures there are enough cells to be assessed by cytology and protein studies, thus this dose was used for future experiments. Only cell morphology was used to assess cell death mechanisms after DTT treatment in the current study, however assays, for example MTT (3-(4,5-Dimethylthiazol-2-yl)-2,5-Diphenyltetrazolium Bromide) assays or TUNEL (terminal deoxynucleotidyl transferase dUTP nick end labelling) assays, would have been more accurate to determine cell viability and conclude if apoptosis was present.

3.5.4 Components of autophagy accumulate within CQ treated cells

To assess CQ as an inhibitor of autophagy, cytology was used to monitor two components involved in the process: LC3B and lysosomes. Both LC3B-GFP puncta and lysosomes accumulated in cells when 10 µM or 40 µM CQ was added and there appeared to be more aggregation of the components at 40 µM implying more autophagosomes and/or autolysosomes were accumulating. At 10 µM, it is possible that autolysosomes were being digested, reducing the accumulation of LC3B-GFP and LysoTracker™. These observations generally correlated with the increase in LC3B-GFP seen in CLs. Endogenous LC3BII also increased as the CQ dose increased in both transfected and NT cells, further supporting the idea that more autophagy can reach completion at 10 µM CQ compared to 40 µM CQ. It is also possible that as autolysosomes accumulated in the presence of 40 µM CQ, further autophagy was induced, however at 10 µM CQ, the accumulation of autolysosomes may not have reached a level where the same amount of autophagy was induced. When nutrients were depleted, there was no obvious difference in the puncta development of LC3B-GFP, however LC3BII levels were potentially higher in cells without FBS compared to those with FBS, although no statistical tests were carried out. This suggested that when autophagy is upregulated, there would be an accumulation of autophagosomes, and in the presence of CQ, there is potentially greater accumulation of autolysosomes as the process is inhibited at a later stage of autophagy. Often the LC3BII/LC3BI ratio is used as an indicator of autophagy function as the rate of conversion of LC3BI to LC3BII and the rate of LC3BII digestion can be determined. In the current experiment, LC3BI levels were difficult to quantify, so only LC3BII levels were used. As this part of the study was for optimisation and assessment of CQ dose, the LC3BII quantity was sufficient to reach a conclusion. For future experiments, 40 µM CQ was selected because it induced clear increases in LC3B-GFP puncta and LC3BII suggesting autophagy was sufficiently inhibited.

3.5.5 Components of the UPS accumulate in MG132 treated cells

To determine the optimal dose of MG132 for inhibiting the UPS, cell morphology and recovery of ubiquitin and HSP70 marker proteins were assessed. When 0.5 µM MG132 was added, there was an increase in rounded cells, a decrease in cells density and an increase in both ubiquitin and HSP70 proteins when compared to control cells. As the dose of MG132 was increased, these changes generally became more marked, except for HSP70. HSP70 increased in cells until they were treated with 10 µM or 50 µM MG132, where levels reduced. The reduced HSP70 at 10 µM and 50 µM MG132 may indicate that proteasome function at these doses is suboptimal, so other pathways may be called upon to degrade proteins. Ubiquitin increased as the dose increased to 1 µM, then at 50 µM because there would be increased polyubiquitination of proteins as cells become more stressed because of treatment, in addition to the enhanced inhibition of the proteasome. Stress was indicated by marked reduction in cell density and the rounding of cells. At lower doses, some proteasome function will be maintained, allowing for a turnover of proteins that reduced presence of cell stress. Additionally, at lower doses, HSP70 may have inhibited apoptosis (Fernández-Fernández *et al.*, 2017), but at the higher doses of 10 µM and 50 µM MG132, where HSP70 was reduced, apoptotic mechanisms may have been promoted. Addition of a TUNEL assay would have allowed investigation of the involvement of apoptosis and an MTT assay can determine general cell viability. Due to time constraints, MTT assays were not carried out. Assessment of LysoTracker™ also indicated that as the MG132 dose increased, lysosomes became more aggregated. For these reasons, 5 µM MG132 was selected as the optimal dose as it ensured cell viability and density were sufficient and stress was at a level that allowed analysis of other proteins of interest, as opposed to proteins/blots being saturated by ubiquitin.

4 Characterisation of extracellular vesicles and their association with SOD1 *in vitro*

4.1 Background

EVs are a heterogenous population of particles that can be isolated from cell culture media using various methods as discussed in Section 1.5. EVs, specifically exosomes, have been implicated in many neurodegenerative diseases including ALS and are thought to play a role in disease pathology (Silverman *et al.*, 2019). It was originally planned to investigate exosomes in this study, however, due to many technicalities which will be discussed in this chapter, the term EVs had to be used. As the main aim was to investigate exosomes, isolation techniques and markers for characterisation were geared towards this specific fraction.

The various EV particles have different sizes and biochemical properties that can be exploited for isolation and characterisation however there is currently no method that is able to completely separate the EV subgroups as there is crossover in some properties including size (Haraszti *et al.*, 2016). The International Society for Extracellular Vesicles (ISEV) developed, and have since updated, the guidelines in Minimal Information for Studies of Extracellular Vesicles (MISEV) to enable standardisation of EV isolation and characterisation across all EV fields (Théry *et al.*, 2018). Differential ultracentrifugation is the most utilised method of EV isolation (Théry *et al.*, 2018) and is considered the gold standard (Momen-Heravi, 2017). The velocities used in differential ultracentrifugation separate particles by size. Theoretically, larger particles will be pulled to the bottom of a centrifuge tube at lower velocities and smaller particles at higher velocities. Ultracentrifugation at a moderate speed, for example 10,000 *xg*, is associated with the retrieval of MVs, while centrifugation at 100,000 *xg* is associated with small EVs or exosomes (Théry *et al.*, 2018). The use of a combination of isolation methods can result in purer EV isolations but comes at a cost of reduced EV material. It has therefore been suggested that researchers determine the best EV retrieval method based on the volume of sample they start with, the volume of sample they need for further investigations, and to determine what contaminants are essential to remove (Brennan *et al.*, 2020).

Currently, there is a lack of consensus for markers of specific EV subtypes, so it is generally encouraged that EVs are described by their size, biochemical composition and origin (Théry *et al.*, 2018). The main method for characterisation of EVs in this thesis was Western blot (WB). Components found in exosomes tend to be of cytoplasmic or plasma membrane origin and they normally lack most proteins from the nucleus, mitochondria and ER (Gomes *et al.*, 2007). For this reason, actin, a cytoskeletal protein, was employed as a marker for EV fraction purity and cellular contamination. Exosomes are enriched in proteins such as CD9, flotillin-1, programmed cell death 6-interacting protein (ALIX; also ALG-2-interacting protein X), CD81 and Tumour suppressor gene 101 (TSG101). Additional markers specific for the cells they were produced from are also used (Chen *et al.*, 2019; Hayashi *et al.*, 2019; Otake, Kamiguchi and Hirozane, 2019; Thompson *et al.*, 2020). Flotillin-1 was selected as a marker for EVs in this study and only the neuroblastoma derived SK-N-SH cell line was used.

EVs can be associated with proteins believed to contribute to disease, including mutant SOD1. For example, CNS derived EVs from non-transgenic and mutant SOD1 transgenic mice, and humans with and without fALS have been investigated. EVs from mutant mice and fALS cases have been associated with significantly more misfolded SOD1 compared to non-transgenic or negative counterparts. Both soluble mutant SOD1 and insoluble aggregates were found in EVs produced from murine and human CNS. These results suggested that EVs with mutant SOD1 from live cells in the murine and human CNS may be enough to induce the misfolding of WT SOD1 and may spread disease in a prion like manner in addition to free SOD1 aggregates from dead or dying cells (Silverman *et al.*, 2019).

EVs derived from cell culture or biological fluids can be used in *in vitro* conditioned media experiments to further investigate their role in homeostasis or disease. Various conditioned media methods have been used successfully to investigate the role EVs in ALS. For example, studies investigating misfolded SOD1 have found some SOD1 mutants in conditioned medium are able to interact with WT SOD1 inside neurone like cells after exposure and change their conformation to the mutant form. Through these experiments, it has also been found that overexpression of WT SOD1 can induce misfolding of SOD1, suggesting that this could be a spontaneous misfolding event in some cases of ALS, especially sALS, and this mutated protein can then be propagated to other cells (Hanspal *et al.*, 2017). Experiments investigating the intercellular propagation of DM mutant SOD1 are currently limited to two studies. Tanaka *et al.*, (2021) transferred culture media from neuroblast cells that had been transfected with WT or mutant SOD1 protein to NT neuroblast cells and found only the DM derived culture media initiated fluorescent SOD1 aggregation within cells. Pfeiffer *et al.*, (2023) studied serum derived exosomes from control and DM dogs and found monomeric SOD1 and TDP-43, another ALS associated protein, were significantly higher in DM exosomes compared to controls. While this result does not provide specific information on the source of the exosomes, it is hoped further refining of the isolation method will allow investigation of neurone specific exosomes. Additionally, proteins associated with serum derived exosomes could be utilised as biomarkers for DM and ALS in the future.

4.2 Hypothesis and aims

The aims of this chapter were based on the hypothesis that EVs can be produced from SK-N-SH cells and isolated from media using differential ultracentrifugation. Additionally, EVs produced from WT- and DM-SOD1-EGFP transfected cells can be associated with the SOD1 protein and spread the protein to other cells in culture in a prion-like manner. The main aims of this chapter were to:

1. Optimise the sequential ultracentrifugation method for the isolation of EVs found in cell culture media produced from NT, WT- and DM-SOD1-EGFP transfected SK-N-SH cells.
2. Investigate the potential association between endogenous SOD1, WT- and DM-SOD1-EGFP and EVs from SK-N-SH cells.
3. Ascertain if EVs associated with WT- or DM-SOD1-EGFP can spread the fusion proteins between cells in a prion-like manner in culture.

4. Determine if the genotype of SOD1 associated with EVs influences the uptake of the protein by NT SK-N-SH cells in culture.

4.3 Materials and Methods

4.3.1 Cell culture and transfection

SK-N-SH cells were cultured and split into 4- and 6-well plates and cell culture flasks, then transfected with WT-SOD1-EGFP or DM-SOD1-EGFP plasmids as described in (Section 2.2) where appropriate. Where EVs were studied, exosome-depleted media (EDM) replaced normal growth media (NGM) 24 hours before EV collection. Methods were derived from Momen-Heravi (2017) and Théry *et al.*, (2018) for EV isolation.

4.3.2 Optimisation of EV isolation

4.3.2.1 Comparison of multiple ultracentrifugation steps to generate EVs from NT cells

The first experiment compared the effect of two or three rounds of centrifugation on the isolation of EVs from NT cells. Aliquots (0.5 ml) of a 5 ml NGM-cell suspension derived from a confluent T75 culture flask were seeded into 2 T25 culture flasks with 5.5 ml NGM. Flasks were cultured for a day before NGM was removed and cells washed with serum free media, then 5 ml EDM was applied for 18-20 hours. EDM was collected individually from both flasks and centrifuged at 110 *xg* for 5 minutes to remove cellular debris. Of this EDM, 1 ml from each flask was collected and TCA precipitation (Section 2.4.1.2) was carried out to concentrate the proteins found in the total media (TM). The remaining 4 ml from each flask was transferred to centrifuge tubes. One tube was centrifuged at 10,000 *xg* for 30 minutes at 4°C while the other tube was kept on ice. The SN was transferred to a fresh tube and the pellet was resuspended in 50 µl lysis buffer (Section 2.4.1.1). The SN was then centrifuged with the other tube at 110,858 *xg* for 2 hours at 4°C. SN from both tubes was discarded and the pellets were resuspended in 50 µl of lysis buffer. Cells in the flasks were washed twice with chilled PBS, then lysed with 250 µl of lysis buffer.

Proteins in the media associated and CL samples were quantified (Section 2.4.3) and aliquots were made containing 5 µg and 10 µg protein for CLs and 5 µg for media associated fractions. SDS-PAGE (Section 2.4.5.1) and WB were performed (Section 2.4.7).

4.3.2.2 Comparison of multiple ultracentrifugation steps to generate EVs from transfected cells

The next experiment studied the effect of two or three centrifugation steps on the isolation of EVs from transfected cells using the experimental parameters used in the NT study (Section 4.3.2.1). Whole 6-well plates were either NT or transfected with pWT-SOD1-EGFP or pDM-SOD1-EGFP (Section 2.2). The day after transfection, cells were rinsed with serum free media, then EDM was applied for 20-24 hours. Media was collected from each plate, giving a total of 9 ml per plate. This was centrifuged at 110 *xg* then 4 ml of SN was transferred to two centrifugation tubes per plate. Left over SN was TCA precipitated (Section 2.4.1.2) and represented TM before ultracentrifugation. One centrifuge tube from each plate was spun at 110,858 *xg* (110,858 only) for 2 hours, and the other at 10,000 *xg* for 30 minutes, then 110,858 *xg* for 2 hours at 4°C. The pellets from each stage were resuspended in 50 µl of lysis buffer and cells were lysed in 100 µl lysis buffer (Section 2.4.1.3). Proteins from media associated fractions and CLs were quantified and aliquots were processed for SDS-PAGE (media associated fractions made to 1 and 5 µg, CL made to 1, 5 and 10 µg) before silver staining (Section 2.4.6.2) and WB (Section 2.4.7) was performed. Native gels (Section 2.4.5.2) with NBT staining (Section 2.4.6.3) were also carried out using 6 µg of protein for CLs and media associated fractions.

4.3.3 EV transfer studies

4.3.3.1 Pilot study

Three 6-well plates of cells were either NT or transfected with pWT-SOD1-EGFP or pDM-SOD1-EGFP. EDM from each plate was collected giving a total of 9 ml EDM per plate and this was centrifuged at 110 *xg* for 5 minutes. The SN from each plate was divided into two centrifuge tubes (4 ml total) and centrifuged at 110,858 *xg* for 2 hours. The SN was discarded, and the pellets were resuspended in 300 µl filter sterilised Dulbecco's PBS (DPBS). Resuspended pellets were recombined for each plate to give a total of 600 µl of EV suspensions. A day before collection of EVs, seven 6-well plates were seeded with 1.5×10^5 cells/well. A 75 µl aliquot of each NT, WT or DM EV suspension was added to a well with cells in every plate while the remaining EVs were stored for protein quantification. Live cell images were captured from every plate for up to seven days and each day, one plate was removed and cells were lysed. After protein quantification, 5 µg aliquots of donor CLs and EVs and recipient CLs from harvest days 1, 3, 5 and 7 were processed for SDS-PAGE (Section 2.4.5.1) and WB (Section 2.4.7).

4.3.3.2 Studies with an intermediate centrifugation step

As a result of the pilot study, two follow up experiments were conducted and further refined to address a potential donor EV cell contamination issue. Both experiments followed the EV isolation protocol involving three centrifugation steps previously described (Figure 2-1B). To generate donor EVs in the follow up experiments, cells in two 6-well plates were transfected with pWT- or pDM-SOD1-EGFP. EVs were collected and resuspended in 200 µl filter sterilised DPBS, then recombined (400 µl total for each genotype) as previously described after centrifugation at 10,000 *xg* for 30 minutes and 110,858 *xg* for 2 hours.

For each experiment, three 4-well plates were seeded with a decreasing number of cells (to compensate for cellular growth during the experimental period) the day before EV collection from donor cells. For the first experiment, the range was 1.6×10^2 to 4×10^4 cells/well (stepwise reduction by 33%), and for the second experiment, the range was 1.25×10^3 to 4×10^4 cells/well (stepwise reduction by 50%). EV suspensions from each genotype and ultracentrifugation step were applied to 1 well in each 4-well plate (first experiment= 70 µl; second experiment= 65 µl). After one, three and six- or seven-days post EV addition, recipient cells were processed for imaging (Section 2.3.3).

4.3.4 Statistical analysis

GraphPad Prism was used to conduct statistical analysis and construct graphs. Royston Shapiro-Wilk tests were carried out on each group of data to assess normality then parametric ordinary one- and two-way ANOVAs were carried out with Bonferroni's multiple comparison test.

4.4 Results

4.4.1 Three centrifugation steps may enrich NT EV fraction

The impact of differential ultracentrifugation on EV recovery from cells was assessed using the EV marker protein flotillin-1. Flotillin-1 found in the 10,000 *xg* and subsequent 110,858 *xg* EV fractions were roughly comparable to the total flotillin-1 found in the EV fraction after one 110,858 *xg* step (Figure 4-1A and B). There was no statistical difference in the quantity of flotillin-1 found in the 110,858 *xg* fractions after one or two ultracentrifugation steps. While not statistically significant, compared to TM, the ultracentrifugation steps appeared to have more flotillin-1, indicating the EV population was enriched. Actin was markedly reduced in all EV fractions compared to CLs (Figure 4-1C), indicating there was little cellular contamination in the media associated fractions. A representative Ponceau S stained blot is presented in Appendix 8.3.3.1.

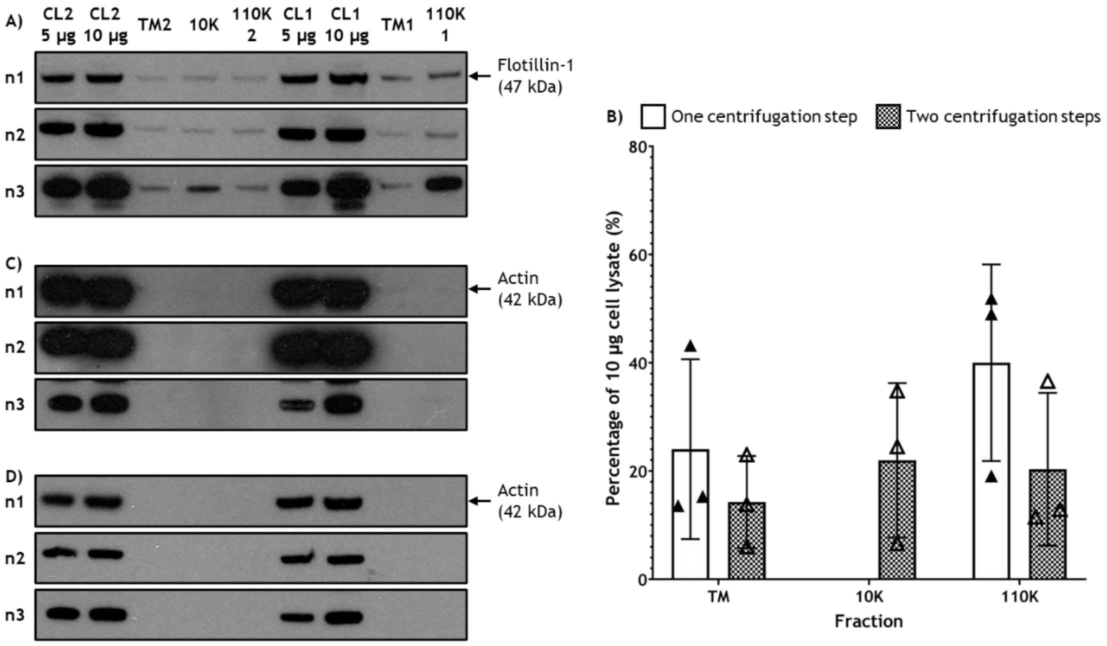

Figure 4-1: EV fraction may be enriched after two ultracentrifugation steps. A) WBs probed with flotillin-1 (*n*=3). In each preparation, lanes corresponded to CL at 5 µg and 10 µg of protein, TM (after low-speed spin to get rid of debris), pellet after the intermediate 10,000 *xg* (10K) centrifugation step and pellet after the 110,858 *xg* (110K) centrifugation step. Band intensities for TM, 10K and 110K fractions were expressed as a percentage of the 10 µg CL band intensities and plotted in the graph in **B)**. There were no statistically significant differences in the recovery of flotillin-1 between the centrifugation speeds using one-way ANOVA with Bonferroni multiple comparisons test. This test was selected instead of a two-way ANOVA because there would be missing values for the 10K fraction in the set of samples with one centrifugation step only. All three preparations were also probed for actin **(C** and **D)**. Blots were overexposed **(C)** to show that minimal actin was in the media associated fractions compared to the CL fraction. In **D)** actin blots were exposed for a short period of time to assess the level of protein loaded in the CLs.

4.4.2 Total protein profiles of NT and transfected EVs are similar

The total protein profiles (Figure 4-2) differed between CLs and the media associated fractions however all media fractions had similar profiles to each other. There was a prominent band in all media associated fractions at approximately 62 kDa and this potentially corresponds to the serum-derived protein albumin present in FBS. Transfected profiles were slightly different from the NT profile in that they had some additional bands and several of the bands had different intensities.

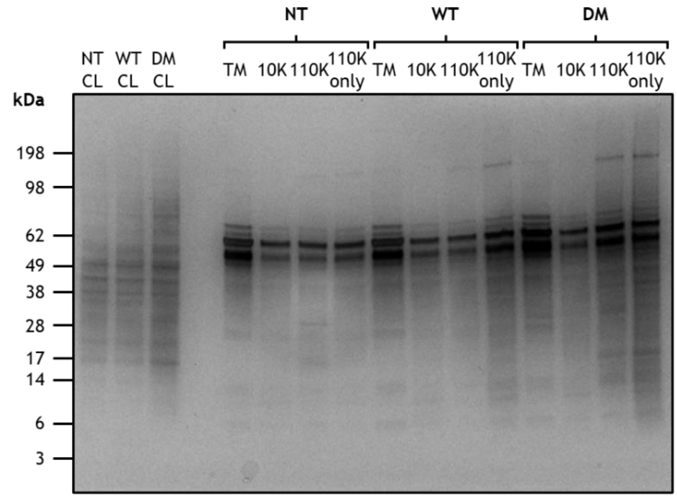

Figure 4-2: Total protein profiles for cells and media associated fractions. The image shows a silver-stained gel to give the total protein profile of the different fractions, with and without transfection with pWT-SOD1-EGFP or pDM-SOD1-EGFP. EVs isolated after 10,000 *xg*, 110,858 *xg* and 110,858 *xg* only centrifugation steps have a similar protein profile, although profiles of transfected EVs are more similar to each other than to NT EVs. CLs from all genotypes have similar profiles.

4.4.3 Characterisation of EVs

Flotillin-1 and actin proteins were used to characterise EVs based on their relative proportions to CLs. Flotillin-1 antibodies produced good signals for most media associated fractions from NT, WT- and DM-SOD1-EGFP transfected cells (Figure 4-3A), however there was high variability in signal intensity. There was no significant difference in the protein found in the 110,858 *xg* fractions of NT, WT- or DM-SOD1-EGFP transfected cells (Figure 4-3B). The additional 10,000 *xg* centrifugation step reduced the mean quantity of flotillin-1 found in the 110,858 *xg* fraction, but this was not statistically significant. Both the 10,000 *xg* and 110,858 *xg* only samples had a higher average level of flotillin-1 than the 110,858 *xg* samples after the intermediate spin in NT, WT- and DM-SOD1-EGFP media fractions, but again, this was not significant. There was an increase in flotillin-1 in the centrifuged fractions compared to the TM for transfected cells, but it was only significant for WT-SOD1-EGFP TM and 10,000 *xg* fractions. Overall, the transfected media associated fractions had higher mean flotillin-1 than NT media associated fractions, but it was not statistically significant. It should be noted that not all samples were normally distributed so a nonparametric test should be selected. GraphPad Prism, the statistical software used in this study, does not have a nonparametric alternative to the ordinary two-way ANOVA. This could affect the sensitivity of the test to significant differences, however parametric tests are generally considered to overestimate the significance of changes, so it is possible similar results would be achieved as not many changes reached statistical significance with the parametric test.

Actin was investigated to confirm that cellular components were reduced in media associated fractions compared to CLs (Figure 4-3C). In all replicates and genotypes, actin was reduced in media associated fractions compared to CLs. There was variation in the distribution of actin across fractions: sometimes, actin was higher in the 10,000 *xg* and 110,858 *xg* only fractions and other times, it was higher in both 110,858 *xg* fractions. Overall, actin content appeared to be higher in the media associated fractions of transfected cells compared to NT. A representative Ponceau S stained blot is presented in Appendix 8.3.3.1.

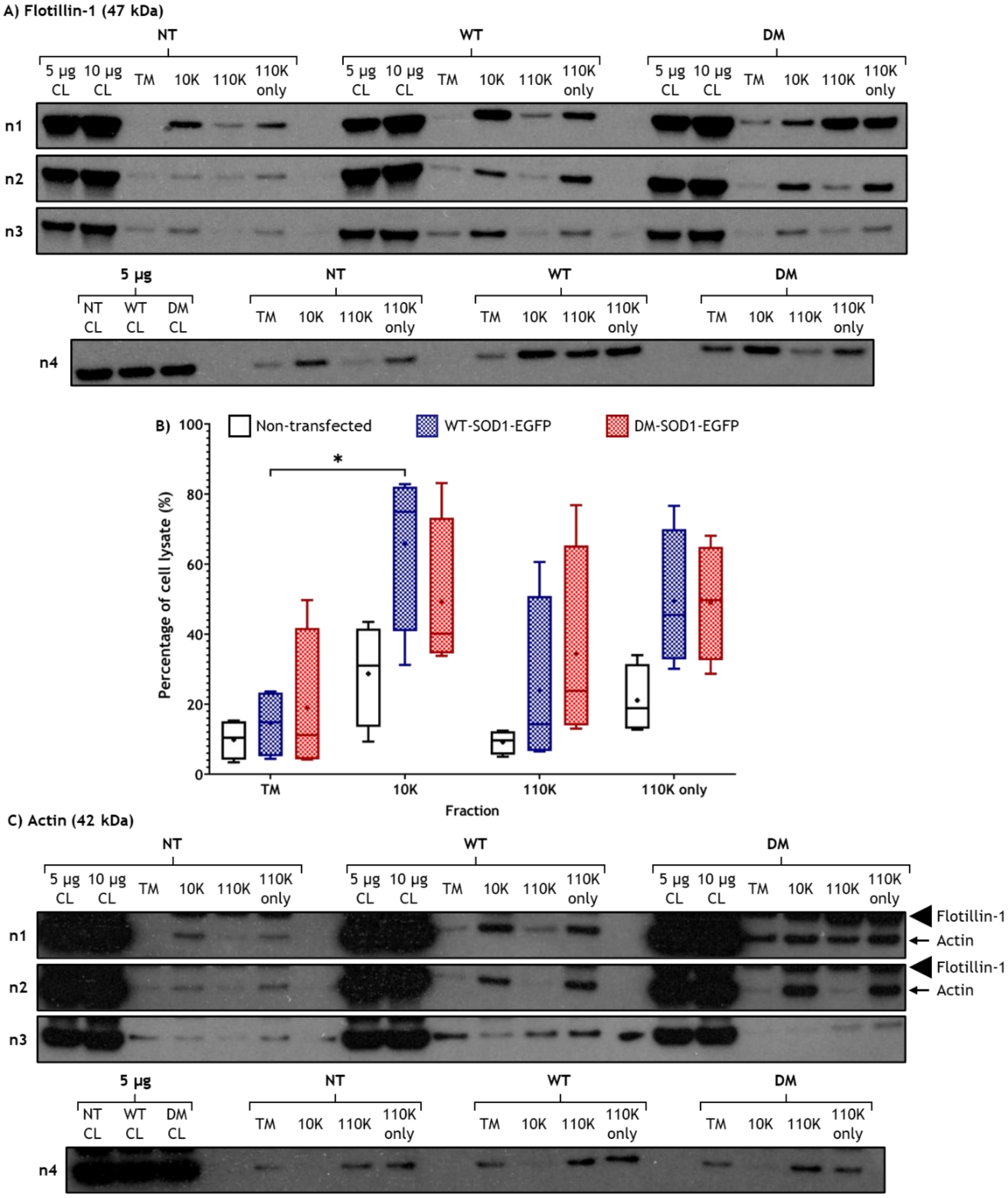

Figure 4-3: Flotillin-1 and actin in CLs and media associated fractions. A) shows WBs containing CL and media fractions probed for flotillin-1. Preparation 4 was loaded differently from preparations 1-3 so that there could be a clear gap between the CLs and media fractions, and only 5 µg of CL was used so the CL did not obscure the media associated bands. The associated graph **(B)** shows the quantity of flotillin-1 in each media fraction as a percentage of the 5 µg CL fraction for each preparation (*n*= 4). As there are three groups (NT, WT and DM), ordinary two-way ANOVA with Bonferroni multiple comparisons test was used to compare changes between genotypes and relevant fractions. A significant difference between two different fractions across two genotypes was excluded for example. **p* ≤ 0.05 for comparison between WT TM and 10K fractions. += mean. **C)** shows saturated WBs containing CL and media fractions probed for actin. CLs were overexposed so that a statement could be made about the purity of the media associated fractions. The blots were originally probed with anti-flotillin-1 antibodies which explains the additional band present at 47 kDa (arrowhead).

4.4.4 Analysis of endogenous and fusion SOD1 in EVs

4.4.4.1 Protein assessment using WB

Endogenous SOD1, WT- and DM-SOD1-EGFP were assessed in CLs and media associated fractions using WB. Endogenous SOD1 was found in all CLs and the SOD1-EGFP fusion proteins were found only in transfected cells when probed with anti-CuZnSOD (Figure 4-4A). The signal for endogenous SOD1 was highest in the NT lysates and SOD1-EGFP was highest in the cells transfected with pWT-SOD1-EGFP. Additionally, the ratio of endogenous SOD1 and SOD1-EGFP in CLs was comparable. In the media fractions (Figure 4-4B), endogenous SOD1 was very faint for all fractions but was slightly more visible in the transfected samples. SOD1-EGFP was omitted from NT media but was present in transfected media. Further, both fusion proteins were enriched after the ultracentrifugation steps when compared to total media. The proportion of endogenous SOD1 present in media associated fractions compared to SOD1-EGFP was lower suggesting that the SOD1 fusion proteins were enriched in EVs (Figure 4-4B).

Anti-GFP was used to further interrogate SOD1 fusion proteins in CLs and media associated fractions. SOD1-EGFP antibodies gave a robust signal in the media fraction of WT- and DM-SOD1-EGFP transfected cells but was absent in the NT media (Figure 4-4C). The overall profile of the fusions proteins in CLs and media associated fractions were similar when probed with anti-CuZnSOD (Figure 4-4B) and anti-GFP (Figure 4-4C). They followed a similar trend where the 10,000 *xg* and 110,858 *xg* only fractions had more SOD1 than the TM and 110,858 *xg* fractions.

Except for the TM fraction, DM-SOD1-EGFP media related fractions had a higher recovery of SOD1-EGFP than the WT-SOD1-EGFP media fractions, although this was not significant for any fraction (Figure 4-4D). This trend was likely influenced by the particularly high DM-SOD1-EGFP intensity found in one preparation (n2; Figure 4-4C). SOD1-EGFP recovery was not significantly different between the 110,858 *xg* fractions from either genotype. The samples with the additional 10,000 *xg* centrifugation step had lower SOD1-EGFP than the samples without the intermediate spin, but this was not statistically significant

(Figure 4-4D). This may indicate that there are various EV types with different buoyancies associated with SOD1-EGFP. For example, the 10,000 *xg* centrifugation step may pull down free SOD1 aggregates and larger EVs, while the 110,858 *xg* centrifugation may isolate smaller EVs including exosomes, thus when there is only one high speed centrifugation, a heterogenous population of free aggregates and EVs may be isolated.

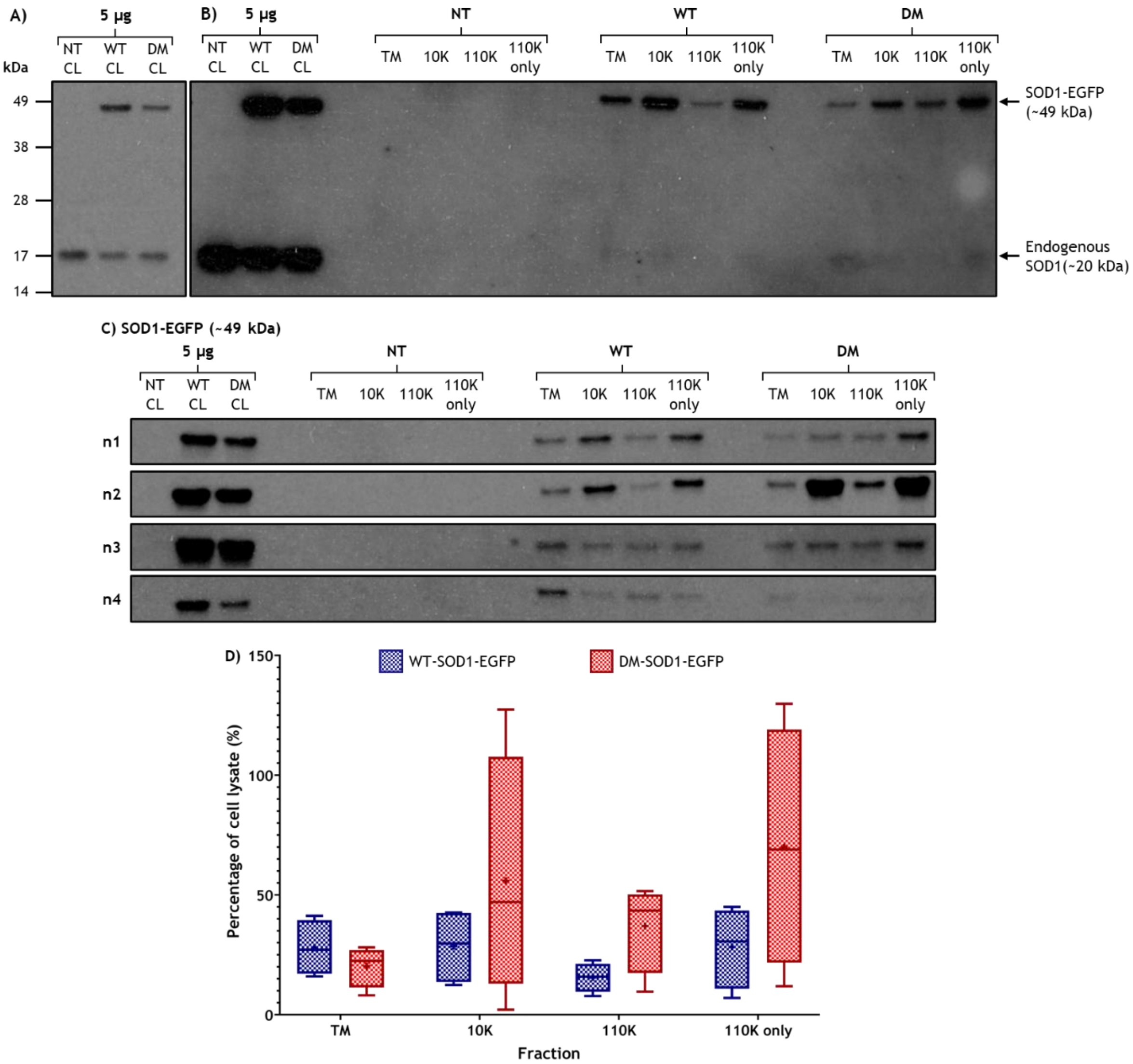

Figure 4-4: SOD1 in CLs and media associated fractions. A) WB showing fusion SOD1 and endogenous SOD1 using anti-CuZnSOD (*n*= 1). On the left, CLs are at a lower exposure to clearly show the levels of SOD in each CL. In **B)**, the WB was overexposed for the CLs to allow endogenous SOD1 to be visualised in the media fractions. CLs and media associated fractions were loaded at a concentration of 5 µg. **C)** shows WBs for SOD1-EGFP found in the CL and media fractions of NT, WT- and DM-SOD1-EGFP transfected cells. The associated graph **(D)** shows the quantity of SOD1-EGFP in each media fraction as a percentage of 5 µg CL for each preparation (*n*= 4). Ordinary two-way ANOVA with Bonferroni's multiple comparison test was used and found no statistically significant changes between genotypes or within fractions. Note, samples failed the Shapiro-Wilk test however GraphPad Prism does not have a nonparametric alternative to the ordinary two-way ANOVA. += mean.

4.4.4.2 SOD1 activity

In the NBT stained native gel, endogenous SOD activity was found in all CLs and appeared comparable across the genotypes (Figure 4-5A). Fusion protein activity was only found in transfected cells and different band patterns were observed for WT- and DM-SOD1-EGFP as previously reported (Qi *et al.*, 2019). Endogenous SOD activity was very weak in the EV fractions of all genotypes compared to the activity in respective CLs (Figure 4-5B). It may also be fainter in the 110,858 *xg* fraction after the intermediate centrifugation step implying that free SOD1 may be removed after the intermediate step and the protein may not be highly associated with small EVs, or it may not be active in this fraction. The additional bands observed in the transfected cells were present in the WT-SOD1-EGFP media fractions, albeit at a lower intensity compared to CLs, but were absent from the DM-SOD1-EGFP fractions.

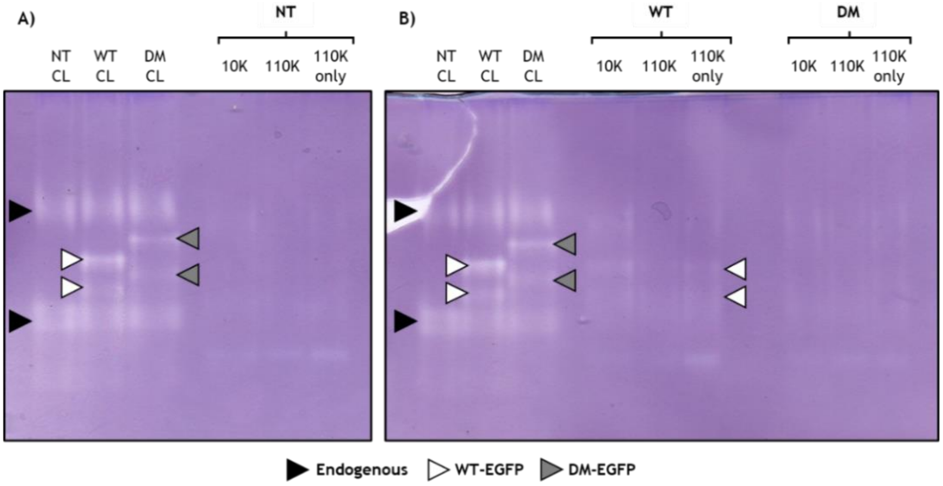

Figure 4-5: SOD activity in CLs and media associated fractions. NBT stained native gel assay of SOD1 activity (*n*=1). Endogenous SOD (black arrowheads), WT-SOD1-EGFP (white arrowheads) and DM-SOD1-EGFP (grey arrowheads) activity can be seen. The first three columns of each gel show SOD activity in NT, WT- and DM-SOD1-EGFP transfected CLs. The following columns in **A)** show SOD activity in NT media fractions and in **B)**, the following lanes are WT- and DM-SOD1-EGFP media fractions. The same protein concentration was used for all CL and media associated fractions (6 μg).

4.4.5 Association between SOD1-EGFP and flotillin-1

The levels of SOD1-EGFP and flotillin-1 were compared to see if the two proteins behave in the same way after ultracentrifugation (Figure 4-6). There were no statistically significant differences in the quantity of flotillin-1 and WT- or DM-

SOD1-EGFP when compared within each fraction. Superficially, the levels of flotillin-1 appeared higher than SOD1-EGFP after ultracentrifugation for WT-SOD1-EGFP transfected cells, but this was not observed for DM-SOD1-EGFP as means appeared very similar. There was significantly more flotillin-1 in the WT-SOD1-EGFP 10,000 *xg* fraction compared to the WT-SOD1-EGFP TM fraction (Figure 4-6A) but for DM-SOD1-EGFP media associated fractions, there were no significant differences (Figure 4-6B).

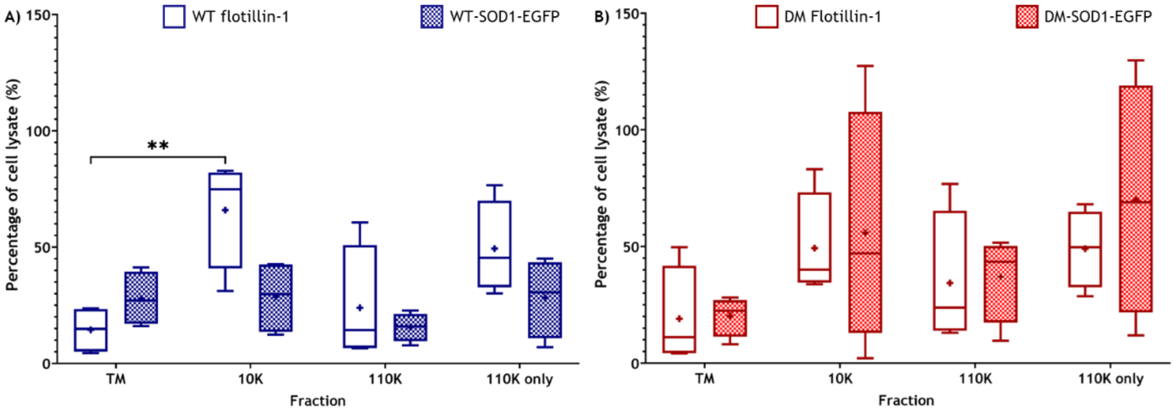

Figure 4-6: SOD1-EGFP and flotillin-1 in media associated fractions. A) and **B)** show flotillin-1 (white fill) and SOD1-EGFP (patterned fill) data for WT-SOD1-EGFP (red) and DM-SOD1-EGFP (blue) transfected cells respectively. Ordinary two-way ANOVA with Bonferroni multiple comparison test used for both genotypes. Only meaningful comparisons were considered. $^{**}p \leq 0.01$. += mean.

When the results from sections investigating actin, flotillin-1 and SOD1, are combined, it suggests ultracentrifugation isolates EVs and that these can be purified based on buoyancy by sequential ultracentrifugation. SOD activity appeared to be slightly reduced in DM-SOD1-EGFP EVs compared to WT-SOD1-EGFP EVs, but the level of CL activity was similar despite differences in banding patterns.

4.4.6 EV transfer pilot study

Donor cells showed efficient transfection with WT- and DM-SOD1-EGFP and were fully confluent before EVs were collected (Figure 4-7A). This was supported by WB when donor CLs were probed with anti-GFP (Figure 4-7B). WT- and DM-SOD1-EGFP were present in the relevant donor EVs and despite the protein being proportional in CLs, it was lower in DM-SOD1-EGFP EVs compared to WT-SOD1-EGF EVs (Figure 4-7B). Actin blots processed after a long exposure period indicated that the donor EVs were void of significant cellular contamination (Figure 4-7B). The Ponceau S stained blot is presented in Appendix 8.3.3.1.

Fluorescence was found in recipient NT cells from day one onwards at decreasing densities, but this was difficult to present sufficiently with cell images. SOD1-EGFP was found in recipient CLs by WB, but the intensity reduced markedly after one day, particularly in DM-SOD1-EGFP EV recipients. Recipient CL samples were loaded equally as shown by the short exposure actin WB (Figure 4-7B). The reduction in SOD1-EGFP may have been the result of cellular clearance pathways disposing of the fusion protein, or, more likely, it may have been a dilution effect caused by a high number of cells. The cellular distribution of SOD1-EGFP was apparently different between cells that received WT-SOD1-EGFP EVs compared to those that received DM-SOD1-EGFP EVs (Figure 4-7C). In the WT-SOD1-EGFP EV recipients, SOD1-EGFP was well distributed around the cytoplasm of cells allowing the processes to be clearly identified. In DM-SOD1-EGFP EV recipients, SOD1-EGFP appeared to be aggregated and less distributed throughout the cytoplasm.

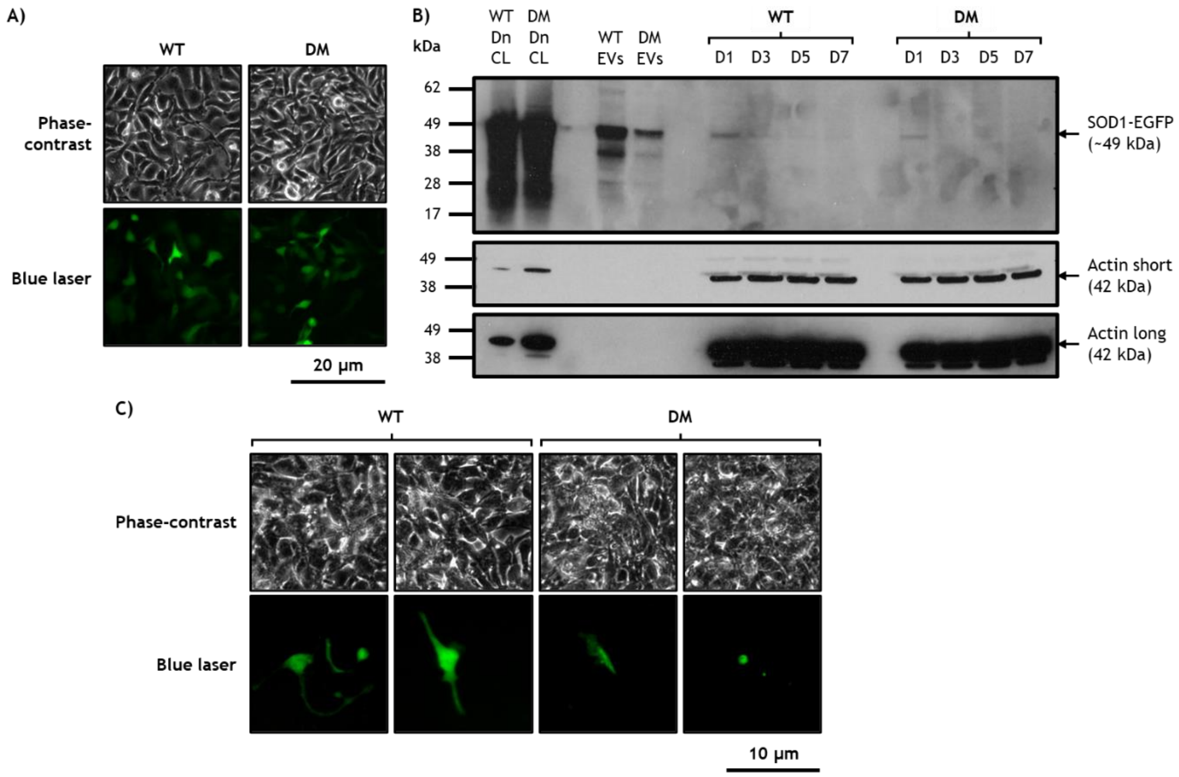

Figure 4-7: EVs may spread WT- and DM-SOD1-EGFP to recipient cells. A) Donor cells expressed WT- and DM-SOD1-EGFP before media was collected. Top row= density of cells before harvesting using phase-contrast microscopy; bottom row= fluorescence observed in the cells. Scale bar= 20 µm. **B)** Top WB= WT- or DM-SOD1-EGFP; middle WB= actin short exposure and bottom WB= actin long exposure. First two lanes contain CL controls (5 µg loaded) from the donor cells which the EVs (next two lanes, 5 µg loaded) were released from. EVs were donated to NT recipient cells which were monitored for seven days after EV application. Cells lysed at days 1, 3, 5 and 7 are presented in the WB (15 µg loaded). Actin was the loading control for CLs and should be reduced in EVs. Additional faint bands in the short exposure are background due to a strong antibody signal and misplacement of the film in the first few seconds of exposure. **C)** Blue laser fluorescent and phase-contrast images of specific areas of SOD1-EGFP labelling. All images captured 6 days after EVs were donated. Scale bar= 10 µm.

4.4.7 Additional centrifugation steps reduced fluorescence transfer

Several potential methodological issues were raised after completion of the pilot study for EV transfer which were taken into consideration for the follow up studies. Fluorescence transfer observed could have been due to cellular contaminants in the EV fraction after the low-speed spin (110 *xg*) and high-speed spin (110,858 *xg*). To resolve this, the first centrifugation step was increased to 800 *xg* and an additional 10,000 *xg* intermediate centrifugation step was introduced before the final 110,858 *xg* step. Additionally, to address the saturation of cells, cell seeding densities were reduced for each day in culture.

Donor cells from both preparations (P1 and P2) displayed efficient transfection rates and were 80% to 100% confluent before EV collection (Figure 4-8A). The general distribution of recipient cells was similar at day one from P1 and P2. Cells were dense in the middle of the coverslip but more widely distributed at the edges (Figure 4-8B). At day three, cells in P2 were well distributed throughout the coverslip without being densely packed. P1 cells started to become well distributed, however they appeared as clusters of cells that were connected (Figure 4-8B). On the final days of fixation, recipient cells from P1 and P2 had a cluster-like distribution of more dense areas of cells. In P2, these clusters were better connected than in P1.

All observations were subjective in the follow up experiments. Fluorescence was found in most fixed recipient coverslips presenting with varying morphology and appeared to be associated with cells on some occasions and disassociated on others. The main morphologies observed are shown in Figure 4-8C and included a clumped appearance or an aggregate-like appearance. Unlike the pilot experiment, there was no clear fluorescence that resembled the morphology of a neurone (Figure 4-7C). In some fields, areas of GFP were near to each other. Overall, there were no clear differences in the morphologies found between days, fraction or genotype applied. The general impression was that fluorescence was more obvious in the cells that received 10,000 *xg* EVs compared to 110,858 *xg* EVs and it was more abundant in those that received DM-SOD1-EGFP EVs than WT-SOD1-EGFP EVs. The abundance of fluorescence was similar between days one and three, but lower at day six/seven. On some occasions it was difficult to see or capture fluorescence and this is indicated in Figure 4-7C by crosses. At day six after application of 110,858 *xg* EVs in P2, GFP particles were so small, it was difficult to capture images with fluorescence microscopy.

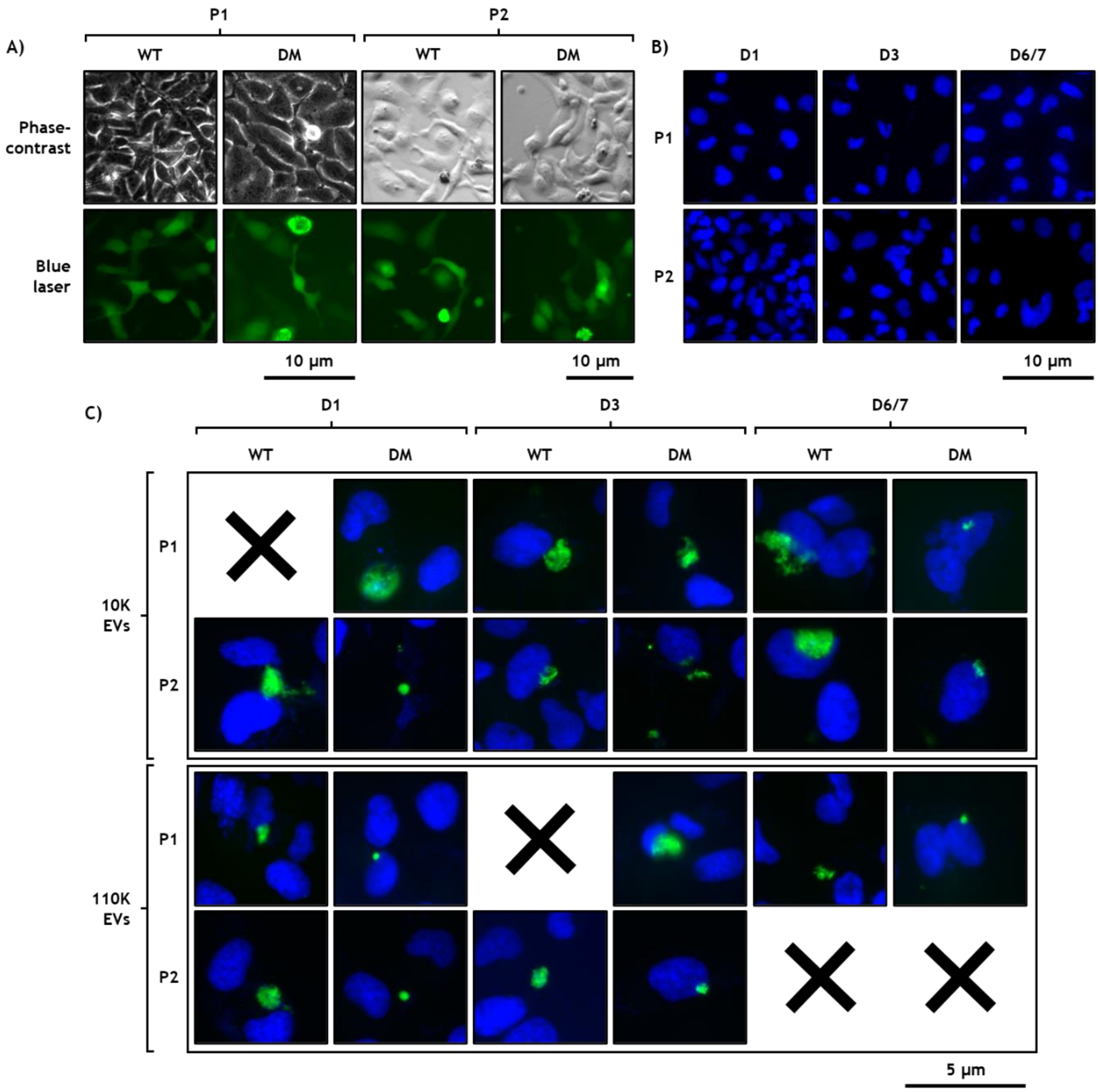
A)
P1
P2
WT
DM
WT
DM
Phase-contrast
Blue laser
10 µm
10 µm
B)
D1
D3
D6/7
P1
P2
10 µm
C)
D1
D3
D6/7
WT
DM
WT
DM
WT
DM
10K EVs
P1
P2
110K EVs
P1
P2
5 µm

Figure 4-8: Further studies confirm EVs may spread WT- and DM-SOD1-EGFP. Images were collected from EV transfer follow up studies P1 and P2. **A)** Blue laser images show donor cells were efficiently transfected and phase-contrast images show donor cells were fully confluent (P1) or 80 to 90% (P2) confluent before EVs were collected. Scale bars= 10 µm. **B)** Representative DAPI stained nuclei images to show recipient cell density at fixation. For P1, cells were fixed at day one, three and seven post EV application and for P2, cells were fixed at one, three- and six-days post EV application. Scale bars=10 µm. **C)** Fluorescence was observed in some cells at day one, three and six or seven, after application of 10,000 *xg* (10K) or 110,858 *xg* (110K) EVs, but the morphology was variable. Scale bar= 5 µm. Crosses signify images were not obtained.

4.5 Discussion

4.5.1 Characterisation of EVs

Théry *et al.*, (2018) suggest particle quantity should be assessed along with markers associated with EV and non-EV components when characterising EVs. Additionally, when using low-specificity methods of EV isolation, including differential ultracentrifugation, it is encouraged to use multiple quantitative methods. Nanoparticle tracking analysis (NTA) was attempted to assess the size of particles being isolated in the EV fraction and roughly quantify the number of those particles. Unfortunately, due to defective equipment and lack of available functional equipment, this was aborted. To compensate, electron microscopy (EM) was investigated however a non-routine optimal method used by the collaborators would first need to be established and due to time constraints, this was not pursued. These methods would be worth implementing in future experiments.

WB for specific marker proteins was the main method of EV characterisation. It is reported in MISEV that at least four protein markers should be used for the characterisation of EVs. Three must be positively associated with EVs and be from transmembrane or cytosolic domains and one must be a negative protein marker. Additionally, a marker of EV fraction purity should be included for example albumin, depending on the source of the EV fraction. This study utilised flotillin-1, a cytosolic protein that can associate with lipids in the plasma membrane, and actin, a cytoskeletal protein. Actin is described in MISEV as being promiscuously incorporated into EVs. In the case of SK-N-SH cells, actin did not appear to be significantly enriched in the EV fraction compared to CLs, so it was deemed acceptable as a negative marker. It would be of benefit to future studies if additional markers were included, particularly from the transmembrane domain of cells, for example a tetraspanin (CD63, CD81). The Exosomal Marker Antibody Sampler Kit (Cell Signalling Technology, USA) was trialled in earlier work in MM’s laboratory, however due to time constraints, could not be fully optimised for this study.

As the size of the vesicles in this study were not able to be determined, the markers, although enriched, are not only found in exosomes, and the specific biogenesis of the vesicles was not assessed, the term “EVs” was adopted to describe particles collected in the study to mitigate misleading conclusions.

4.5.2 Assessment of differential ultracentrifugation

4.5.2.1 Three centrifugation steps reduced vesicle recovery

Existing EV literature suggests multiple centrifugation steps should be used to isolate exosomes from samples. In a proteomic and lipidomic study by Haraszti *et al.*, (2016), cellular debris was removed from cell culture medium by centrifugation at 300 *xg* for 10 minutes. The SN was ultracentrifuged at 10,000 *xg* for 30 minutes to isolate MVs in the pellet, and the SN was ultracentrifuged again for 90 minutes at 100,000 *xg* to produce an exosome enriched pellet. Other studies have also found that pellets after centrifugation around 100,000 *xg* are enriched in exosomes (Momen-Heravi, 2017). The levels of EV associated flotillin-1 in the current study suggest the EV fraction was being purified as flotillin-1 isolated after three centrifugation steps was reduced compared to samples after two centrifugation steps. The level of protein remaining after the intermediate step suggested that two EV populations of different sizes or buoyancies were recovered. Overall, proteins collected after three centrifugation steps were reduced compared to two steps by approximately half.

A decision was made regarding the method for downstream experiments by balancing the quality of the EV fraction recovered with the volume required for detailed investigation of relevant proteins. As a result, further experiments investigating the propagation of SOD1 by EVs and the effect of different treatments on EV production (to be discussed in Chapter 5) were carried out with just two centrifugation steps initially. Some significant findings were made so it was later deduced that the additional intermediate centrifugation step should be introduced. The effect this had on the transfer of EVs is reported in this chapter and treatment results will be discussed in Chapter 5. For future studies, it may be worth considering scaling up the experiments so a larger volume of EVs can be isolated, allowing for the additional centrifugation step to be included with sufficient EV quantities leftover for further protein analysis. It should be noted however that methodological changes, including increased transfection reagent volume and centrifuge rotor change, would result in marked increases in the reagents used. Even though a heterogenous population of EVs was isolated in this study, valuable information was garnered regarding the potential for EVs to propagate misfolded SOD1. Misfolded SOD1 has been found in both exosomes and MVs for example, albeit at higher levels in exosomes compared to MVs (Silverman *et al.*, 2019).

4.5.2.2 Contamination of the EV fraction by non-EV materials and cells

It is not possible to isolate only EVs from culture and so there are several possible contaminants. Instead, it must be decided what absolutely must be excluded based on the specific study (Théry *et al.*, 2018). Non-EV objects, including proteins, for example albumin and globulins, lipids and lipoproteins, can be found in EVs isolated from media containing serum (Haraszti *et al.*, 2016). Some can be abundant, including albumin in the current study, and this can interfere with the assessment of particles and biomarkers. Adaptations to EV isolation can be made, for example by increasing the number of centrifugation steps and/or including filters (Brennan *et al.*, 2020) or chromatography (Zamboni *et al.*, 2022), but some of these methods can result in loss of or damage to EVs and a reduction in useable material (Brennan *et al.*, 2020). Alternatively, albumin can be reduced after EV isolation using albumin depletion kits/methods, but these could also remove other proteins of interest bound to it.

Cellular contamination of the EV fraction can occur if centrifugation steps are not optimal. In this study, actin was used as a marker of cellular contamination and while present in some fractions, it was reduced compared to CLs loaded at the same protein concentration. Generally, levels were lowest after three centrifugation steps compared to two steps, suggesting cells that were not pulled down by the first low speed spin may be removed after the second 10,000 *xg* spin. As actin is a cytoskeletal protein found in cells, it is possible that it could be present in EVs or exosomes but it is described as displaying “promiscuous incorporation into EVs” meaning it is not consistently associated with EVs (Théry *et al.*, 2018). Further, the pilot EV transfer study used two centrifugation steps to isolate EVs and WB showed that actin was not detectible in the donor EVs. If there were just a few living cells carried over however, this would not necessarily be detected by the WB as the level of actin in the whole 5 µg sample would be low. This means it could not be guaranteed that the fluorescence detected by fluorescence microscopy in the pilot study was from EVs and not cells. To investigate this further, EVs were generated from three centrifugation steps and both fractions were applied to cells. Additionally, the first centrifugation step was increased from 110 *xg* to 800 *xg* to further ensure cellular contamination was removed. Despite these adaptations, fluorescence was still observed in recipient cells that received EVs after 10,000 *xg* and 100,858 *xg* centrifugation suggesting cellular contamination was not a significant problem. In the follow up experiments with three centrifugation steps, there was generally a reduction in visible fluorescence and diffuse cytoplasmic distribution of SOD1-EGFP compared to two rounds of centrifugation, but there were also fewer cells so recipient cell density may be an important factor. Overall, the current study confirmed that SOD1 positive donor EVs were able to transfer SOD1-EGFP to recipient cells *in vitro*.

4.5.3 Transfection procedure may influence EV production

Flotillin-1 found in the NT media fractions appeared lower overall compared to both transfected sets of samples but although not statistically significant, it suggests the transfection procedure may affect the secretion of EVs. It has been found that adding a fluorescent tag to a protein can alter the biochemical properties of that protein (Draper *et al.*, 2020), so it is possible that cells actively remove the larger fusion protein. Endogenous SOD1 was less visible in NT EVs compared to transfected EVs, but it was higher in NT CLs compared to transfected ones, as shown in the WB and NBT stained native gel. This implies that endogenous SOD1 may be found in low volumes in the extracellular environment and less is being moved out of the cell because it is properly folded and does not have an additional protein attached making it larger. Endogenous SOD1 may have been elevated in transfected EVs because these cells are already expelling more SOD1-EGFP due to the fluorescent tag. It is worth taking these findings into account however, as the principle aim of this study was to compare fusion WT- and DM-SOD1-EGFP, the method remains valid.

4.5.4 SOD1 is found in the EV fraction from cell culture media

4.5.4.1 Is there evidence for SOD1 and EV association *in vitro*?

Despite some variation, there was no statistically significant difference between the levels of flotillin-1 and WT- or DM-SOD1-EGFP in any of the EV associated fractions (after 10,000 *xg*, 110,858 *xg* and 110,858 *xg* only). This shows SOD1 was pulled down with EVs, however at this level, it is not clear how SOD1 and EVs interact. Free aggregates, potentially released from dead/dying cells, can be isolated within the EV fractions (Hanspal *et al.*, 2017; Théry *et al.*, 2018). Additionally, flotillin-1 is associated with many EV subpopulations while SOD1 may interact with specific EV subpopulations. The physical interaction between EVs and mutant SOD1 is not clear, for example, SOD1 may be found within the vesicles or at the surface (Silverman *et al.*, 2019). To be certain of the interaction, methods that look at the size and morphology, for example NTA or EM, should be used. Another way to better understand the interaction is to manipulate pathways that are known to affect EV production and see how this influences the production of SOD1 within the EV fraction.

4.5.4.2 SOD1 may have different activity levels in the EV fraction

Flotillin-1 in NT, WT and DM-SOD1-EGFP media fractions was comparable and SOD1-EGFP in transfected media fractions were similar between genotypes however SOD1 activity varied between genotypes. Endogenous SOD activity was found in NT, WT- and DM-SOD1-EGFP media associated fractions, but it was less active than the respective CLs. This suggests SOD1 present may be misfolded or there may have been modifications made to the protein due to passing through clearance pathways. Further, activity appeared lower after the three centrifugation steps, possibly suggesting larger aggregates were collected after the intermediate step. Both WT endogenous and fused SOD1 were more active in EVs compared to DM endogenous and fused SOD1. This may imply that DM-SOD1-EGFP associated with EVs may be dysfunctional.

4.5.5 Transfer of WT and mutant SOD1 is possible *in vitro*

4.5.5.1 Current methodological difficulties

There were some methodological constraints in the EV transfer study that made it difficult to clearly ascertain if EVs can spread SOD1 *in vitro*, however it provided a valuable insight into the behaviour of SOD1 when in WT and mutant form. As mentioned previously, the biochemical element of the pilot study only identified clear SOD1-EGFP in recipient cells at day one post EV application and this appeared to reduce at subsequent days. There may have been a dilution effect caused by a saturation of cells in wells as the days passed due to the same number of cells being plated into each well for the initial experiment. For the WB, other more abundant proteins may overshadow the lower abundant SOD1 as more cells are present, resulting in a low SOD1 signal. This was considered for further experiments and resulted in fewer cells being plated down for the later days. Two different serial dilutions were used for the follow up experiments which resulted in fewer cells being present at the last day of the experiment. Unfortunately, very few cells were present at the end of both experiments and fluorescence could not be detected in some cases. For future experiments, the optimal dilution of cells should be investigated to ensure there are enough cells at the beginning of the experiment for cell-EV interactions and enough cells at the end of the experiment to analyse proteins. It is possible that a certain density of cells must be present when EVs are applied to facilitate uptake of the EVs/fluorescent protein and subsequent propagation to other cells. It may also suggest EVs have an ‘expiry date’ as when the cell density does increase at later days, there was still no obvious fluorescence associated with aggregates or cells. Determining the optimal seeding densities would also help to quantitatively assess fluorescent images. This was difficult due to the low level of fluorescence in the EV transfer experiments for several reasons. As cells were fixed, it is possible that some cells were washed off the coverslips during the fixation process. Interestingly, some authors have reported that cells containing SOD1 aggregates may be more likely to be washed off during the fixation procedure than those without aggregates (Tanaka *et al.*, 2021). In some cases, it was difficult to distinguish if GFP was associated with nuclei, and therefore cells, or if they were extracellular. The inclusion of an additional cytoskeletal stain would have been useful to outline the full area of each cell. One candidate is phalloidin, a red stain that binds to actin filaments in cells. Further, some fluorescent areas were miniscule or faint making it very difficult to capture images. It may be worth using another form of microscopy, for example confocal microscopy, in the future.

4.5.5.2 Recipient cell condition

This study used healthy NT human SK-N-SH cells as recipient cells. It has been suggested *in vivo* that an element of damage may need to occur in CNS cells (MNs and/or glia) in order for mutant SOD1 to have the pathological effects observed in ALS (Gomes *et al.*, 2007). In relation to the current study, it is possible that NT, WT- and DM-SOD1-EGFP transfected cells have different susceptibilities to uptake WT and mutant SOD1. For example, healthy NT or WT-SOD1-EGFP cells may be less likely to take in WT or mutant SOD1, while diseased cells (transfected with pDM-SOD1-EGFP), may be more likely to take in mutant SOD1 and/or less WT-SOD1. A possible experiment would be to stress recipient cells before the addition of EVs and continue the experiment as described previously. Additionally, a further *in vitro* experiment to assess the interaction of EV associated and recipient cell SOD1 would be to transfect donor cells with WT- or DM-SOD1-EGFP and collect their EVs before transferring them to recipient cells transfected with another SOD1 fusion protein, for example WT- or DM-SOD1-Cherry (Qi *et al.*, 2019). The use of the green and red fusion proteins would allow clear visibility of interactions between WT- and DM-SOD1-EGFP and determine if the genotype of recipient cell SOD1 influences uptake of SOD1 or conformation changes.

Future investigations should assess the impact of the cellular origin of EVs and recipient cells on the transfer of SOD1. As all CNS cells are thought to play a role in DM pathology (Johnston *et al.*, 2000; Ogawa *et al.*, 2014; Story *et al.*, 2020), it is possible that EVs from one cell type may affect another. Additionally, if one cell type is stressed or in otherwise suboptimal conditions, the rate of uptake of EVs should be analysed. This could be assessed by collecting EVs from WT and DM CSF or tissue and transferring them to cells, for example SK-N-SH, in culture and assessing SOD1 spread in recipient cells. As the EVs would not be collected from one specific cell type, further analysis (for example proteomics) of the EVs should be carried out to determine the origin.

Finally, a primary cell culture of DM cells could be generated to investigate how SOD1 interacts with cells. Cells could be differentiated into specific cell types, and they could be chemically manipulated to produce EVs that could be further analysed for SOD1 and the ability of it to propagate to other cells in culture. Having a primary culture would also allow investigation of the uptake of WT- or DM-SOD1-EGFP. A potential source of primary cells may be mesenchymal stem cells (MSCs) which can be differentiated into neurone-like and glia-like cells (Kim *et al.*, 2002; Tohill *et al.*, 2004).

Instead of transferring media from donor cells to recipient cells, other conditioned medium experiments could be pursued. For example, cocultures separated by a transwell insert with a filter membrane that only allows certain sizes of particles through could be of value. These experiments also come with disadvantages, particularly when it comes to cost (Hanspal *et al.*, 2017).

4.6 Conclusions

Three centrifugation steps potentially isolate purer EV fractions than those isolated after two centrifugation steps, however this comes at the cost of lower material for downstream applications. WT- and DM-SOD1-EGFP is associated with the EV fraction and preliminary studies show these fusion proteins can be spread between cells.

5 *In vitro* investigation of protein processing, SOD1 aggregation and extracellular vesicles

5.1 Background

Many cell clearance and toxicity pathways have been implicated in DM and ALS pathophysiology and were described in Section 1.4. These pathways often closely interact thus changes to the balance of activation and inhibition of pathways could cause disruption to cell proteostasis. This has been found to lead to neurodegenerative diseases including Parkinson's disease (Liu, Liu and Yang, 2019). Disruption of cellular clearance pathways *in vitro* can increase SOD1 aggregates in DM-SOD1 expressing cells (Nakamae *et al.*, 2015) suggesting clearance pathways and SOD1 aggregation are linked. ALS related *in vitro* cell culture studies have shown that mutations in the *SOD1* gene can induce SOD1 aggregation and oxidative stress and negatively impact the proteasome (Urushitani *et al.*, 2006). The ubiquitin proteasome pathway (UPS), autophagy, unfolded protein response (UPR), ER stress, apoptosis and programmed cell death type II are thought to have roles in DM, but how they interact is still not clear. These pathways and how they are investigated have been discussed in detail in Section 1.4 and Chapter 3 respectively, so only key details will be described here.

5.1.1 Summary of protein processing pathways

Surplus, misfolded or damaged proteins can be degraded by the UPS or autophagy by proteasomes or lysosomes respectively. As proteins are first labelled with ubiquitin protein for degradation by the proteasome, ubiquitin can be assessed as a marker for the pathway (Fernández-Fernández *et al.*, 2017). To further assess the importance of the UPS in cells, the chemical MG132 can be employed as a proteasome inhibitor (Guo and Peng, 2013). When proteins are due to be degraded by the autophagy pathway, a membrane encapsulates debris and transports it, now termed an autophagosome, to the lysosome where the contents are digested. LC3B is a constituent of the autophagosome membrane and is used to assess autophagy. Further, LC3BI is converted to and incorporated into the membrane as LC3BII providing a means to investigate autophagy flux (Ogawa *et al.*, 2015; Renna *et al.*, 2010; Xu, Camfield and Gorski, 2018). Chloroquine (CQ) can be added to cells to inhibit autophagy at the level of autolysosome digestion (Schrezenmeier and Dörner, 2020). If surplus, misfolded or damaged proteins are not cleared, they can accumulate and induce ER stress which results in the activation of the UPR to rectify the problem by reducing production of proteins, refolding or removing proteins. If homeostasis does not return, the apoptotic cell death pathway is initiated (Hetz, 2012; Yokota *et al.*, 2018). If the autophagy pathway is defective, this can result in programmed cell death type II (Ogawa *et al.*, 2015). RNA encoding activating transcription factor 3 (ATF3), BiP, Bcl2, CHOP and XBP1 proteins can be used to determine if ER stress has been initiated and assess different stages of the UPR (Chang *et al.*, 2019; Ku and Cheng, 2020; Yokota *et al.*, 2018). ATF3 is a transcription factor that can be activated by ER stress. In healthy cells, ATF3 is found at low levels but expression is increased by numerous exogenous and endogenous stressors. Depending on the cellular conditions and which promotor interacts with the ATF3 protein, ATF3 may be inhibitory or stimulatory and is thought to have a role in metabolic and immunologic regulation (Ku and Cheng, 2020). General reducing agents, for example dithiothreitol (DTT) can be used as a non-specific inducer of ER stress (Oslowski and Urano, 2011) and has been used to investigate ALS associated SOD1 (Tiwari and Hayward, 2005).

5.1.2 Extracellular vesicles (EVs)

As previously discussed (Section 1.5), EVs are secreted from most cells and play a role in homeostasis but have also been implicated in various neurodegenerative diseases. EVs have been associated with the spread of specific pathogenic proteins (Hosaka *et al.*, 2019; Silverman *et al.*, 2019) and they may give an indication of how functional protein disposal and intercellular transport is due to their contents (Thompson *et al.*, 2020). In ALS studies for example, when SOD1 mutant MNs are surrounded by WT cells, the ALS phenotype is delayed in expression or ameliorated altogether. The opposite is also true; when WT MNs are surrounded by cells expressing mutant SOD1, they are negatively impacted. These findings suggest mutant SOD1 is found in the extracellular environment in ALS (Urushitani *et al.*, 2006). To investigate EVs, flotillin-1 can be used as a marker (Théry *et al.*, 2018).

5.1.3 Crosstalk between protein processing pathways

Autophagy and EV generation (specifically exosomes) involve the use of some of the same molecular machinery and regulatory mechanisms. Some have suggested that exosome secretion and autophagy may respond cooperatively to different stimuli to allow cells to cope with stress and maintain homeostasis. They share similar roles in that they eliminate redundant proteins and other components, and each pathway can compensate for a deficiency in the other. The luminal pH of microvesicular bodies (MVBs) has been found to contribute to the outcome of the MVBs; if luminal pH becomes acidic, MVBs are more likely be processed through the autophagy pathway while if they are not acidified, they are more likely to fuse with the plasma membrane and release exosomes. Neuronal cells are thought to utilise autophagy and exosome production to protect themselves from proteotoxicity from protein aggregates. There are still many areas to be investigated to determine what makes a cell choose a pathway. For example, it may be that there are different populations of MVBs or different signals that govern whether MVBs merge with lysosomes, autophagosomes or the plasma membrane (Xu, Camfield and Gorski, 2018). When autophagy is initiated, autophagosomes can fuse with MVBs to form amphisomes which are degraded by the lysosome, inhibiting EV secretion. When autophagy is inactive, MVBs can fuse with the plasma membrane to secrete exosomes (Jahangiri *et al.*, 2022).

EV secretion can be upregulated by the IRE1α and PERK pathways involved in ER stress and the interaction between ER stress and EVs has been initially studied in other neurological diseases including Parkinson’s and Alzheimer’s diseases. EVs can be described as a cause and consequence of ER stress as spread of diseased EVs to other cells may cause ER stress, while EV production may be the consequence of ER stress, but there are an array of other interactions that must be considered when determining the mechanisms of disease (Ye and Liu, 2022). The UPR arms can initiate autophagy when activated under ER stress and can also promote MVB formation and EV secretion (Jahangiri *et al.*, 2022).

Bcl2 is a family of proteins that are involved in the modulation of apoptosis. It is activated under stress conditions in cells to initiate a cascade that results in apoptosis, but under normal conditions, Bcl2 is antiapoptotic and is involved in maintaining mitochondrial membranes. Bcl2 has been found to have stimulatory and inhibitory effects on autophagy. Due to the interaction between Bcl2, autophagy and apoptosis, Bcl2 is thought to act like a switch for going between autophagy and apoptosis to maintain homeostasis (Liu, Liu and Yang, 2019).

5.2 Hypothesis and aims

The aims of this chapter were built on the hypothesis that disruption to protein processing pathways by inducing ER stress, inhibiting autophagy or inhibiting the UPS using DTT, CQ or MG132 will influence the production of SOD1 aggregates and SOD1 positive EVs in cell culture. Further, it was hypothesised that SOD1 activity is also impacted by changes to protein processing pathways. The main aims of this chapter were to:

1. Identify RNA and protein markers of ER stress, autophagy and the UPS to monitor the efficiency of treatments applied to disrupt these protein processing pathways in SK-N-SH cell culture.
2. Determine if induction of ER stress or inhibition of autophagy or the UPS affects WT- or DM-SOD1-EGFP aggregation in transfected SK-N-SH cells.
3. Investigate if induction of ER stress or inhibition of autophagy or the UPS affects EV composition or production from NT, WT- and DM-SOD1-EGFP transfected SK-N-SH cells in culture.
4. Establish if induction of ER stress or inhibition of autophagy or the UPS affects WT-, DM-SOD1-EGFP or endogenous SOD activity in SK-N-SH cells and EVs in culture.

5.3 Materials and Methods

5.3.1 Cell culture, transfection and treatment

The general workflow for this chapter is shown in Figure 5-1 but specifics are given in each section. SK-N-SH cultures were maintained (Section 2.2) and seeded onto 4-well ($4x10^4$ cells/well) or 6-well ($2.5x10^5$ cells/well) plates for SOD1 aggregate or protein studies respectively (Appendix 8.2.1). Transfection with pWT- or pDM-SOD1-EGFP was conducted on day two as described in Section 2.2.2.2. Treatments were conducted on day three and are described in the following sections. On day four, normal growth media (NGM) was replaced with exosome-depleted media (EDM) so EVs could be isolated on day five.

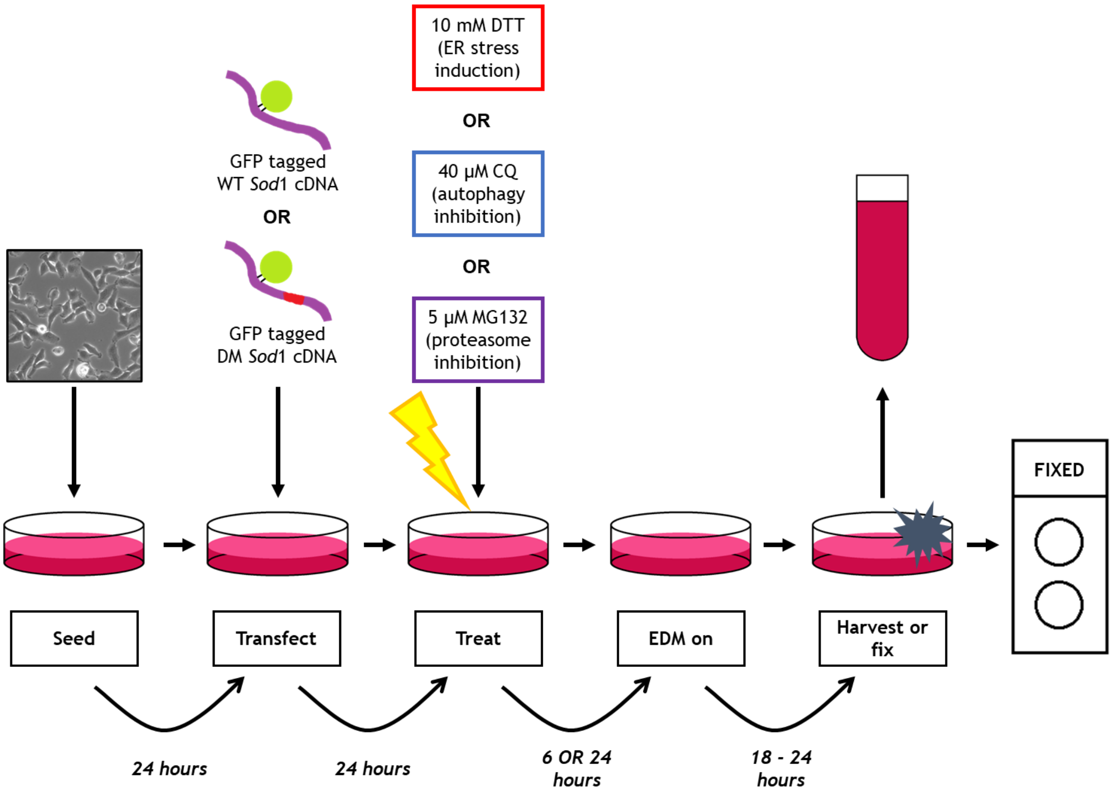
10 mM DTT (ER stress induction)
OR
40 µM CQ (autophagy inhibition)
OR
5 µM MG132 (proteasome inhibition)
GFP tagged WT *Sod1* cDNA
OR
GFP tagged DM *Sod1* cDNA
FIXED
Seed
Transfect
Treat
EDM on
Harvest or fix
24 hours
24 hours
6 OR 24 hours
18 - 24 hours

Figure 5-1: Summarised workflow for treatment studies. The general processes used for this chapter are summarised in the workflow and any specific adjustments made are detailed in relevant sections. Cells were seeded onto plates at day one, then transfected with pWT- or pDM-SOD1-EGFP 24 hours later. On day 3, cells were treated (if applicable) with 10 mM DTT for 6 hours to induce ER stress or 40 µM CQ for 24 hours to inhibit autophagy or 5 µM MG132 for 24 hours to inhibit the UPS. When treatment was complete, media was replenished with EDM and cells incubated for a further 18 to 24 hours. What happened after this period depended on the particular experiment: cell fixation for SOD1 aggregate studies, cell lysis for protein investigation or media collection for EV study.

5.3.1.1 Study of ER stress: DTT treatment

NGM was removed from each well and replaced with NGM containing either no DTT (control) or 10 mM DTT (filter sterilised) for 6 hours. EDM replaced NGM and cells were incubated for a further 18 to 20 hours before cells were fixed for the aggregate study (Section 2.3.3) or washed, lysed (Section 2.4.1.3) and quantified (Section 2.4.3) for protein analysis or processed for RNA analysis (Section 2.5.1). For EV studies, media was also collected.

5.3.1.2 Study of autophagy: CQ treatment

To inhibit autophagy in experiments involving pWT- or pDM-SOD1-EGFP, NGM was removed from each well 24 hours after transfection and replaced with NGM containing either no CQ (control) or 40 µM CQ (filter sterilised) for 24 hours. NGM was removed and EDM was applied for 24 hours before cells were fixed for the aggregate study (Section 2.3.3) or washed, lysed (Section 2.4.1.3) and quantified (Section 2.4.3) for protein examination or processed for RNA analysis (Section 2.5.1). For EV experiments, media was collected.

5.3.1.3 Study of the UPS: MG132 treatment

The day after transfection, NGM was replaced and DMSO or 5 µM MG132 was added to cells for 24 hours. EDM replaced NGM after this period and cells were incubated for a further 24 hours. Cells were fixed for analysis of SOD1 aggregates (Section 2.3.3) or lysed for protein (Section 2.4.1.3) or RNA (Section 2.5.1) investigation. Media was collected and further processed before protein investigation.

5.3.2 EV isolation

5.3.2.1 EV isolation with two centrifugation steps

For DTT and original CQ experiments, media was pooled from each genotype and treatment then it was centrifuged at a 110 *xg* for 5 minutes followed by 110,858 *xg* for 2 hours to isolate EVs as described in Section 2.4.1.1. For the initial MG132 experiments, media was centrifuged at 800 *xg* for 5 minutes instead of

110 *xg*. All pellets were lysed in 50 µl lysis buffer then proteins were quantified (Section 2.4.3).

5.3.2.2 EV isolation with three centrifugation steps

For follow up MG132 and CQ experiments, media was pooled from each genotype and treatment, then centrifuged at 800 *xg* for 5 minutes. The SN was further centrifuged at 10,000 *xg* for 30 minutes, then 110,858 *xg* for 2 hours to isolate EVs (Section 2.4.1.1). Pellets were resuspended in 50 µl of lysis buffer and proteins quantified (Section 2.4.3).

5.3.3 Protein analysis

SDS-PAGE (Section 2.4.5.1) for WB (Section 2.4.7) used 10 µg protein for CLs and 5 µg for EVs. CLs were included as controls in the EV blots at 1 µg or 5 µg. Antibodies used in this chapter were anti-actin, anti-flotillin, anti-GFP, anti-LC3 and anti-ubiquitin (details in Table 2-2). For Coomassie Blue staining (Section 2.4.6.1) of CLs, samples were made to 5 µg (DTT) or 10 µg (CQ and MG132) for SDS-PAGE while EVs (with CL controls) for silver staining (Section 2.4.6.2) were made to 2 µg (DTT) or 1 µg (CQ and MG132) for SDS-PAGE. Excess DTT in the DTT treated samples could influence the silver stain reaction because it is a strong reducing agent, so iodoacetamide was added to each denatured sample in the DTT experiment to give a final concentration of approximately 35 mM. Sample mixtures were incubated at 70°C for 10 minutes. Iodoacetamide changed the sample pH from base to acid in some cases, so 1µl of 1M Tris-base was added to correct the pH to ~pH 7.4. For native NBT stained gels (Section 2.4.6.3) CLs and EVs were made to 10 µg.

5.3.4 RNA analysis

After media was removed, 400 µl TRIzol™ Reagent was applied to cells then it was washed over the bottom of the well several times before being collected. Chloroform (80 µl) was added then the samples were vortexed for ~30 seconds. Samples were incubated on ice for 5 minutes before being centrifuged at 16,060 *xg* for 15 minutes at 4°C. The top aqueous, clear layer was collected then 4 µl glycogen (1 µg/µl) was added. RNA was precipitated using 500 µl of 100% isopropanol and incubated for 10 minutes at RT. Samples were centrifuged at 16,060 *xg* for 15 minutes at 4°C then the SN was discarded. RNA was washed with 400 µl of 70% ethanol and centrifuged at 12,298 *xg* (10,000 rpm on Biofuge) for 8 minutes at 4°C. The SN was removed, the pellet centrifuged again for 2 minutes to ensure removal of SN, then it was air dried for 10 minutes at RT. For storage at -20°C, 100 µl RNAse free water was added to the samples. RNA was quantified and integrity assessed (Section 2.5.2).

cDNA was generated using SuperScript™ IV (SSIV) First Strand Synthesis System (Invitrogen, UK) and SuperScript™ III (SSIII) Reverse Transcriptase (Invitrogen, UK; Section 2.5.3). Most samples were resuspended in 230 µl, but all DTT treated cDNA were resuspended in less water to compensate for reduced RNA. The quantity and purity of the resultant cDNA was recorded (Section 2.5.2).

RT-PCR was validated with untreated NT and transfected SK-N-SH cells (Section 0) using primers for *Cyc*, *GAPDH*, *ATF3*, *Bcl2*, *BiP*, *CHOP* and *XBP1*. After validation, *GAPDH* was included with every run as a loading control and *ATF3*, *BiP* and *XBP1* primers were used. *Rumpshaker* (*Rsh*) mouse cDNA and MQ were used as control samples in every PCR run. *Rsh* cDNA was previously found to have various stress markers present (McLaughlin *et al.*, 2007). The PCR cycle shown in Figure 2-2 was used and PCR products were loaded onto 2% UltraPure™ Agarose gels. Purified *XBP1* PCR products were further digested with *Pst1*-HF (Section 2.5.6) to indicate if XBP1t was spliced or unspliced. Only XBP1u contains the *Pst1* digestion site (McLaughlin et al., 2007). Primer characterisation (Appendix 8.3.1.3) showed *ATF3*, *BiP*, *GAPDH* and *XBP1* primers were compatible with the SK-N-SH derived samples but overall, *Cyc*, *Bcl2* and *CHOP* primers were not. *GAPDH* was successful as a housekeeping primer as it gave bands of the same size and intensity for each sample. *Cyc* was trialled as a housekeeping primer, however levels were not consistent in SK-N-SH derived cDNA, so it was not used further.

5.3.5 SOD1 aggregate visualisation

To assess SOD1 aggregation after treatment, cells were fixed and DAPI stained (Section 2.3.3) a day after EDM was applied. Using fluorescence microscopy, the total number of cells, transfected cells and SOD1 aggregates were manually counted using Image J (Appendix 8.2.4.4). Three fields were selected from each coverslip and were selected based on the distribution of nuclei to minimise selection bias.

5.3.6 Statistical analysis

Statistical analysis and graph construction was carried out using GraphPad Prism. Royston Shapiro-Wilk tests were carried out for each group to determine if they were normally distributed. Appropriate parametric or nonparametric tests were selected and are included in the results for each study.

5.4 Results

5.4.1 Impact of the reducing agent DTT on protein processing

5.4.1.1 Confirmation of ER stress induction after DTT treatment

After checking RNA integrity (Appendix 8.3.1.1), PCRs were conducted using *BiP*, *ATF3* and *XBP1* primers. *BiP* (Figure 5-2A) and *ATF3* (Figure 5-2B) were elevated in DTT treated cells compared to controls, but it was only significant for *BiP* (WT C vs WT DTT $p \leq 0.01$; DM C vs DM DTT $p \leq 0.05$). This indicated that the UPS had been upregulated as a result of DTT treatment. The slight increase for *ATF3* in DTT treated cells is likely driven by one preparation. There were no differences in *ATF3* or *BiP* between genotypes. Total *XBP1* (*XBP1t*) appeared slightly elevated in DTT treated cells compared to controls, but this was not significant (Figure 5-2C). There were no significant differences between genotypes. After *Pst1* digestion of *XBP1t*, unspliced *XBP1* (*XBP1u*) was the dominant subtype in control samples indicating *XBP1* was inactive so the UPR and subsequent ER stress had not been activated. In DTT treated samples, the dominant subtype was spliced *XBP1* (*XBP1s*), indicating the UPR had been activated and ER stress was initiated (Figure 5-2D). A low level of *XBP1u* was also present in treated samples.

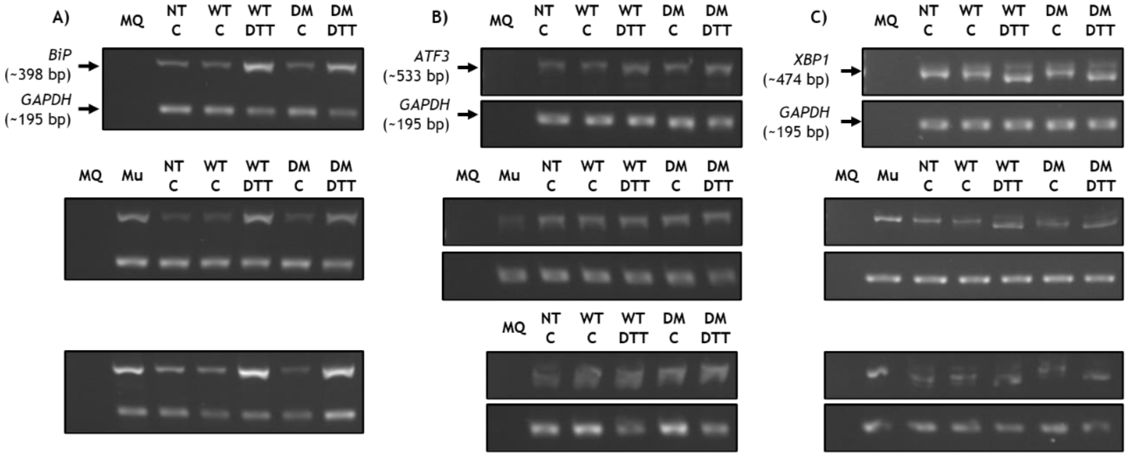

	NT Con	WT Con	WT DTT	DM Con	DM DTT
BiP	34.5 ± 17.7%	41.9 ± 21.8%**	163.8 ± 43%**	28.9 ± 5.0%*	126.7 ± 41.4%*
ATF3	63.4 ± 21.5%	68.3 ± 23.0%	120.2 ± 62.3%	77.1 ± 21.8%	142.9 ± 48.4%
XBP1t	88.0 ± 28.9%	79.4 ± 28.9%	109.0 ± 6.7%	68.1 ± 24.1%	104.2 ± 9.4%

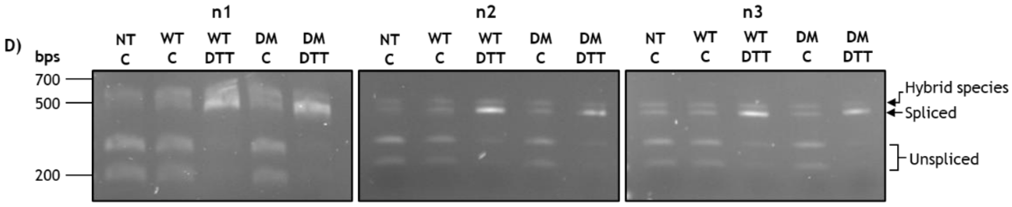

Figure 5-2: Analysis of RNA from DTT treated cells. Three multiplex PCRs using cDNA were run with primers for *BiP* and *GAPDH* in the same reaction. Products were separated in a gel (**A**) and the bands were quantified. *BiP* was expressed as a percentage of *GAPDH* for each sample then presented in the table (mean ± SD). Separate reactions for *ATF3* and *GAPDH* were performed at the same time in triplicate. Again, products were separated in a gel (**B**), then *ATF3* was expressed as a percentage of *GAPDH*. Ordinary one-way ANOVAs with Bonferroni multiple comparison tests were conducted for *BiP* and *ATF3*. Statistically different groups are indicated with * ($p \leq 0.05$) or ** ($p \leq 0.01$). *XBP1t* and *GAPDH* reactions were included in the same run then products were separated on a gel (**C**). In n3, there was a defect in the gel, however the bands could still be quantified. Bands were quantified then *XBP1t* was expressed as a percentage of GAPDH and presented in the table. For *XBP1t*, the NT control group was not normally distributed so a Kruskal-Wallis test with Dunn's multiple comparison test was conducted. *XBP1t* was digested with *Pst*1 then the product was separated on a gel (**D**). When *XBP1* is spliced, it cannot be digested but when unspliced, it is digested and four separate bands are visible.

5.4.1.2 Total protein profiles with and without DTT treatment

There were no obvious differences in the total protein distribution between genotypes, or control and DTT treated CLs (Figure 5-3A). In EVs (Figure 5-3B), there were no differences between genotypes, but there were bands between 98 and 198 kDa that were present in the majority of DTT treated EVs but absent from controls. Another band around 28 kDa was present in all EVs but was darker in treated samples compared to controls. The intense bands roughly at the 62 kDa marker and between the 49kDa and 62 kDa markers were present in all EV samples and possibly reflect proteins abundant in the culture media. When CLs and EVs were compared, the CLs had a more heterogenous population of proteins compared to EVs. In EVs, bands in the 49 kDa to 62 kDa range were more intense compared to CLs. Differences in the overall intensity of proteins in a sample were due to loading rather than changes to the protein in the sample. Total protein profiles for all preparations are presented in Appendix 8.3.3.3.

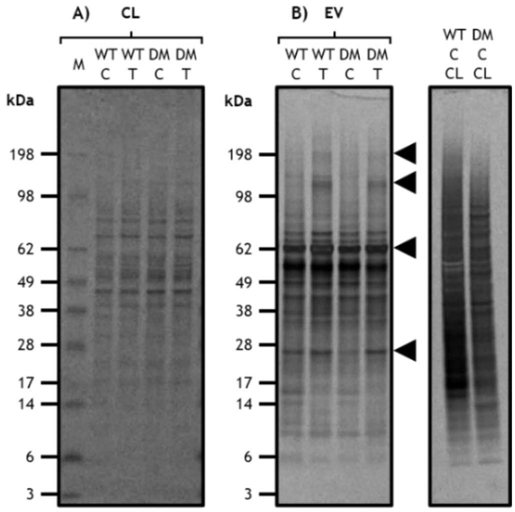

Figure 5-3: Representative total protein profiles for DTT treatment. A) Representative total protein profiles of CLs from cells transfected with pWT-SOD1-EGFP and pDM-SOD1-EGFP, with (T) or without (C) DTT treatment. Prep 2 out of 5 is shown in the one gel stained with Coomassie Blue. **B)** is the total protein profile of EVs for Prep 2 using silver staining. EVs are from cells that were transfected with pWT-SOD1-EGFP or pDM-SOD1-EGFP and either not treated or treated with DTT. Arrowheads indicate areas where there was variation in protein bands. The last two lanes represent control WT- and DM-SOD1-EGFP CLs.

5.4.1.3 Analysis of SOD1, flotillin-1 and actin proteins

SOD1-EGFP and flotillin-1 in CLs was quantitively assessed for all treatment groups and genotypes (Figure 5-4A and B). Treatment with DTT reduced SOD1-EGFP and flotillin-1 in WT-SOD1-EGFP transfected CLs by an average of 16.8% and 21.8% respectively but these changes were not significant. In DM-SOD1-EGFP transfected CLs, SOD1-EGFP and flotillin-1 were reduced by an average of 10.4% and 30.2% respectively. This change was non-significant for SOD1-EGFP but significantly reduced for flotillin-1 ($p \leq 0.05$). This reduction in flotillin-1 may reflect a reduction in cell density due to cell loss after DTT treatment, however the loading control, actin, and gel staining showed protein loaded was comparable between CLs. It may therefore reflect changes to plasma membrane composition. There were no significant changes in the proteins within or between genotypes.

SOD1-EGFP and flotillin-1 in EVs was quantitively assessed for all treatment groups and genotypes (Figure 5-4C and D). In the EVs from WT-SOD1-EGFP transfected cells, SOD1-EGFP and flotillin-1 were reduced by an average of 60.2% and 27.4% respectively while the same proteins were reduced by an average of 72.6% and 55.0% respectively from DM-SOD1-EGFP transfected cells. Therefore, for both genotypes, there was an apparent reduction in the production of SOD1 positive EVs, but it was non-significant with nonparametric statistical tests ($p= 0.0625$). Nonparametric tests were used as the residuals of the samples belonging to the SOD1-EGFP groups were not normally distributed so failed the Shapiro-Wilk test. Samples belonging to the flotillin-1 group were normally distributed however it was decided that using the same tests for all groups would be more consistent. There was no significant difference in either of the proteins within or between genotypes using these tests. With the parametric equivalent test however, DM flotillin-1 and WT- and DM-SOD1-EGFP were significantly reduced after treatment in EVs compared to untreated controls (DM flotillin-1 $p \leq 0.05$; WT-SOD1-EGFP $p \leq 0.05$; DM-SOD1-EGFP $p \leq 0.001$). This suggests that if the sample number was increased and this led to a change to normal distribution for SOD1-EGFP, there may be significance in samples and may suggest there was a reduction in EV production after DTT treatment from DM-SOD1-EGFP transfected cells, but not WT-SOD1-EGFP cells.

Actin in the EV fraction was markedly lower that CL controls showing cellular contamination was low. A representative Ponceau S stained blot is presented in Appendix 8.3.3.2.

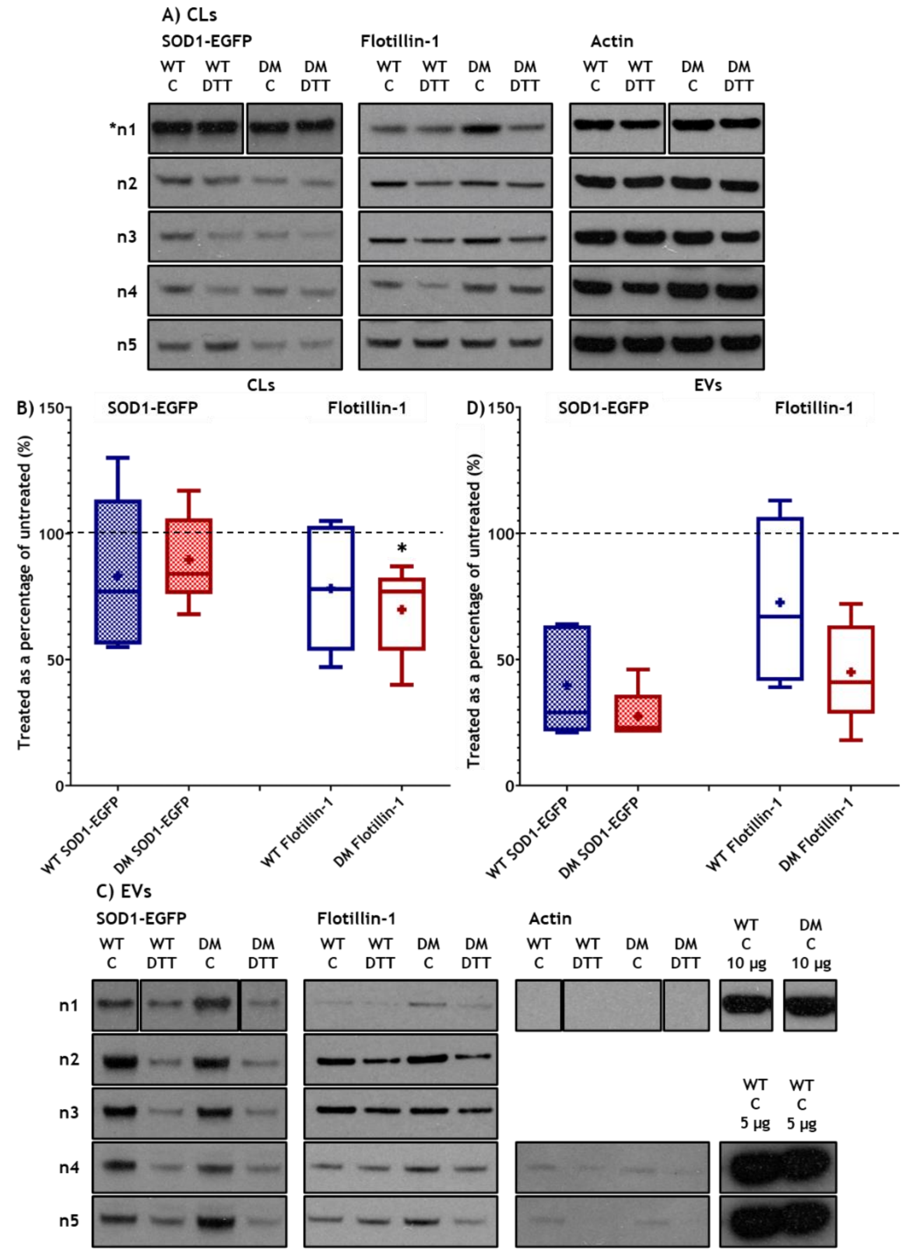

Figure 5-4: DTT treatment effect on CLs and EVs. A) shows WBs for SOD1-EGFP, flotillin-1 and actin in CLs for control and DTT treated samples. Protein was loaded at a concentration of 10 µg. The blot for n1 was cropped but the whole image is available in Appendix 8.3.3.6. **B)** The graph contains the results from all five CL preparations when probed with GFP or flotillin-1 (*n*= 5). Residuals were normally distributed so parametric ratio paired t-tests were used to determine if there were changes to the level of protein compared to untreated controls after treatment. Ordinary one-way ANOVA with Bonferroni multiple comparisons test were used to compare protein levels between genotypes and the two proteins. **C)** shows WBs for SOD1-EGFP, flotillin-1 and actin in EVs for control and DTT treated samples. EVs were loaded at 5 µg and CL control protein concentrations were 10 µg for preparation 1 (n1) and 5 µg for preparations 4 (n4) and 5 (n5). Actin blots were carried out for preparations 2 (n2) and 3 (n3) but CL controls were not clear. This is suspected to be because protein was loaded at 1 µg for these preparations. Flotillin-1 was however observed so it could be that the blot was affected by reprobing. Uncropped actin blots for n1, n4 and n5 are presented in Appendix 8.3.3.6. **D)** The graph contains the results from all five EV preparations when probed with the same antibodies (*n*= 5). Data were not normally distributed so Wilcoxon matched-pairs signed rank test were used to determine if there were changes in protein values in treated EVs compared to untreated EVs. Kruskal-Wallis with Dunn's multiple comparisons tests were used to compare genotypes and flotillin-1 and SOD1-EGFP. Results in the graph are presented as treated band intensity as a percentage of the untreated band intensity. Dotted line= 100%. += mean. **p* ≤ 0.05.

5.4.1.4 SOD activity in CLs and EVs is different

Native gels with NBT staining were carried out to assess the enzymatic activity of endogenous SOD and fusion SOD1-EGFP (Figure 5-5). Endogenous SOD activity was present in all CLs and in transfected CLs, additional activity for the SOD1 fusion protein was present. The lower band of endogenous SOD activity appeared slightly reduced in the DTT treated cells from all genotypes and the fusion protein bands were also slightly reduced in intensity. The change in activity of SOD1-EGFP appeared to be greater in the DM-SOD1-EGFP transfected CLs (Figure 5-5A). In EVs, the upper band of endogenous SOD was difficult to observe from all genotypes but does not appear to be completely dysfunctional in many of the EV samples (Figure 5-5B). The lower band of endogenous SOD was present in all EV samples and may have been slightly reduced in DTT treated transfected EVs, but not NT EVs. It was only possible to show SOD1-EGFP activity in WT-SOD1-EGFP transfected EVs that were untreated. In the DM-SOD1-EGFP control and treated EVs, it was difficult to see double banding, suggesting DM-SOD1-EGFP associated with EVs was not active.

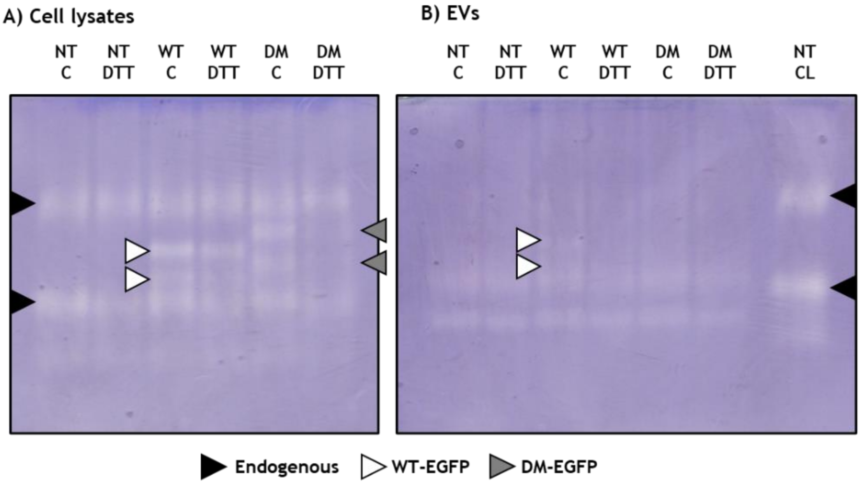

Figure 5-5: DTT treatment affects SOD activity. A) and **B)** NBT stained native gels were used as an assay of SOD1 activity (*n*= 1) in CLs and EVs respectively. Endogenous SOD (black arrowhead), WT-SOD1-EGFP (white filled arrowhead) and DM-SOD1-EGFP (grey filled arrowhead) activity can be seen.

5.4.1.5 Influence of DTT treatment on autophagy

To assess autophagy function, CL WBs were probed with anti-LC3B, then LC3BI and LC3BII were quantified and the LC3BII/LC3BI ratio calculated (Figure 5-6). The LC3BII/LC3BI ratio increased in samples treated with DTT by an average of 110.4% in WT-SOD1-EGFP CLs and 177.0% in DM-SOD1-EGFP cells. This increase was only significant for DM-SOD1-EGFP cells (*p* ≤ 0.05). The higher ratios in the treated samples compared to untreated may suggest there is disruption to the digestion of autolysosomes (increased LC3BII). There were no statistically relevant changes to the ratio between genotypes.

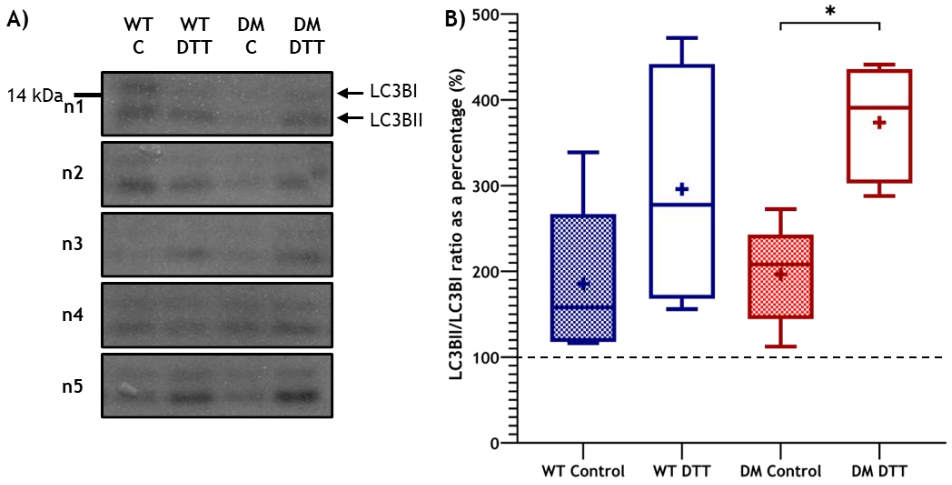

Figure 5-6: DTT treatment affects the LC3BII/LC3BI ratio in transfected cells. A) shows all WBs (*n*= 5) containing CLs that were probed with anti-LC3B. The LC3BI and LC3BII bands from all five preparations were quantified and plotted in the graph **(B)**. One preparation was excluded in the WT DTT group as it was an outlier (1446.2%). An ordinary one-way ANOVA with Bonferroni's multiple comparisons test was used to compare the ratios between treatments and genotypes. += mean. *$p \leq 0.05$.

5.4.1.6 Cell morphology, SOD1-EGFP transfection efficiency and aggregation

Healthy SK-N-SH cells form processes with other cells in culture after they have adhered to the bottom of the vessel they are grown in. After treatment with DTT for six hours, cells became more rounded in morphology and there were fewer processes extending from the cells (Figure 5-7A). Furthermore, DAPI staining showed treated cells had a higher number of fragmented nuclei (Figure 5-7B). This phenomenon, known as karyorrhexis, combined with cell rounding and loss are indicative of apoptosis (Elmore, 2007). There were no clear morphological differences between plasmid genotypes. Cells were efficiently transfected with pWT- or pDM-SOD1-EGFP (45 ± 1.7% and 44 ± 2.6% respectively; Figure 5-7C). DTT did not appear to effect transfection efficiency (Figure 5-7D). DTT treatment significantly increased the average percentage of cells with SOD1-EGFP aggregates (Figure 5-7E) compared to controls in both genotypes ($p \leq 0.01$). Overall, DM-SOD1-EGFP control and treated cells had a higher average percentage of aggregates when compared to their WT-SOD1-EGFP counterparts, but this was not statistically significant (Figure 5-7F).

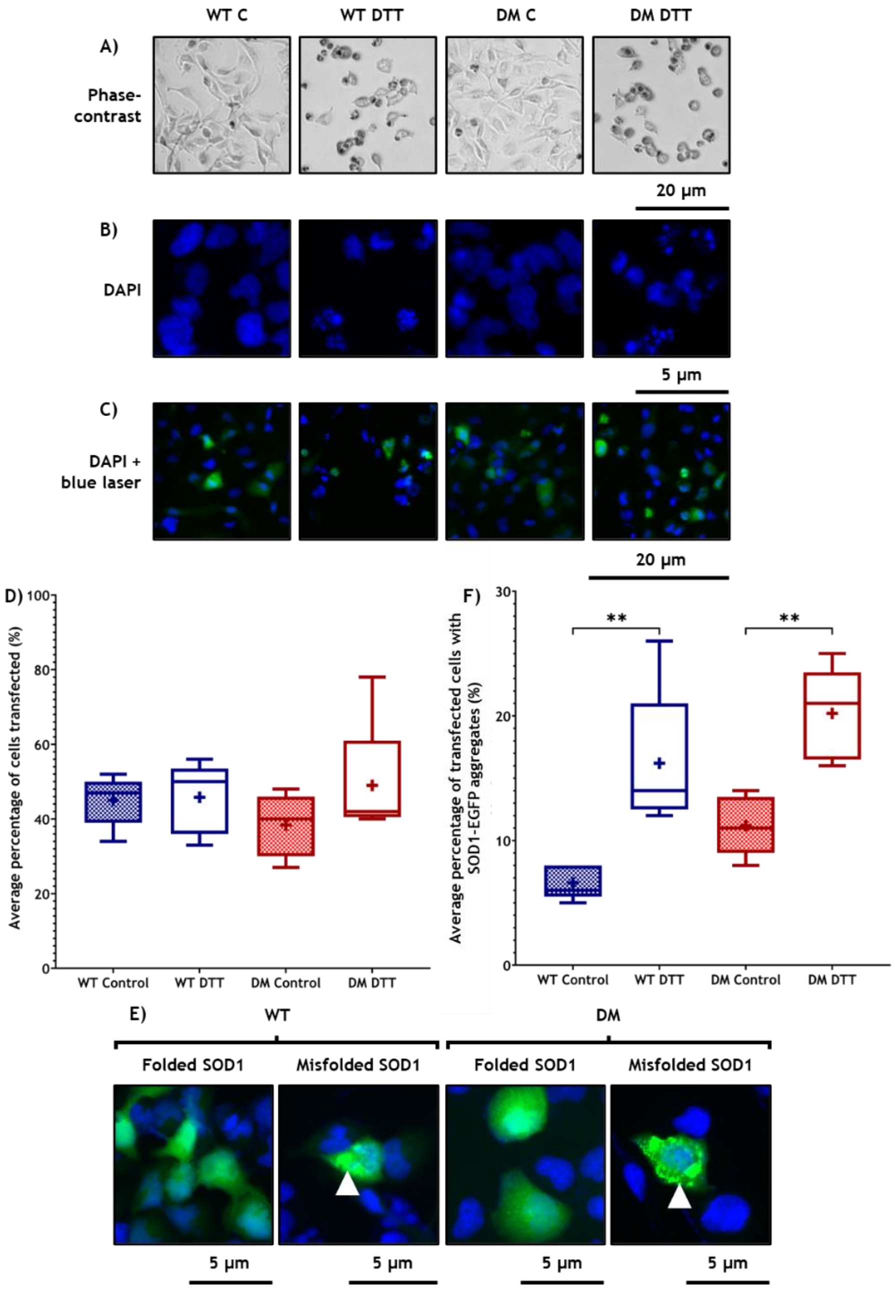
WT C
WT DTT
DM C
DM DTT
A)
Phase-contrast
20 µm
B)
DAPI
5 µm
C)
DAPI + blue laser
20 µm
D)
Average percentage of cells transfected (%)
0
20
40
60
80
100
WT Control
WT DTT
DM Control
DM DTT
F)
Average percentage of transfected cells with SOD1-EGFP aggregates (%)
0
10
20
30
**
**
WT Control
WT DTT
DM Control
DM DTT
E)
WT
DM
Folded SOD1
Misfolded SOD1
Folded SOD1
Misfolded SOD1
5 µm
5 µm
5 µm
5 µm

Figure 5-7: Cytology of DTT treated cells. A) Phase-contrast images from 6-well plates. Scale bar= 20 µm. **B)** DAPI stained nuclei from 4-well plates. Scale bar= 5 µm. **C)** Wide field images of cells to demonstrate transfected efficiency. Blue= DAPI stained nuclei; green= SOD1-EGFP. Scale bar= 20 µm. **D)** Graph shows the average percentage of transfected cells in control and treated cells (*n*= 5). Kruskal-Wallis with Dunn's multiple comparisons tests was used to make comparisons between groups. **+**= mean. Mean ± SEM: WT C 45 ± 2.1%; WT DTT 46 ± 2.7%; DM C 39 ± 2.5%; DM DTT 49 ± 4.1%. **E)** merged images of stained nuclei with SOD1-EGFP (200X for WT misfolded, 400X for the rest). When SOD1 misfolds, it becomes aggregated (white arrowheads). Scale bars= 5 µm. **F)** average percentage of transfected cells with SOD1-EGFP aggregates in control and treated cells (*n*= 5). Ordinary one-way ANOVA with Bonferroni multiple comparisons tests was used to compare groups. **+**= mean. $^{**}p \leq 0.01$. Mean ± SEM: WT C 6 ± 0.5%; WT DTT 16 ± 1.7%; DM C 11 ± 0.8%; DM DTT 20 ± 1.3%. Images for **D)** and **F)** were captured from three different fields at 100X magnification within each slide, then transfected cells and aggregate counts were averaged for each slide and plotted in the graphs.

5.4.2 Impact of autophagy disruption by CQ treatment

5.4.2.1 ER stress was not induced by CQ treatment

After checking RNA integrity (Appendix 8.3.1.1), PCRs were conducted to determine if ER stress had been induced by CQ. cDNA derived from RNA was probed for *ATF3*, *BiP*, *XBP1t*, *XBP1u* and *XBP1s*. *BiP* levels were consistent across treatment groups and genotypes while mean *ATF3* was slightly, but non-significantly, elevated in CQ treated samples (Figure 5-8A and B). *XBP1t* levels were similar between control and treated samples within each genotype. There was a significant reduction of *XBP1t* in DM-SOD1-EGFP controls compared to WT-SOD1-EGFP controls (*p* ≤ 0.05; * in Figure 5-8C) and a similar trend was noted for the treated samples, but this was not statistically significant. *XBP1u* was the dominant subgroup present in all samples showing ER stress was not induced by autophagy inhibition (Figure 5-8D).

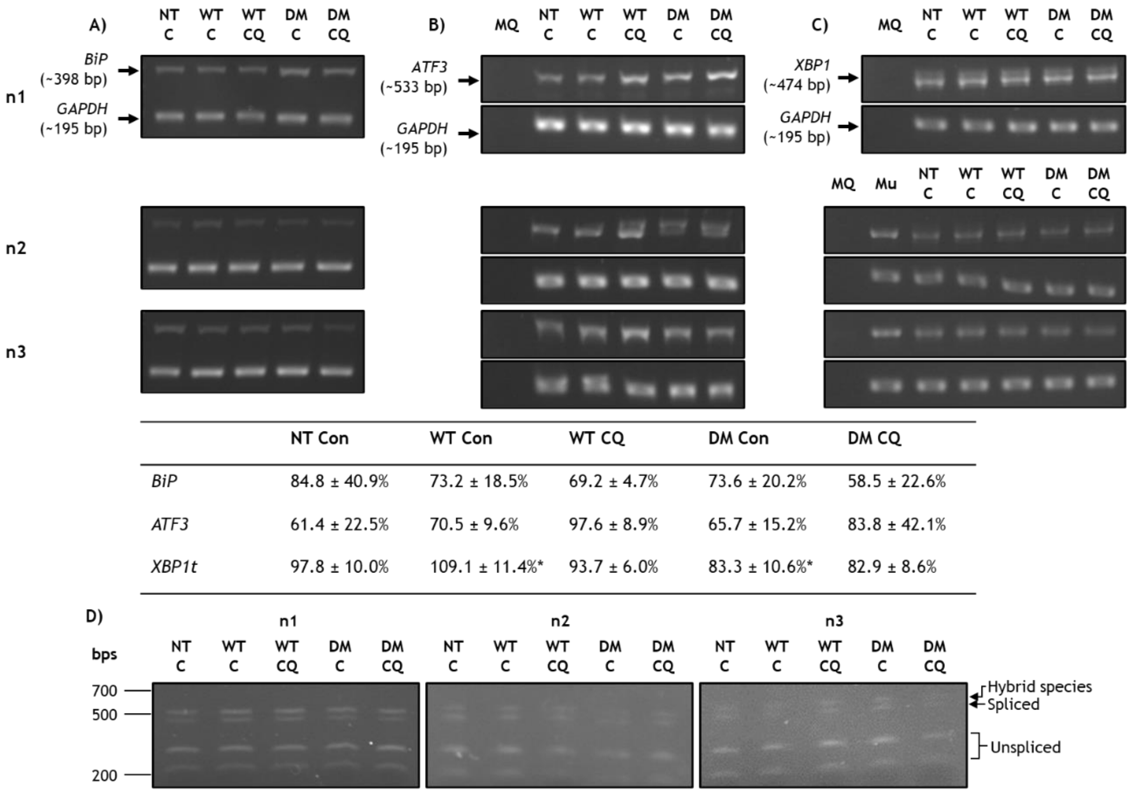

	NT Con	WT Con	WT CQ	DM Con	DM CQ
BiP	84.8 ± 40.9%	73.2 ± 18.5%	69.2 ± 4.7%	73.6 ± 20.2%	58.5 ± 22.6%
ATF3	61.4 ± 22.5%	70.5 ± 9.6%	97.6 ± 8.9%	65.7 ± 15.2%	83.8 ± 42.1%
XBP1t	97.8 ± 10.0%	109.1 ± 11.4%*	93.7 ± 6.0%	83.3 ± 10.6%*	82.9 ± 8.6%

Figure 5-8: Analysis of RNA derived from control and CQ treated cells. PCRs using RNA derived cDNA with primers for *BiP* (**A**), *ATF3* (**B**), *XBP1t* (**C**) and *GAPDH* were conducted then products were separated in a gel. Bands were quantified and *BiP*, *ATF3* or *XBP1t* were expressed as a percentage of *GAPDH* then presented in the table (mean ± SD). Statistical tests were ordinary one-way ANOVA with Bonferroni's multiple comparisons test for *BiP* and *XBP1t* and Kruskal-Wallis with Dunn's multiple comparison test for *ATF3*. *$p \leq 0.05$. **D)** shows gels containing *Pst*1 digested *XBP1t* PCR products. Multiple bands between ~200 and ~500 bps show *XBP1u* was the main species present.

5.4.2.2 Total protein profiles with and without CQ treatment

CL and EV profiles differed as previously described with CLs having a more heterogenous protein distribution (Figure 5-9). There were no clear differences in the CL total protein profiles when NT and transfected cells were compared, and when control and treated cells were compared (Figure 5-9A). NT control samples from two preparations were faint because the wells were contaminated with TRIzol™ during protein/RNA extraction which resulted in protein precipitation (Appendix 8.3.3.4). Harvested EVs had a similar overall profile to that observed for DTT treatment (Figure 5-3). When comparing profiles between NT and transfected cells, they appeared similar (Figure 5-9B). Profiles of EVs from cells treated with CQ appeared to have a more heterogenous mixture of proteins compared to controls. EVs had concentrated bands between 49 and 62 kDa (possibly albumin) and between 98 and 198 kDa. Total protein profiles for all preparations are presented in Appendix 8.3.3.4.

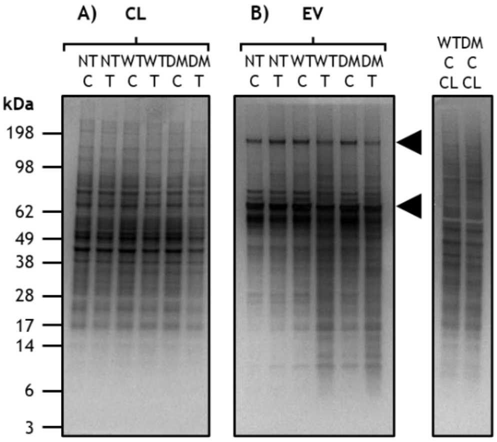

Figure 5-9: Representative total protein profiles for CQ treated cells. A) shows a representative total protein profile in CLs for Prep 4 out of 5 preparations using Coomassie Blue staining. Cells were either non-transfected or transfected with pWT-SOD1-EGFP or pDM-SOD1-EGFP. Some cells were not treated with CQ (C) while others were treated with CQ (T). **B)** is a representative total protein profile for EVs from Prep 4 out of 5 preparations using silver staining. Arrowheads indicate intense bands found in EVs. Three lanes had CL controls from NT, WT- and DM-SOD1-EGFP control cells, but NT was missing in the EV control lane due to contamination of lysates with TRIzol™ during protein/RNA extraction from culture plates.

5.4.2.3 Confirmation of autophagy disruption with CQ

LC3BII/LC3BI ratio was used to confirm CQ treatment inhibited autophagy by quantifying the conversion from LC3BI to LC3BII (Figure 5-10). NT control and treated samples had the biggest increase in ratios (267%; $p = 0.067$; Figure 5-10B) suggesting LC3BII accumulated. Further analysis of LC3BI and LC3BII (Figure 5-10C) showed there was significantly more LC3BII than LC3BI ($p \leq 0.05$) and, there was significantly more LC3BII in treated NT samples compared to untreated samples ($p \leq 0.001$). CQ inhibits autophagy at the level of the autolysosome preventing LC3BII degradation (Schrezenmeier and Dörner, 2020), so this explains these changes and confirms CQ had the desired effect.

For transfected cells, there was an average percentage increase in LC3BII/LC3BI ratio of 160.0% and 103.6% for WT-SOD1-EGFP and DM-SOD1-EGFP after CQ treatment, but this was not statistically significant (Figure 5-10B). When LC3BI and LC3BII were further investigated (Figure 5-10D), there were no significant differences in the protein levels as a consequence of CQ treatment and there were no differences between the subtypes within each genotype. As the ratios were higher after CQ treatment in all groups, it suggested autophagy was inhibited to some extent. For transfected samples, the fusion protein may initiate autophagy as cells may try to clear the protein, resulting in a higher level of LC3BI and a reduced ratio change compared to NT cells. There were no significant differences in LC3BII/LC3BI ratios between genotypes, but NT control and DM-SOD1-EGFP control LC3B ratios were borderline significant ($p = 0.0504$). There were no statistical differences in LC3B subtypes between genotypes.

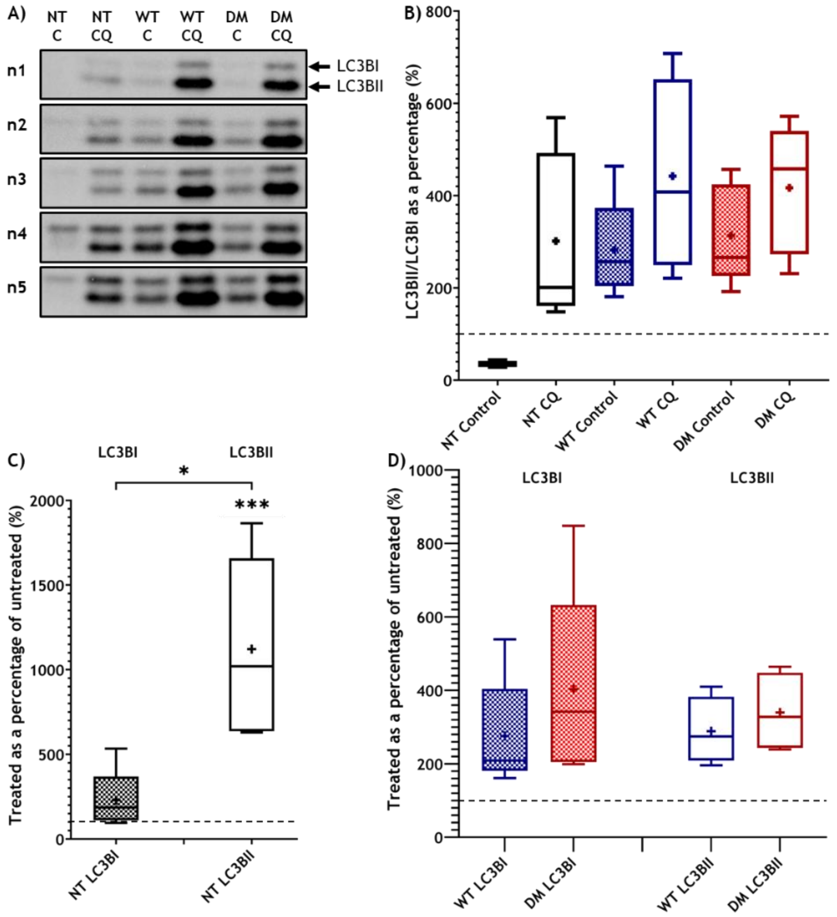

Figure 5-10: Comparison of LC3B ratios between treatment groups in CLs. A) All WBs for LC3BI and LC3BII around 14 kDa in CL samples. Protein concentration loaded was 10 µg. These bands were quantified for five replicate experiments, the LC3BII/LC3BI ratio calculated and expressed as a percentage in the graph **(B)**. For NT control CLs *n*= 4 as an outlier was excluded (209%). Statistical analysis in the form of ordinary one-way ANOVA with Bonferroni multiple comparisons tests were used. **C)** and **D)** LC3BI and LC3BII were expressed separately as a percentage of treated over untreated for NT **(C)** and WT- and DM-SOD1-EGFP **(D)** so changes could be clearly seen. In **C)**, residuals were normally distributed, so ratio paired t-tests were used to determine differences between treated and untreated samples. To compare LC3BI and LC3BII, a paired t-test was used. In **D)**, there was one outlier in LC3BII for WT- and DM-SOD1-EGFP genotypes (1249% and 1824% respectively), so these were excluded from analysis. Not all groups were normally distributed, so Wilcoxon matched-pairs signed rank tests were used to check for differences between treated and untreated samples and a Kruskal-Wallis with Dunn's multiple comparisons test was carried out to compare genotypes and LC3B. Dotted line= 100%. += mean. **p* ≤ 0.05; ****p* ≤ 0.001.

5.4.2.4 Analysis of SOD1, flotillin-1 and actin proteins

SOD1-EGFP was increased by an average of 81% and 135% in WT- and DM-SOD1-EGFP CLs respectively after CQ treatment, but these changes were not statistically significant using nonparametric tests (Figure 5-11A and B). Nonparametric tests were used because samples within the WT-SOD1-EGFP group were not normally distributed. For consistency, the same test was used for all control and treated comparisons. CQ treated WT- and DM-SOD1-EGFP were borderline significantly higher in CLs compared to untreated (WT- and DM-SOD1-EGFP *p*= 0.0625). When the parametric equivalent test was used, both reached significance (WT-SOD1-EGFP $p \leq 0.05$; DM-SOD1-EGFP $p \leq 0.01$). The increase is likely due to increased accumulation in cells due to lack of autolysosome digestion. Flotillin-1 was very similar across treatment groups and genotypes with only an 18% and 10% reduction for WT-SOD1-EGFP and DM-SOD1-EGFP respectively. This is likely to represent a small change to plasma membrane composition in treated samples. There was significantly more SOD1-EGFP than flotillin-1 for WT-SOD1-EGFP ($p \leq 0.05$) and DM-SOD1-EGFP ($p \leq 0.05$) CLs.

SOD1-EGFP was increased in WT-SOD1-EGFP EVs by an average of 12% but reduced by an average of 20% in DM-SOD1-EGFP EVs when cells were treated with CQ. Neither of these changes were statistically significant and there were no statistical differences between genotypes (Figure 5-11C and D). Flotillin-1 was increased by an average of 43% and 10% in WT-SOD1-EGFP and DM-SOD1-EGFP EV samples respectively after CQ treatment. The change was only significant for WT-SOD1-EGFP EVs ($p \leq 0.01$). Using an ordinary one-way ANOVA with Bonferroni's multiple comparisons test, no significant difference was found in flotillin-1 between genotypes, however using an unpaired t-test, there was a significant difference. The WT-SOD1-EGFP EV fraction had more flotillin-1 compared to the DM-SOD1-EGFP EV fraction ($p \leq 0.05$), possibly indicating more EVs were being produced from WT-SOD1-EGFP cells. SOD1-EGFP and flotillin-1 were not significantly different within genotypes. Actin in the EV fraction was variable but generally, levels were comparable or lower than levels found in CL controls. It should be noted that 5 μg of EV proteins and 1 μg of CL protein was loaded, showing levels were lower overall in the EV fraction compared to CLs. A representative Ponceau S stained blot is presented in Appendix 8.3.3.2.

CL and EV results taken together may suggest CQ increased the production of EVs from WT-SOD1-EGFP transfected cells as flotillin-1 was significantly increased in the EV fraction. In the DM-SOD1-EGFP transfected cells, this mechanism may be defective as there was no significant change in flotillin-1 when CQ was added compared to controls. The average amount of WT- and DM-SOD1-EGFP was increased in treated cells, although not significantly, while SOD1-EGFP in the EV fraction was much closer to the untreated values. It may suggest SOD1 was not incorporated into EVs due to autophagy inhibition, potentially eventually leading to an increase of the protein intracellularly.

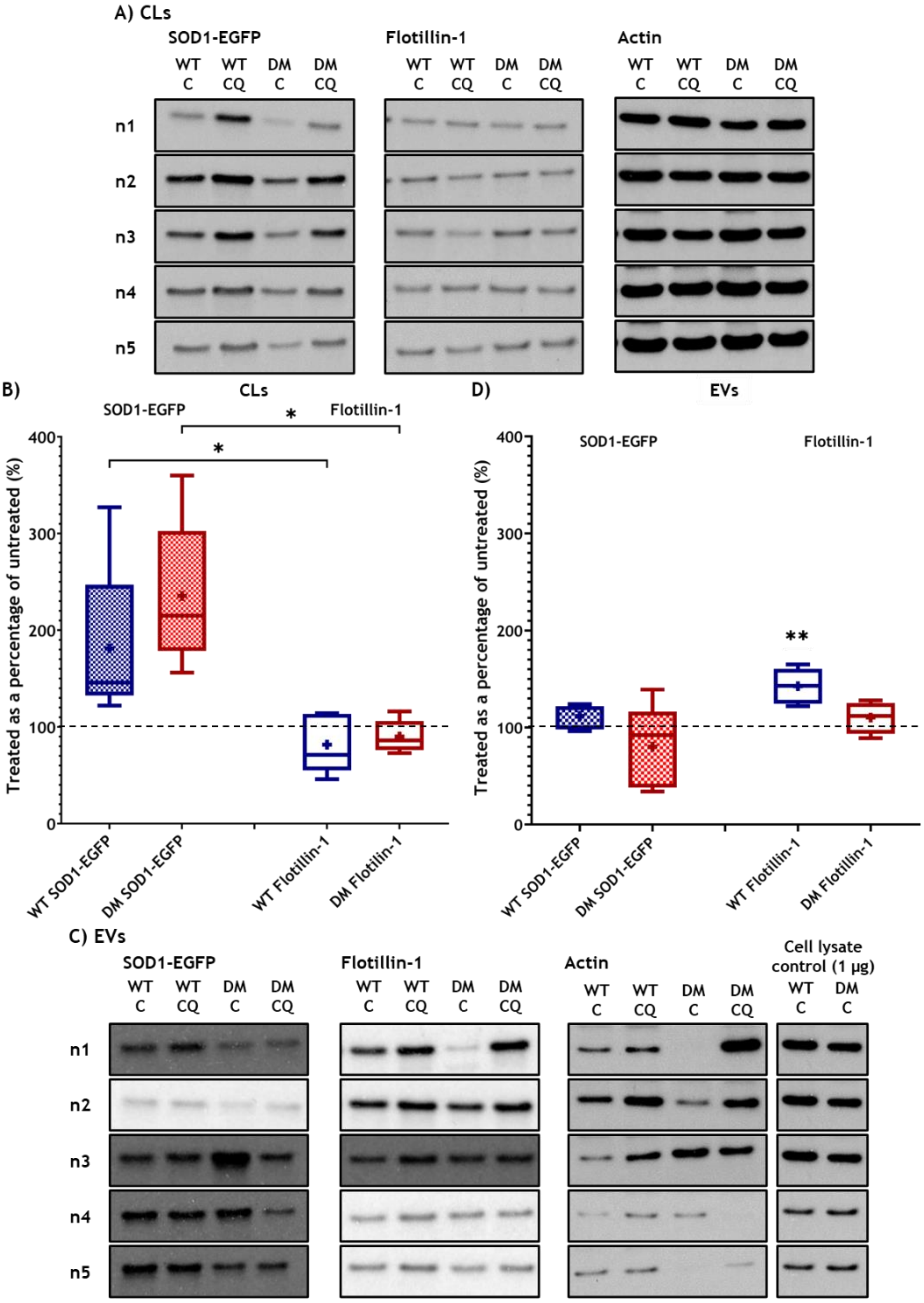

Figure 5-11: The effect of CQ treatment on CLs and EVs. A) and **C)** WBs for SOD1-EGFP, flotillin-1 and actin in CLs and EVs respectively. **A)** Protein concentration= 10 µg. **C)** Protein concentrations: EVs= 5 µg; CLs= 1 µg. SOD1-GFP and flotillin-1 were quantified then treated values expressed as a percentage of untreated and plotted in the graphs in **B)** and **D)** for CLs and EVs respectively. For CLs (*n*= 5), Wilcoxon matched-pairs signed rank test compared treated and untreated samples. Kruskal-Wallis with Dunn's multiple comparisons tests compared genotype and protein. For EVs (SOD1-EGFP *n*= 5; flotillin-1 WT *n*= 5, DM *n*= 4) an outlier (n1= 1192%) was excluded from DM flotillin-1 as it skewed results causing an abnormal distribution of residuals. Actin levels were also particularly high in the EV fraction from CQ treated samples and almost missing from the control EV fraction so this may reflect this observation. Ratio paired t-tests analysed changes to proteins caused by treatment. Ordinary one-way ANOVA with Bonferroni multiple comparisons test compared genotypes and proteins. Dotted line= 100%. += mean. $*p \leq 0.05$; $**p \leq 0.01$. Uncropped WBs are presented in Appendix 8.3.3.7.

LC3B proteins were also investigated in EVs (Figure 5-12). The ratio was not applicable for EV evaluation, so LC3BI and LC3BII levels in treated samples were expressed as a percentage of untreated protein (Figure 5-12B and C). There was an average increase in LC3BI by 165.0% in NT EVs, 314.4% in WT-SOD1-EGFP EVs and 238.2% in DM-SOD1-EGFP EVs after CQ treatment. For WT-SOD1-EGFP and DM-SOD1-EGFP EVs, this was a significant increase compared to untreated samples (WT-SOD1-EGFP $p \leq 0.01$; DM-SOD1-EGFP $p \leq 0.05$). For LC3BII, treatment increased values by an average of 1321.8% for NT EVs, 164.8% for WT-SOD1-EGFP EVs, and 166.0% for DM-SOD1-EGFP EVs. This was a significant increase for all groups: NT $p \leq 0.0001$; WT-SOD1-EGFP $p \leq 0.05$ and DM-SOD1-EGFP $p \leq 0.01$. This suggests that EVs may be used to remove surplus cellular LC3BII and/or autophagosomes/autolysosomes when autophagy is inhibited in cells, in addition to LC3BI. The difference between LC3BI and LC3BII levels associated with EVs after treatment was only significant for NT EVs ($p \leq 0.05$). When the treatment and genotype was also compared (not shown), there was significantly more LC3BII in NT EVs after CQ treatment compared to WT-SOD1-EGFP EVs ($p \leq 0.0001$) and DM-SOD1-EGFP EVs ($p \leq 0.0001$). The significant increase in LC3BII seen in the NT EV group compared to transfected EV groups after treatment could be because minimal or no LC3BII was visible in the WBs for NT control cells (Figure 5-12A), making the difference between control and treated LC3BII very different. The effect of CQ treatment on LC3BI levels was similar between NT and transfected cells.

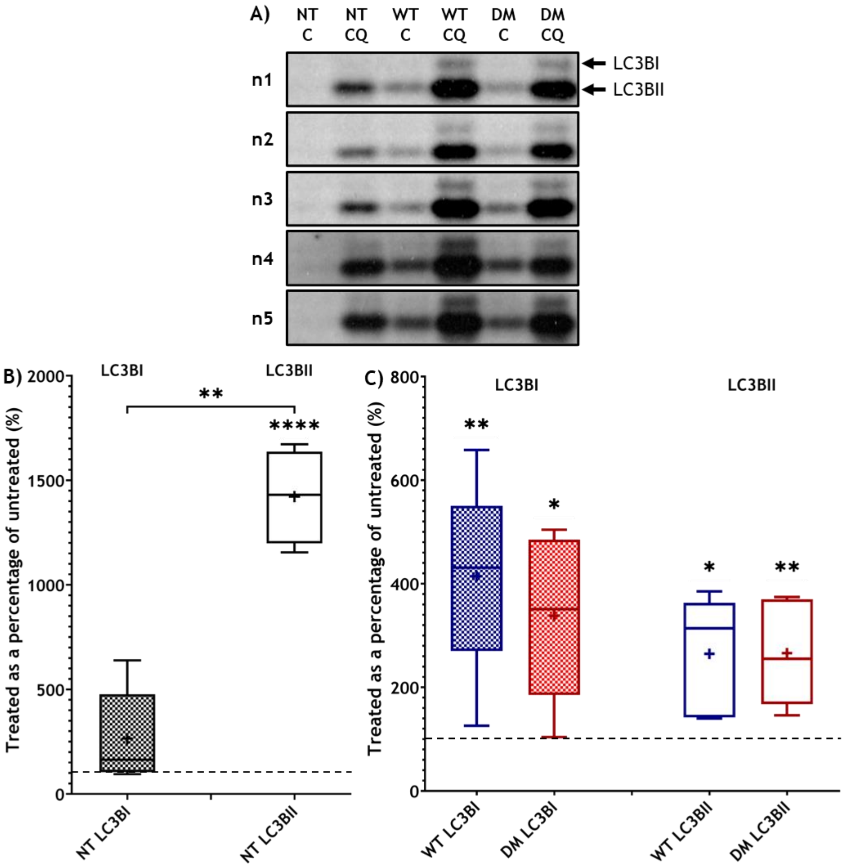

Figure 5-12: The effect of CQ on LC3B subtypes associated with EVs. A) all EV WBs with LC3BI and LC3BII around 14 kDa. LC3BI and LC3BII were expressed separately as treated as a percentage of untreated for NT **(B)** and WT- or DM-SOD1-EGFP **(C)**. One outlier in NT LC3BII (2793%) was excluded. Ratio paired t-tests compared treated and untreated samples. For NT EVs a paired t-test was used to compare the LC3B subtypes and for the transfected EVs, an ordinary one-way ANOVA with Bonferroni's multiple comparisons test was used. += mean. **p* ≤ 0.05; ***p* ≤ 0.01; ****p* ≤ 0.001; *****p* ≤ 0.0001.

5.4.2.5 SOD1 activity

The usual endogenous SOD and fusion SOD1 protein bands were clearly observed in CLs (Figure 5-13A and C). Fusion protein activity appeared to be marginally increased for both WT- and DM-SOD1-EGFP treated samples in the first attempt of the method. After repeating the NBT stained gel with another preparation, there was no clear difference in fusion protein activity between control and treated CLs. Endogenous SOD did not appear to change between genotype or treatment. In EVs, endogenous SOD activity was difficult to identify in all genotypes and treatments (Figure 5-13B and D). Both WT- and DM-SOD1-EGFP fusion protein bands were present in EVs with and without CQ treatment in both preparations, suggesting the proteins retained activity.

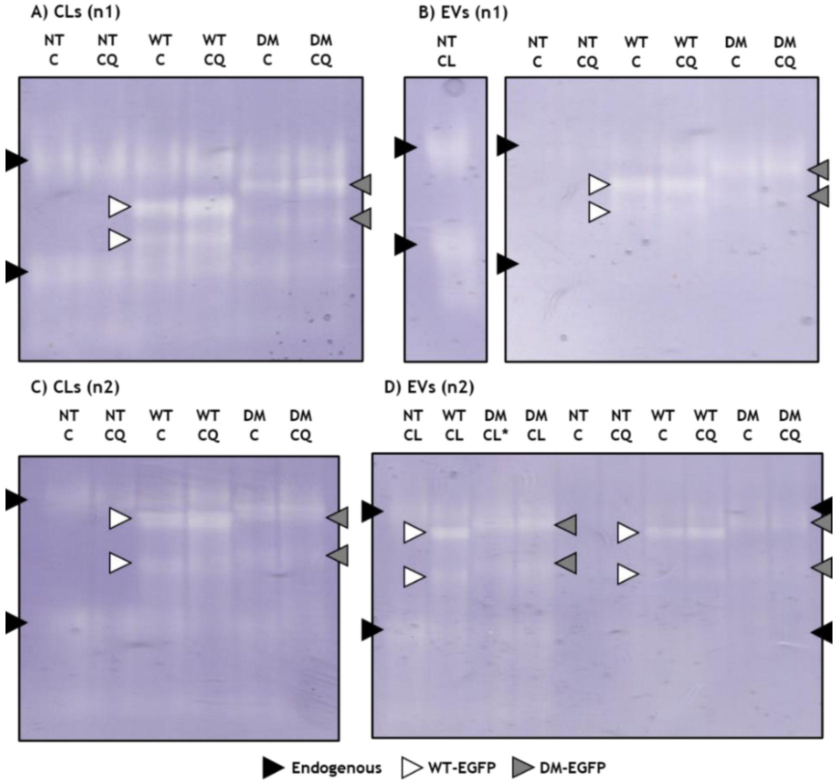
A) CLs (n1)
NT C
NT CQ
WT C
WT CQ
DM C
DM CQ
B) EVs (n1)
NT CL
NT C
NT CQ
WT C
WT CQ
DM C
DM CQ
C) CLs (n2)
NT C
NT CQ
WT C
WT CQ
DM C
DM CQ
D) EVs (n2)
NT CL
WT CL
DM CL*
DM CL
NT C
NT CQ
WT C
WT CQ
DM C
DM CQ
Endogenous
WT-EGFP
DM-EGFP

Figure 5-13: The effect of CQ treatment on SOD activity in CLs and EVs. Presented above are NBT stained native gels which were used to assay SOD1 activity in CLs (**A)** and **C)**) and EVs (**B)** and **D)**). Endogenous SOD (black arrowhead) activity, WT-SOD1-EGFP (white filled arrowhead) and DM-SOD1-EGFP (grey filled arrowhead) activity can be seen. The assay was performed using one preparation, then it was repeated with another preparation to ensure activity observed in the EV fractions was repeatable. In **B)**, the image was cropped to save space as there were multiple empty wells between the EV samples and CL control. Plasmid activity remained present in EVs after repeating. In **D)**, there was an additional DM CL control as there was a loading error (denoted*).

5.4.2.6 Cell morphology, transfection efficiency and aggregation of SOD1-EGFP

There appeared to be more rounded cells in the CQ treated cells compared to controls and there was a loss of cells (Figure 5-14A). There were no obvious differences in the morphology of control or CQ treated nuclei in either genotype (Figure 5-14B). The average percentage of cells transfected with pWT-SOD1-EGFP and pDM-SOD1-EGFP was 55 ± 2.5% and 56 ± 3.0% (mean ± SEM) respectively. CQ may have increased the rate of transfection as shown by an increase in the CQ means compared to controls, but this was not statistically significant (Figure 5-14C and D). CQ treatment increased the percentage of SOD1-EGFP aggregates (Figure 5-14E) observed in WT- and DM-SOD1-EGFP cells, but this was only statistically significant for DM-SOD1-EGFP cells ($p \leq 0.01$). Overall, there were more SOD1-EGFP aggregates in the DM-SOD1-EGFP samples compared to WT-SOD1-EGFP counterparts, but the difference was only significant between treated samples ($p \leq 0.01$; Figure 5-14F).

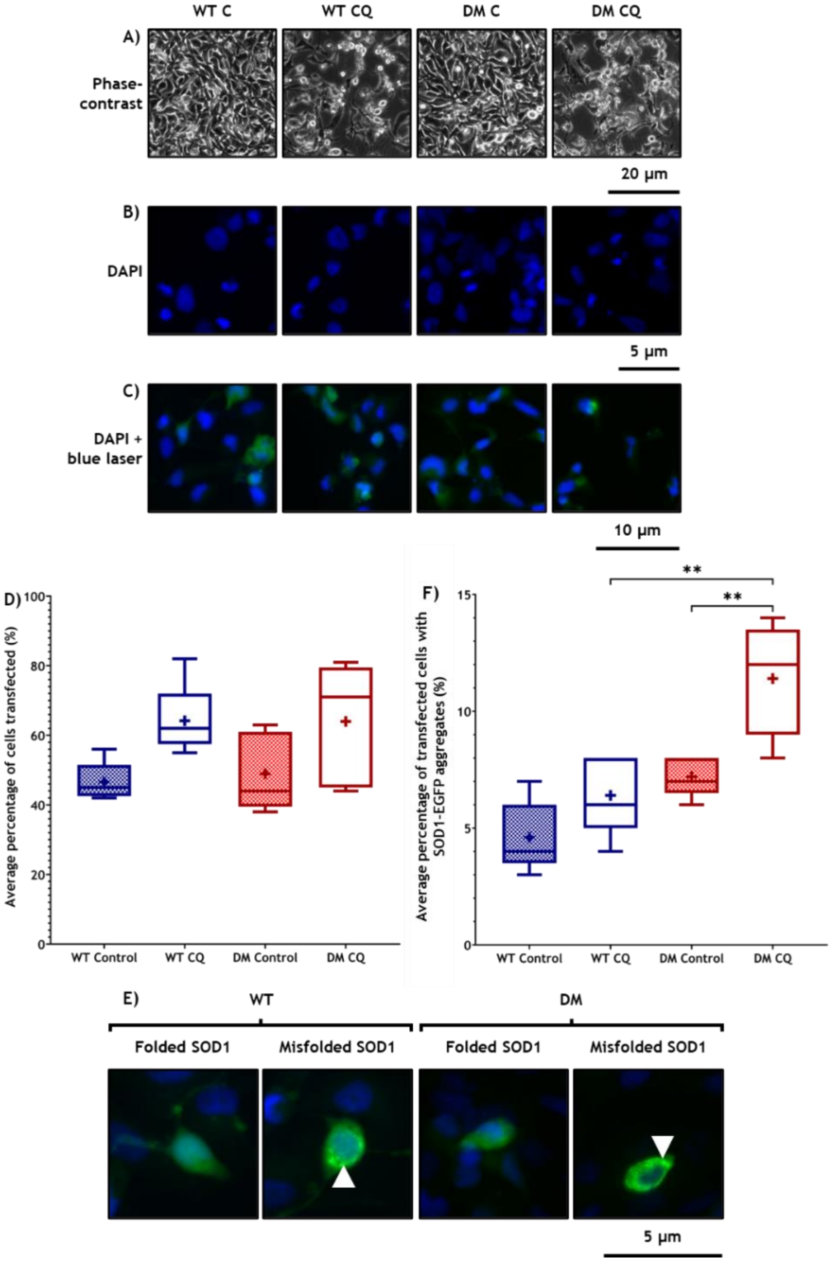
WT C
WT CQ
DM C
DM CQ
A)
Phase-contrast
20 µm
B)
DAPI
5 µm
C)
DAPI + blue laser
10 µm
D)
Average percentage of cells transfected (%)
0
20
40
60
80
100
WT Control
WT CQ
DM Control
DM CQ
F)
Average percentage of transfected cells with SOD1-EGFP aggregates (%)
0
5
10
15
**
**
WT Control
WT CQ
DM Control
DM CQ
E)
WT
DM
Folded SOD1
Misfolded SOD1
Folded SOD1
Misfolded SOD1
5 µm

Figure 5-14: Cytology of cells treated with CQ. A) Phase-contrast images from 6-well plates used for the protein experiments. Scale bar= 20 µm. **B)** Images of DAPI stained nuclei to demonstrate the nucleic morphology. Scale bar= 5 µm. **C)** Wide field fluorescent images to demonstrate transfection efficiency. Blue= DAPI stained nuclei and green= SOD1-EGFP. Scale bar= 10 µm. **D)** The graph shows the average percentage of WT- and DM-SOD1-EGFP transfected cells in control and treated cells (*n*= 5). Images were captured from three different fields at 100X magnification within each slide then transfected cell and aggregate counts were averaged for each slide and plotted in the graph. An ordinary one-way ANOVA with Bonferroni multiple comparisons test was used to compare groups. += mean. Mean ± SEM: WT C 47 ± 2.5%, WT CQ 64 ± 4.7%, DM C 49 ± 3.2%, DM CQ 64 ± 4.4%. **E)** composite images of DAPI stained nuclei with SOD1-EGFP. When SOD1-EGFP misfolds, it forms aggregates (white arrowheads). Scale bar= 5 µm. The graph in **F)** shows the average percentage of WT- and DM-SOD1-EGFP transfected cells with SOD1-EGFP aggregates in control and treated cells (*n*= 5). Images were captured as described for **D)**. An ordinary one-way ANOVA with Bonferroni multiple comparisons test was used. += mean. $^{**}p \leq 0.01$. Mean ± SEM: WT C 5 ± 0.5%; WT CQ 6 ± 0.8%; DM C 8 ± 0.7%; DM CQ 11 ± 0.9%.

5.4.3 Impact of proteasome inhibition by MG132

5.4.3.1 Assessment of RNA

After checking RNA integrity of MG132 treated samples (Appendix 0), RT-PCR was carried out using primers for *ATF3*, *BiP*, *XBP1* and *GAPDH*. *BiP* was significantly increased in both WT- and DM-SOD1-EGFP treated cells compared to controls (p ≤ 0.01; Figure 5-15A), suggesting the UPS had been upregulated. There were no differences in *BiP* between genotypes. *ATF3* was not effected by treatment or genotype statistically, but there was a 54% difference in the mean *ATF3* present in DM-SOD1-EGFP control and treated cells that was not present in WT-SOD1-EGFP cells (Figure 5-15B). There were no statistically significant differences in *XBP1t* between genotypes or treatments (Figure 5-15C). *XBP1u* was the dominant subtype present in control cells (Figure 5-15D) but *XBP1u* and *XBP1s* were present in treated cells, suggesting ER stress had been initiated.

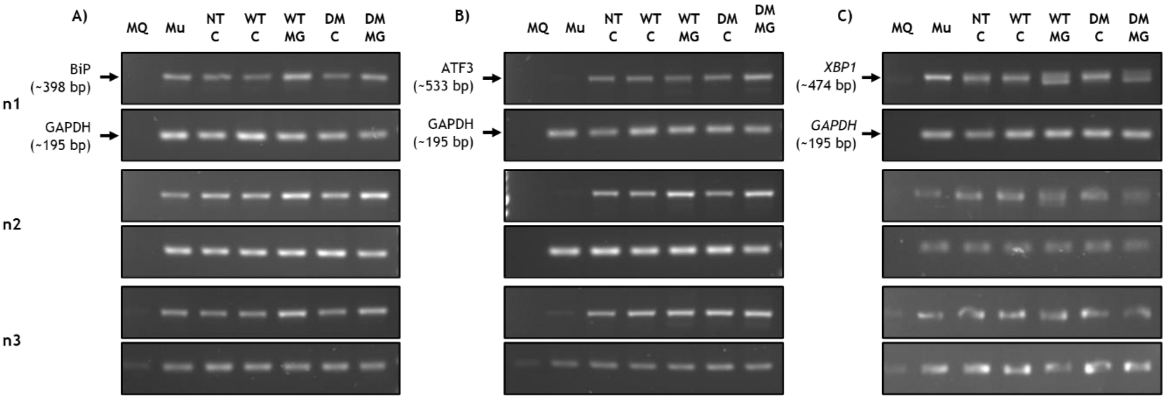

	NT Con	WT Con	WT MG132	DM Con	DM MG132
BiP	73.3 ± 18.7%	59.7 ± 17.9%**	121.7 ± 14.8%**	66.3 ± 1.5%††	126.0 ± 18.5%††
ATF3	95.3 ± 44.8%	103.0 ± 73.3%	107.7 ± 54.0%	84.3 ± 31.3%	137.7 ± 4.9%
XBP1t	105.7 ± 18.5%	106.7 ± 28.0%	126.7 ± 51.7%	89.3 ± 12.5%	62.7 ± 11.0%

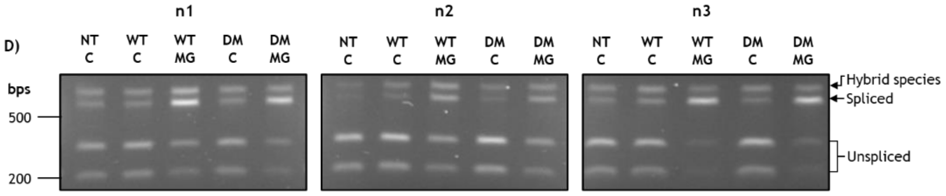

Figure 5-15: Analysis of gene expression after MG132 treatment. *BiP* (**A**), *ATF3* (**B**), *XBP1t* (**C**) and *GAPDH* PCR products were separated in a gel, quantified then expressed as a percentage of *GAPDH* and presented in the table (mean ± SD). Statistical tests were ordinary one-way ANOVA with Bonferroni's multiple comparisons test (*BiP* and *XBP1t*) or Kruskal-Wallis with Dunn's multiple comparison test (*ATF3*). $^{**}p \leq 0.01$ and $^{\dagger\dagger}p \leq 0.01$. **D)** gels containing *Pst*1 digested *XBP1t* PCR products. Multiple bands between ~200 and ~500 bps show *XBP1u* was the main species present, however, there was evidence of *XBP1s* in MG132 treated cells.

5.4.3.2 Total protein profiles

The general total protein profiles for EVs and CLs were similar to those seen before for DTT and CQ treatments. Profiles looked similar between control and treated CLs, but there was an additional band seen only in the MG132 treated cells at around 62 kDa (Figure 5-16A). EV profiles looked similar between treatment groups overall, but the EVs from treated cells appeared to have a more heterogenous population of proteins compared to untreated EVs (Figure 5-16B). There were additional proteins between 14 and 17 kDa in EVs from treated cells that were not apparent in control EVs. All gels are found in Appendix 8.3.3.5.

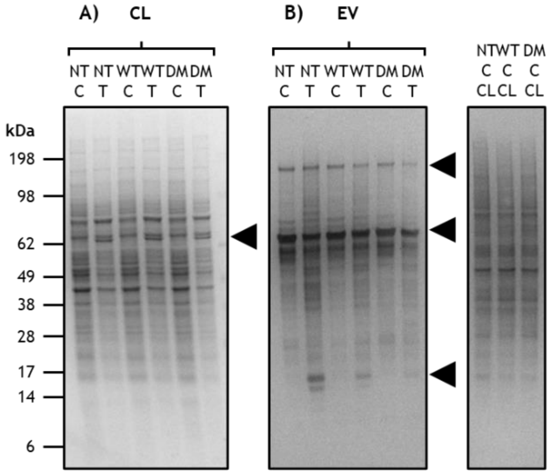

Figure 5-16: Total protein profiles of CLs and EVs in MG132 study. A) shows a representative total protein profile for CLs from one of three preparations (Prep 3) using Coomassie Blue staining. Cells were either NT or transfected with pWT- or pDM-SOD1-EGFP. Some cells were untreated (C) while others were treated with MG132 (T). **B)** is a representative total protein profile for EVs from one of the three preparations (Prep 3) using silver staining. Three lanes were CL controls from NT, WT- and DM-SOD1-EGFP transfected control cells. Arrowheads indicate bands of interest.

5.4.3.3 Increased ubiquitination confirmed the proteasome was inhibited

MG132 is a proteasome inhibitor and proteasome function can be monitored by assessing ubiquitination of proteins within cells. In this study, there was increased ubiquitination of proteins after the addition of MG132, as shown in the WBs (Figure 5-17A), indicating the proteasome was effectively inhibited. Ubiquitinated proteins were increased by 71%, 87% and 77% in treated NT, WT- and DM-SOD1-EGFP transfected cells respectively. The increase was only statistically increased for WT-SOD1-EGFP cells ($p \leq 0.01$), but NT cells were borderline significant (*p*= 0.0672). There was considerable variation between preparations for NT and DM-SOD1-EGFP transfected cells, so increasing the number of replicates would be of benefit to obtain more representative means. For example, for NT CLs with three samples, this is likely being driven by one replicate that pulled the mean down. The opposite could be true for DM-SOD1-EGFP cells where one replicate pulls the mean up. Nevertheless, there was clearly proteasomal inhibition induced by MG132 but there were no clear differences in the level of ubiquitination between NT and transfected cells.

EVs produced from these cells were also probed for ubiquitin (Figure 5-17B). Qualitative assessment showed ubiquitination was also increased in MG132 treated EVs of all genotypes. NT EVs may have had more ubiquitination than the EVs from transfected cells as the bands were slightly darker.

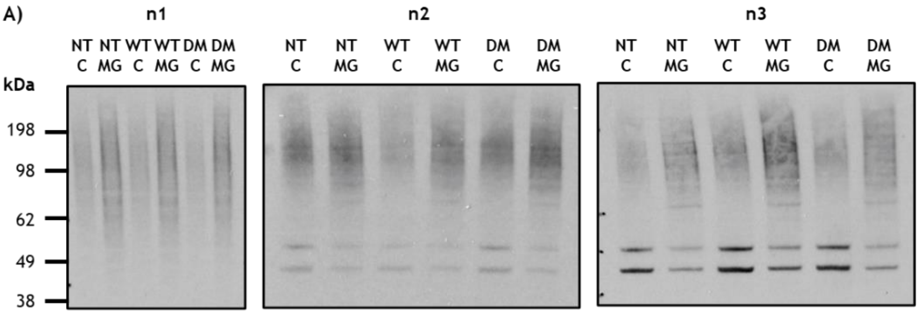
A)
n1
NT C
NT MG
WT C
WT MG
DM C
DM MG
n2
NT C
NT MG
WT C
WT MG
DM C
DM MG
n3
NT C
NT MG
WT C
WT MG
DM C
DM MG
kDa
198
98
62
49
38

	NT (MG132/Con)	WT (MG132/Con)	DM (MG132/Con)
Mean±SD	171.3 ± 39.1%	186.7 ± 15.3%	176.7 ± 54.9%
p value (MG132/Con)	0.0672 (ns)	0.0060 (**)	0.0901 (ns)

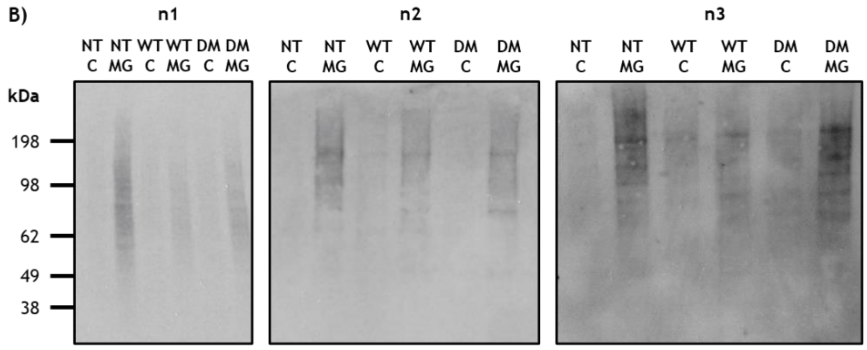
B)
n1
NT C
NT MG
WT C
WT MG
DM C
DM MG
n2
NT C
NT MG
WT C
WT MG
DM C
DM MG
n3
NT C
NT MG
WT C
WT MG
DM C
DM MG
kDa
198
98
62
49
38

Figure 5-17: MG132 treatment effect on ubiquitination within CLs and EVs. A) WBs probed with ubiquitin to label ubiquitinated proteins. The bands were quantified and treated samples were expressed as a percentage of the untreated samples. The mean percentages with SDs are presented in the table for NT, WT- and DM-SOD1-EGFP CLs. Ratio paired t-tests were used to evaluate the percentage difference between control and treated samples. Further, an ordinary one-way ANOVA with Bonferroni's multiple comparisons test was used to compare values between genotypes. $^{**}p \leq 0.01$. Stronger single bands at around 42 and 47 kDa were residual actin and flotillin-1 from the previous two probes. **B)** Blots containing EVs from cells treated or untreated with MG132 were probed with anti-ubiquitin.

5.4.3.4 Effect of MG132 treatment on SOD1-EGFP, flotillin-1 and actin proteins

SOD1-EGFP was significantly increased after MG132 treatment in CLs from both genotypes ($p \leq 0.05$). For WT-SOD1-EGFP transfected cells, there was an average increase of 199% and for DM-SOD1-EGFP transfected cells, it was 411%. There were no statistical differences between the genotypes (Figure 5-18A and B). For flotillin-1, there was an average decrease of 29% and 38% for WT- and DM-SOD1-EGFP respectively after MG132 treatment, but this was not a statistically significant change (Figure 5-18A and B). There was significantly more SOD1-EGFP than flotillin-1 in the DM-SOD1-EGFP transfected CLs ($p \leq 0.05$). Actin levels were similar between cells but may have been marginally reduced in treated cells (Figure 5-18A). These results suggest there is potentially a loss of cells, disruption to the cytoskeleton or membranous components and an accumulation of SOD1-EGFP in cells treated with MG132.

In the EV fraction, there was also an average increase in SOD1-EGFP (WT-SOD1-EGFP= 251% and DM-SOD1-EGFP= 243%) and was statistically significant for DM EVs ($p \leq 0.01$) and bordering on significance for WT EVs ($p= 0.06$). The lack of significance in WT-SOD1-EGFP EVs is likely due to the variation in individual samples (Figure 5-18C and D). Flotillin-1 was reduced in the EV fractions of WT- and DM-SOD1-EGFP EVs by an average of 67% and 56% (Figure 5-18C and D). The change was statistically significant for WT-SOD1-EGFP derived EVs only ($p \leq 0.01$) and borderline significant for DM-SOD1-EGFP derived EVs ($p= 0.0668$). Actin was markedly reduced in the EV fraction compared to CL controls showing there was minimal cellular contamination in the fraction (Figure 5-18C). A representative Ponceau S stained blot is presented in Appendix 8.3.3.2. Overall, these results suggest MG132 treatment prevented the production of EVs to some extent from cells and that the SOD1-EGFP present in this fraction could be associated with free protein.

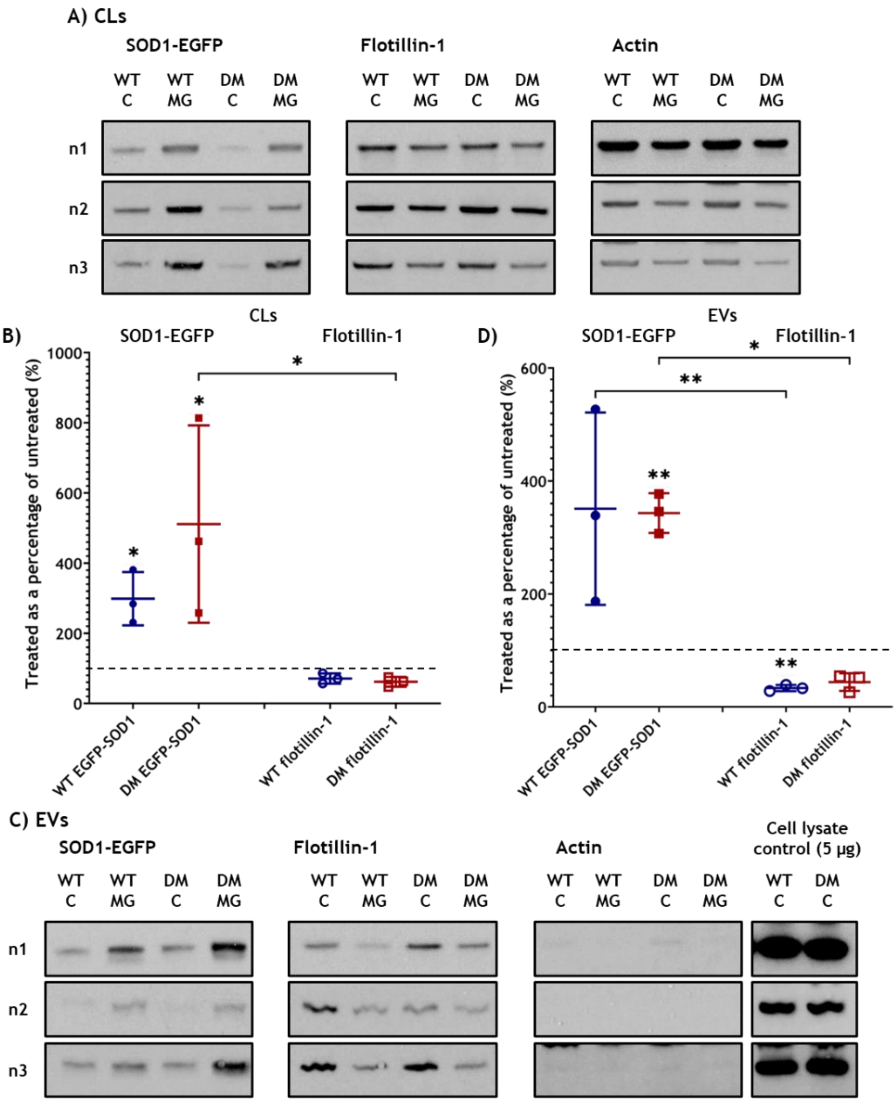

Figure 5-18: The effect of MG132 treatment on CLs and EVs. A) WBs for SOD1-EGFP, flotillin-1 and actin in CLs for control and MG132 treated samples. Protein concentration= 10 µg. **B)** The graph contains the results from all three CL preparations when probed with GFP or flotillin-1 (*n*= 3). Ratio paired t-tests were used to determine if there were changes to the level of protein before and after treatment. Ordinary one-way ANOVA with Bonferroni multiple comparisons test compared protein levels between genotypes and the two proteins. The midline represents the mean. **C)** WBs for SOD1-EGFP, flotillin-1 and actin in EVs for control and MG132 treated samples. Protein concentration= 5 µg. **D)** The graph contains the results from all three EV preparations when probed with GFP or flotillin-1 (*n*= 3). Ratio paired t-tests were used compare protein levels before and after treatment. Ordinary one-way ANOVA with Bonferroni multiple comparisons test were used to compare protein levels between genotypes and the two proteins. The midline represents the mean. Dotted line represents 100%. *$p \leq 0.05$; **$p \leq 0.01$.

5.4.3.5 MG132 treatment and SOD1 activity

The usual bands identified previously in this study and in Qi *et al.*, (2019) were identified in untreated and MG132 treated CLs (Figure 5-19). Fusion protein activity looked similar with and without MG132 treatment, but endogenous SOD may have been mildly reduced after MG132 treatment. Endogenous SOD activity was not clear in control or treated EVs, but it was noted that the proteins appeared to accumulate in the wells instead of running into the gel, potentially because the stacking gel was too dense.

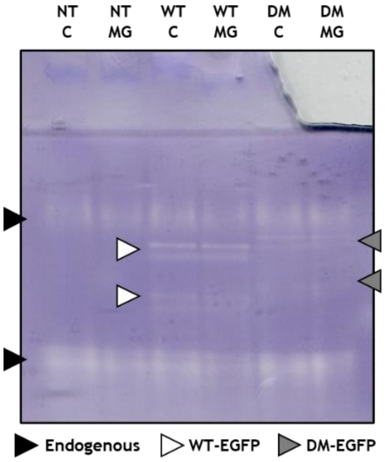

Figure 5-19: The effect of MG132 treatment on SOD activity in CLs. NBT stained native gel used to assay SOD1 activity in CLs with and without MG132 treatment. Endogenous SOD (black arrowhead) activity, WT-SOD1-EGFP (white filled arrowhead) and DM-SOD1-EGFP (grey filled arrowhead) activity can be seen. The assay was performed using one preparation (*n*= 1).

5.4.3.6 Cell morphology, SOD1-EGFP transfection efficiency and aggregation

There were more rounded cells present in MG132 treated cells compared to control cells and this was accompanied by cell loss (Figure 5-20A). Nuclei in treated cells more frequently displayed a horseshoe shape rather than oval shape (Figure 5-20B). Cells treated with MG132 formed an island like distribution where clusters of cells formed (Figure 5-20C). There were no clear differences between genotypes. Cells were efficiently transfected with pWT- or pDM-SOD1-EGFP (34 ± 2.5% and 27 ± 2.7% respectively; Figure 5-20D). MG132 appeared to significantly increase the transfection efficiency of the plasmids (pWT-SOD1-EGFP $p \leq 0.01$; pDM-SOD1-EGFP $p \leq 0.05$), but this may be an artefact due to more intense fluorescence. There were no differences between genotypes. MG132 treatment significantly increased the number of transfected cells with SOD1 aggregates ($p \leq 0.0001$; Figure 5-20E and F). This suggests proteasome inhibition had a marked impact on SOD1-EGFP clearance from cells. Further, there were significantly more aggregates in treated DM-SOD1-EGFP transfected cells compared to treated WT-SOD1-EGFP cells ($p \leq 0.05$). The mean number of transfected cells with aggregates was slightly higher in DM-SOD1-EGFP controls compared to WT-SOD1-EGFP controls, but this was not statistically significant.

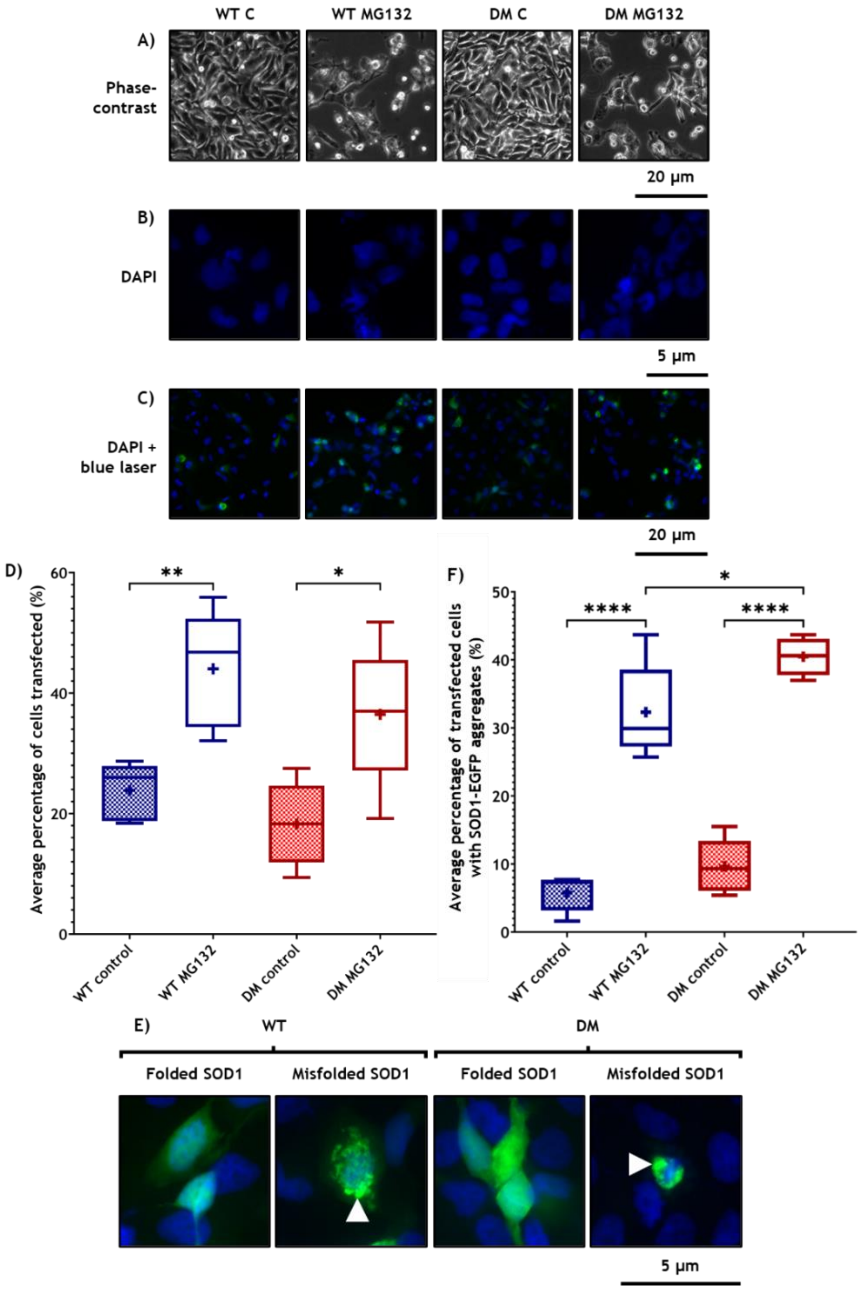
WT C
WT MG132
DM C
DM MG132
A)
Phase-contrast
20 µm
B)
DAPI
5 µm
C)
DAPI + blue laser
20 µm
D)
Average percentage of cells transfected (%)
60
40
20
0
**
*
WT control
WT MG132
DM control
DM MG132
F)
Average percentage of transfected cells with SOD1-EGFP aggregates (%)
50
40
30
20
10
0
****
*
****
WT control
WT MG132
DM control
DM MG132
E)
WT
DM
Folded SOD1
Misfolded SOD1
Folded SOD1
Misfolded SOD1
5 µm

Figure 5-20: Cytology of cells treated with MG132. A) Phase-contrast images from 6-well plates used for the protein experiments. Scale bar= 20 µm. **B)** DAPI stained nuclei of control and MG132 treated cells. Scale bar= 5 µm. **C)** Wide field fluorescent images to demonstrate the transfection efficiency of the plasmids. Blue= DAPI stained nuclei and green= SOD1-EGFP. Scale bar= 20 µm. **D)** The graph shows the average percentage of WT- and DM-SOD1-EGFP transfected cells in control and treated cells (*n*= 5). Images were captured from three different fields at 100X magnification within each slide, then transfected cell and aggregate counts were averaged for each slide and plotted in the graph. An ordinary one-way ANOVA with Bonferroni multiple comparisons test was used to compare groups. Mean ± SEM: WT C 24 ± 2.1%, WT MG132 44 ± 2.8%, DM C 18 ± 2.0%, DM MG132 36 ± 3.7%. **+**= mean. $^{*}p \leq 0.05$; $^{**}p \leq 0.01$. **E)** composite images of DAPI stained nuclei with SOD1-EGFP. When SOD1-EGFP misfolds, it forms aggregates (white arrowhead). Scale bar= 5 µm. The graph in **F)** shows the average percentage of WT- and DM-SOD1-EGFP transfected cells with SOD1-EGFP aggregates in control and treated cells (*n*= 5). Images were captured as described for **D)**. An ordinary one-way ANOVA with Bonferroni multiple comparisons test was used. Mean ± SEM: WT C 6 ± 0.7%; WT MG132 10 ± 1.1%; DM C 32 ± 2.6%; DM MG132 40 ± 2.4%. **+**= mean. $^{*}p \leq 0.05$; $^{****}p \leq 0.0001$.

5.4.4 SOD1 aggregation in control cells

In the DTT, CQ and MG132 studies, using an ordinary one-way ANOVA with Bonferroni's multiple comparisons test to compare the effect of genotype and treatment on SOD1 aggregation, there were no significant differences found between untreated WT- or DM-SOD1-EGFP transfected cells, contrary to published studies (Qi *et al.*, 2019). When unpaired t-tests were used to compare WT- and DM-SOD1-EGFP untreated controls, there were statistically significant differences in aggregation between genotypes in the DTT and CQ studies, but not MG132; DM-SOD1-EGFP was found to aggregate more than WT-SOD1-EGFP ($p \leq 0.01$). As discussed previously in Chapter 3, the use of media depleted in exosomes may have an impact on the ability of EVs to spread the misfolded SOD1 protein, so this could lead to the reduced significance observed in the current study. Nevertheless, DM-SOD1-EGFP untreated cells consistently presented with an upwards trend in SOD1 aggregation propensity compared to WT-SOD1-EGFP untreated cells.

5.4.5 Evidence of crosstalk between protein processing pathways

5.4.5.1 Effect of autophagy inhibition on UPS

Some WBs containing control and CQ treated samples were probed with an anti-ubiquitin antibody to assess the effect of autophagy inhibition on the UPS. The general ubiquitin profiles were similar between CLs and EVs, but there was an additional band between 14 kDa and 17 kDa in the CLs of transfected cells (Figure 5-21). NT control CLs from preparations one and two were contaminated with TRIzol™ during sample extraction leading to protein precipitation and low ubiquitin and actin levels. Ubiquitin was quantified for transfected CLs only and results showed there were no statistically significant changes to ubiquitination in treated CLs compared to controls for either genotype (Figure 5-21A). The means were elevated in WT- and DM-SOD1-EGFP transfected cells by 25% and 28% respectively suggesting the pathway was utilised by treated cells, even if it was not significantly upregulated. The EV study was qualitative because part of the blot was compromised for a couple of samples, but it was of sufficient quality to be described. It could be seen that there were consistently more ubiquitinated proteins present in the CQ treated EVs compared to the controls (Figure 5-21B). This potentially suggests ubiquitinated proteins were secreted from cells in association with EVs.

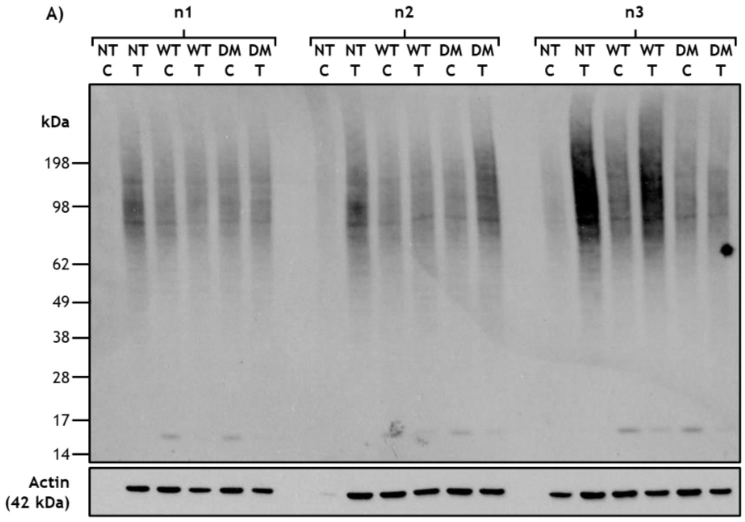
A)
n1
n2
n3
NT NT WT WT DM DM
C T C T C T
kDa
198
98
62
49
38
28
17
14
Actin
(42 kDa)

	WT (CQ/Con)	DM (CQ/Con)
Mean ± SD	125.0 ± 53.9%	128.3 ± 54.4%
p value (CQ/Con)	0.5579 (ns)	0.4818 (ns)

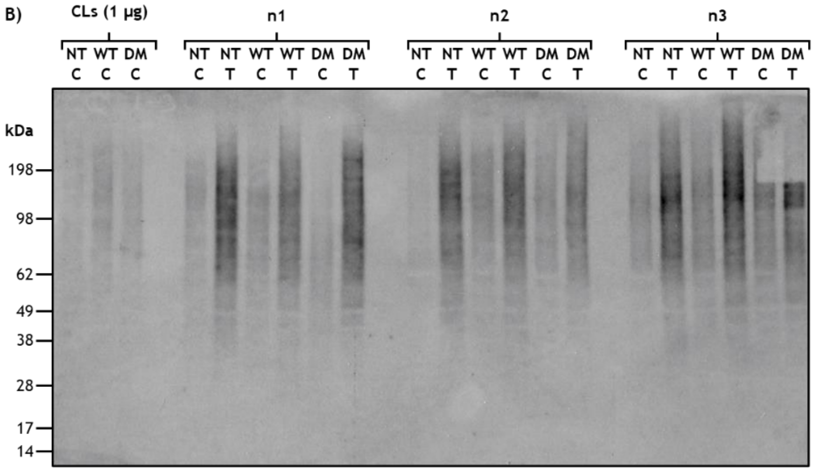
B)
CLs (1 µg)
NT WT DM
C C C
n1
n2
n3
NT NT WT WT DM DM
C T C T C T
kDa
198
98
62
49
38
28
17
14

Figure 5-21: CQ treatment may upregulate pathways including the UPS. A) CLs from n1-n3 were separated in a gel and probed with anti-ubiquitin and anti-actin antibodies. NT untreated for n1 and n2 were contaminated with TRIzol™ during the sample collection which led to protein precipitation therefore, ubiquitin and actin levels were very low. No issues were found with other samples. CL ubiquitin was quantified, and treated values were expressed as percentage of controls. These are found in the table (mean ± SD) with the corresponding *p* value. **B)** The EV blot containing n1-n3 was reprobed with an anti-ubiquitin antibody. As ubiquitin binds to proteins that are destined to be degraded by the proteasome, the protein appears as a smear as the proteins being tagged by ubiquitin will be of varying sizes.

5.4.5.2 Effect of proteosome inhibition on autophagy pathway

The effect of MG132 treatment on autophagy was assessed using the LC3BII/LC3BI ratio in CLs (Figure 5-22A). Based on the percentage difference in ratios between control and treated samples, MG132 caused an increase in ratio by 32% in WT-SOD1-EGFP and 1.5% in DM-SOD1-EGFP transfected cells, but these changes were not statistically significant. There were no statistical differences between genotypes. These results imply autophagy was functional after MG132 treatment in both genotypes. The WBs show clear increases in the levels of LC3BI and LC3BII protein in treated cells compared to untreated cells, so the bands were quantified separately and levels in treated samples were expressed as a percentage of untreated levels. The average increase in LC3BI in treated WT- and DM-SOD1-EGFP transfected CLs was 502% and 250%, but these were not statistically different from untreated cells. The percentage change in LC3BI from WT-SOD1-EGFP CLs was borderline significant (p= 0.0546). For LC3BII, the average increase in WT- and DM-SOD1-EGFP transfected CLs was 1187% and 291% respectively. These changes were also not statistically significant at this stage, however LC3BII in DM-SOD1-EGFP was borderline significant (p= 0.0593). These results suggest autophagy had been marginally upregulated in MG132 treated cells and the LC3BII/LC3BI ratios imply it was functional.

Analysis of LC3BII in EVs produced from these cells (Figure 5-22B) showed there was an increase in the average percentage of the protein by 50% and 60% from WT- and DM-SOD1-EGFP cells, however these changes were not statistically significant. It was noted that LC3BII in DM-SOD1-EGFP transfected EVs was bordering on significance (p= 0.0687). There was no difference in the change between genotypes.

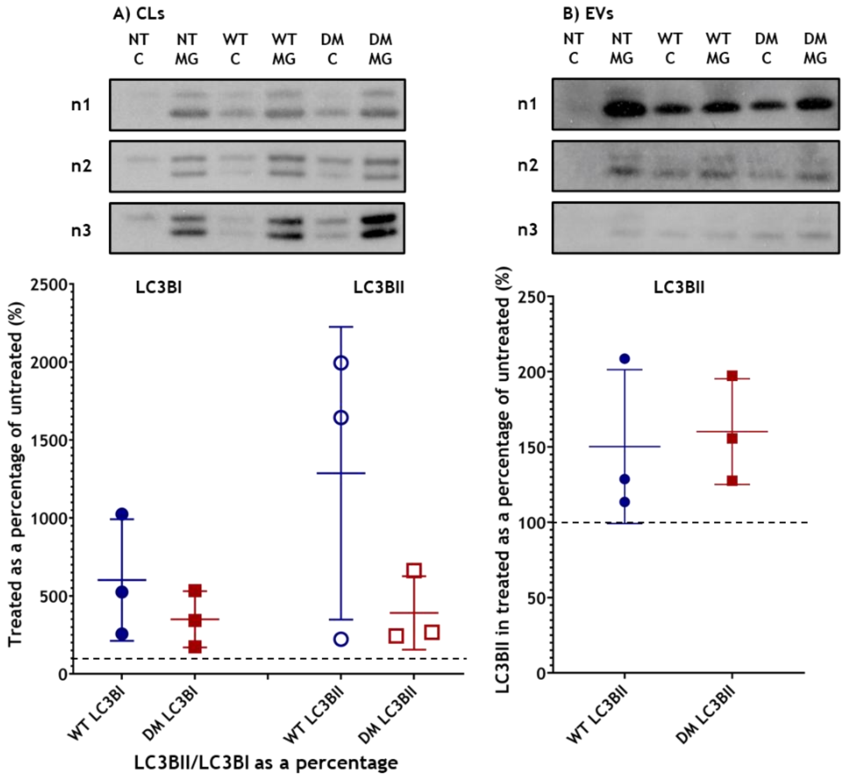

LC3BII/LC3BI as a percentage

WT Con	WT MG132	DM Con	DM MG132
78.6 ± 55.6%	110.2 ± 19.0%	101.0 ± 54.7%	102.5 ± 12.4%

Figure 5-22: MG132 treatment effect on LC3B in CLs and EVs. A) LC3BI and II were clearly visible in CLs from control and treated cells (*n*= 3) so the bands were quantified, expressed as a percentage of treated over untreated and plotted in the graph. The LC3BII/LC3BI ratios were calculated and are presented in the table (mean ± SD). **B)** Only LC3BII was clearly visible in EVs (*n*= 3), so only LC3BII was quantified and expressed as a percentage (treated over untreated), then plotted in the graph. The dotted lines represent 100%.

5.4.6 The effect of three centrifugation steps on EVs

MG132 and CQ treatment experiments were repeated and EVs were isolated with an additional intermediate centrifugation step. MG132 significantly increased WT- and DM-SOD1-EGFP in transfected cells by 157% ($p \leq 0.01$) and 239% ($p \leq 0.05$) respectively while CQ increased SOD1-EGFP by 110% ($p \leq 0.05$) and 126% ($p \leq 0.05$) respectively (Figure 5-23A and D). These increases were likely to be caused by lack of clearance of the protein due to inhibited pathways. There were no statistically significant differences between genotypes or treatments. MG132 reduced flotillin-1 by 42% ($p \leq 0.01$) and 30% and CQ reduced the protein by 12% and 13% in WT- and DM-SOD1-EGFP transfected CLs respectively (Figure 5-23B and E). The reductions may reflect some cell loss however actin levels were consistent between CLs (Figure 5-23C), so flotillin-1 levels may reflect changes to the plasma membrane/lipid raft composition. There were no statistically significant differences between genotypes or treatments.

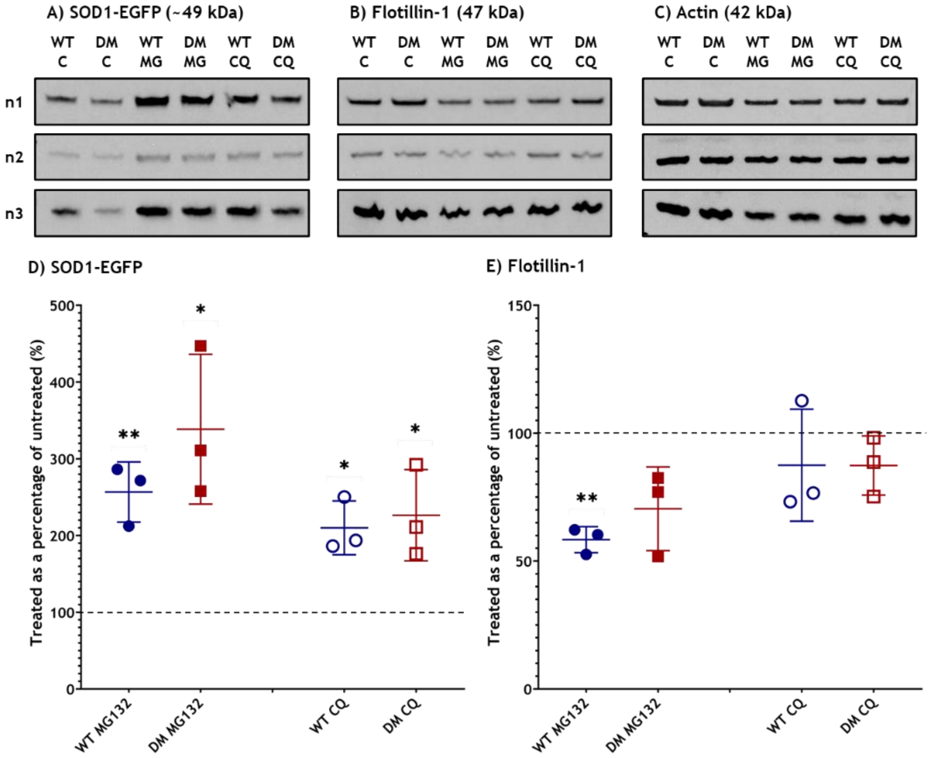

Figure 5-23: Comparison of SOD1-EGFP and flotillin-1 in CLs after CQ or MG132 treatment. **A)**, **B)** and **C)** show WBs for SOD1-EGFP, flotillin-1 and actin in CLs for control, CQ and MG132 treated samples. Protein concentration= 10 µg. The graphs contain the results from all three CL preparations (*n*= 3) when probed with GFP **(D)** or flotillin-1 **(E)**. Ordinary one-way ANOVA with Bonferroni multiple comparisons test was used to compare protein levels between genotype and the treatment. Ratio paired t-tests were used to compare control and treated samples. The midline represents the mean. Dotted lines= 100%. $^*p \leq 0.05$; $^{**}p \leq 0.01$.

The same proteins were also investigated in EVs produced from these cells that had been collected after 10,000 *xg* and 110,858 *xg* (Figure 5-24). The MG132 or CQ treated values for the 10,000 *xg* and 110,858 *xg* fractions were expressed as a percentage of the 10,000 *xg* or 110,858 xg DMSO control fractions. In the WT-SOD1-EGFP 10,000 *xg* and 110,858 *xg* EVs from cells treated with CQ, there was an average increase of 181% and 522% compared to controls while DM-SOD1-EGFP EVs were increased by 190% and 721% in the same fractions (Figure 5-24C). In the 110,858 *xg* fraction of WT-SOD1-EGFP cells, there was significantly more SOD1-EGFP in the fraction from CQ treated WT-SOD1-EGFP transfected cells than untreated cells ($p \leq 0.01$). There were no apparent differences between genotypes. The differences could indicate that surplus SOD1-EGFP is associated with the 110,858 *xg* more than the 10,000 *xg* fraction after CQ treatment, but statistics with a sample number of three do not fully support this. Flotillin-1 from the same WT-SOD1-EGFP EV fractions was increased by 25% and 292% and from DM-SOD1-EGFP EV fractions, it increased by 76% and 183%. There were no statistical differences observed at this stage, however the average changes may suggest the EV pathway, especially the small EV/exosome pathway (EVs from 110,858 *xg* fraction) in transfected cells, may be upregulated (Figure 5-24C) and may be associated with SOD1-EGFP.

After MG132 treatment, SOD1-EGFP was decreased in the 10,000 *xg* fraction from WT-SOD1-EGFP cells by 3% and increased in DM-SOD1-EGFP cells by 125% (Figure 5-24D). For the 110,858 *xg* fraction, WT- and DM-SOD1-EGFP was increased by 116% and 193% respectively. Flotillin-1 on the other hand was reduced in both fractions from both genotypes as follows: WT-SOD1-EGFP 10,000 *xg*= 73%; DM-SOD1-EGFP 10,000 *xg*= 73%; WT-SOD1-EGFP 110,858 *xg*= 83%; DM-SOD1-EGFP 110,858 *xg*= 84% (Figure 5-24D). There were no statistically significant changes between untreated and MG132 treated cells, and there were no differences between genotypes. The mean differences suggest MG132 markedly reduced the production of EVs from cells and that SOD1-EGFP in this fraction may be associated with vesicles and found as free aggregates.

Statistics were also retrieved between treatments and showed there was a significant difference in flotillin-1 in WT- and DM-SOD1-EGFP 110,858 *xg* fractions when treated with MG132 and CQ (WT-SOD1-EGFP MG132 vs CQ $p \leq 0.05$; DM-SOD1-EGFP MG132 vs CQ $p \leq 0.05$). Actin levels were lower in the EV fraction of all samples compared to respective controls (Figure 5-24E). A representative Ponceau S stained blot is presented in Appendix 8.3.3.2.

Combined, the results suggest EV production is generally reduced after proteasome inhibition and increased after autophagy inhibition. SOD1-EGFP appears to be associated with EVs, particularly from control and CQ treated cells, but after MG132 treatment of cells, free SOD1-EGFP may be the main constituent of the fraction.

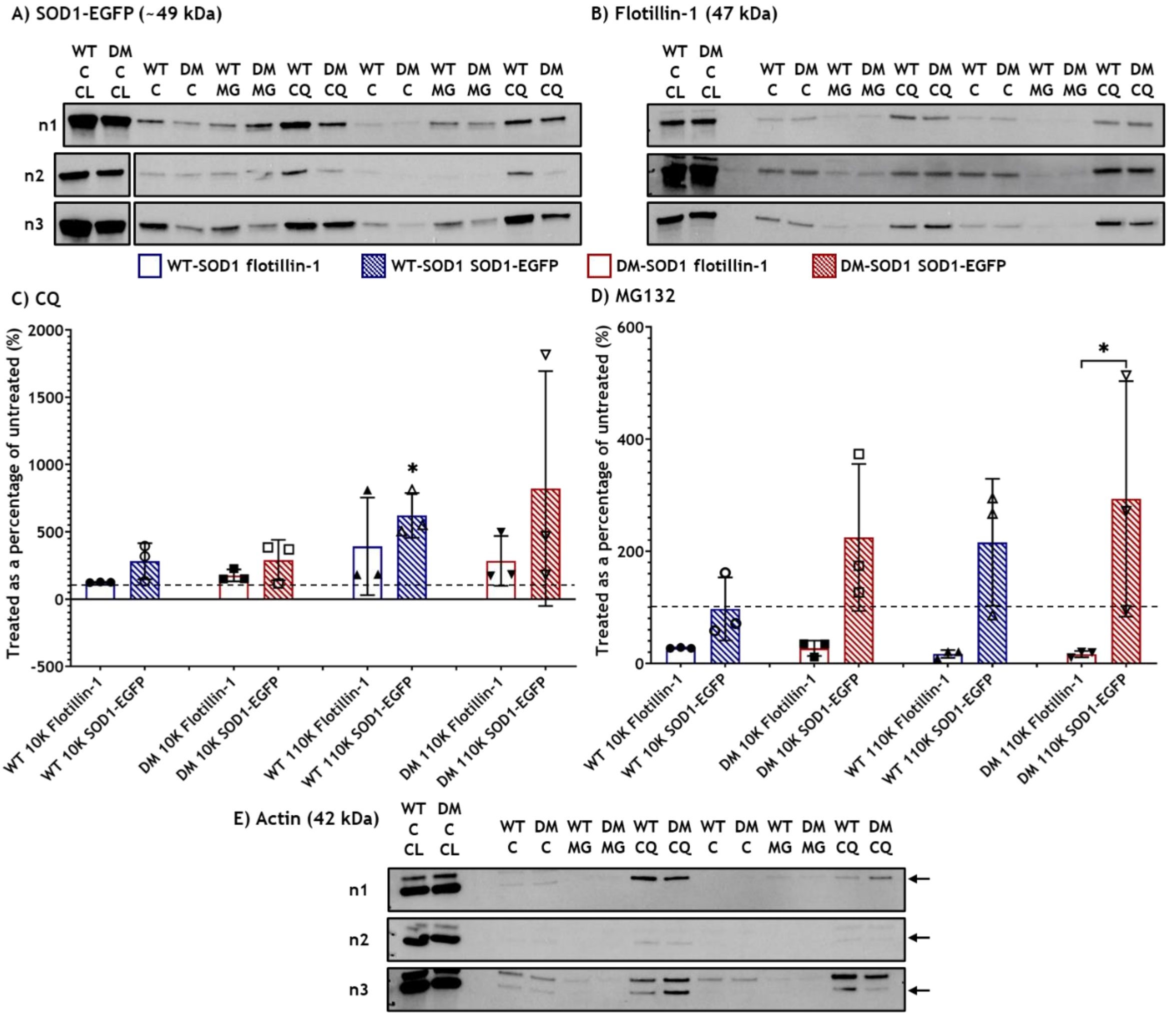

Figure 5-24: Comparison of SOD1-EGFP and flotillin-1 in EVs isolated using three centrifugation steps after CQ or MG132 treatment of cells. A) and **B)** show WBs for SOD1-EGFP and flotillin-1 in EVs respectively after 10,000 *xg* (10K) and 110,858 *xg* (110K) spins for control, CQ and MG132 treated samples. Protein concentration= 5 µg. An extra well was left empty between CLs and EVs for n2 and n3 GFP blots but not n1, so n2 and n3 blots were cropped to remove the extra well for labelling purposes. Full blots are presented in Appendix 8.3.3.9. The graphs contain the results from EV preparations when probed with GFP (*n*= 3) or flotillin-1 (*n*= 3) for CQ (**C**) and MG132 (**D**) studies. The midline represents the mean. Kruskal-Wallis with Dunn's multiple comparison test was used to compare genotypes, centrifugation steps and protein. To compare treated with untreated, Wilcoxon matched-pairs signed rank tests were used. Dotted lines= 100%. **E)** shows three blots that were originally probed with anti-flotillin-1 and were reprobed with anti-actin. The arrow points to actin as residual flotillin-1 could still be seen in some samples.

5.5 Discussion

5.5.1 Effect of autophagy inhibition on SOD1-EGFP processing

Cellular SOD1-EGFP was significantly increased after autophagy inhibition and the increase was more profound in the DM-SOD1-EGFP transfected CLs compared to WT-SOD1-EGFP transfected CLs. When aggregates were assessed, only DM-SOD1-EGFP showed significantly more aggregation compared to controls. ALS studies have shown that mutant SOD1 is more likely to be an autophagy substrate than WT-SOD1 (Renna *et al.*, 2010), suggesting mutant SOD1 could accumulate in autophagosomes. As autophagy was inhibited at the level of autophagosome-lysosome digestion, this could lead to the significant increase in DM-SOD1-EGFP aggregates and not WT-SOD1-EGFP aggregates. Undigested autophagosomes and autolysosomes are associated with insufficient autophagy clearance and are accompanied by reduced formation of new autophagosomes, indicating there is a negative feedback loop (Baron *et al.*, 2017). This loop may be dysfunctional in cells expressing mutant SOD1. One potential suggestion for this dysfunction could be the interaction between mutant SOD1, LC3 and p62. p62 can interact with and sequester various ALS associated SOD1 mutants in inclusions and it can interact with LC3 suggesting it acts as a selective adapter protein between mutant SOD1 and autophagy. p62 can bind to polyubiquitinated proteins and to mutant SOD1 directly (Gal *et al.*, 2009) and can accumulate when autophagy (or the proteasome) is inhibited and when mutant SOD1 is present. Onesto *et al* (2011) found mutant SOD1 caused the blockage of autophagic flux as indicated by increased LC3 and p62. Furthermore, p62 has been found to accumulate in DM spinal cords leading to the suggestion that autophagy flux is perturbed in DM (Ogawa *et al.*, 2015).

EV secretion appeared to be upregulated in WT-SOD1-EGFP transfected cells but not DM-SOD1-EGFP transfected cells which raised the possibility that the EV pathway was upregulated in WT-SOD1-EGFP transfected cells by increasing the fusion of MVBs to the plasma membrane to secrete EVs rather than with lysosomes (Jahangiri *et al.*, 2022; Xu, Camfield and Gorski, 2018). WT-SOD1-EGFP levels in the EV fraction were not significantly different from untreated controls suggesting alternative pathways may have been utilised to prevent accumulation and aggregation of SOD1, and/or proteins were prevented from misfolding. It is therefore suggested that the presence of the *Sod*1 mutation restricted the use of alternative pathways for clearance. Many alternative pathways are proposed to be utilised by cells when autophagy is deficient including, but not limited to, non-canonical Golgi membrane associated degradation (Baron *et al.*, 2017), LC3-dependent EV loading and secretion (Leidal and Debnath, 2020), exophagy (Ejlerskov *et al.*, 2013), chromogranin-mediated exocytosis (Urushitani *et al.*, 2006) and karyoptosis (Baron and Fanto, 2018), a novel cell death mechanism that results from inhibited autophagy.

In the current study, LC3B was increased in the EV fraction from transfected cells so it is possible that these components were incorporated into EVs, or they may represent independent clearance pathways, all with the aim to reduce the overall load on cell protein processing pathways. LC3 enrichment has been associated with EVs in other studies, but LC3 (specifically LC3BII) can be secreted from cells independently. LC3BII was found by Leidal and Debnath (2020) to be enriched within a subset of intraluminal vesicles (ILVs) in MVBs indicating that 1) there is a population of EVs likely to be mediated by LC3 and 2) EVs represent a heterogenous population of vesicles from different pathways. They found that disruption to the components involved with LC3-conjugation resulted in a reduction in LC3 and EV production. As a result, the authors suggest a novel pathway is utilised by cells and named it LC3-dependent EV loading and secretion (LDELS)(Leidal and Debnath, 2020). This alternative pathway provides a possible explanation for the changes observed in the current study.

In neurones, autophagosomes are often formed in axons due to the high turnover of proteins at synapses for example, while lysosomes are mainly found in the cell body of the neurone. It is thought amphisomes are therefore formed between autophagosomes and MVBs to aid transport of the cargo to lysosomes (Cai and Ganesan, 2022). It has been found in a model of Parkinson’s disease that pathological monomeric and oligomeric forms of α-synuclein protein could be secreted from cells in association with amphisomes by a secretion pathway called exophagy where amphisomes fuse with the plasma membrane. Exophagy appears to be separate from exosome secretion and may be induced by disruption to lysosomal fusion/degradation (Ejlerskov *et al.*, 2013). Together these findings indicate that the *Sod*1 mutation may cause aberrant interactions with other proteins that may be important for the induction of alternative protein processing pathways.

Ubiquitination was marginally increased after autophagy inhibition in transfected cells and was similar between WT- and DM-SOD1-EGFP transfected cells, suggesting this pathway did not appear to play a significant role in SOD1-EGFP specific processing. Nevertheless, the results suggest the UPS is upregulated when autophagy is inhibited, however there was ubiquitin present in EVs suggesting the system was overwhelmed.

There appeared to be a reduction in cell density after CQ treatment, but this was not caused by ER stress induced apoptosis. At the stage of cell death in the experiments, it is likely programmed cell death type II was the cause of cell loss (Ogawa *et al.*, 2015). The changes in cellular morphology and cell loss were not obviously different between plasmid genotype, however cell viability studies were not carried out so a comparison between genotypes could not be made. The microscopic observations of cells and EVs produced by cells with autophagy inhibition suggested a novel cell death pathway may be utilised. Karyoptosis is proposed to be associated with microvesicles (MVs) that bud from cells when autophagy is defective and other pathways are insufficient to reinstate homeostasis. These MVs, enriched in lamin B1, p62 and LC3, are present at low levels when autophagy is functional. When autophagy is chronically inhibited, nuclei morphology, cytoplasm disorganisation and DNA damage occur and lamin B1 accumulates and associates with cytoplasmic and nuclear components (originally destined for autophagy or not) which are subsequently secreted as MVs (Baron and Fanto, 2018). To better understand cell viability, assays including MTT or TUNEL could be conducted to quantify cell loss and rule out death by apoptosis.

With an additional centrifugation step included to refine EV isolation, there were no significant differences in EV production between untreated and treated cells or between genotypes. It is possible that with two centrifugation steps, more EVs were collected and, as there were differences in the original initial centrifugation speeds (110 xg vs 800 xg), cellular contamination may have been present, falsely increasing the apparent EV population (Théry *et al.*, 2018). There was also a difference in sample number with the three-step centrifugation experiment only having *n*= 3 rather than *n*=5 or more. There was an upwards trend in WT-SOD1-EGFP in the EV fraction of both experiments, but it only reached significance in the high-speed spin. This suggests EVs with a smaller diameter, for example exosomes, were upregulated more than EVs of a larger diameter, for example MVs. These findings taken together support the hypothesis that alternative pathways (flotillin-1 dependent or independent) were recruited to dispose of WT-SOD1-EGFP when autophagy was induced, but this may have been defective for DM-SOD1-EGFP removal. Effect of proteasome inhibition on SOD1 processing

Proteasome inhibition significantly increased the level of SOD1-EGFP in CLs and this was reflected by a significant increase in the percentage of cells with WT- and DM-SOD1-EGFP aggregates. Other *in vitro* cell culture studies of DM have found alterations in the proteasome pathway led to increased aggregation of mutant SOD1 (Nakamae *et al.*, 2015). Previous studies of human mutant SOD1 in a MN cell line found mutant SOD1, but not WT-SOD1, accumulates in resting conditions with limited activation of autophagy leading authors to suggest the proteasome may be important for the processing of mutant SOD1. After treatment with MG132, both WT and mutant SOD1 presented with increased aggregation (Onesto *et al.*, 2011).

The total protein profile of CLs showed there was a protein at 62 kDa in cells with proteasome inhibition that was not present in any other sample in this study. Based on the molecular weight and conditions, it could be suggested that this protein is p62. p62 can bind to ubiquitinated proteins and direct them to the autophagy pathway. The protein has been found to be upregulated in the presence of proteasome inhibitors and it is thought that the expression of this protein initiates autophagy when the proteasome pathway is overwhelmed. The protein is thought to sequester ubiquitinated proteins in vesicles before they are degraded (Sha *et al.*, 2018) and this could also explain the morphology of aggregates in cells treated with MG132. Looking at LC3B, autophagy appeared to be upregulated, however changes to this pathway were marginal again raising the possibility that alternative pathways, discussed for autophagy inhibition, were employed.

Despite EVs appearing to be downregulated after proteasome inhibition, there were significant increases in WT- and DM-SOD1-EGFP in the EV fraction. When the proteasome of embryonic fibroblasts transfected with human WT or mutant SOD1 was inhibited, an increase in SOD1 secretion to the media was also observed (Urushitani *et al.*, 2006). In the present study, further assessment of the EV fraction found small and large EVs were downregulated after proteasome inhibition and SOD1-EGFP was associated with the pellet after moderate- and high-speed centrifugation. LC3BII showed an upwards trend in the EV fraction but only approached statistical significance for DM-SOD1-EGFP (p= 0.0687). Nevertheless, it indicates LDELS (LC3-dependent EV loading and secretion) was potentially recruited by cells to reduce the strain of proteasome inhibition on autophagy machinery. The significant increase in DM-SOD1-EGFP aggregates compared to WT-SOD1-EGFP when the proteasome is inhibited may suggest that these alternative pathways are more efficient when SOD1 is in the WT conformation and less effective when the *Sod*1 mutation is present.

Cell morphology and density when the proteasome was inhibited showed cell death occurred, however *XBP1s* was found at low levels and is not likely to explain all cell death. Morphological changes were similar to that of autophagy inhibition rather than widespread protein misfolding in the treated cells when cells were analysed/harvested. The increased levels of *BiP* imply there was ER stress, so it is possible that the apoptosis pathway was triggered and, had the cells been harvested at a later stage, apoptosis may have been the main cell death pathway initiated. There were no clear indications that one SOD1-EGFP genotype affected these processes more than the other. A cell viability assay (MTT or TUNEL) could be useful here to assess the quantity of dead/dying cells in culture. Further, TUNEL assays in particular would be able to determine if apoptosis was present. Additionally, it should be noted that some caution is required when using a multiplex PCR, as was performed with *BiP* and *GAPDH*, as the reaction can run short of nucleotides, potentially influencing results. In the current group of experiments, and the other *in vitro* culture experiments reported, the intensity of *BiP* and *GAPDH* bands did not appear to vary considerably, except for those that were treated with MG132 (and DTT), so nucleotide shortages were not likely to be an issue. Free SOD1 aggregates can be secreted from dead and dying cells and can be collected after high-speed centrifugation (Hanspal *et al.*, 2017; Silverman *et al.*, 2019; Théry *et al.*, 2018), so it is possible that the SOD1-EGFP found in the fraction were produced from overwhelmed, dying and dead cells.

Flotillin-1 is a protein found in cell membranes associated with EVs and lipid rafts. Lipid rafts are microdomains found in the plasma membrane of cells that are enriched in lipids (specifically cholesterol and sphingolipids) and various proteins, including flotillin-1. Lipid rafts are involved with the physical interactions between neurones and glia, the endosomal pathway and cellular signalling (Zhai *et al.*, 2009). This set of experiments appeared to show that proteasome inhibition may have an impact, albeit mild, on the incorporation of proteins (including flotillin-1) into lipid rafts/plasma membranes, so it could be surmised that proteasome inhibition affects lipid rafts and this could compromise the EV pathway. Lipid rafts are involved with the formation of several vesicles including those of the endosome pathway and many subtypes of EVs. Disruption to protein or lipid constituents of lipid rafts can affect the secretion of vesicles (Sapoń *et al.*, 2023), so it is possible they play a role here. One study in the ALS field discussed the impact of disruption to an ER chaperone protein called SigR1 and found changes in ER morphology, induction of ER stress, defective calcium regulation and cell death. Mutations in the *SigR1* gene have been found to worsen the progression of the ALS phenotype in SOD1 mutant mice which was improved when treated with SigR1 agonists. Further, SigR1 distribution has been found to be altered in sALS and fALS cases. Downregulation of SigR1 can lead to autophagosome accumulation and defective autophagosome-lysosome fusion. Additionally, reduction of SigR1 can lead to lipid raft disorganisation which can have a negative impact on vesicular pathways causing aberrant accumulation of vesicles within MVBs, defects in the transport of vesicles from the ER to Golgi apparatus, changes to endosomal sorting, MVB formation and the movement of endosomes to lysosomes. In addition to endosome pathway disruption, destabilisation of lipid rafts can have negative effects on calcium regulation. Lipid rafts regulate many Ca^{2+} channels and knockdown of SigR1 was found to disrupt these rafts and caused disruption to Ca^{2+} regulation. SigR1 normally interacts with BiP but when Ca^{2+} levels are reduced in the ER, the proteins dissociate from each other. This results in increased Ca^{2+} signalling to the mitochondria. Ca^{2+} intracellular signalling within neurones is perturbed in many neurodegenerative diseases including ALS. Neurones are sensitive cells so even mild changes to Ca^{2+} levels can lead to long term cellular damage (Vollrath *et al.*, 2014).

5.5.2 Widespread protein misfolding, ER stress and protein processing

DTT is a reducing agent that disrupts protein processing by preventing the formation of disulphide bonds inside and between proteins and has been used in various studies to investigate protein folding and processing pathways after nonspecific ER stress induction (Oslowski and Urano, 2011; Tiwari and Hayward, 2005). In the current study, DTT treatment increased the percentage of cells with SOD1-EGFP aggregates significantly. As previously described (Section 1.4.1), SOD1 has a disulphide bond that is integral to the proper folding of the protein, thus DTT could have a direct impact on SOD1 folding and aggregation. DTT could also have an indirect affect by causing mass protein misfolding and inducing ER stress which also impacts protein processing. ER stress induction was confirmed in treated cells therefore it is likely that DTT enhanced the misfolding and aggregation of SOD1 in WT- and DM-SOD1-EGFP transfected cells and, combined with the misfolding of other proteins, induced ER stress leading to apoptosis. TUNEL assays were not carried out to confirm the presence of apoptosis, however they would be of value to confirm this hypothesis in the future.

While there was an increase in the density of WT- and DM-SOD1-EGFP aggregates after DTT treatment, WBs did not reflect this. This could be explained by the insoluble nature of SOD1 aggregates: insoluble SOD1 aggregates may not be lysed by lysis buffer and therefore may be restricted to the pellet fraction during sample processing (Section 2.4.1.3). As the supernatant is the fraction used for protein studies, it is possible soluble SOD1 was the main type investigated. Crisp *et al.*, (2013) found soluble SOD1 was comparable between control and DM samples but insoluble SOD1 in the pellet fraction increased in DM samples. Alternatively, it is possible that the same quantity of SOD1-EGFP was present in control and treated cells, but the misfolded conformation may be dominant in treated cells whereas the native form may be the dominant form in untreated cells (Onesto *et al.*, 2011). Although SOD1 aggregation was significantly enhanced in WT- and DM-SOD1-EGFP DTT treated cells compared to controls, there were no significant differences in the number of SOD1-EGFP aggregates or the level of the protein between WT- and DM-SOD1-EGFP transfected CLs, with or without DTT treatment.

Flotillin-1 was reduced in CLs after DTT treatment, but only significantly in DM-SOD1-EGFP CLs. This could suggest a change in the incorporation of flotillin-1 into the plasma membrane/lipid rafts and EVs, or it may reflect overall disruption of lipid rafts, potentially because of direct disruption to proteins or due to disruption to the pathways leading to lipid raft incorporation. SOD1 has been associated with lipid rafts on multiple occasions and it has been suggested that interactions between lipid rafts and aggregated mutant SOD1 could impact the various pathways lipid rafts are involved in (Zhai *et al.*, 2009). Further, post translational modifications of flotillin-1 can affect the cellular location of the protein: palmitoylation (addition of palmitic acid) is vital for the translocation of flotillin-1 out of the ER to the plasma membrane while SUMOylation (addition of SUMO proteins) translocate the protein from the ER to the nucleus. If palmitoylation is deficient, flotillin-1 cannot leave the ER and therefore accumulates (Jang *et al.*, 2019).

The apparent reduction in EV production when ER stress is induced contrasts the finding that stress is often associated with increased EV (specifically exosome) production (Hessvik and Llorente, 2018). It is possible that, as a result of disruption to the EV pathway, MVBs (containing ILVs which become exosomes) fused with autophagosomes to form amphisomes that were subsequently digested by lysosomes more than being fused to the plasma membrane and released as exosomes (Jahangiri *et al.*, 2022). Autophagy flux appeared to be increased in the presence of DTT although it was only significantly upregulated in DM-SOD1-EGFP transfected cells. As widespread protein misfolding, the UPR and ER stress were present, it is likely autophagy was upregulated by several mechanisms including the UPR, as suggested by the general upwards trend in *XBP1t* (Jahangiri *et al.*, 2022). SOD1-EGFP was reduced in the EV fraction after

treatment suggesting it was processed by alternative pathways, for example autophagy. The resultant accumulation of WT- and DM-SOD1-EGFP aggregates within cells indicate these pathways may have been overwhelmed and were not able to process all misfolded SOD1/proteins before SOD1 aggregates formed.
SOD1 activity

Using the native gel SOD activity assay, ER stress appeared to be the main contributor to reduced SOD activity in CLs while autophagy inhibition appeared to increase activity in the fraction. Activity in WT-SOD1-EGFP transfected EVs was generally maintained in untreated cells, however induction of ER stress appeared to reduce activity while autophagy inhibition maintained it. DM-SOD1-EGFP EVs were less consistent as on some occasions, activity was not observed in untreated EVs, while on other occasions, it was present. It is possible that DM-SOD1-EGFP levels were absent because it is not incorporated into EVs as easily as WT-SOD1, as suggested in ALS studies (Gomes *et al.*, 2007), so it is worth pursuing this further.

The lack of SOD1-EGFP activity in EVs after ER stress induction may have several explanations; 1) there was less SOD1 in treated EVs, 2) SOD1 in EVs was dysfunctional due to changes in protein folding or 3) there were fewer SOD1 positive EVs being produced from treated cells. If extracellular SOD1 is dysfunctional or reduced *in vivo*, this could have ramifications for pathology. For example, human WT-SOD1 associated with exosomes has been found in the extracellular space of MN cell culture, suggesting SOD1 may have a role in protecting cells from free radicals in the extracellular environment (Gomes *et al.*, 2007). This implies that if SOD1 is dysfunctional outside of cells, this could lead to an eventual build-up of free radicals, resulting in oxidative stress which has been identified in DM (Ogawa *et al.*, 2011). Further assessment is required to confirm these speculations and could include the use of commercially available SOD1 activity assays.

5.5.3 Considerations and future work

The findings reported in this chapter are relevant to neurones, but other cell types may behave differently to these treatments. Neuronal ALS studies for example have found the expression of *SOD1* mutations in neurones do not induce ALS alone, so other cells must be involved in disease pathogenesis (Urushitani *et al.*, 2006). Studies with DTT, CQ and MG132 could be repeated in oligodendrocytes, microglia and astrocytes to give a more complete picture of the events occurring in the CNS environment. Further, mutant SOD1 present in the extracellular environment is thought to contribute to microgliosis and MN death in ALS (Urushitani *et al.*, 2006), so further studies could utilise co-cultures to understand the interaction between cells of the CNS. Primary mesenchymal stem cells (MSCs) from the bone marrow of a DM case submitted to the UoGSAH have recently been cultured by Mohammad Ghasemzadeh Hasankolaei and MM. These cells have the potential to be differentiated into neuronal and glial cells and express endogenous mutant SOD1. This will allow for better investigation of pathways and SOD1 activity and would also allow for investigation of multiple pathways concurrently. This would be beneficial to see if SOD1 aggregation and SOD1/EV secretion is changed after the subsequent inhibition or activation of other pathways. These studies would allow the investigation of the progression of DM as current literature suggests multiple pathways interact to cause the pathology and clinical signs, and it could help to develop treatment options.

Cellular stress is thought to play role in DM *in vivo* (Yokota et al., 2018) however in the current study using the *in vitro* cell culture system, the DM *Sod*1 mutation failed to induce ER stress independent of treatments implying that other factors may be involved. The temporal relationship between specific pathway disturbances and protein processing could have an impact on various aspects of the study. Cells potentially needed to be exposed to pathway disrupting drugs for a prolonged period of time to induce suspected ER stress, given that DM *in vivo* can progress over a period of months or years. As MSCs already express the mutant SOD1, this could potentially allow for longer term experiments as it removes the need for a transfection step.

5.6 Conclusions

The key changes in this chapter are presented in Table 5-1. Overall, inhibition of the autophagy pathway appeared to have a more significant effect on the processing of DM-SOD1-EGFP compared to WT-SOD1-EGFP. The endosomal pathway appeared to be important for the processing and secretion of SOD1-EGFP through flotillin-1 associated, LC3 associated and amphisome pathways, however the presence of the DM associated *Sod*1 mutation appeared to interrupt the efficiency of these pathways, potentially because of aberrant protein-protein and/or protein-lipid interactions.

The general conclusion reached after proteasome inhibition was that SOD1-EGFP appears to be released from cells, however the EV pathway may not be the main means of secretion of the protein as it was generally downregulated after proteasome inhibition. This may be a consequence of disruption to plasma membranes/lipid rafts. Results further suggest that the autophagy pathway was employed, however alternative pathways may have been predominantly utilised. Alternative pathways may have been more functional in WT-SOD1-EGFP cells compared to DM-SOD1-EGFP transfected cells as there were significantly more aggregates in DM-SOD1-EGFP transfected cells compared to the WT-SOD1-EGFP cells after proteasome inhibition. All of these factors may have contributed to ER stress and the UPR appeared to be in the early stages of initiation.

Nonspecific induction of ER stress suggests widespread protein misfolding causes disruption to plasma membranes or lipid rafts of cells expressing DM-SOD1-EGFP and this may influence downstream processes including the formation and/or production of EVs. This appears to impact the processing of DM-SOD1-EGFP as it aggregates in cells and may not be incorporated well into EVs. The action of widespread protein misfolding does not appear to impact WT-SOD1-EGFP transfected cells as significantly thus indicating the *Sod*1 mutation makes cells more susceptible to protein processing disruption, at least at the level of EVs.

	CQ		MG132		DTT	
Action	Autophagy inhibitor		Proteasome inhibitor		Reducing agent	
SOD1 genotype	**WT**	**DM**	**WT**	**DM**	**WT**	**DM**
BiP expression	ns	ns	↑**	↑**	↑**	↑*
ER stress induced?	No	No	Yes	Yes	Yes	Yes
CL flotillin-1	ns	ns	ns	ns	ns	↑*
CL SOD1-EGFP	ns (↑†)	ns (↑†)	↑*	↑*	ns	ns
EV flotillin-1	↑**	ns	↓**	ns (↓†)	ns	ns (↓†)
EV SOD1-EGFP	ns	ns	ns (↑†)	↑**	ns (↓†)	ns (↓†)
SOD1 aggregation	ns	↑**	↑****	↑****	↑**	↑**

Table 5-1: Summary of the effect of treatment in cell culture. Presented in the table are the key findings in CLs and EVs after treatment of cells with CQ, MG132 and DTT. Only the changes observed after two centrifugation steps are presented as all three treatments were used. $^{*}p \leq 0.05$; $^{**}p \leq 0.01$; $^{***}p \leq 0.001$; $^{****}p < 0.0001$; † indicates changes were borderline significant.

Combined, this study highlights that multiple protein processing pathways are likely to be influenced by the presence of the *Sod*1 mutation and progression of DM is likely to reflect a cascade of changes to these pathways.

6 *Ex vivo* assessment of DM spinal cord proteins

6.1 Background

As previously discussed, DM is presumptively diagnosed antemortem by ruling out other causes of clinical signs using neurological examination, blood and CSF tests and MRI. Genetic tests for mutations in the *Sod*1 gene are used to rule in DM as a cause of clinical signs. DM is definitively diagnosed post-mortem by histopathological examination of the spinal cord where lesions associated with axon degeneration and demyelination are observed. Currently, there are no specific biomarkers used for DM, but this is a common goal amongst many researchers as biomarkers allow for reliable and early detection of disease and the monitoring of disease progress. To identify reliable biomarkers, a greater understanding of the disease mechanisms and processes is required, and this can also advance treatment discovery. As the CNS is a heterogenous mixture of cells and components which interact and contribute to DM, it is difficult to reproduce the minutiae of the complex environment. Additionally, the CNS is difficult to sample with CSF being the most direct means of assessment. Unfortunately, the retrieval of a CSF sample is relatively invasive, so steps to find a marker from blood is the goal (Pfeiffer *et al.*, 2023).

Omics technologies including, but not limited to, proteomics, metabolomics and lipidomics can help to understand different cells and pathways in cells as taken together, they give a fuller picture. The genome, transcriptome, proteome and metabolome interact to perform an array of biological processes, and this can be referred to as the interactome. In addition to environmental factors, these elements cooperate to form a phenotype (Tan *et al.*, 2016). Omics technologies are used to understand the structure and dynamics of the different cellular biomes and provide an avenue to quantify different components including transcripts, proteins, metabolites and lipids (Addepalli and Mullangi, 2020). For example, a faulty enzyme (protein) can influence the metabolism or formation of metabolites and lipids. Many proteins and lipids are vital for the normal functioning of the CNS as they make up a significant proportion of the system. Hundreds of proteins, metabolites and lipids can be highlighted by omics technologies so sophisticated bioinformatic techniques are used to give a thorough understanding of how the different products link. In this thesis, basic investigations were carried out on selected proteins that had relevance to CNS cells, clearance and toxicity pathways and EVs. Some non-cell type specific markers have already been discussed in previous chapters, but additional cell type specific and neurodegenerative markers will be introduced in this section.

6.1.1 The proteome

The proteome is a vast network of proteins that interact with each other and other molecules to ensure homeostasis is maintained within cells and organisms. As discussed extensively in other chapters, proteins have various roles including, but not limited to, intra- and extracellular signalling, the transport of molecules across the plasma membrane and the maintenance of functional proteins. The study of complex proteomes has become more accessible as technology has improved the resolution and timescale of results from samples. In addition to protein identification and quantification, proteomics can be used to investigate interactions between various proteins. A further benefit of proteomics is that it allows for investigation of post translational modifications (PTMs) of proteins including phosphorylation, acetylation, methylation and ubiquitination, modifications that can increase the number of functions associated with proteins (Hedl *et al.*, 2019). Mass spectrometry (MS) is often used as it can analyse samples quickly with high specificity and sensitivity while using a minimal amount of sample. The limitations of using MS for omics studies are that it is expensive and generates large datasets that often need expert guidance (Yang *et al.*, 2019).

6.1.2 Summary of common omics techniques

Many proteomics techniques can be used to assess proteins in a sample. As liquid chromatography-MS (LC-MS) was the main method used here, it will be further described. Initially, proteins are enzymatically digested into peptides by proteases then separated by LC. Peptides are separated in liquid conditions which allow all peptides in a sample to migrate at different velocities, meaning each component will take a different amount of time to travel from the inlet to the detector of the machine. This is termed the retention time and is unique to each component of a sample. Chromatography is utilised for its sensitivity and results in better molecule identification. Peptides are eluted from the LC membrane, then ionised by adding or removing protons into a MS and analysed. MS uses the mass-to-charge ratio (m/z) of ions in a sample which is converted to peaks to determine the molecular weight of peptides in a sample. Peptides can be further assessed by additional fragmentation in tandem MS (MS/MS). Sequenced peptides are compared to protein databases to identify corresponding proteins (Hedl *et al.*, 2019; Tan *et al.*, 2016).

To undertake a quantitative analysis of proteins within samples, peptides can be labelled after protease digestion with stable isotopes using the Tandem Mass Tag (TMT) system. Multiple samples to be compared are labelled separately, then pooled together and fractionated before being analysed by MS. TMT allows MS to compare identical peptides from the various samples as reporter ions present in the system allow conversion of TMT signal intensity to peptide quantity (Hedl *et al.*, 2019).

6.1.3 Cell specific markers

Neurone specific enolase (NSE), specifically γ-enolase, is an enzyme involved in glycolysis that can be used as a maker for all neurones in the CNS and PNS. NSE can also provide information on the metabolism within neurones and is used as a serum and CSF biomarker for several cancers and other brain related diseases and injuries (Isgrò, Bottoni and Scatena, 2015). Neurofilaments are structural proteins found in neurones and are conserved between humans and dogs. Two subunits, neurofilament heavy chain (NfH) and neurofilament light chain (NfL), are abundant in axons and their presence in the CSF, serum or plasma has been associated with injury and disease in the CNS and are likely to result from neurone degeneration and axonal damage (Panek *et al.*, 2020; Toedebusch *et al.*, 2017). Phosphorylated NfH is being investigated as a serum and CSF biomarker of canine spinal cord injury and human ALS and has been reported to be elevated in DM CSF compared to age matched controls (Toedebusch *et al.*, 2017). NfL in plasma is associated with aging and has shown promise as a biomarker for ALS. In DM and other neurodegenerative diseases, NfL levels have been reported to be even higher compared to age matched controls (Panek *et al.*, 2020).

Myelin is a lipid rich component produced by oligodendrocytes in the CNS and is composed of multiple proteins including proteolipid protein (PLP) and its smaller DM20 isoform, myelin basic protein (MBP), myelin oligodendrocyte glycoprotein (MOG) and myelin associated glycoprotein (MAG) (Traiffort *et al.*, 2021). PLP/DM20 is a major myelin protein that accounts for approximately 50% of proteins in the structure. DM20 is the dominant isoform present in the early stages of myelin formation while PLP is the dominant isoform later in development. The main function of the PLP/DM20 transmembrane protein is thought to be maintenance of the integrity of compact myelin. MBP constitutes approximately 30% of myelin and has multiple isoforms, several of which can be grouped into the abundant classic MBP proteins and the less abundant Golli-MBP proteins. Classic MBP proteins are associated primarily with maintenance of myelin structure while Golli-MBP proteins can be found in oligodendrocytes and neurones and have many roles in the immune system and can help to facilitate process/neurite outgrowth (Campagnoni and Skoff, 2001). Oligodendrocyte processes extend to and wrap around axons while leaving unmyelinated areas called nodes of Ranvier to facilitate saltatory conduction of electrical impulses (Traiffort *et al.*, 2021). Myelin interacts with axons at the paranodal region of axons where the myelin protein neurofascin 155 interacts with axonal contactin-associated protein (Caspr) and contactin-1 (Pan and Chan, 2017). In addition to their role in conduction of electrical signals, oligodendrocytes are important for maintaining axons by ensuring components essential for metabolic processes reach the axon (Traiffort *et al.*, 2021). The myelin protein 2′,3′-cyclic-nucleotide 3′-phosphodiesterase (CNP) disrupts the compact nature of myelin at the membrane to allow the diffusion of metabolites through the myelin sheath to the axon. The sources of energy, pyruvate and lactate for example, diffuse across the myelin sheath to the axon (Traiffort *et al.*, 2021).

Astrocytes also interact with axons and provide structural and metabolic support. These glial cells interact with other cells in the CNS including blood vessels, facilitating the transfer of nutrients to and from neurones. Astrocytes consist of multiple proteins including glial fibrillary acidic protein (GFAP), S100 calcium binding protein ß (S100ß) and vimentin. GFAP and vimentin are structural proteins while S100ß is a cytoplasmic protein. GFAP has various isoforms and is often found in astrocytes in the white matter while S100ß is often associated with those in the grey matter. Vimentin can be used to differentiate astrocytes in the CNS, however it can also be found in other cell types including fibroblasts, macrophages and some immune cells. GFAP and vimentin are known to increase in the CNS when neurodegeneration is present and can indicate astrocyte activation. S100ß is secreted from astrocytes and become downregulated within cells in times of cellular stress. In patients with brain injuries, this protein has been found to be elevated in the serum and may be indicative of injury severity (Jurga *et al.*, 2021). Another important function of astrocytes is to remove the excitatory neurotransmitter glutamate from the extracellular environment using excitatory amino acid transporters (EAATs) to prevent excitotoxicity in neurones as previously discussed (Section 1.4.7.2).

Microglia are the resident immune cells of the CNS and can be identified by the ionised calcium binding adaptor molecule (Iba-1) protein. This cell type has neuroprotective functions but can become neurotoxic and they have been linked to disease progression in ALS (Toedebusch *et al.*, 2018). It is therefore possible that many cell types may be involved in the disease process associated with DM.

6.2 Hypothesis and aims

This chapter was primarily focussed on validating the *in vitro* findings of this thesis using tissues from control and DM spinal cord tissue and generating future hypotheses. The specific aims of this chapter were based on the hypothesis that protein processing pathways, including autophagy and the UPS, are negatively impacted by the *Sod*1 mutation and SOD1 aggregation in DM. Furthermore, investigating changes to these pathways and cell specific markers in the cervical and thoracic spinal cord regions will help to better understand the temporal changes and disease progression in DM.

The main aims of this chapter were to:

1. Recruit, genotype and histopathologically confirm DM cases.
2. Conduct proteomic analysis on spinal cord tissues to understand the proteome in control and DM spinal cord segments and validate the *in vitro* findings regarding protein processing changes.
3. Conduct biochemical analysis on control and DM spinal cord tissue to validate and complement proteomic results.
4. Use biochemistry and proteomics to compare protein markers in cervical and thoracic spinal cord segments of control and DM dogs to determine if the segments may represent different timepoints in the DM disease process.

6.3 Materials and Methods

6.3.1 Case recruitment, diagnosis and collection

6.3.1.1 Summary of case recruitment process

An advertisement in the form of a poster/leaflet (produced by LEB; Appendix 8.2.5.1) was distributed to clients of the UoGSAH, other veterinary practices and the dog unit at Police Scotland by Catherine Stalin (CES). A webpage was also in initial stages of development by LEB but this was ultimately not published due to time constraints.

When DM was suspected after a neurological examination, owners were offered a standard clinical work-up at a significantly reduced cost. This included haematology, biochemistry of blood and CSF, a spinal MRI and out-sourced *Sod*1 genotyping (Laboklin, UK). Owner consent was imperative for any involvement in the study (Appendix 8.2.5.2) and ethical approval from The School of Veterinary Medicine Ethics and Welfare Committee was granted (application number EA10/20). If DM was presumptively diagnosed, dogs were recruited to the study and had regular check-ups at a reduced clinic fee on the condition that animals were submitted for post-mortem when euthanised. After euthanasia, several tissues were collected for histopathological, biochemical and omics investigation. Histopathological examination was conducted before further biochemical and omics investigation to officially confirm DM. Non-neurological controls were provided by the UoGSAH and the Scottish Society for Prevention of Cruelty to Animals (SSPCA) after owner consent was obtained. The SSPCA were the legal owners of controls CON1, CON2 and CON3. Due to confidentiality procedures, specific information related to age and medical history were not provided.

6.3.1.2 Neurological examination

Neurological examinations to assess posture, gait, reflexes and responses were carried out by specialists in veterinary neurology at the UoGSAH. Motor function was assessed by walking the canine back and forth and postural reactions were investigated using the paw replacement and hopping tests. Spinal reflexes were assessed using a reflex hammer on the muscles of the limbs near joints, and by testing the withdrawal reflex in the limbs. Further, the perineal and cutaneous trunci reflexes provided more information regarding the function of the spinal nerves. These reflexes test different segments of the spinal cord and are therefore able to locate where lesions may be present. Cranial nerve function was also examined. Dogs were evaluated for pain by palpation of the spine and muscles along the back and neck. Pain was indicated if there was vocalisation or whining by the dog, if the dog turned its head in the direction of touch or tried to bite the clinician or were licking their lips and had dilated pupils. The scale used in Griffiths (1982) was used to grade the severity of findings.

6.3.1.3 Haematology and biochemistry

Routine diagnostic testing was carried out by the University of Glasgow's Veterinary Diagnostic Services (VDS). These tests are used to rule out other causes of peripheral neuropathy including meningitis, diabetes mellitus, and Cushing's disease. Blood samples were also sent to an external organisation for *Sod*1 genotyping for diagnostic purposes (Laboklin, UK). Controls were genotyped inhouse and DM cases were included to confirm the result from Laboklin.

6.3.1.4 MRI

MRIs were performed by clinicians at the UoGSAH to visualise the brain and spinal cord of dogs using the 1.5 Tesla scanner (Siemens Magnetom Essenza, Siemens Healthcare Ltd, UK). This imaging was used to exclude disc diseases and compressive lesions although these may be present concurrently with DM.

6.3.1.5 Collection of DM and control case material

Control cases were either euthanised at the UoGSAH after owner consent or they were donated from the SSPCA after euthanasia (Table 6-1). Blood samples were only collected from DM cases, not control cases. Aliquots of uncoagulated whole blood were made and used for further *Sod*1 genotyping (see 6.3.2). Cadavers were transported to the University of Glasgow post-mortem rooms and all tissues were collected within five hours of death by MM with assistance from LEB in some cases (3/4 DM cases, 2/8 controls), PM room technicians and often pathologists.

Table 6-1: List of cases used in this study.

Study no.	Date collected	Breed	Age (years)	Sex	Official diagnosis
DM1	24/10/2019	GSD	9.6	F	DM (pelvic limbs non-ambulatory at euthanasia)
DM2	21/09/2020	GSD	10.0	M	DM (pelvic limbs non-ambulatory at euthanasia)
DM3	26/04/2022	GSD	9.3	F	DM (pelvic limbs non-ambulatory at euthanasia)
DM4	31/07/2017	GSD	8.0	M	DM (pelvic limbs non-ambulatory at euthanasia)
CON1	06/05/2022	PBD	UKN	M	No known medical issues. *
CON2	27/06/2022	PBM	UKN	M	No known medical issues. *
CON3	03/10/2022	AC	UKN	M	No known medical issues. *
CON5	19/08/2022	CSP	10.0	M	Degenerative encephalopathy suspected (clear thoracolumbar MRI)
CON6	08/09/2022	SBT	9.5	F	Suspected thromboembolic event (brain or lungs)

Listed in the table are the clinical cases that were used in this study. All DM cases were submitted to UoGSAH. The official diagnosis is the primary cause of death or euthanasia. *Dogs were donated from the SSPCA with no known medical issues. Age, breed and sex information was not provided due to confidentiality arrangements and is thus an approximation based on post-mortem observations. **UKN**= unknown. **PBD=** Pitbull type breed; **PBM=** Pitbull mastiff mix; **AC=** Akita cross; **SBT=** Staffordshire bull terrier; **CSP=** Cocker Spaniel.

Spinal cord material was collected from DM and control dogs based on the following protocol. In some control cases, there was variation in segments collected. The spinal cord was exposed by shearing off the dorsal surface of the vertebral column. The spinal cord segments were distinguished by suturing the transition between the cervical and thoracic regions and the thoracic and lumbar regions. Several segments were removed from the spinal cord dura mater and snap-frozen in an ethanol ice bath. Care was taken to ensure part of the dura stayed intact so the remaining cord could be suspended in 10% formalin (3.7% formaldehyde, 1% methanol in water), a fixative that preserves tissue and cell morphology and composition so they can be visualised downstream (Thavarajah *et al.*, 2012). After fixation of the spinal cord, segments C3/C4 (cervical) and

T12 (thoracic) were removed and trimmed in the transverse and longitudinal planes before being loaded into cassettes for tissue processing. LEB contributed to trimming tissue from DM1 to DM3 under the guidance of various staff from VDS. DM4 was from a previous study and fixed material was not available.

6.3.1.6 Histopathology

All stages of histology were performed by VDS and DM was confirmed in cases by pathology residents supervised by accredited veterinary pathologists (DM1 and DM2) or Pamela Johnston (PJ; DM3) and further assessed for this thesis by LEB with help from PJ. DM4 was assessed previously.

Tissues were routinely processed in an automated tissue processor machine (Excelsior™ AS Tissue Processor, Thermo Scientific, UK) for 17 hours after being fixed in formalin. Briefly, tissues were dehydrated in solutions with increasing concentrations of ethanol. Alcohol and paraffin wax are immiscible, so tissues were cycled through xylene to clear the tissue of alcohol, then cycled through paraffin wax. Tissues were embedded in paraffin wax and cut into 2 μm thick sections using a microtome (Shandon™, Thermo Scientific, UK). Sections were attached to charged glass slides and baked at 60°C for 1 hour. Sections were stained using a standard procedure for haematoxylin and eosin (HE) staining and most reagents were made in house by VDS. Briefly, slides were submerged in Histo-Clear (National Diagnostics, USA) to deparaffinise sections, then hydrated though a series of decreasing alcohol solutions. Sections were stained with Gill’s haematoxylin for 5 minutes then differentiated in 1% acid alcohol and blued in Scott’s tap water substitute (STWS). Sections were counterstained with Putts eosin then dehydrated through increasing alcohol concentrations and returned to Histo-Clear. Sections were mounted with glass coverslips before being scanned with a Motic EasyScan Infinity 60 Slide Scanner up to 40X magnification. Scans were investigated and imaged using the Leica Aperio Image Scope software (v12.4.6.5003).

6.3.2 Nucleic acid analysis

6.3.2.1 Extraction of genomic DNA from blood samples

gDNA was extracted from whole blood samples using the DNeasy™ Blood and Tissue Kit (Qiagen, Germany) as per manufacturer's instructions. Briefly, 100 µl of blood was lysed with proteinase K (activity 40 mAU/mg protein) then incubated in a buffer containing guanidine hydrochloride at 56°C for 10 minutes. Absolute ethanol was added to the mixture before it was transferred into a DNeasy™ Mini spin column and centrifuged at ≥6000 *xg* for 1 minute. The DNA was washed in 2 steps using 2 buffers with a 1 minute ≥6000 *xg* centrifugation in between them, then centrifuged for 3 minutes at 20,000 *xg*. DNA was eluted from the membrane by applying an elution buffer (containing 10 mM Tris-hydrochloride, 0.5 mM EDTA, pH 9), incubating the mixture for 1 minute at RT, then centrifuging it for 1 minute at 6000 *xg*. The concentration (ng/µl) and purity (260/280 ratio) of gDNA was determined using the *Nucleic Acid* DNA-50 program with the NanoDrop. gDNA from controls was extracted from tissue using the same Qiagen kit following the manufacturer's protocol by MM.

6.3.2.2 *Sod*1 genotyping

The inhouse assay developed and reported in Shafie, Anderson and McLaughlin (2013) was used to determine the *Sod*1 genotype of controls and to confirm the DM genotypes in cases. The method is an RFLP assay based on the presence or absence of the *Hyp*AV enzyme restriction site. Genotyping was primarily conducted by MM with assistance from LEB. RT-PCR (Section 2.x) was carried out with DM cases using the following *Sod*1 primers designed by Shafie, Anderson and McLaughlin (2013): forward 5′-GCC TGT TGT GGT ATC AGG AAC CA-3′; reverse 5′-AGA GTC AAA AAC CGG C TT TGT GGA-3′ (Eurofins, Germany). The *Sod*1 primers produce a DNA fragment 236 bps long that contains both the *Sod*1:c.118G>A mutation and the *Hpy*AV restriction site which is only present in WT *Sod*1. Each PCR reaction had a final volume of 25 µl made up of REDTaq™ ReadyMix™ PCR Reaction Mix, 5 pmol per reaction of forward and reverse primers and 100 ng of gDNA. Where the volume of gDNA was under 11 µl, MQ water was added. DNA was denatured at 94°C for 5 minutes then 94°C for 1 minute, primer annealing occurred at 58°C for 1 minute then DNA strands were extended at 72°C for 1 minute then 72°C for 10 minutes. This cycle was repeated 32 times in total before the PCR products were visualised using SYBR Safe DNA-stained gels (Section 0) with a 100 bp DNA ladder.

PCR products were purified (Section 2.5.5) then digested at the *Hpy*AV restriction enzyme site using the protocol described by Shafie, Anderson and McLaughlin (2013). Each reaction mixture with a total volume of 25 µl contained the *Hpy*AV enzyme (2 U/µl), 2.5 µl 10X CutSmart™ BSA Buffer (New England BioLabs, UK), 2.5 µl 10X NEBuffer™ 4 (New England BioLabs, UK) and 200 ng PCR product. The buffers added ensure the *Hpy*AV enzyme works at 100% activity. Samples were incubated at 37°C for 30 minutes then incubated at 65°C for 15 minutes to stop the reaction. The digested products were separated on a 2.5% agarose gel with 1X TBE and 1X SYBR Safe DNA stain after adding loading buffer (final 1X concentration) to each sample. When samples produced bands at 204 bp and 32 bps under UV light, they were assigned WT (*Sod*1:c.118G/G) status as the nucleotide sequence had been cleaved. A single band at 236 bp indicated the sample was a homozygous mutant (*Sod*1:c.118A/A) because the nucleotide sequence was not cleaved. Bands at 236 bp, 204 bp and 32 bp indicated the sample was heterozygous (*Sod*1:c.118A/G).

6.3.2.3 Extraction of RNA from spinal cord tissue

Powdered cervical and thoracic segments of the spinal cord used for protein investigation (Section 6.3.3.1) were weighed to approximately 50 mg before 1 ml of TRIzol™ reagent was added along with a 5 mm diameter stainless-steel ball. Samples were homogenised in a ball mill (Retsch Mixer Mill MM 400, Germany) for 2 minutes at 30 Hz. Samples became significantly frothy, and had a high lipid content (due to myelin), so the optional centrifugation step in the manufacture’s protocol was followed. After centrifugation at 16,060 *xg* for 5 minutes at 4°C, the translucent SNs were transferred to fresh tubes, then samples were incubated on ice for 5 minutes. Chloroform (200 µl) was added, and samples were vortexed for approximately 30 seconds. Samples were incubated on ice for 3 minutes and centrifuged for 15 minutes at 16,060 *xg* (4°C) to separate the sample into the 3 phases. The top aqueous layer containing RNA was collected and 4 µl of glycogen was added. RNA was precipitated with 500 µl of isopropanol for 10 minutes on ice. The RNA was precipitated after centrifugation at 16,060 *xg* for 10 minutes and the SN was removed. The RNA precipitate was washed by vortexing the samples with 1 ml of 75% ethanol, the RNA was pelleted again by centrifugation at 12,298 *xg* (10,000 rpm on Biofuge) for 8 minutes. Most of the SN was removed before the samples were centrifuged for a further 2 minutes. The remaining SN was removed and the RNA pellet was air dried for 10 minutes. RNA was resuspended in 50 µl of RNAse free water and a NanoDrop was used to measure the RNA content. Using 500 ng of RNA, a 1.5% agarose gel with SYBR safe stain was used to separate the samples to determine the integrity of RNA (Section 2.5.2). cDNA was generated using the method described in Section 2.5.3.

6.3.2.4 Investigation of stress primers in control and DM samples

Using the method described in 2.5, *ATF3*, *BiP*, *Cyc* and *XBP1* primers (Table 2-4) were characterised with pooled samples of cervical control, cervical DM, thoracic control and thoracic DM cDNA, murine *rsh* cDNA and control and DTT treated human SK-N-SH cDNA (results presented in Appendix 8.3.2). Subsequently, all cervical and thoracic samples were run individually and SK-N-SH control and DTT treated samples were present as controls. For tissue sample PCRs, there were no multiplex PCRs. PCR products were visualised in 2% agarose gels with TAE buffer. *XBP*1 PCR products were further purified and digested with *Pst1*-HF as described in Sections 2.5.5 and 2.5.6. Digested products were visualised in 2% agarose gels with TBE buffer.

6.3.3 Protein analysis

6.3.3.1 Initial spinal cord tissue processing

Five control cases out of a pool of eight and four DM cases were used for proteomics and biochemistry. Due to equipment restraints, only five controls (CON1, CON2, CON3, CON5 and CON6) were used and were selected based on the lack of neurological signs and presence of the homozygous WT *Sod*1 genotype. Available cervical spinal cord segments from C3 to C6 and thoracic spinal cord segments T9 to T13 from control and DM cases were further processed for biochemical and omics analysis. All segments were powdered in liquid nitrogen using a mortar and pestle then stored at -70°C.

6.3.3.2 Protein extraction for biochemistry and investigative proteomics

Protein extraction was based on methods described in Hesse *et al.,* (2019) and Nelvagal *et al.,* (2020) and was optimised as described in Appendix 8.3.4.1. Aliquots of powdered samples were made to roughly 50 mg (precise range= 52 mg to 60 mg). Chilled extraction buffer (1 ml; 2% SDS and 100 mM Tris-HCl) and a 5 mm stainless-steel ball was added to each powdered sample for homogenisation in a ball mill (Retsch Mixer Mill MM 400, Germany) at 30 Hz for 2 minutes. Samples were centrifuged at 380 *xg* for 3 minutes then 200 µl and 600 µl of the SN was removed and put into fresh tubes. The 200 µl aliquot was used for proteomics and the 600 µl aliquot was used for protein biochemistry. In the 600 µl tubes, 6 µl of protease inhibitor cocktail (Sigma Aldrich, USA) was added, this was excluded from the smaller aliquot to ensure there was no interference with downstream trypsin digestion. All samples were vortexed then incubated on ice for 20 minutes with an additional vortex at 10 minutes and 20 minutes. After incubation, samples were centrifuged for 20 minutes at 16,060 *xg* at 4°C. The SN was removed, assayed (Section 2.4.3) and stored at -20°C (working biochemistry stock) or -70°C (proteomics and biochemistry stock).

6.3.3.3 Sample processing for peptides

The following protocol is based on a standard method used at GP and was conducted by LEB under the supervision of Suzanne McGill (SM; GP). Individual samples were made to 2 µg/µl with SDT-lysis buffer (4% SDS, 100 mM Tris-HCl at pH 7.6 and 0.1M DTT) to denature proteins. A pooled sample with control and DM cervical and thoracic samples was made to 1 µg/µl in SDT-lysis buffer.

Before being added to a Microcon-30kDa Centrifugal Filter Unit with Ultracel-30 membrane (Millipore, USA), 200 µl of urea UA buffer (8 M urea (Sigma Aldrich, USA), in 0.1 M Tris-HCl at pH 8.5) was added to each sample, then vortexed. Once in the filter unit, the samples were centrifuged at 16,100 *xg* for 15 minutes, then the flowthrough was discarded. A further 200 µl of UA buffer was added to all samples and the pool and centrifuged at 16,100 *xg* for 15 minutes. To prevent the reformation of disulphide bonds and alkylate samples for optimal enzymatic conditions, 100 µl 0.05 M iodoacetamide was added to all samples and the pool. After a short vortex, samples were incubated for 20 minutes at RT in the dark. Samples were centrifuged at 16,100 *xg* for 10 minutes then proteins in the column were washed 3 times in 100 µl UA buffer and centrifuged at 16,100 *xg* for 10 minutes each time. Proteins were further washed 3 times in 50 mM ammonium bicarbonate (ABC) buffer and centrifuged at 16,100 *xg* for 10 minutes after each wash.

For enzyme digestion of proteins, samples in the columns were incubated overnight at 37°C with 120 µl of 50 mM ABC and Trypsin (enzyme to protein ratio 1:100). The next day, columns were transferred to clean tubes and samples were centrifuged at 16,100 *xg* for 10 minutes to pull down peptides present in the solution, so flowthrough was retained. To ensure all peptides were washed through the filter, 50 µl of 10% acetonitrile (ACN) was added before the samples were centrifuged again at 16,100 *xg* for 10 minutes. Some samples were further centrifuged to ensure all solutions were passed through the filter. Samples were acidified with 50% trifluoracetic acid (TFA) to make a final 1% concentration of TFA. Samples were then dried in a vacuum centrifuge for 90 minutes and resuspended in 100 mM TEAB. Peptide concentrations were determined using a Nanodrop (DeNovix DS 11). Values returned were within the range of 0.36 µg/µl and 0.92 µg/µl.

6.3.3.4 TMT labelling

The following protocol was provided and performed by SM. To summarise, two 10plex TMT experiments were carried out; one for cervical samples and another for thoracic samples. TMT 10plex Label Reagents (Thermo Scientific, UK) were equilibrated to RT, then 8 µl of anhydrous ACN was dissolved in each vial (one for each sample) for 5 minutes. Protein digests (16 µg in 25 µl) from each sample were added to the TMT Label Reagent vials then incubated for an hour at RT. Each sample (2 µl) was pooled in a fresh tube, 3 µg of this added to a 96-well plate and dried down using a SpeedVac in preparation for nanoflow HPLC electrospray tandem mass spectrometry (nLC-ESI-MS/MS). The remainder was stored at -80°C.

6.3.3.5 nLC-ESI-MS/MS

The following protocol was provided and performed by SM. Using the auto-sampler from the nanoflow uHPLC system RSLCnano (Thermo Scientific, UK), the dried pool of labelled peptides was solubilised in 20 µl of 5% ACN and 0.5% formic acid. Online detection of peptide ions was by electrospray ionisation MS with an Orbitrap Fusion mass spectrometer (Thermo Scientific, UK). The LC eluent was ionised by interfacing the LC coupling device to a NonoMate Triversa (Advion Bioscience, US) using an electrospray voltage of 1.7 kV. With an injection volume of 5 µl, the reconstituted protein digest was desalted and concentrated for 10 minutes on a 0.3 mm x 5 mm trap column at a flow rate of 25 µl/minute using 1% ACN and 0.1% formic acid.

Peptides were separated on a Pepmap C18 reversed phase column (50 cm x 75 µm, 2 µm particle size and 100 Å pore size; Thermo Scientific, UK) using a solvent gradient at a fixed solvent flow rate of 0.3 µl/minute. The solvent gradient was composed of reagents A and B which were 0.1% formic acid in water and 0.08% formic acid in 80% ACN respectively. The solvent gradient was as follows: 4% reagent B for 1.5 minutes, 4 to 60% reagent B for 178.5 minutes, 60 to 99% reagent B for 15 minutes then it was held at 99% reagent B for 5 minutes. The column was equilibrated for 10 minutes in initial conditions before the next injection.

The Orbitrap fusion MS performed a high-resolution precursor scan at 120,000 RP (over a mass range of 400 to 1600 *m/z*) followed by top speed CID fragmentation and detection of the top precursor ions from the MS scan in the linear ion trap using turbo scan speed. HCD was performed on the top precursor ions with up to 10 SPS precursor scans isolated with the precursor ion and any TMT loss ions excluded from the selection. Orbitrap detection of the TMT quantitation label from the fragmentation was acquired at a resolution of 50,000 with a mass range 100-500 *m/z*.

6.3.3.6 Protein identification

Proteome Discoverer (version 2.4; Thermo Fisher Scientific, UK) was used to identify, quantify and statistically assess proteins from nLC-ESI-MS/MS data. Proteins were assigned using the Sequest HT search engine to interrogate protein sequences from the NCBI *Canis lupus familiaris* taxonomy. The threshold of precursor mass tolerance was 10 ppm and the fragment mass tolerance was 0.6 Da. Proteins containing less than two unique peptides that matched the NCBI database were excluded from analysis as they could not be confidently identified. Some proteins were identified as low-quality proteins so the sequence associated with the accession number was processed with a FASTA search using the EMBL-EBI service (https://www.ebi.ac.uk/Tools/sss/fasta/).

The scaled abundances were used to assess proteins of interest in individual samples and the *p* value of each fold change (FC) was calculated using a one-way ANOVA model with Tukey as the post-hoc test. The adjusted *p* values were calculated using the Benjamini-Hochberg correction to account for the false discovery rate.

Functional and Gene Ontology (GO) analysis was performed using DAVID (https://david.ncifcrf.gov/; Huang da, Sherman and Lempicki (2009a) and Huang da, Sherman and Lempicki (2009b)). Volcano plots were created using R Studio (R version 4.3.1 (2023-06-16 ucrt)). GraphPad Prism was used to plot functional and GO analysis data and to plot and statistically reassess individual scaled abundances for proteins of interest.

6.3.3.7 Western Blot

The samples containing protease inhibitor cocktail were used for WB. Samples were made to 10 µg then proteins were separated by SDS-PAGE (Section 2.4.5.1) and processed for WB (Section 2.4.7). All antibody information is available in Table 2-2. In addition to actin, flotillin-1, LC3, CuZnSOD and ubiquitin antibodies, antibodies were included for markers of CNS cells and were anti-NSE (neurones), anti-PLP (myelin/oligodendrocytes) and GFAP (astrocytes). Proteins of interest raised in proteomic analysis were probed for and were vimentin and lactate dehydrogenase (LDH).

6.3.3.8 Native gel with NBT staining

Protein samples used for biochemical analysis were diluted by a factor of five then processed and separated in a native gel (Section 2.4.5.2). The NBT staining procedure was followed as normal (Section 2.4.6.3), but incubation times for riboflavin and NBT were increased to 30 minutes.

6.3.4 Data and statistical analysis

WBs and PCR product gels were quantified as previously described using ImageJ. GraphPad Prism was used for graphical and statistical analysis of WB and PCR data. All groups were tested for normal distribution of residuals using the Royston Shapiro-Wilk normality test. For nucleic acid and basic protein investigations, comparisons made between control and DM groups were assessed using unpaired t-tests (parametric) or Mann-Whitney tests (nonparametric). When spinal cord segments were included in analysis, ordinary one-way ANOVA with Bonferroni’s multiple comparisons tests or Kruskal-Wallis with Dunn’s multiple comparisons tests were used for normally or abnormally distributed residuals respectively.

6.4 Results

6.4.1 Diagnosis of DM

DM cases recruited to this study initially presented as ambulatory, ataxic and paretic and were euthanised when they became non-ambulatory, usually with some movement still present. All suspected DM cases were genotyped using the outsourced company (Laboklin, UK) and this was confirmed with an inhouse *Sod*1 genotyping method (Figure 6-1). All control dogs were genotyped inhouse only (Figure 6-1A). For *Sod*1 homozygous WT, an intense band was seen at 204 bps due to digestion by the *Hpy*AV restriction enzyme. Sometimes faint bands were present at 236 bps due to incomplete digestion of some fractions (likely due to method rather than DNA sequence). For cases homozygous for the *Sod*1 mutation, only one intense band was visible at 236 bps as the DNA was not digested by the restriction enzyme. For heterozygous cases, intense bands were seen at 204 bps and 236 bps as both WT and mutant *Sod*1 alleles were present.

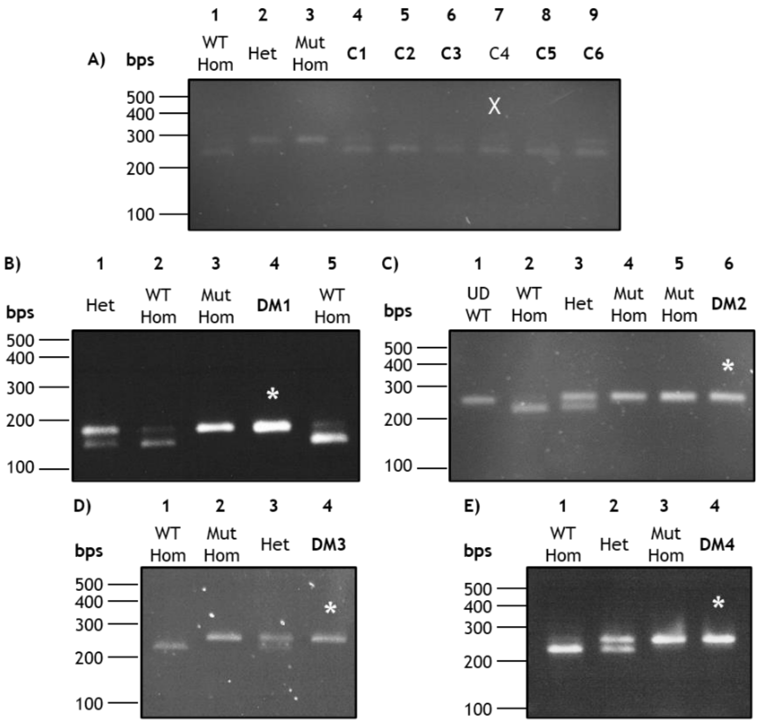

Figure 6-1: *Sod*1 genotyping for all dogs used in this study. Purified *Sod*1 PCR products were digested with *Hpy*AV, then products were separated in an agarose gel. As the cases were actively recruited throughout the duration of this project, they were genotyped as the samples became available. Every run contained control samples for WT homozygotes (WT Hom), heterozygotes (Het) and DM/mutant homozygotes (Mut Hom). In some cases, there was an undigested WT control (UD WT). Only WT *Sod*1 was cut by the enzyme and this was visualised by a lower band when compared to the undigested product. Homozygous mutant *Sod*1 cannot be cut by the enzyme, so *Sod*1 remains undigested and appears the same as the undigested WT sample. Heterozygous animals have one WT and mutant copy of *Sod*1, so *Hpy*AV digestion results in a double band pattern. **A)** contains the genotypes for all control (C1-6) samples used in this study and they all matched the WT homozygous control. C4 (lane 7) was not used for proteomics and is denoted with an X. The signal was weak in the gel, so the contrast of the image was adjusted to allow visualisation of the bands. **B)** contains DM1 (lane 4) and controls. This was performed by MM and LEB early in the project. The migration pattern is slightly different from normal due to an error when making the gel, however the banding patterns were as expected. **C)** contains DM2 (land 6) and controls. **D)** contains DM3 (lane 4) and controls. **E)** contains DM4 (lane 4) and controls. **A)**, **C)**, **D)** and **E)** were provided by MM.

All DM cases were assessed for evidence of pathology associated with the disease, but only DM1 to 3 were available for investigation in this study. Control material from a previous study was included from a *Sod1:c.118G* homozygous eight-year-old male GSD.

At high magnification (40X), the white matter of cervical and thoracic sections from control cases appeared within normal limits (Figure 6-2A), while in DM, white matter of the dorsal, lateral and ventral funiculi had occasional vacuoles containing degenerate axonal material and macrophages (Gitter cells). Degenerating axons swell before being digested and were visible as axonal spheroids (Figure 6-2B) which are subsequently digested by Gitter cells in digestion chambers (Figure 6-2C). Both lesions were found at varying degrees in DM cases and were observed in transverse and longitudinal sections. In longitudinal sections, the axonal spheroids and digestion chambers were often seen extending along a significant length of each affected axon (Figure 6-2D and E). Lesions appeared asymmetrically in all funiculi but were most abundant in the dorsal and dorsolateral funiculi, particularly in the fasciculus gracilis and corticorubrospinal tracts. The lesions described are typical of DM and suggest Wallerian degeneration was present.

In the grey matter of all sections, pyramidal neurones with large cell bodies were clear (Figure 6-2F). Lipofuscin, a yellow-brown pigment, was found in most sections from all cases and is considered a “wear and tear” pigment which accumulates in the neurones of older dogs. Given that the age range of dogs assessed in this study was eight to ten years old, this finding is age related. Most neurones were observed to be within normal limits, but the occasional swollen neurone was seen in DM cases (Figure 6-2G). Chromatolytic neurones (Figure 6-2H) were observed at varying numbers in the grey matter of DM cervical and thoracic cords only. Mild gliosis was present in the grey and white matter of some DM spinal cords but not the control.

Overall, pathology was most severe in the thoracic region of the spinal cord in all DM cases. DM1 appeared to be the most pathologically affected while DM2 and DM3 had mild to moderate pathology.

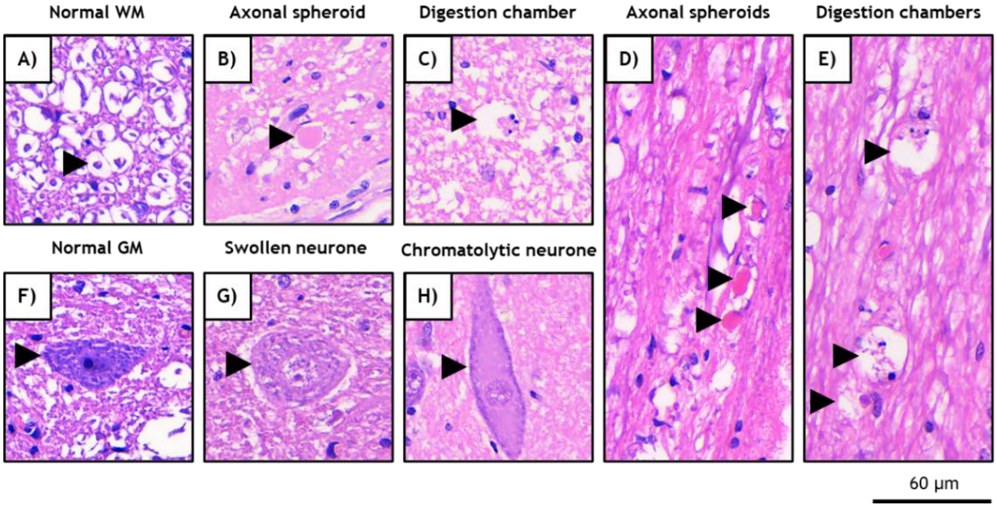

Figure 6-2: Examples of normal and DM spinal cord histology. A) Normal appearance of axons within the white matter (WM) in the transverse plane from a control case; one example is highlighted with an arrowhead, but they are abundant in the image. **B)** Axonal spheroid (arrowhead) in the DM white matter; transverse plane. **C)** Digestion chamber consisting of axonal debris and a Gitter cell (arrowhead) found in the DM white matter; transverse plane. **D)** Longitudinal section showing the length of a swollen axon (arrowheads). **E)** Longitudinal section containing multiple digestion chambers (arrowheads), which are likely to be along the same axon. **F)** Typical pyramidal neurone (arrowhead) found in the grey matter (GM); transverse plane from a control case. **G)** Swollen neurone in the grey matter of a DM section (arrowhead); transverse plane. **H)** Chromatolytic neurone (arrow) in the DM grey matter; longitudinal section. All images were captured at 40X magnification and the scale bar= 60 µm.

6.4.2 Nucleic acid analysis

Analysis of RNA integrity and primer characterisation for tissue derived samples are presented in Appendix 8.3.2. PCR reactions with *ATF3*, *BiP*, *XBP1t* and *cyc* (housekeeping) primers were used for canine samples (Figure 6-3). No significant changes were observed in DM cervical or thoracic spinal cord segments compared to controls for any of the primers, and there were no significant changes between spinal cord segments within control and DM groups. Further *Pst1*-HF digestion of *XBP1t* PCR products showed *XBP1t* was unspliced in all control and DM samples, indicating ER stress was not induced. The assay worked correctly as the product from SK-N-SH cells treated with dithiothreitol (DTT; ER stress inducer), was spliced and therefore undigested, as is the case when ER stress is induced.

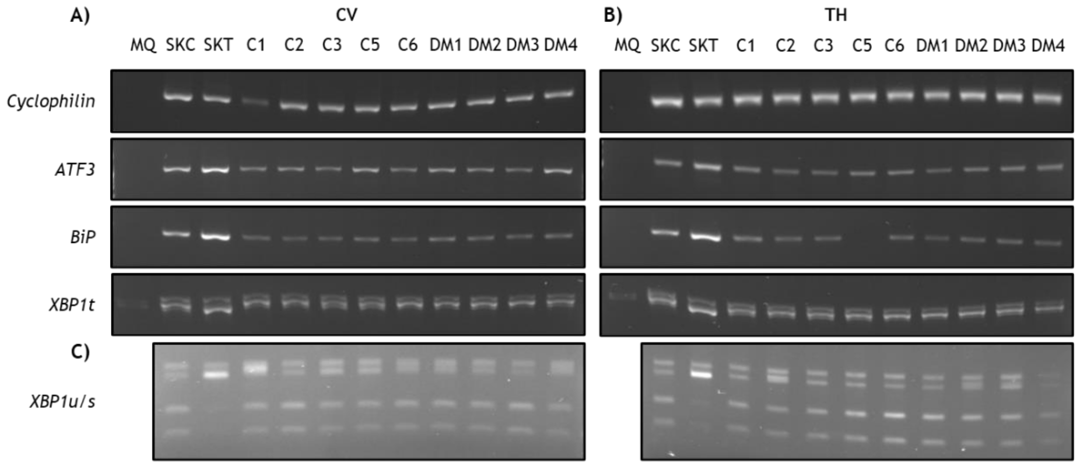
A)
CV
MQ SKC SKT C1 C2 C3 C5 C6 DM1 DM2 DM3 DM4
B)
TH
MQ SKC SKT C1 C2 C3 C5 C6 DM1 DM2 DM3 DM4
Cyclophilin
ATF3
BiP
XBP1t
C)
XBP1u/s

D)	C.CV	DM.CV	C.TH	DM.TH
BiP	45.2 ± 35.6%	42.0 ± 6.5%	36.0 ± 9.4%	28.8 ± 5.0%
ATF3	59.0 ± 37.7%	52.3 ± 19.0%	51.2 ± 10.9%	54.5 ± 9.3%
XBP1t	95.8 ± 65.9%	63.5 ± 7.6%	59.8 ± 2.6%	53.8 ± 9.2%

Figure 6-3: Comparison of RNA markers in canine spinal cord segments. cDNA from control and DTT treated SK-N-SH cells and control and DM cervical and thoracic spinal cord were used in PCR reactions with primers for *Cyc*, *ATF3*, *BiP* and *XBP1t*. PCR products were separated in 2% agarose gels for each spinal region (CV in **A**, TH in **B**) and quantified. *XBP1t* PCR products were further purified and digested with the *Pst*1-HF enzyme to check for the splicing of *XBP1t* (**C**). The quantity of PCR products for *ATF3*, *BiP* and *XBP1t* primers were expressed as a percentage of the quantity of *Cyc* and are presented in the table (mean ± SD) in **D**). Control *n*= 5 and DM *n*= 4, except for *ATF3* C.TH where *n*= 4. Ordinary one-way ANOVA with Bonferroni's multiple comparisons tests were used to compare values of each primer between control and treated spinal cord segments and spinal cord region. There were no significant changes found for any group using the current primers.

6.4.3 Protein overview in spinal cord samples

6.4.3.1 Total protein profile

The total protein profiles of control and DM spinal cords appeared similar when stained with Coomassie Blue (Figure 6-4). Further, the general profiles appeared similar between cervical and thoracic segments. There was potential enrichment of proteins in the thoracic region of DM spinal cords around 50 kDa compared to other segments from DM and control cases. Additionally, in the control samples, there was marginal enrichment of proteins at around 20 kDa compared to some DM cases.

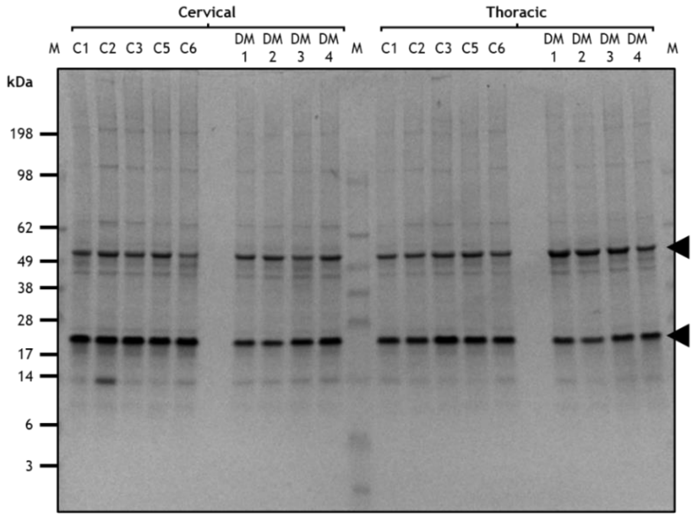

Figure 6-4: Total protein profile for control and DM spinal cord regions. Proteins were separated in a gel then stained with Coomassie blue stain. After destaining and rehydrating the gel, images were captured. Overall, the protein profiles were similar between cervical and thoracic segments and between control and DM cases, but there was variation in the concentration of staining around 20 kDa and 50 kDa (arrowheads).

6.4.3.2 Proteomics overview

A total of 693 proteins were identified with two or more unique peptides in canine spinal cords using TMT nLC-ESI-MS/MS. This accounted for 77% of peptides being quantified and the general distribution of $\log_2$FC with respective *p* values are plotted in Figure 6-5 for all comparisons.

Between the spinal regions within control and DM cases, 287 and 267 proteins respectively had a *p* value ≤ 0.05. Differences in protein expression between spinal cord regions may occur because of functional and size differences, for example the thoracic region was often slimmer than the cervical region. Adding a $\log_2$FC threshold (±0.5) further reduced the number of proteins and provided an insight into the differentially expressed proteins (Figure 6-5E).

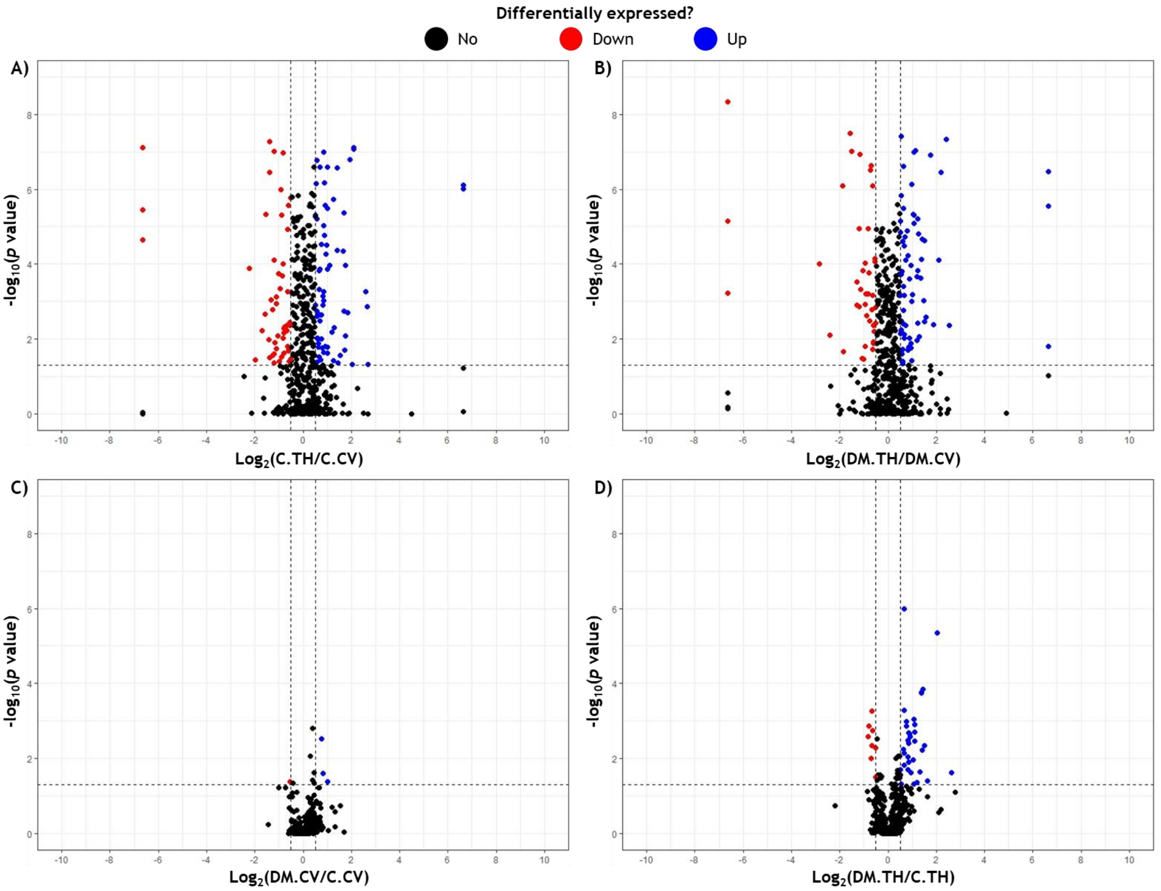

E)

	Differentially expressed?			
Comparison	● **No**	● **Down**	● **Up**	**Missing log$_2$FC**
C.TH vs C.CV	421	52	69	151
DM.TH vs DM.CV	431	41	71	150
DM.CV vs C.CV	598	1	3	91
DM.TH vs C.TH	550	8	36	99

Figure 6-5: Volcano plot assessment of TMT proteomics data. The log$_2$FC and *p* values for every speculative protein identified was plotted in a graph. The *p* value was plotted as –log10 for better distribution of points. **A)** Control thoracic versus cervical region. **B)** DM thoracic versus cervical region. **C)** DM versus control cervical region. **D)** DM versus control thoracic region. The horizontal dotted line indicates where *p*= 0.05 and the vertical lines indicate -0.5 and 0.5 log$_2$FC. Red and blue dots indicate proteins which could be considered differentially expressed (red= down; blue= up) while black dots indicate proteins which are less likely to be differentially expressed. Proteins missing a log$_2$FC value were not plotted as it is not possible to determine if they were not present in the sample due to biology, or they were below detectible limits, or there was an issue with the method. Values are listed in the table (**E**).

Comparison of cervical spinal cord segments from control and DM cases highlighted ten proteins found to be significantly different between groups ($p \leq 0.05$) and these are listed in Table 6-2. One protein, sterol carrier protein 2, was labelled as a low-quality protein, so a FASTA search was carried out with the protein sequence to check it was correct. The sequence was between 77% and

88% similar to sterol carrier protein 2 from other species, so this result was accepted.

Table 6-2: Differentially expressed proteins in the cervical spinal cord.

Protein	Accession (NCBI Db)	Unique peptides	$\log_2$(DM.CV/C.CV)	*p* value	Adjusted *p* value
L-lactate dehydrogenase A chain isoform X1	XP_035559651.2	7	0.38	0.002	1.000
Cathepsin D	XP_025277475.1	5	0.77	0.003	1.000
Sterol carrier protein 2*	XP_035571784.1	3	0.29	0.009	1.000
ATP synthase subunit g, mitochondrial-like	XP_038527460.1	2	0.44	0.024	1.000
Neuromodulin isoform X1	XP_025332627.1	9	0.82	0.026	1.000
Calmodulin-2 isoform X2	XP_048971829.1	7	0.39	0.038	1.000
Vimentin	XP_025301333.1	39	1.00	0.042	1.000
Proteolipid protein (PLP)	CAA39025.1	8	-0.53	0.042	1.000
BTB/POZ domain-containing protein KCTD12	XP_038287136.1	11	0.45	0.046	1.000
Tenascin isoform X6	XP_038536899.1	8	-0.42	0.047	1.000

*NCBI database indicated “low quality protein” in protein name. A FASTA search was conducted for the protein sequence corresponding to the accession number to confirm the sequence matched the protein name.

In the thoracic spinal cord, 62 proteins had different expression levels in control and DM groups ($p \leq 0.05$) and are shown in Table 6-3. In addition to sterol carrier protein 2, NfL was labelled as a low-quality protein, so a FASTA search was carried out with the protein sequence. The NfL sequence was around 98% aligned to the human form of the protein, so it was accepted as an identified protein in the canine samples.

Table 6-3: Differentially expressed proteins in the thoracic spinal cord.

Protein	Accession (NCBI Db)	Unique peptides	$\log_2$(DM.TH/C.TH)	*p* value	Adjusted *p* value
L-lactate dehydrogenase A chain isoform X1	XP_035559651.2	7	0.68	1.00E-06	0.001
Vimentin	XP_025301333.1	39	2.04	4.41E-06	0.003
Filamin-c isoform X1	XP_038542119.1	38	1.46	1.44E-04	0.029
Galectin-3	P38486.3	2	1.39	1.70E-04	0.029
Annexin A1	XP_025279092.1	12	1.38	1.83E-04	0.030
Glial fibrillary acidic protein isoform X2	XP_025296567.3	3	0.67	0.001	0.051
Neurofilament heavy polypeptide isoform X12	XP_048958020.1	50	-0.66	0.001	0.051
Alpha-actinin-1 isoform X5	XP_853103.1	11	1.08	0.001	0.062
Cathepsin D	XP_025277475.1	5	0.75	0.001	0.066
Bg chain bg, 60S acidic ribosomal protein P0	4V5Z	4	0.77	0.001	0.066
Heterogeneous nuclear ribonucleoprotein H isoform X1	XP_025302540.1	2	1.12	0.001	0.069
Proteolipid protein (PLP)	CAA39025.1	8	-0.78	0.001	0.072
Cadherin-2 precursor	NP_001274085.2	2	0.75	0.001	0.072
Neurofilament medium polypeptide isoform X1	XP_543237.3	64	-0.64	0.002	0.090
Vip21	CAA78151.1	2	1.12	0.002	0.096
60S acidic ribosomal protein P2	XP_038279466.1	2	0.85	0.002	0.101
Calponin-3 isoform X6	XP_038410567.1	4	0.9	0.002	0.105
Neurofilament light polypeptide*	XP_003639928.2	48	-0.83	0.003	0.122
Heat shock-related 70 kda protein 2	XP_038529770.1	10	0.93	0.003	0.123
2',3'-cyclic-nucleotide 3'-phosphodiesterase isoform	XP_005624533.1	32	-0.46	0.003	0.129
Myosin-9	Q258K2.1	9	0.84	0.003	0.138
Protein S100-A10	XP_038309276.1	2	1.12	0.003	0.140
BTB/POZ domain-containing protein KCTD12	XP_038287136.1	11	0.86	0.004	0.158
Apolipoprotein E	XP_533644.1	9	1.51	0.005	0.163
Breast carcinoma-amplified sequence 1 isoform X3	XP_038290045.1	2	-0.67	0.005	0.163
Cytosolic acyl coenzyme A thioester hydrolase isoform X1	XP_038379156.1	7	-0.51	0.005	0.169
Ras suppressor protein 1 isoform X1	XP_038514263.1	3	0.65	0.006	0.170
Chloride intracellular channel protein 1	NP_001239067.1	2	1.42	0.006	0.181
Angiotensinogen	XP_025304321.1	4	0.68	0.007	0.197
Four and a half LIM domains protein 1 isoform X1	XP_038306890.1	2	0.49	0.009	0.197
Plectin isoform X22	XP_005628109.1	79	0.41	0.009	0.197

*NCBI database indicated “low quality protein” in protein name.

Table 6-3 (cont’d): Differentially expressed proteins in the thoracic spinal cord.

Protein	Accession (NCBI Db)	Unique peptides	$\log_2$(DM.TH/C.TH)	*p* value	Adjusted *p* value
Heat shock 70 kda protein 4L isoform X1	XP_025276349.1	6	**	0.009	0.197
Moesin isoform X1	XP_025321840.1	8	0.84	0.009	0.197
Phosphate carrier protein, mitochondrial isoform X1	XP_038544248.1	6	-0.69	0.010	0.197
Ezrin isoform X1	XP_038509437.1	8	0.32	0.010	0.197
Adenosine kinase isoform X1	XP_025290656.1	2	1.03	0.011	0.197
Vinculin isoform X14	XP_038347906.1	12	0.86	0.013	0.225
Thioredoxin	XP_025288383.1	4	0.67	0.015	0.255
Protein S100-A6	XP_038428821.1	4	0.82	0.020	0.292
Ubiquitin-conjugating enzyme E2 N	XP_025294578.1	4	0.51	0.020	0.292
Aldehyde dehydrogenase, mitochondrial isoform X1	XP_048957770.1	11	0.39	0.021	0.292
Neuroblast differentiation-associated protein AHNAK isoform X22	XP_048952464.1	2	1.32	0.024	0.292
Annexin 2	AAR00321.1	10	0.95	0.024	0.292
Mimecan	XP_025279468.1	4	2.64	0.024	0.292
Tropomyosin alpha-3 chain	NP_001239140.1	2	0.38	0.025	0.292
40S ribosomal protein s2-like	XP_038528879.1	3	0.45	0.025	0.292
Secernin-1	XP_038542766.1	7	-0.42	0.027	0.292
Ankyrin-2 isoform X5	XP_013965380.1	12	0.5	0.027	0.292
Ubiquitin carboxyl-terminal hydrolase isozyme L1	XP_025293476.1	11	-0.33	0.028	0.298
Gamma-enolase isoform X2	XP_003639985.1	13	-0.28	0.031	0.325
Myelin-associated glycoprotein isoform X1	XP_038513383.1	9	-0.52	0.032	0.334
Peroxiredoxin-6	XP_537190.5	11	0.33	0.033	0.343
Pyruvate kinase PKM isoform X2	XP_038298794.1	3	-0.3	0.034	0.344
Grp94	AAA17708.1	12	0.48	0.034	0.344
Sterol carrier protein 2*	XP_035571784.1	3	0.37	0.034	0.346
Dihydropyrimidinase-related protein 5	XP_038309117.1	11	-0.44	0.038	0.372
Prolargin	XP_025276998.1	5	1.63	0.039	0.383
Acylphosphatase-2 isoform X1	XP_025322840.1	2	1.21	0.043	0.404
Histone H3.1 isoform X1	XP_038302066.1	6	0.31	0.047	0.421
Fibroblast growth factor 1 isoform X2	XP_013963577.1	2	1.08	0.049	0.421
Capping protein (actin filament) muscle z-line, alpha 2	AAR16268.1	2	0.53	0.049	0.421
Alcohol dehydrogenase class-3	NP_001239084.1	2	0.15	0.049	0.421

*NCBI database indicated “low quality protein” in protein name. Note, gamma-enolase is the NCBI database name for NSE. **$\log_2$FC was absent for “heat shock protein 70 kda protein 4L isoform X1” due to an incomplete dataset.

6.4.3.3 Functional and GO analysis

GO is a form of gene annotation that allows investigation of genes and their products at the level of their molecular function, biological process and location in cells (cellular component). This can help to understand the function of genes in a dataset and help to understand the biological significance of the up- or downregulation in expression (Gene Ontology Consortium, 2006). Kyoto Encyclopedia of Genes and Genomes (KEGG) is another gene annotation service that allows interrogation of gene function in relation to specific biological pathways. It is able to flag pathways that contain several genes of interest when inputted (Kanehisa and Goto, 2000).

Only KEGG pathway analysis returned hits in the cervical cord and this is likely due to the small number of genes associated with the differentially expressed proteins. Three KEGG pathways were highlighted, and these were “Glucagon signalling pathway”, “Estrogen signalling pathway” and “Tuberculosis” (Figure 6-6A). Further assessment found that the genes were linked to the pathways at the level of glycolysis, cell signalling and the endosome respectively.

KEGG pathway (Figure 6-6B) and GO (Figure 6-6C-E) analyses were conducted with the genes that corresponded to the proteins that were significantly different between the control and DM thoracic cords. KEGG pathways were related to energy metabolism, cell structure, adhesion and signalling. Further GO analysis of molecular function, cellular components and biological processes showed genes were important for calcium ion and ion channel binding, neuronal and axonal development, energy metabolism and cell signalling.

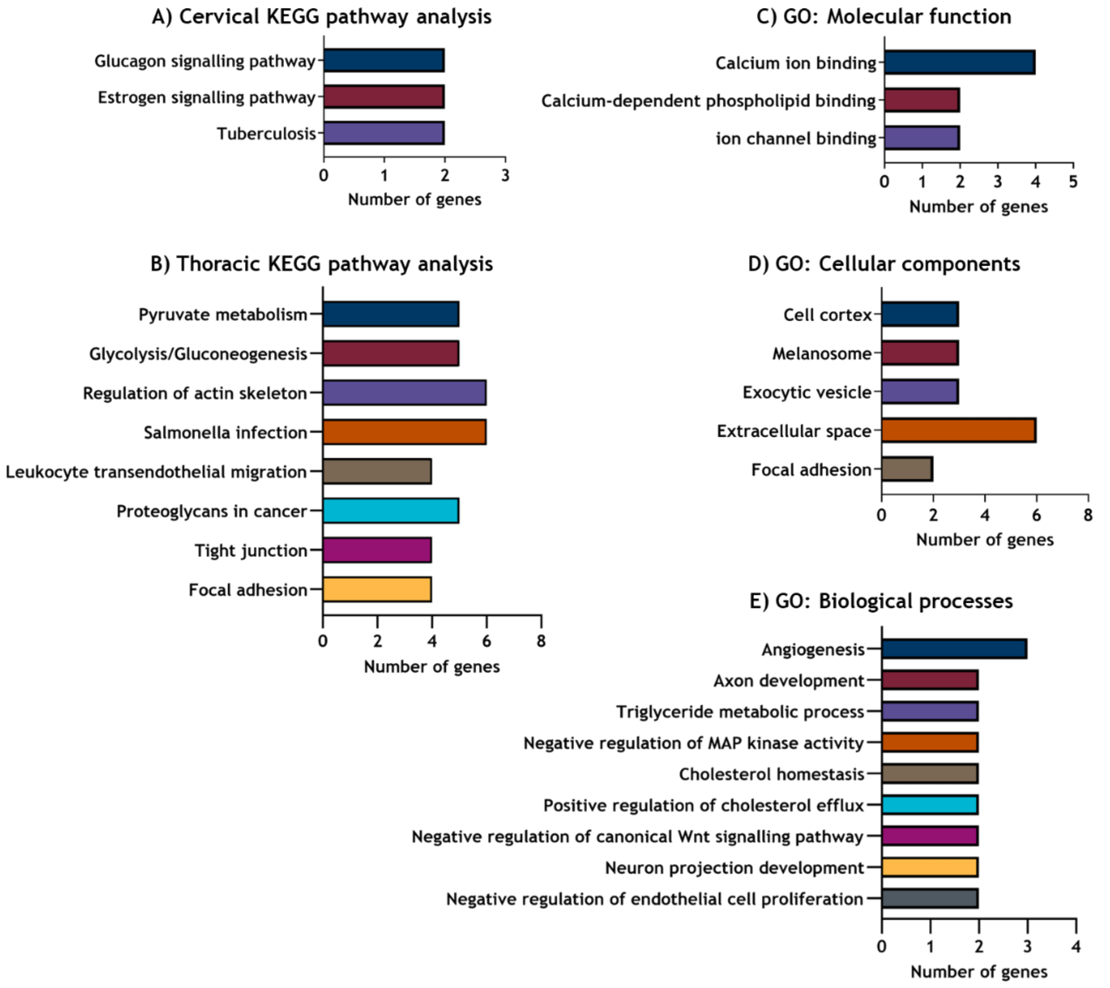

Figure 6-6: KEGG pathway and GO analysis of the spinal cord. The genes correlating to each protein that was significantly different between control and DM groups in the cervical and thoracic regions of the spinal cord were copied into DAVID for assessment. Hits in the KEGG pathway section were found in cervical (**A**) and thoracic regions (**B**). GO hits were only available for the thoracic region. GO was separated into molecular function (**C**), cellular components (**D**) and biological processes (**E**).

6.4.4 Analysis of specific protein markers

6.4.4.1 Neurone specific markers

Specific neurone associated proteins were examined to assess neuronal integrity in the cervical and thoracic segments. The number of unique peptides, $\log_2$FC, FC *p* value and adjusted *p* values are found in Figure 6-7A. Abundance values of proteins of interest were plotted into graphs and each protein was compared between control and DM cords for cervical (Figure 6-7B) and thoracic (Figure 6-7C) cords separately. There were no statistically significant changes between control and DM groups in the cervical region for any of the selected proteins. In the thoracic cord, NSE, NfL, NfM and NfH were significantly downregulated in the DM cords compared to controls (NSE, NfL and NfM $p \leq 0.01$; NfH $p \leq 0.001$). These changes are likely to reflect a reduction in axons/neurones. Further assessment between spinal cord regions within each group showed NfL and NfH were statistically lower in DM thoracic segments compared to cervical segments (NfL $p \leq 0.05$; NfH $p \leq 0.01$), but there were no changes between the segments in the control group. This suggests there was a significant loss of axons/neurones between segments in the DM cases. Contactin-1 was significantly higher in the thoracic segment of control and DM spinal cords compared to the cervical region (both $p \leq 0.001$). As the changes were present in both groups, it is likely to reflect a normal difference in the protein.

NSE was validated with WB (Figure 6-7D) and was statistically similar between control and DM cervical cords but significantly reduced in the thoracic cord of DM cases compared to controls ($p \leq 0.05$). This may indicate there was axonal/neuronal loss in the DM thoracic cord, but not the cervical cord or in the control cases. Further assessment showed in controls, there was significantly more NSE present in the thoracic region compared to the cervical region ($p \leq 0.05$). The lack of statistical significance between segments in the DM cases may further suggest there is axonal/neuronal loss in the thoracic region but not the cervical region. CL controls were positive for NSE as expected due to their neuroblastoma origin.

A) Protein	Accession (NCBI Db)	Unique peptides	$\log_2$(DM.CV/C.CV)	*p* value	Adjusted *p* value	$\log_2$(DM.TH/C.TH)	*p* value	Adjusted *p* value
NSE	XP_003639985.1	13	-0.02	1.000	1.000	-0.28	0.031	0.325
NfL*	XP_003639928.2	48	-0.26	0.732	1.000	-0.83	0.003	0.122
NfM	XP_543237.3	64	-0.08	0.925	1.000	-0.64	0.002	0.090
NfH	XP_048958020.1	50	-0.32	0.484	1.000	-0.66	0.001	0.051
Contactin-1	XP_025333060.1	13	0.05	1.000	1.000	-0.01	1.000	1.000

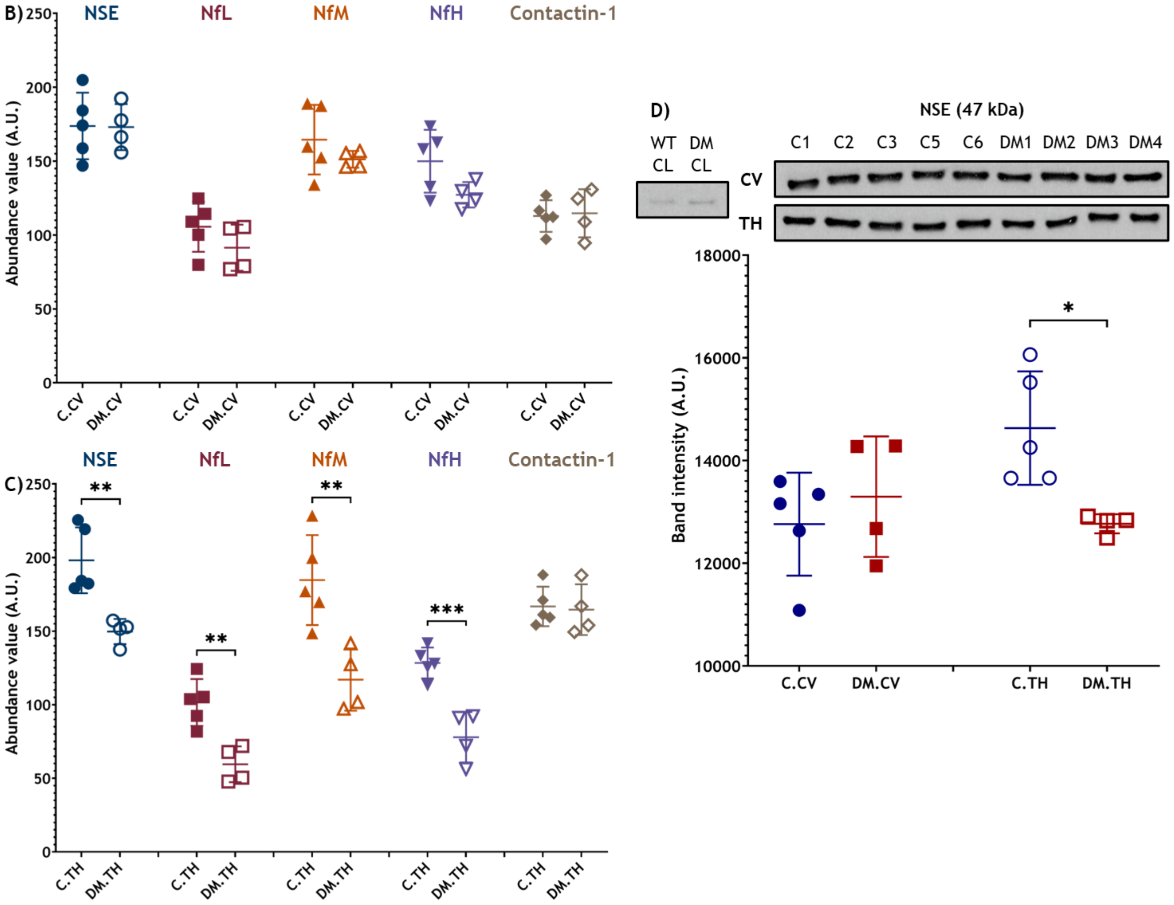

Figure 6-7: Neurone associated proteins in canine spinal cord. A number of neurone associated proteins were extracted from the proteomics dataset and interrogated. **A)** The table summarises important information for each protein including the number of unique peptides, $\log_2$FC, FC *p* value and adjusted *p* values. *NCBI Database indicated "low quality protein" in protein name. The abundance values obtained from TMT proteomic analysis for the neurone associated proteins were plotted in separate graphs for cervical (**B**) and thoracic (**C**) spinal cord regions. Unpaired t-tests were used to compare each protein between control and DM cases in each spinal cord segment. **D)** NSE was visible in WBs for cervical and thoracic segments. Bands were quantified and plotted in the graph. Unpaired t-tests were used to compare control and DM protein levels within each spinal segment. *$p \leq 0.05$; **$p \leq 0.01$; ***$p \leq 0.001$; ****$p < 0.0001$.

6.4.4.2 Myelin proteins

Specific proteins associated with myelin were further investigated from proteomic data to assess the integrity of myelin. The number of unique peptides, $\log_2$FC, *p* value and adjusted *p* values are found in the table in Figure

6-8A. Abundance values of proteins of interest were plotted in graphs and each protein was compared in control and DM cervical (Figure 6-8B and C) and thoracic (Figure 6-8D and E) segments separately. Two isoforms of MBP were identified by proteomics and a BLAST comparison was conducted with the protein sequences to confirm how similar they were. They were 89% similar (BLAST result in Appendix 8.3.4.4), however the proteomics analysis identified 3 and 5 unique peptides for MBP X1 and X4, so they were considered as 2 separate isoforms.

PLP and MBP X1 were the only proteins that showed statistical significance between control and DM samples in the cervical region. Both proteins were lower in the DM group compared to controls (PLP $p \leq 0.001$; MBP X1 $p \leq 0.05$). This may indicate that myelin in DM cases was starting to change structurally. In the thoracic region, PLP, MBP X4, MAG and CNP were significantly reduced in the DM cord (PLP and MBP X4 $p \leq 0.01$; MAG $p \leq 0.05$; CNP $p \leq 0.001$) while MBP X1 was increased in the DM group compared to the control group ($p \leq 0.05$). These differences may indicate further disruption to the normal myelin structure in DM and possible attempts to regenerate oligodendrocyte processes or signal to immune cells (MBP X1).

PLP and MAG were significantly higher in the thoracic region of the control group compared to the cervical region (both $p \leq 0.05$), but there was no statistical difference between the segments in the DM group. These changes indicate there are natural differences between the two segments and may relate to the number of myelinated fibres present at each region. MBP X1 was significantly lower in the thoracic region of the control group compared to the cervical region ($p \leq 0.05$), but this was not observed in the DM group, probably because levels were decreased in the cervical region and increased in the thoracic region in DM. NF was significantly higher in the cervical region of the DM spinal cord compared to the thoracic region ($p \leq 0.05$), but no differences were seen in the control group. The change in DM may suggest NF was starting to be effected by the demyelination process in the thoracic region, but it was not enough to be significantly different from control levels in the same region.

A)

Protein	Accession (NCBI Db)	Unique peptides	$\log_2$(DM.CV/C.CV)	*p* value	Adjusted *p* value	$\log_2$(DM.TH/C.TH)	*p* value	Adjusted *p* value
PLP	CAA39025.1	8	-0.53	0.042	1.000	-0.78	0.001	0.072
MBP X1	XP_048967610.1	3	-1.02	0.060	1.000	0.67	0.438	1.000
MBP X4	XP_048967616.1	5	-0.26	0.665	1.000	-0.86	0.075	0.533
MOG	XP_038302591.1	8	0.12	0.987	1.000	-0.11	0.760	1.000
MAG	XP_038513383.1	9	-0.24	0.664	1.000	-0.52	0.032	0.334
CNP	XP_005624533.1	32	-0.26	0.240	1.000	-0.46	0.003	0.129
NF	XP_005640830.2	9	0.16	0.893	1.000	0.03	0.946	1.000

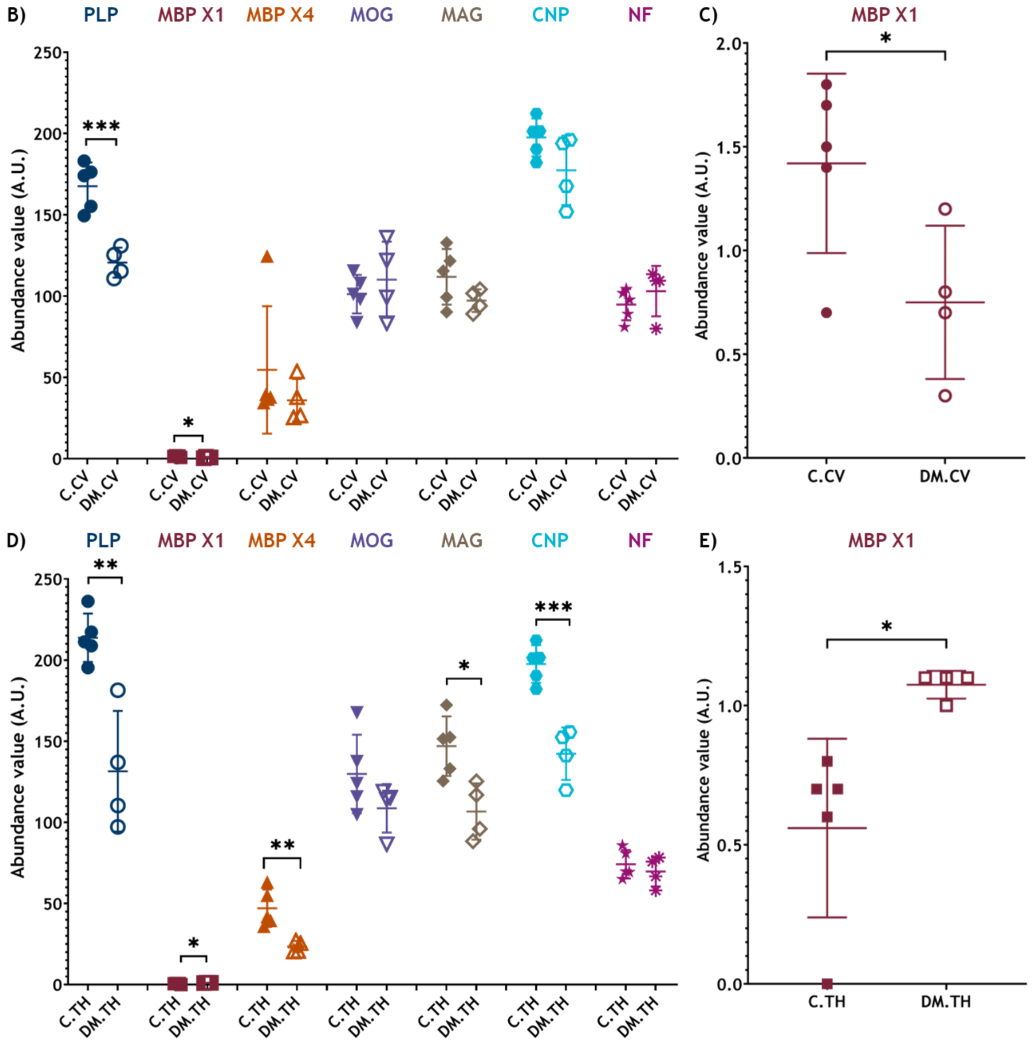

Figure 6-8: Myelin associated proteins in canine spinal cord. A number of myelin associated proteins were extracted from the proteomics dataset and interrogated. **A)** The table summarises important information for each protein including the number of unique peptides, $\log_2$FC, FC *p* value and adjusted *p* values. The abundance values obtained from TMT proteomic analysis for selected proteins were plotted in separate graphs for cervical (**B** and **C**) and thoracic (**D** and **E**) spinal cord regions. Unpaired t-tests (PLP, MBP X1 CV, MBP X4 TH, MOG CV, MAG, CNP and NF TH) and Mann-Whitney tests (MBP X1 TH, MBP X4 CV, MOG TH and NF CV) were used to compare each protein between control and DM cases. MBP X1 had very low levels, so these were plotted again by themselves to make the statistical change clearer for cervical (**C**) and thoracic (**E**) regions. $^*p \leq 0.05$; $^{**}p \leq 0.01$; $^{***}p \leq 0.001$.

PLP and DM20 were visible in WBs derived from tissues and probed with anti-PLP (Figure 6-9A). PLP and DM20 were quantified and plotted separately (Figure 6-9B and C respectively), then the PLP to DM20 ratio was presented to assess the turnover of myelin (Figure 6-9D). PLP was significantly reduced in the DM cervical and thoracic regions compared to controls ($p \leq 0.05$). DM20 also appeared to be reduced, however this was not statistically significant for either spinal cord segment. The PLP to DM20 ratio was significantly reduced in DM cervical cords compared to controls, potentially reflective of the significant reduction in PLP but not DM20. The ratio was not statistically different between groups in the thoracic region.

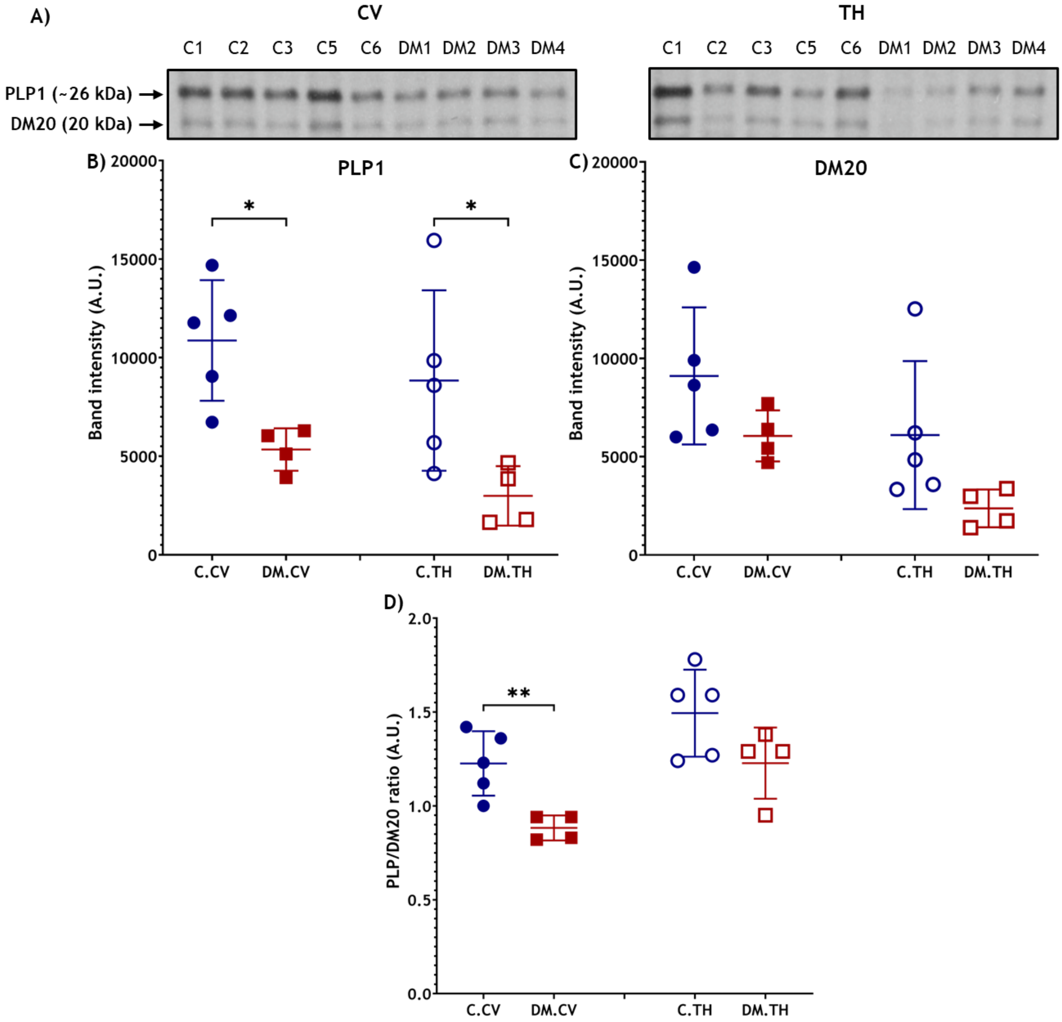

Figure 6-9: Biochemical investigation of myelin PLP and DM20. A) PLP and DM20 were visible after WB in the cervical and thoracic regions and were used as markers of myelination. Band intensities were quantified for both proteins, then they were plotted in the graphs shown in **B)** and **C)**. Each protein was compared between control and DM in both segments using unpaired t-tests. Finally, the ratio of PLP to DM20 was calculated and plotted in graph **D)** for the cervical and thoracic regions. Unpaired t-tests compared the ratios between control and DM groups for both segments. $^{*}p \leq 0.05$; $^{**}p \leq 0.01$.

6.4.4.3 Astrocyte and microglia proteins

Key microglial proteins including Iba-1, were not identified in the proteomics dataset but several astrocyte associated proteins were extracted for further analysis. The number of unique peptides, $\log_2$FC, *p* value and adjusted *p* values are found in Figure 6-10A. Abundance values of astrocyte proteins were plotted in graphs to compare each protein between control and DM cervical (Figure 6-10B) and thoracic (Figure 6-10C) regions separately. Vimentin and EAAT1 were significantly upregulated in the DM cervical spinal cord compared to the control group (both $p \leq 0.05$). This could indicate that astrocytes were being activated in DM cords. These proteins continued to be significantly upregulated in the DM thoracic region ($p < 0.0001$) and were accompanied by an upregulation in GFAP ($p \leq 0.01$). S100ß was borderline significantly lower in the DM thoracic region compared to the control group ($p = 0.061$) and followed the trend often seen for activated astrocytes. Together, these changes reflect the astrogliosis often observed in DM spinal cord histopathology. When comparing spinal segments within each group, vimentin and EAAT1 were significantly higher in the DM thoracic segment compared to the cervical segment (vimentin $p \leq 0.01$; EAAT1 $p \leq 0.05$), but this was not observed in controls. This suggests the astrogliosis was localised to the area of most pathology, the thoracic region.

The astrocyte marker GFAP was assessed by WB (Figure 6-10D), however the antibody did not produce a clean blot, probably because of the various isoforms, so caution was exercised when interpreting results. There was a clear band at the expected molecular weight for GFAP (50 kDa) and this was quantified, plotted and assessed. In cervical and thoracic regions, DM cases had significantly more GFAP than controls ($p \leq 0.001$). There were no statistical differences between segments within each group when further analysis was applied. CL controls were negative for GFAP. Results suggest there was significant astrogliosis in the DM spinal cord sections compared to controls. WB with vimentin (Figure 6-10E) showed the protein was higher in the DM group compared to the control group in both spinal cord segments ($p \leq 0.001$), further indicating the presence of astrogliosis in the DM cord.

A)

Protein	Accession (NCBI Db)	Unique peptides	$\log_2$(DM.CV/C.CV)	*p* value	Adjusted *p* value	$\log_2$(DM.TH/C.TH)	*p* value	Adjusted *p* value
GFAP	XP_025296567.3	3	0.30	0.407	1.000	0.67	0.001	0.051
S100B	XP_025318003.1	2	-0.12	0.994	1.000	-2.20	0.182	0.863
Vimentin	XP_025301333.1	39	1.00	0.042	1.000	2.04	4.41E-06	0.003
EAAT1	XP_025292002.1	8	0.46	0.096	1.000	0.60	0.123	0.701

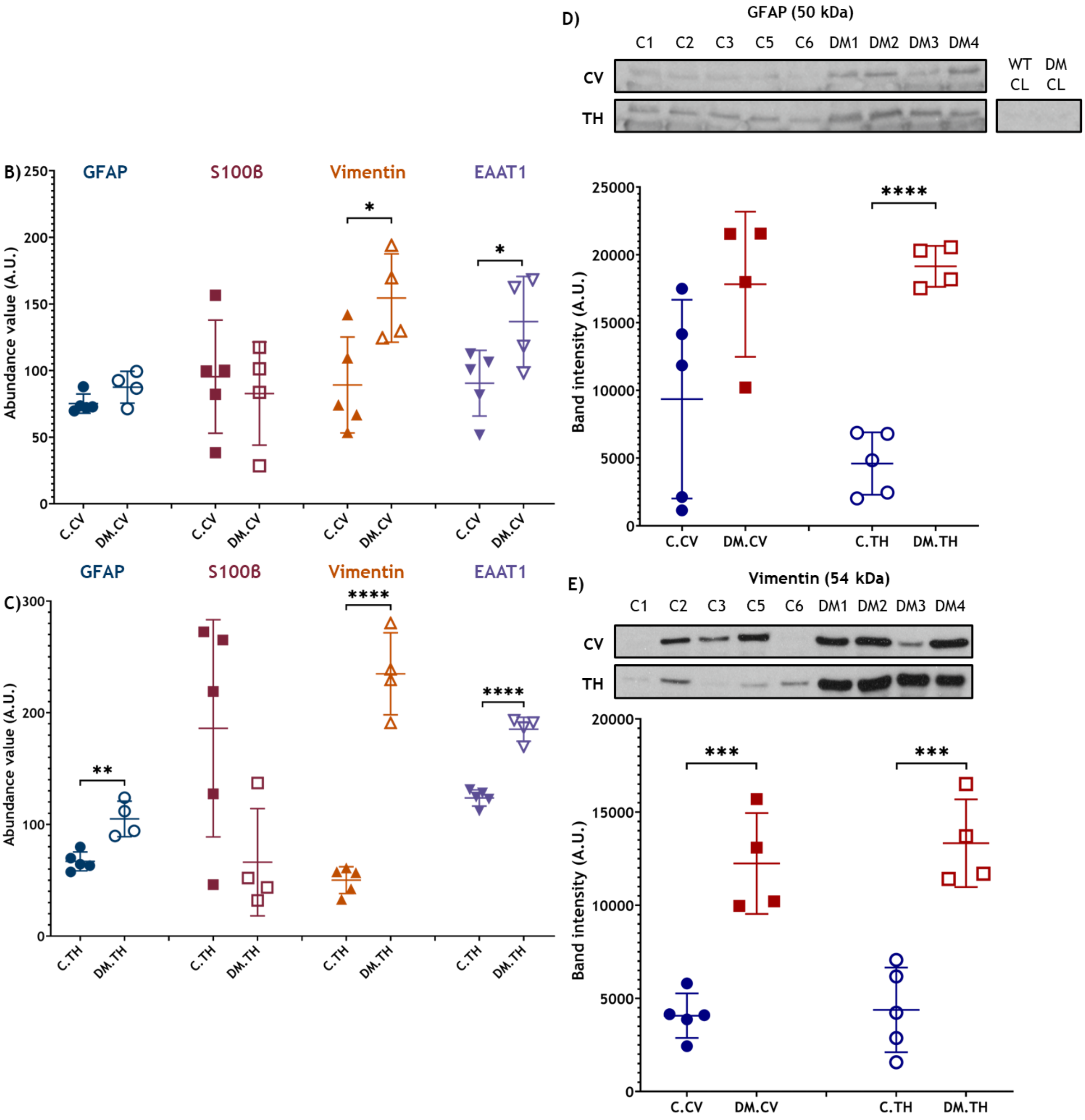

Figure 6-10: Glia associated proteins in canine spinal cord. A number of glia associated proteins were extracted from the proteomics dataset and interrogated. **A)** The table summarises important information for each protein including the number of unique peptides, $\log_2$FC, FC *p* value and adjusted *p* values. The abundance values obtained from TMT proteomic analysis for the selected proteins were plotted in separate graphs for cervical (**B**) and thoracic (**C**) spinal cord regions. Unpaired t-tests (TH GFAP, S100B, vimentin and EAAT1) and Mann-Whitney tests (CV GFAP) were used to compare each protein between control and DM cases. **D)** GFAP was visible in WBs for cervical and thoracic segments. The blots were not clean, so caution is to be used when interpreting values. Bands were quantified and plotted in the graph. **E)** vimentin was assessed in WBs for cervical and thoracic regions. Unpaired t-tests were used to compare control and DM protein levels within each spinal segment. $^*p \leq 0.05$; $^{**}p \leq 0.01$; $^{***}p \leq 0.001$; $^{****}p \leq 0.0001$.

6.4.4.4 Housekeeping proteins

Several proteins used as housekeeping markers in the *in vitro* and *ex vivo* experiments were further analysed. The number of unique peptides, $\log_2$FC, FC *p* value and adjusted *p* values are found in Figure 6-11A. The abundance values of housekeeping proteins were plotted for each case in graphs and each protein was assessed between control and DM cervical (Figure 6-11B) and thoracic (Figure 6-11C) regions separately. There were no statistical differences between control and DM groups in the cervical region, but ß-actin was significantly upregulated in the DM group compared to controls in the thoracic region ($p \leq 0.01$). This could be initially explained by active astrogliosis and/or structural disruption of axons. ß-actin was used as a housekeeping protein to ensure samples were equally loaded into gels for WB (Figure 6-11D). This suggests actin is not an appropriate loading control for use in canine spinal cord tissue undergoing neurodegeneration. There were no statistically significant changes in the values between spinal cord sections within each group. Nitrocellulose membranes were stained with Ponceau S and were used to determine that proteins were equally loaded (Appendix 8.3.4).

Cyc was significantly higher in the thoracic region of control and DM groups compared to the cervical region (control $p < 0.0001$; DM $p \leq 0.001$) and GAPDH was borderline significantly higher in control cervical regions compared to the thoracic segment ($p= 0.055$), but this was not observed for DM. These differences are likely to reflect normal changes in abundance of cells or their outward processes within each region of the spinal cord.

A)

Protein	Accession (NCBI Db)	Unique peptides	$\log_2$(DM.CV/C.CV)	*p* value	Adjusted *p* value	$\log_2$(DM.TH/C.TH)	*p* value	Adjusted *p* value
ß-actin	XP_025282077.1	7	0.08	0.978	1.000	0.32	0.051	0.433
Cyclophilin	XP_038545202.1	8	-0.12	0.998	1.000	0.01	0.999	1.000
GAPDH	NP_001003142.2	11	-0.03	0.999	1.000	0.02	1.000	1.000

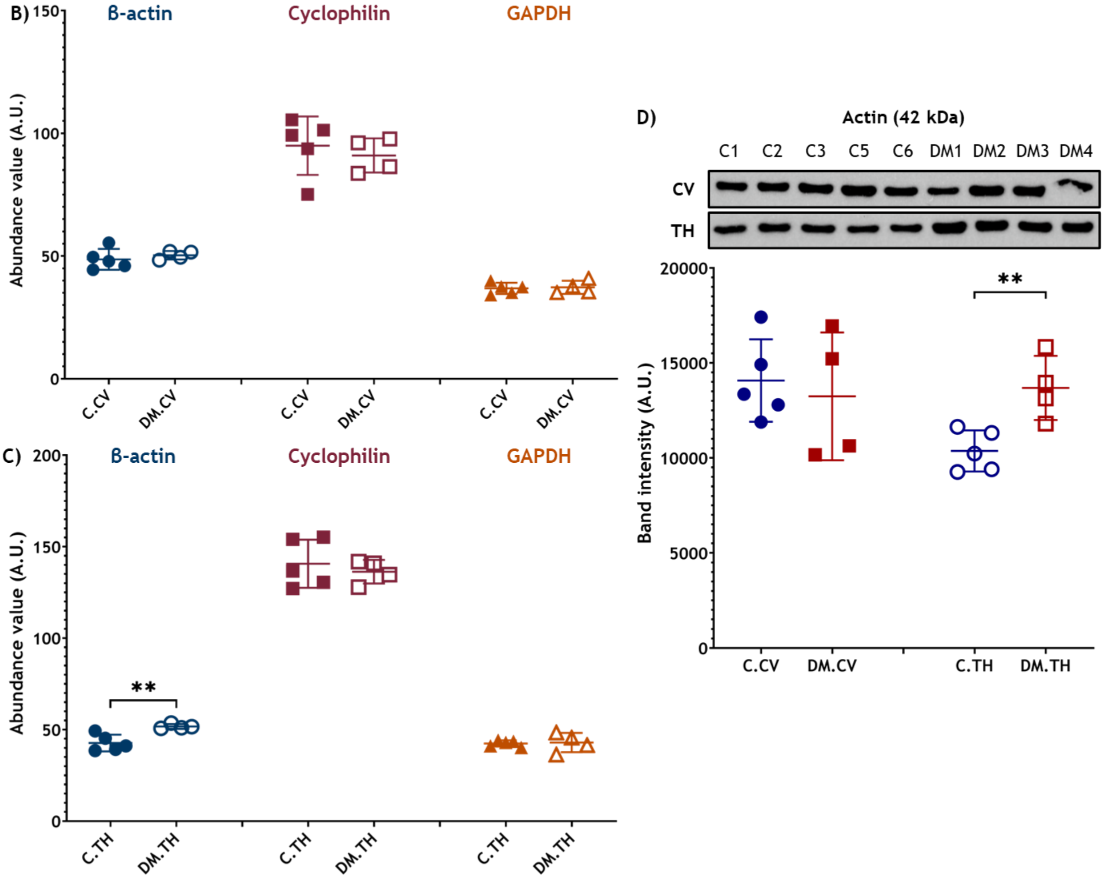

Figure 6-11: Housekeeping proteins in canine spinal cord. A number of housekeeping proteins were extracted from the proteomics dataset and interrogated. **A)** The table summarises important information for each protein including the number of unique peptides, $\log_2$FC, FC *p* value and adjusted *p* values. The abundance values obtained from TMT proteomic analysis for proteins used as housekeeping markers were plotted in separate graphs for cervical (**B**) and thoracic (**C**) spinal cord regions. Unpaired t-tests were used to compare each protein between control and DM cases. **D)** Actin was visible in WBs for cervical and thoracic segments. Bands were quantified and plotted in the graph. Unpaired t-tests were used to compare control and DM protein levels within each spinal segment. $^{**}p \leq 0.01$.

6.4.4.5 Cell clearance and toxicity pathway associated proteins

Multiple proteins have been used in this thesis to study cell clearance and toxicity pathways and are discussed in detail in Section 1.4. XBP1, ATF3 and ASK1 proteins were not found in the current dataset. E2 conjugating enzyme (E2) and proteasome subunit alpha type-1 (PSMA1) were used to assess the UPS. The dataset was interrogated for other UPS components, but they were either not statistically different or had incomplete datasets so were not assessed further at this stage. BiP, HSP70-1, HSP90ß, calnexin (CNX) and protein disulfide-isomerase (PDI) were markers to assess protein folding and the UPR. Cathepsin D (CTSD) is a proteolytic enzyme found in lysosomes and was used as a marker for autophagy. Annexin A1 (ANXA1) is associated with apoptosis. The number of unique peptides, $\log_2$FC, FC *p* value and adjusted *p* values are found in Figure 6-12A. Abundance values of proteins associated with cell clearance and toxicity were plotted in graphs and each protein compared between control and DM cervical (Figure 6-12B) and thoracic (Figure 6-12C) regions separately. Chaperones BiP, HSP70-1, HSP90ß and CXN were statistically similar between groups in the cervical spinal cord although using an unpaired t-test, HSP90ß was bordering on significance (p= 0.058) for upregulation in the DM group. In the thoracic cord, BiP and HSP90ß were significantly increased in the DM group compared to controls (BiP $p \leq 0.01$; HSP90ß $p \leq 0.05$). BiP and HSP90ß possibly indicate the upregulation of processes involved in rectifying protein misfolding while the absence of a significant difference in HSP70-1 indicates ER stress was not induced in either group or spinal cord region. BiP was borderline significantly lower in the thoracic region compared to the cervical region in controls only (p= 0.06). HSP70-1 and HSP90ß were significantly higher in the cervical region from both groups compared to the thoracic region (HSP70-1 control $p \leq 0.01$ and DM $p \leq 0.05$; HSP90ß control $p \leq 0.05$ and DM $p \leq 0.01$). This is likely to reflect the normal difference in cell numbers between each spinal cord region as opposed to being a pathological feature. CXN showed an upwards trend in the DM thoracic cord compared to controls, but this was not confirmed with statistics. In the control group, CXN levels were significantly higher in the cervical region compared to the thoracic region, but this did not occur in the DM samples.

E2 was only statistically different between control and DM samples in the thoracic region ($p \leq 0.05$) potentially indicating there was an upregulation of ubiquitination of proteins. E2 levels were significantly higher in control and DM cervical cords compared to the thoracic region which likely reflects natural variation in the cord. PSMA1 was statistically similar in both groups in both spinal cord regions implying this enzyme in the 20S proteasomal subunit was potentially not upregulated in the presence of more ubiquitinated proteins.

PDI was not statistically different between groups in either region of the spinal cord, however, in the DM thoracic cord, there was an increase compared to controls that was borderline significant with a stringent Mann-Whitney test ($p= 0.064$). There was a significant difference between DM cervical and thoracic regions ($p \leq 0.05$), but not controls. This suggests PDI was starting to become increased in the DM thoracic region.

CTSD was significantly upregulated in the cervical and thoracic regions of the DM group compared to controls (cervical $p \leq 0.05$; thoracic $p \leq 0.001$) but were similar between regions within the same groups. This could indicate upregulation of lysosomal degradation in autophagy, but CTSD was potentially also translocated to the cytoplasm causing the general degradation of proteins, and/or apoptosis may have been induced. ANXA1 was borderline significantly increased in the cervical region of DM cords ($p= 0.064$) and was significantly increased in the thoracic cord ($p \leq 0.001$) compared to controls. ANXA1 is suspected to have roles in inflammation and apoptosis, so upregulation may indicate general apoptosis and/or changes in microglia.

A)

Protein	Accession (NCBI Db)	Unique peptides	$\log_2$(DM.CV/C.CV)	*p* value	Adjusted *p* value	$\log_2$(DM.TH/C.TH)	*p* value	Adjusted *p* value
BiP	XP_863385.3	10	0.02	0.985	1.000	0.47	0.335	1.000
HSP70-1	NP_001003067.2	13	-0.05	1.000	1.000	0.07	0.991	1.000
HSP90B	XP_022281802.1	6	0.22	0.306	1.000	0.13	0.473	1.000
PSMA1	XP_048954783.1	3	0.08	0.967	1.000	0.31	0.788	1.000
E2	XP_025294578.1	4	-0.07	0.956	1.000	0.51	0.020	0.292
PDI	XP_025324109.3	9	0.15	0.997	1.000	0.48	0.197	0.918
CTSD	XP_025277475.1	5	0.77	0.003	1.000	0.75	0.001	0.066
CNX	XP_035552617.1	8	-0.03	1.000	1.000	0.17	0.517	1.000
ANXA1	XP_025279092.1	12	0.67	0.061	1.000	1.38	1.83E-04	0.030

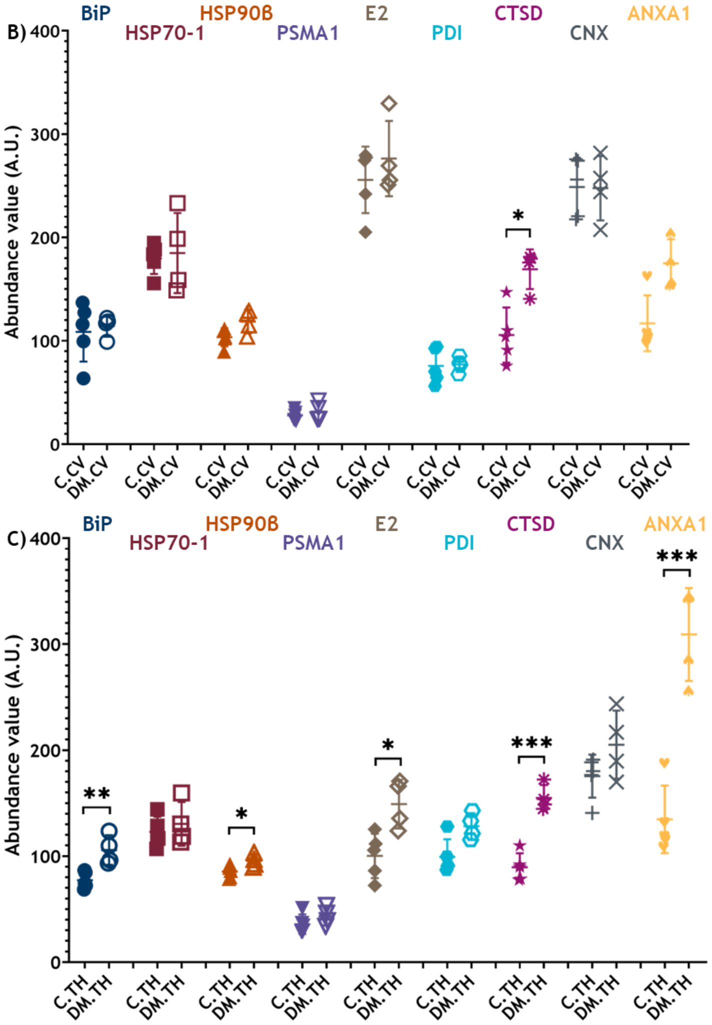

Figure 6-12: Proteins associated with cellular clearance and toxicity pathways in canine spinal cord. A number of proteins associated with cellular clearance and toxicity pathways were extracted from the proteomics dataset and interrogated. **A)** The table summarises important information for each protein including the number of unique peptides, $\log_2$FC, FC *p* value and adjusted *p* values. The abundance values obtained from TMT proteomic analysis for specific proteins were plotted in separate graphs for cervical (**B**) and thoracic (**C**) spinal cord regions. Unpaired t-tests (BiP, HSP70, HSP90B, PSMA1, E2, PDI CV, CTSD TH, CNX and ANAX1 TH) and Mann-Whitney tests (PDI TH, CTSD CV and annexin A1 CV) were used to compare each protein between control and DM cases. *$p \leq 0.05$; **$p \leq 0.01$; ***$p \leq 0.001$.

LC3 only had one unique peptide and an incomplete dataset in proteomics, so other proteins associated with autophagy were assessed. LC3BI (Figure 6-13A) and LC3BII (Figure 6-13B) were present in all samples using WB but LC3BI was more clearly observed. LC3BI but not LC3BII was significantly upregulated in DM cervical regions compared to controls ($p \leq 0.05$). In the thoracic region, LC3BII but not LC3BI was significantly upregulated in the DM group compared to the control group. These data were further assessed to understand the autophagy flux by expressing LC3BII values as a ratio of LC3BI (Figure 6-13C). The ratio was lower in the DM samples compared to controls in the cervical region, but this was not statistically significant ($p= 0.066$). In the thoracic segments, DM samples had a significantly higher LC3BII/LC3BI ratio ($p \leq 0.01$). This possibly suggests there was an accumulation of LC3BII in the DM thoracic spinal cords. Analysis with an ordinary one-way ANOVA showed control ratios were significantly different between cervical and thoracic regions ($p \leq 0.001$) but were statistically similar between DM regions.

Ubiquitin was not found in the TMT dataset, likely because the ubiquitin protein itself is very small and is usually attached to other proteins. Ubiquitination of proteins was observed in all samples using WB (Figure 6-13D) and most of the area pictured was quantified and plotted in a graph (Figure 6-13E). Ubiquitin was significantly upregulated in cervical and thoracic regions in the DM group compared to the control group (cervical $p \leq 0.05$ and thoracic $p \leq 0.01$) indicating more proteins were labelled for degradation by the UPS in the DM cord. It could also indicate that the UPS was less efficient at degrading ubiquitinated proteins.

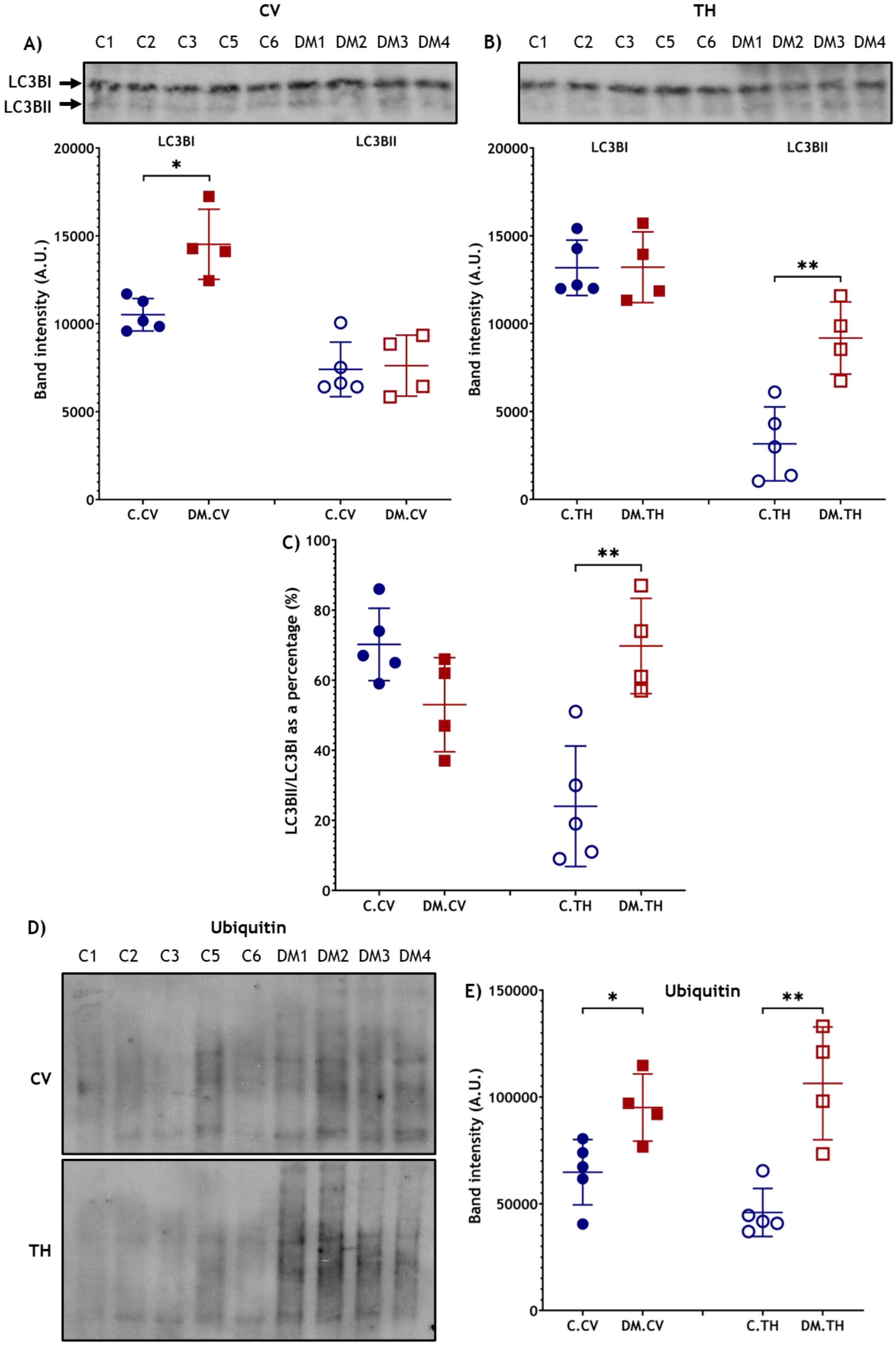

Figure 6-13: Biochemical investigation of autophagy and the proteasome. LC3BI and LC3BII were visible in WBs for cervical **A)** and thoracic **B)** segments. Bands were quantified and LC3I and LC3II were plotted in the respective graphs. Mann-Whitney tests were used to compare control and DM cases within the cervical segment and unpaired t-tests were used to compare control and DM protein levels within the thoracic segment. **C)** LC3BII to LC3BI ratio was also plotted to understand the turnover of the autophagy related protein. **D)** Ubiquitination of proteins was visible in all samples. The visible smear was quantified and plotted in the graph (**E**). $^*p \leq 0.05$; $^{**}p \leq 0.01$.

6.4.4.6 Proteins associated with neurodegenerative diseases

SOD1 and SOD2 along with two proteins associated with neurodegenerative disease, apolipoprotein E (apoE) and Tau, were selected for analysis. The number of unique peptides, $\log_2$FC, FC *p* value and adjusted *p* values are found in Figure 6-14A. The abundance values of proteins associated with neurodegeneration were plotted for each case in graphs and each protein was assessed between control and DM cervical (Figure 6-14B) and thoracic (Figure 6-14C) regions separately. There were no statistical differences between control and DM groups in the cervical region, but apoE and Tau were significantly different in the DM group compared to controls in the thoracic region (apoE $p < 0.0001$; Tau $p \leq 0.05$). The increased in apoE may have reflected a change in lipid turnover and the decrease in Tau probably indicated the presence of neurodegenerative processes within the cord associated with axonal/neuronal loss. ApoE was significantly higher in the DM thoracic cord compared to the cervical region only ($p \leq 0.001$) and further emphasises that the protein was important in DM.

SOD1 and SOD2 were not statistically different between DM and control spinal cords. SOD1 was significantly higher in the control thoracic region compared to the cervical region ($p \leq 0.05$), but this difference was not statistically relevant in the DM group. SOD2 was statistically higher in the thoracic region of both groups compared to respective cervical regions ($p < 0.0001$). It is possible the differences in SOD1 and SOD2 between the segments reflects a difference in the demand for neutralisation of free radicals between the different segments as previously postulated (Coates and Wininger, 2010).

A)

Protein	Accession (NCBI Db)	Unique peptides	log$_2$(DM.CV/C.CV)	*p* value	Adjusted *p* value	log$_2$(DM.TH/C.TH)	*p* value	Adjusted *p* value
ApoE	XP_533644.1	9	0.74	0.209	1.000	1.51	0.005	0.163
Tau	XP_048970590.1	4	0.18	0.962	1.000	-0.78	0.127	0.701
SOD1	AAL61608.1	5	0.28	0.820	1.000	-0.07	1.000	1.000
SOD2	XP_025278450.1	3	-0.11	1.000	1.000	0.08	0.999	1.000

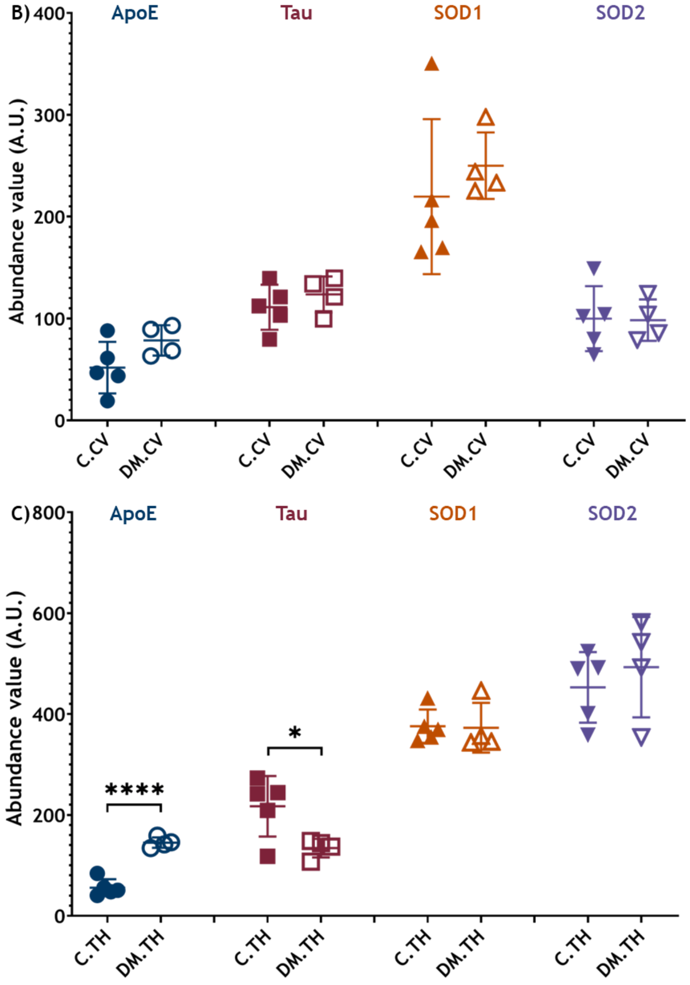

Figure 6-14: Proteins associated with neurodegenerative diseases in canine spinal cord. A number of proteins associated with neurodegeneration were extracted from the proteomics dataset and interrogated. **A)** The table summarises important information for each protein including the number of unique peptides, log$_2$FC, FC *p* value and adjusted *p* values. The abundance values obtained from TMT proteomic analysis for selected proteins were plotted in separate graphs for cervical (**B**) and thoracic (**C**) spinal cord regions. Unpaired t-tests (apoE, Tau, SOD1 CV and SOD2) and Mann-Whitney tests (SOD1 TH) were used to compare each protein between control and DM cases. **p* ≤ 0.05; *****p* < 0.0001.

As SOD1 was a protein of interest throughout this thesis, it was assessed by biochemistry. Two clear bands were visible in the tissue: one at ~16 kDa and one at ~64 kDa. The 16 kDa band likely represents the SOD1 monomer while the larger band may be due to the antibody binding to a non-specific protein, or it could have bound to a larger SOD1 species, for example oligomers. For the purposes of this study, the larger band will be treated as soluble oligomers. Both bands were quantified and plotted into graphs (Figure 6-15A for monomer, Figure 6-15B for oligomers) and the oligomers were further expressed as a ratio of the monomer to look at the potential conversion of monomers to oligomers (Figure 6-15C). The monomer generally appeared to be lower in the DM cervical and thoracic regions compared to controls, however this was only statistically significant in the cervical region ($p \leq 0.05$). The oligomer fraction was not statistically different between control and DM groups. The oligomer to monomer ratio was higher in the DM groups compared to controls, but this was only statistically relevant in the thoracic region of the spinal cord ($p \leq 0.05$). It could be surmised that this indicates there is an accumulation of SOD1 oligomers that could be associated with early SOD1 aggregate formation.

The activity of SOD1 within tissue was assessed with a native NBT stained gel and there was a clear loss of colour in the control samples, but not in the DM samples (Figure 6-15D). The absence of achromatic areas suggests there was loss of SOD1 activity in DM samples in both spinal cord regions. The overall appearance of SOD1 activity was different in the tissue samples compared to that observed for *in vitro* derived CLs and EVs.

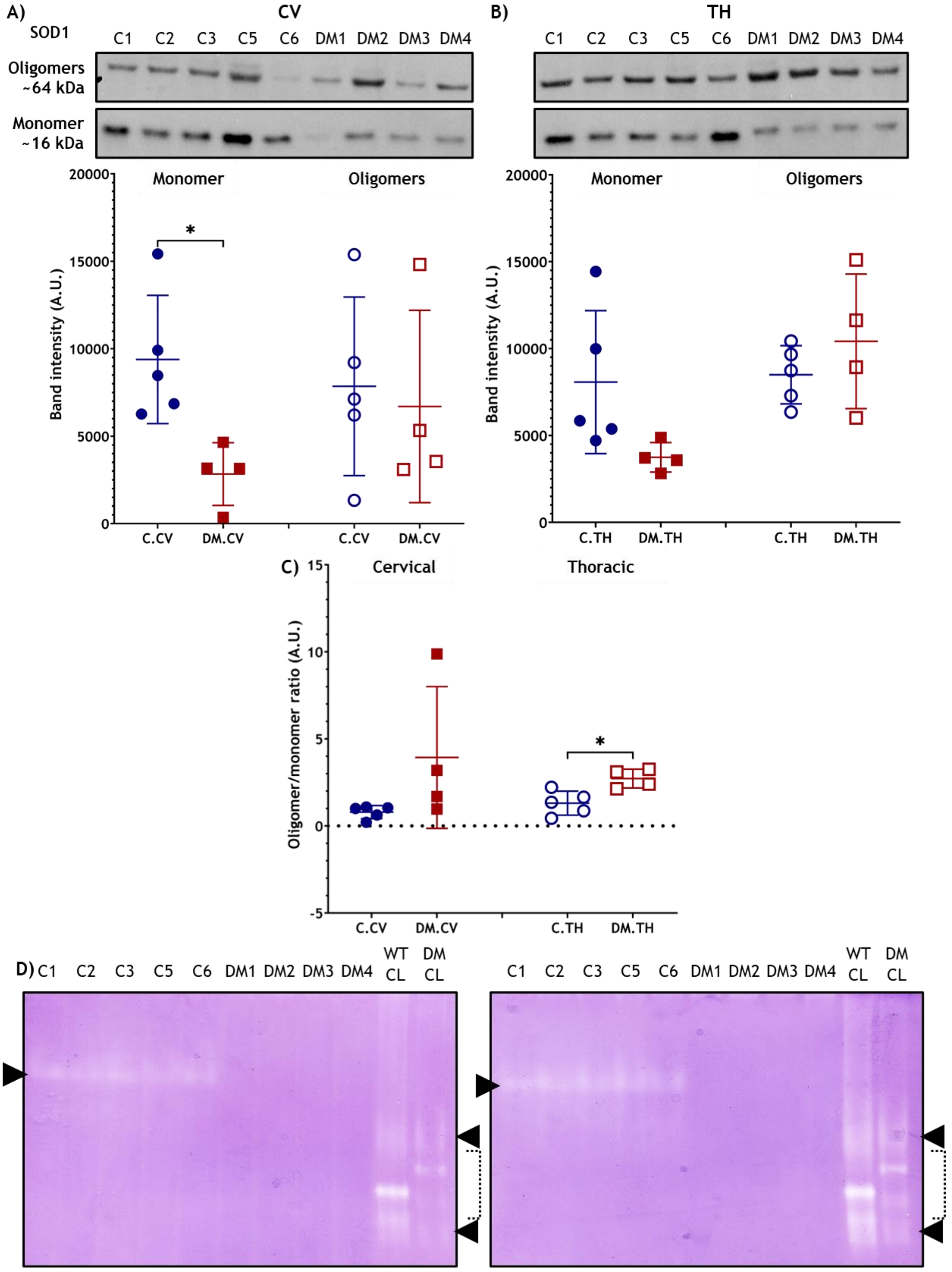

Figure 6-15: SOD1 protein and SOD activity in canine spinal cord regions. Proteins were separated in a gel then nitrocellulose membranes were probed with anti-CuZnSOD. Based on the molecular weight of the upper band in **A)**, it likely represents SOD1 oligomers, and the lower band represents the SOD1 monomer (~16 kDa). Bands were quantified and the band intensities (A.U.) were plotted in the graphs shown in **B)** and **C)** for cervical and thoracic regions. Unpaired t-tests were used to compare the band intensity of each SOD1 subunit with each genotype for the spinal cord segments separately. $^*p \leq 0.05$. **D)** Proteins were separated in a native gel and ultimately stained with NBT. SOD activity was still present in control cords, but not DM cords for both sections. WT- and DM-SOD1-EGFP control CLs from a previous experiment were included as positive controls for SOD activity. Endogenous SOD activity is highlighted by the arrowhead. In the CLs, the usual additional bands corresponding to the fusion protein activity were visible between two endogenous bands (area highlighted by the dotted bracket). The gel images were brightened to make the contrast clearer.

6.4.4.7 Proteins associated with EVs

The main EV marker used in *in vitro* studies was flotillin-1, but this was not identified in the TMT analysis so other EV markers, CD9, CD81 and ALIX were assessed further. The number of unique peptides, $\log_2$FC, FC *p* value and adjusted *p* values are found in Figure 6-16A. The abundance values of proteins associated with EVs were plotted for each case in graphs and proteins were compared between control and DM cervical (Figure 6-16B) and thoracic (Figure 6-16C) regions separately. CD9, CD81 and ALIX were statistically similar between control and DM groups in both cervical and thoracic regions of the cord. As these proteins were used to assess EVs, at this level, it appears there were no differences in the EV generation or production between groups or spinal cord sections.

CD81 was significantly higher in the DM thoracic cord compared to the cervical region ($p \leq 0.05$), but this difference was not observed in controls, potentially indicating CD81 was starting to increase in the DM thoracic cord. Caution must be exercised however as only one unique peptide was identified for CD81. CD9 was significantly higher in the cervical region of both groups compared to the thoracic region ($p \leq 0.01$) and this is likely to reflect a difference in the cell numbers between the spinal cord regions.

Flotillin-1 was investigated in tissue using WB. Flotillin-1 was present in all tissues (Figure 6-16D) and was statistically similar between groups in the cervical region but significantly decreased in the DM group compared to the control group in the thoracic region ($p \leq 0.01$). No other changes were observed between cervical and thoracic regions for either group. This change may indicate changes to plasma membrane/lipid raft integrity which could have an influence on EV formation/production.

A)

Protein	Accession (NCBI Db)	Unique peptides	log$_2$(DM.CV/C.CV)	*p* value	Adjusted *p* value	log$_2$(DM.TH/C.TH)	*p* value	Adjusted *p* value
CD9	XP_038315661.1	3	-0.16	0.988	1.000	-0.16	0.889	1.000
CD81	XP_038309992.1	1	0.06	0.848	1.000	0.25	0.908	1.000
ALIX	XP_005634263.1	7	-0.15	0.997	1.000	0.10	0.992	1.000

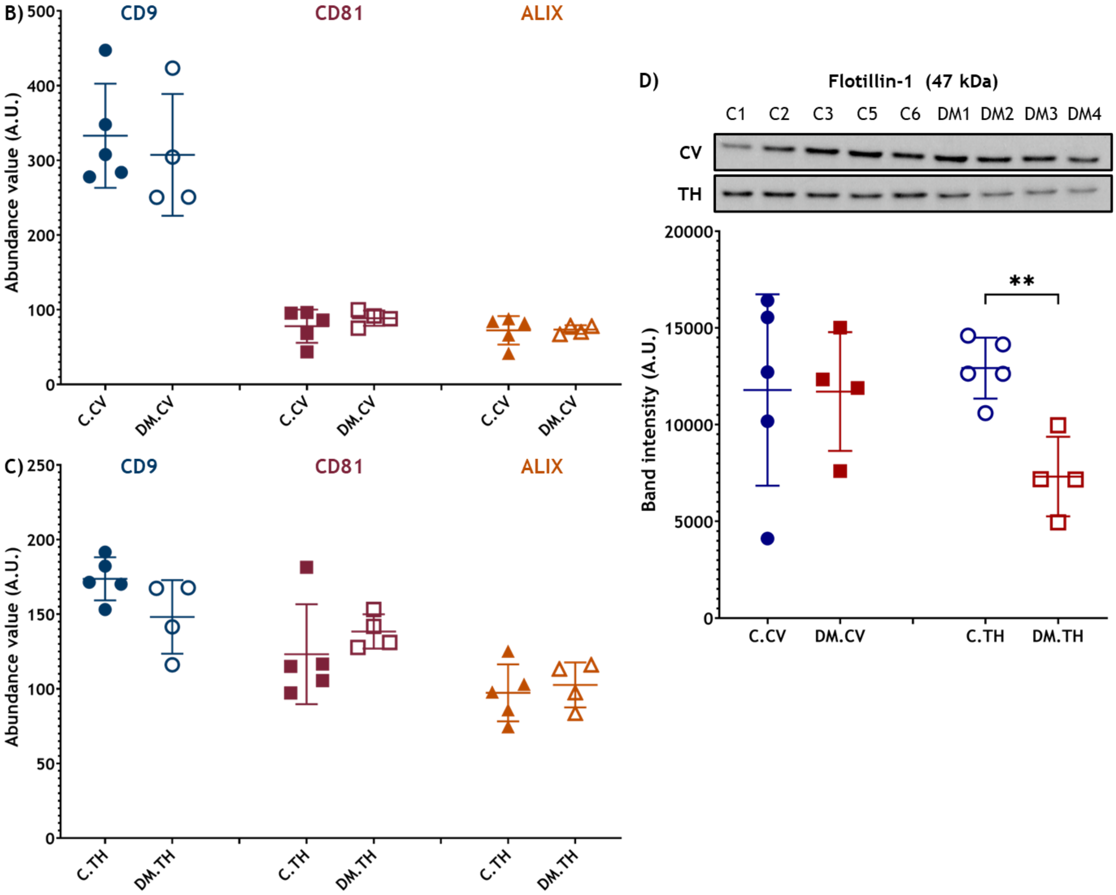

Figure 6-16: EV associated proteins in canine spinal cord. A number of proteins associated with EVs were extracted from the proteomics dataset and interrogated. **A)** The table summarises important information for each protein including the number of unique peptides, log$_2$FC, FC *p* value and adjusted *p* values. The abundance values obtained from TMT proteomic analysis for EV proteins were plotted in separate graphs for cervical (**B**) and thoracic (**C**) spinal cord regions. Unpaired t-tests (CD9, CD81 CV and ALIX) and Mann-Whitney tests (CD81 TH) were used to compare each protein between control and DM cases. **D)** Flotillin-1 was visible in WBs for cervical and thoracic segments. Bands were quantified and plotted in the graph. Unpaired t-tests were used to compare control and DM protein levels within each spinal segment. $^{**}p \leq 0.01$.

6.4.5 Additional proteins were selected for biochemical validation

Multiple proteins were significantly different between control and DM spinal cords. Specific proteins were selected based on the availability of antibodies for further validation. The number of unique peptides, $\log_2$FC, FC *p* value and adjusted *p* values are found in Figure 6-17A for l-lactate dehydrogenase A chain (LDHA) and l-lactate dehydrogenase B chain (LDHB). LDHA is associated with catalysing pyruvate to lactate while LDHB is associated with catalysing the reverse reaction (Ross *et al.*, 2010). The abundance values of proteins of interest were plotted for each case in graphs to compare each protein between control and DM cervical (Figure 6-17B) and thoracic (Figure 6-17C) regions separately. LDHA, but not LDHB, was significantly upregulated in cervical and thoracic segments of DM cases compared to controls (cervical $p \leq 0.01$; thoracic $p \leq 0.05$). With biochemistry, there were no statistically significant changes in LDH between DM and control groups in either spinal segment (Figure 6-17D). The difference in results between techniques may be explained by the binding of the LDH antibody to both LDHA and LDHB isoforms as the antibody was not raised specifically against one LDH isoform (MM correspondence with Abcam). A BLAST was conducted comparing the LDHA and LDHB protein sequences using the NCBI accession numbers raised by proteomics (Appendix 8.3.4.5). Sequences were 75% similar, so it is possible the LDH antibody binds to an epitope found within the similar sequence. Nevertheless, the apparent increase in LDHA in the DM spinal cord suggests there are changes to energy metabolism in DM.

A)

Protein	Accession (NCBI Db)	Unique peptides	$\log_2$(DM.CV/C.CV)	*p* value	Adjusted *p* value	$\log_2$(DM.TH/C.TH)	*p* value	Adjusted *p* value
LDHA	XP_035559651.2	7	0.38	0.002	1.000	0.68	1.00E-06	0.001
LDHB	XP_025311104.1	11	0.01	0.999	1.000	-0.05	0.926	1.000

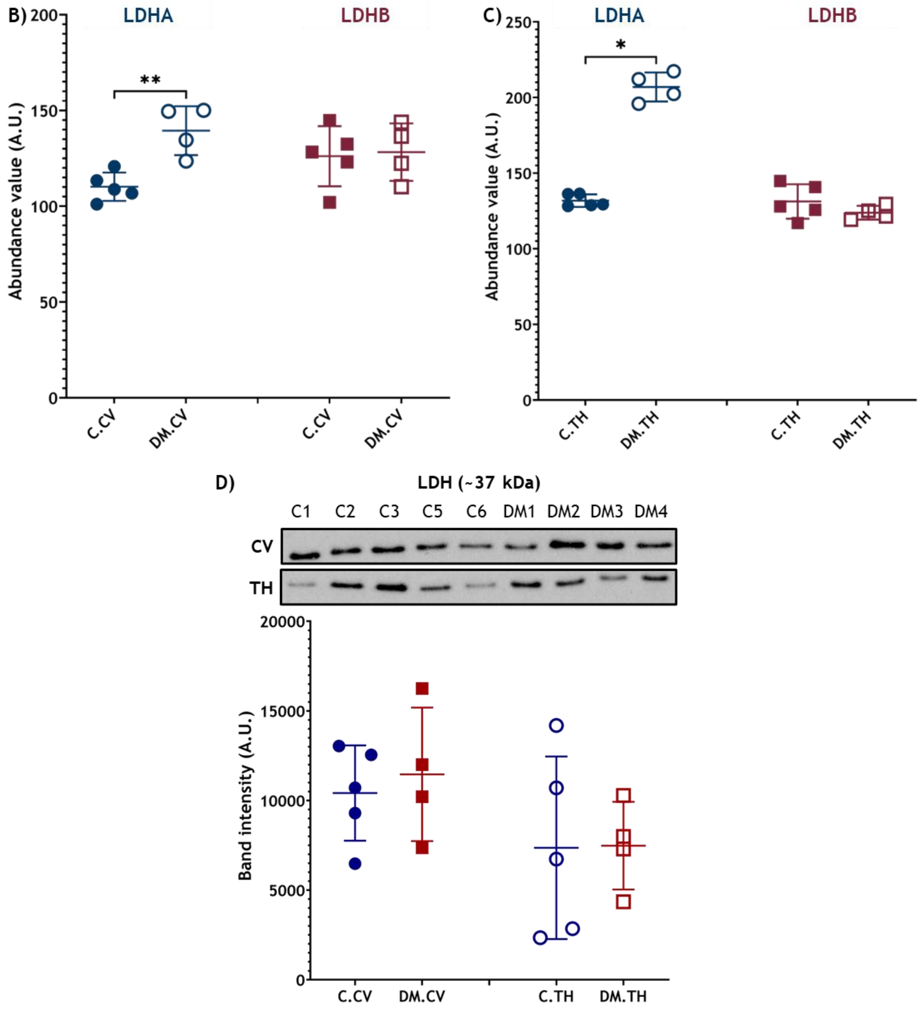

Figure 6-17: Additional proteins selected for validation with biochemistry. LDHA and LDHB were extracted from the proteomics dataset and interrogated. **A)** The table summarises important information for each protein including the number of unique peptides, $\log_2$FC, FC *p* value and adjusted *p* values. The abundance values obtained from TMT proteomic analysis for LDHA and LDHB were plotted in separate graphs for cervical (**B**) and thoracic (**C**) spinal cord regions. Unpaired t-tests (LDHA CV and LDHB) and Mann-Whitney tests (LDHA TH) were used to compare each protein between control and DM cases. $^*p \leq 0.05$; $^{**}p \leq 0.01$. **D)** Proteins were separated in a gel then the nitrocellulose membrane was probed with anti-LDH. Bands were quantified and values plotted in the graph. Unpaired t-tests were used to compare protein values within each spinal cord segment.

6.5 Discussion

6.5.1 Analysis of gene expression using mRNA

In future mRNA-based experiments, it may be worthwhile to include additional housekeeping primers to ensure samples are loaded consistently as some genes may vary depending on the disease state or tissue analysed (as discussed in Section 6.5.4 for example).

The lack of statistical differences in stress markers between DM and control samples at the level of mRNA contrasted previous studies of DM spinal cord tissue. Yokota *et al.*, (2018) found most genes associated with ER stress showed increased expression in DM spinal cord. *BiP*, *XBP1t* and *XBP1u* were moderately upregulated while *XBP1s* and ASK1 were significantly upregulated. Other apoptosis regulating proteins were not increased suggesting that specific UPR pathways involving the XBP1s and ASK1 proteins play a role in DM. The difference in findings between the current study and that of Yokota *et al.*, (2018) could be explained by the breed and age of animals used in the two studies. In the previous study, samples originated from PWCs that had succumbed to respiratory failure or pneumonia, likely due to reaching the end stage of DM, while in the current study, GSDs only displayed pelvic limb clinical signs. Findings could therefore represent two different stages of DM and/or breed differences which may be compounded by the physiological complications associated with respiratory failure.

6.5.2 Methodological considerations for protein assessment

6.5.2.1 Protein recovery from the canine spinal cord

Some proteins of interest were not presented because datasets were incomplete. This could have been the result of complications with protein extraction or processing. A trial experiment was performed before investigative proteomics to assess the efficiency of the protein extraction method (presented in Appendix 8.3.4.1). Significantly more protein was recovered from the SN compared to the pellet ($p \leq 0.05$), however an average of 23.4% of the total protein (pellet + SN) was left in the pellet. This protein may represent insoluble proteins and aggregates, membrane associated proteins and cellular debris. Further, due to the high lipid content of the spinal cord, the detergents used may not have sufficiently digested lipids meaning any proteins associated with lipids may have been lost. This may have been more important for proteomics studies as further processing using centrifugation before running the samples through the MS may have omitted these proteins, while in biochemical studies, no further processing was with centrifugation was carried out, so lipid associated proteins may still have been included. This could explain why flotillin-1, a protein associated with lipids, was identified using biochemistry, but not proteomics. For future proteomics studies, an additional step using sonication before protein denaturation may be beneficial. Finally, some protein abundances may be below the limit of detection with MS. Further, 23% of peptides were not assigned to a protein potentially because peptides were too long or short, or there may have been aberrant interactions between peptides after digestion

6.5.2.2 Potential dilution effect due to heterogenous sample

As the total spinal cord homogenate was used to extract proteins, samples will reflect a mixture of cell specific proteomes so the relative abundance of cell specific or pathway specific proteins will vary considerably. This could explain why proteins associated with microglia and EVs for example were difficult to quantify using proteomics. As DM is often reported to be non-cell autonomous (Nakamae *et al.*, 2015), it would be beneficial to separate the different CNS components, for example white matter and grey matter, in samples. This would allow for better assessment of pathological processes occurring in neurones and glia and it would minimise the dilution effect caused by the large proportion of myelin proteins and lipids for example. Further, validation using a targeted WB approach is advantageous as antibodies have high avidity therefore even a limited signal from a protein can be detected that may otherwise be missed by MS (for example LC3 in the current study).

6.5.2.3 Note on proteomics assessment

Proteins identified in TMT nLC-ESI-MS/MS were filtered using unadjusted *p* values (one-way ANOVA) instead of adjusted *p* values (Benjamini-Hochberg) as the latter uses a more stringent post hoc test which potentially missed some of the genuine biological changes. As this study was particularly interested in control versus DM in each spinal cord region separately, the less stringent one-way ANOVA with further unpaired t-tests or Mann Whitney tests were deemed acceptable. Log_2FC values below -0.5 and above 0.5 were highlighted in the volcano plots to give a better idea of which proteins were differentially expressed. This was particularly valuable for assessing the difference between spinal cord regions within each group. When comparing groups within the same spinal region however, few proteins reached this log_2FC threshold, so all proteins where $p \leq 0.05$ were included in the tables and for KEGG and GO analysis. Ultimately, in addition to generating new hypotheses, the use of proteomics in this study was to attempt to validate *in vitro* findings *ex vivo* and to test the hypothesis set out in Section 1.6, so specific proteins were also studied. Proteins of interest identified in proteomics must be further validated with biochemical tests before definitive statements can be made.

One of the limitations in this study is the small sample size. This can impact the power of statistical tests and may be one of the reasons that the post hoc test often produced nonsignificant adjusted *p* values. Also, the low number of genes associated with proteins means the numbers of genes associated with KEGG pathways and GO were low. Nevertheless, this study provided many meaningful insights into the processes involved in DM pathology.

6.5.3 Investigation of cell specific proteins

6.5.3.1 Neurones

The number or neurones present in HE sections were not quantified, however there were no noticeable losses. There was evidence that neurones were compromised to some extent as chromatolytic and swollen morphologies were present. There were clear losses of axonal material in the thoracic spinal cord sections of DM dogs. There was also loss of axons from the cervical region, however these changes were not as substantial as those seen in the thoracic region. The reduction of several neurone specific proteins identified in proteomics (NSE, NfL, NfM and NfH) and validated by biochemistry (NSE) in the thoracic cord, but not the cervical cord, may reflect the marked reduction in axons in the thoracic region, but mild reduction in the cervical region. In addition to the loss of axons, changes in the proteins assessed, particularly NSE, may indicate there are changes to neuronal metabolism. As previously discussed, the proteins assessed here have been investigated in several neurodegenerative diseases, including ALS, as biomarkers, so it is possible that they could be used in DM, however they may not be able to distinguish between DM and other neurodegenerative diseases. The absence of statistically significant changes in the cervical region may indicate the proteins are not produced early enough in disease to be detected before clinical signs develop, but they could be valuable indicators for prognosis if used with markers that do change.

6.5.3.2 Myelin

The proteomics study found PLP and MBP X1 were significantly reduced in the cervical region of DM cords compared to controls. In the thoracic region, PLP, MBP X4 and MAG were significantly lower in the DM group compared to controls and MOG had a downward trend, but this was not statistically supported. In a previous study, *MBP*, *MOG* and *MAG* gene expression in the DM spinal cord were assessed and it was found that *MBP* expression was significantly reduced compared to controls, *MOG* was statistically similar between groups and there was a general downward trend observed for *MAG*, but this did not reach statistical significance (Golubczyk *et al.*, 2019). Changes in the myelin organisation in the spinal cord of rats with an ALS associated SOD1 mutation were observed before symptoms were shown and proceeded to become more disorganised in paralysed cases. PLP and MBP were downregulated and this was accompanied by a reduction in phospholipids, cholesterol and cerebrosides (Traiffort *et al.*, 2021). In humans, increased levels of MBP in CSF samples can indicate there is an injury to myelin or a demyelinating disease is present in the CNS of patients. In a study of DM CSF samples, CSF attained from the lumbar region had significantly more MBP than the same region in controls and DM CSF from the cisterna magnum. In the cisterna magna derived CSF, there were no significant differences between control and DM groups (Oji *et al.*, 2007). Taken together, it can be suggested that the reduction in myelin proteins observed in the current study may be a reflection of myelin and oligodendrocyte loss in the DM spinal cord that is most advanced in the thoracic region.

In the thoracic region, MBP X1 was increased in the DM group compared to controls. MBP X1 is speculated to have roles in the immune system and in process outgrowth. The increase may indicate that oligodendrocytes were trying to regenerate lost processes and/or it could signify a signalling event to recruit microglia. In the study by Golubczyk *et al.*, (2019) they found monocarboxylate 4, a protein associated with microglia and astrocytes was elevated, but further assessment of microglia should be performed before any conclusions made on the functional significance of MBP X1 can be made.

Biochemistry allowed validation of PLP levels and the DM20 isoform. PLP was also signifcantly downregulated in the DM group in both the cervical and thoracic segments. DM20 was not statistically different, however a downward trend was observed in both regions in the DM groups, but it was more apparent in the thoracic region. These findings further imply that myelin was being lost in the DM spinal cord at both the cervical and thoracic region. Interestingly, as previously reported, NSE was not signifcantly different in the cervical region, so it is possible that this change in PLP indicates there was a structural change in the compactness of myelin before signficant changes were seen in the neuronal markers. Generally, demyelination is considered to be a secondary process to axonal degeneration in DM (Coates and Wininger, 2010), but in ALS, it is still a debated topic as there is evidence of myelin perturbations before axon degeneration and vice versa (Traiffort *et al.*, 2021).

CNP also showed downregulation in the DM dogs in this study compared to controls, but it only reached statistical significance in the thoracic region. As this protein is involved in allowing metabolites through the myelin sheath to the axon, it is possible that down regulation will negatively impact the ability of metabolites to go between the two structures. Literature shows that in CNP knockout mice, myelin remains present, however axonal degeneration appears in the corresponding myelinated axons (Traiffort *et al.*, 2021). As the current study also indicated a significant reduction in structural MBP, it is likely that the change in CNP is a consequence of structural abnormalities to myelin and it raises the possibility that axonal and/or oligodendrocyte metabolism could be affected in DM.

Oligodendrocyte CNP has also been used to demonstrate the interaction between neurodegeneration and lipid rafts. In normal conditions, 40% of CNP is thought to associate with the lipid raft fraction of cells and it can also associate with the actin and tubulin cytoskeletons of oligodendrocytes. Disruption to either of these networks can lead to changes in CNP organisation in addition to lipid changes (cholesterol specifically). It has therefore been suggested that CNP, in association with lipid rafts, can affect the cytoskeletal structure of myelin and axons (Hinman *et al.*, 2008).

Taken altogether, oligodendrocytes and myelin appear to be markedly affected in the earlier stages of DM in the thoracic spinal cord and this could affect the structure of myelin which could have subsequent effects on metabolic pathways between oligodendrocytes and neurones.

6.5.3.3 Astrocytes

Upon astrocyte activation, S100ß is known to be downregulated and secreted from cells while GFAP and vimentin are upregulated (Jurga *et al.*, 2021). S100ß showed a downwards trend in DM thoracic cord compared to controls. Previous studies have found that changes to this protein can be detected in the serum of patients with brain injuries and may indicate severity. It may therefore be worth investigating this protein further in biomarker studies (Jurga *et al.*, 2021). GFAP and vimentin results in this study aligned with astrocyte activation, at least in the thoracic region in both proteomic and biochemical analyses. Vimentin was also significantly higher in the cervical region when investigated with proteomics and validated with biochemistry suggesting astrocytes were potentially becoming activated in the region. As this precedes significant changes in neuronal markers but accompanies changes in myelin proteins, it could be surmised that early stages of demyelination initiated an astrocytic response. Assessment of GFAP gene expression by Golubczyk *et al.*, (2019) showed there was an upwards trend in DM cords, but it was not statistically significant. The lack of significance in the previous study may be suggestive of methodological differences, breed differences (GSDs not used) or may indicate a different stage of disease as the dogs studied were at an advanced stage of DM compared to the dogs studied in the current project. It could be postulated that astrocytes are recruited in the earlier stages of DM, but as the disease progresses and becomes more chronic, other cell types such as microglia may become activated (Golubczyk *et al.*, 2019). Typical markers of microglia were not identified in the proteomic dataset so this cannot be substantiated in the current study, however it may drive a potential hypothesis for future work.

EAATs found at the astrocyte surface are important for removing obsolete glutamate from the extracellular matrix to protect neurones from excitotoxicity (Ogawa *et al.*, 2014). Here, EAAT1 was significantly upregulated in the cervical and thoracic region of the spinal cord of DM dogs compared to controls (unpaired t-test). Glutamate reuptake can be regulated by changes to EAAT expression and activity and EAAT expression can be altered by neuronal signals. Some studies have found that increasing the concentration of extracellular glutamate can increase reuptake by astrocytes in a dose dependent manner and this can be facilitated by the upregulation of EAAT1 expression at the astrocyte surface (Duan *et al.*, 1999). Lipid rafts (introduced in Section 0) play a role in trafficking components to the plasma membrane and EAATs, particularly EAAT2, have been found in this fraction. Disruption to some lipids within the lipid raft fraction (specifically cholesterol) has been shown to negatively impact EAAT glutamate uptake (especially EAAT2) due to disruption to the transport of EAATs to the cell surface (Butchbach *et al.*, 2004). In a previous study of EAAT protein expression in DM PWCs using IHC, EAAT1 expression level was not statistically different between DM and control sections. EAAT2 was found to be downregulated in the same study (Ogawa *et al.*, 2014) but EAAT2 was not identified in the current dataset. The differences highlighted in the current study may warrant further investigation into both EAATs as it could indicate that the transporters have different expression levels between breeds and/or between disease stages. Further, it may be possible that early in DM, EAAT expression may increase to reduce the likelihood of excitotoxicity from the increased demand from neurones, but later in disease, lipid rafts and/or other cellular structural components, such as the actin cytoskeleton (explained in next section) may become disrupted, affecting the transport of EAATs to the cell surface. This hypothesis may fuel future work, but as vimentin and GFAP markers were generally upregulated in the present study, it is possible that the increase in EAAT1 was a consequence of increased astrocyte activation in the DM spinal cord.

DM HE sections displayed mild hypercellularity that is consistent with gliosis, however identification of astrocytes specifically is challenging with HE alone (correspondence with UoG neuropathologist Angelika Rupp). Before publication, immunohistochemistry (IHC) for an astrocyte marker, for example GFAP, will be carried out on control and DM sections to validate the proteomic and biochemical findings regarding astrocyte activation/proliferation.

6.5.4 Investigation of housekeeping proteins

Three proteins used as housekeeping markers in *ex vivo* and *in vitro* RNA and protein studies were assessed by proteomics. β-actin was significantly different in the DM thoracic cord compared to controls, but no differences were observed in the cervical region. This was validated by WB indicating that β-actin may not be appropriate as a loading control in DM studies. Results from the proteomics study highlighted GAPDH or Cyc as alternatives for further validation. The increase of β-actin in DM may be the result of the significant increases in astrocytes, increasing hypercellularity in the spinal segment or it could indicate regeneration of neurones and oligodendrocytes/processes. It could also indicate structural changes in CNS cells which could be linked to changes to lipid rafts which has been suggested by researchers in the ALS field (Zhai *et al.*, 2009). The current project suggests the actin cytoskeleton is affected early in DM and this may have ramifications for cell structure and transportation of lipid rafts, EVs, proteins and more. For example, early on, EAAT expression at the astrocyte cell surface may increase to prevent excitotoxicity, but later in disease, changes to lipid rafts and the actin cytoskeleton may lead to downregulation of the transporters as observed in other studies (Duan *et al.*, 1999; Ogawa *et al.*, 2014). The interactions between lipid rafts, the cytoskeleton and oligodendrocytes were discussed previously (Section 6.5.3.2).

6.5.5 Markers of neurodegeneration found in DM cord

6.5.5.1 SOD1 associated with DM

There was no significant difference in the proteomic abundance of SOD1 in DM or control groups. With further biochemical analysis, monomers and oligomers were identified and assessed individually. Monomers showed a downwards trend in cervical ($p \leq 0.05$) and thoracic regions ($p = 0.0807$) in the DM samples compared to controls. Oligomers were similar in control and DM groups in both regions, but a mild increase was potentially starting to appear in the DM group. When the oligomer to monomer ratio was assessed, it was higher in the DM group of both spinal cord regions but only significant in the thoracic region ($p \leq 0.05$). It is possible that the oligomers represent the soluble oligomer species suggested in some studies to precede insoluble aggregate formation (Draper *et al.*, 2020; Tiwari and Hayward, 2005). Oligomers are formed when monomers accumulate and can start off soluble and become insoluble (Wakayama *et al.*, 2022). These oligomers recruit monomers and their growth plateaus when monomers decrease, at least in studies investigating ALS associated SOD1 mutants (Hanspal *et al.*, 2017). The findings in the current study indicate there may be increase conversion of monomers to oligomers in both regions of DM cases compared to controls, but it is only significant for the thoracic region. Insoluble SOD1 was not assessed, but before further publication, this would benefit the study as it may indicate if there was also an increase in insoluble SOD1 oligomers and aggregates. To assess insoluble SOD1, IHC of the canine tissue with anti-SOD1 and biochemical assessment of the pellet fraction from tissues should be considered.

In a previous study by Pfeiffer *et al.*, (2023), monomeric SOD1 from the thoracic cord of dogs was quantified by WB and a significant increase in monomeric SOD1 was reported in the DM cord compared to controls. In the current study, monomers appeared lower in the DM cord compared to controls. The DM stage of dogs in both studies were approximately the same (between Grade 2 and Grade

3), but there were differences in the breeds used. It is possible that the pathological mechanisms are slightly different between the breeds, however methodological differences in SOD1 isolation and analyses may explain the differences more effectively. A previous study investigating human WT and mutant SOD1 in a MN derived cell line found monomeric mutant SOD1 was lower than WT-SOD1 after WB analysis despite mutant SOD1 presenting with more aggregates than WT-SOD1 with microscopy. They suggested this could be because some mutant SOD1 was sequestered into insoluble aggregates, and/or there was increased clearance of the monomeric mutant form. When monomeric and oligomeric SOD1 was assessed together using flow cytofluorometric analysis, mutant and WT SOD1 levels were comparable (Onesto *et al.*, 2011) likely reflecting more soluble and less insoluble SOD1 in WT samples and more insoluble and less soluble SOD1 in the mutant group. DM studies have found a similar trend: Crisp *et al.*, (2013) found soluble SOD1 was comparable between DM and control animals while insoluble SOD1 in the pellet fraction increased as DM progressed. Draper *et al.*, (2020) have also reported significantly more SOD1 in WT expressing cells than in cells expressing mutant SOD1 and suggest this change could be due to the negation of insoluble SOD1 from WBs. This further suggests the insoluble fraction should be investigated in the current study along with assessment *ex vivo* (IHC).

The apparent change in the ratio of monomers to oligomers suggests there was a change in the population of SOD1 species that may influence the level of active dimers in the tissue. There are mixed reports on the impact of the E40K SOD1 mutation on the activity of the protein, but generally, as the mutation does not occur within the metal binding regions, activity is thought to be retained. Furthermore, *in vitro* experiments using recombinant E40K SOD1 proteins have found the protein retains enzymatic activity (Crisp *et al.*, 2013; Qi *et al.*, 2019). In the current study assessing SOD activity in tissues, it was found that activity was lost in the DM tissues. Evidence to corroborate this *ex vivo* finding was not found in the DM field, however SOD1 activity loss has been reported in various studies of ALS cases assessed in a report by Saccon *et al.*, (2013). Despite this, a change in SOD1 activity is not thought to cause DM or ALS but is considered a contributing factor to pathogenesis as loss of function could contribute to oxidative stress and changes to cellular metabolism. It has also been noted that loss of function and gain of function by SOD1 in ALS may be interlinked and contribute to ALS progression (Saccon *et al.*, 2013). Draper *et al.*, (2020) also acknowledged that in DM, activity has only been addressed in recombinant SOD1 proteins and not endogenous SOD1. The previously introduced bone marrow derived mesenchymal stem cells from DM cases would allow more accurate assessment of endogenous E40K mutant SOD1.

6.5.5.2 Nonspecific neurodegeneration markers

The proteomics dataset was interrogated for various markers for DM and neurodegenerative diseases but some, including α-synuclein and specific proteins associated with fALS, were not identified. ApoE is found in the CNS and is predominantly produced by astrocytes. It is thought to play a role in lipid recycling and to influence myelin and neurone membrane turnover. Upon damage to cells, lipids that have been dispelled from cells are taken up by astrocytes where apoE is attached, then these complexes are secreted and used for the generation of myelin and neuronal membranes (Hesse *et al.*, 2000). ApoE was significantly higher in the thoracic region of DM cords compared to controls in this study, potentially suggesting there was an increase in lipids in the environment that were subsequently attached to apoE and released into the milieu for the reformation of myelin membranes and potentially also neuronal membranes. This could also link in with the increase in MBP X1 in the same samples in suggesting oligodendrocytes were regenerating/developing new processes.

Tau is a neuronal microtubule-associated protein that is involved in axon transport and neurone structure. It has been proposed that total Tau levels in the CSF could act as a biomarker for ALS diagnosis as levels are significantly increased in patients compared to controls. Further, it was associated with an older age at onset, fast progression and higher volumes were found in those ALS patients with a spinal onset. The increased levels of this protein in the CSF are thought to reflect the significant axonal loss found in ALS (Agnello *et al.*, 2021). In the current proteomic dataset, Tau was significantly decreased in the thoracic region of DM dogs compared to controls, potentially suggesting a similar mechanism in DM.

6.5.6 Cell clearance/toxicity pathway investigation

6.5.6.1 Heat shock protein response

HSP70-1 was similar between control and DM groups in both spinal cord regions further suggesting in conjunction with gene expression results that ER stress was not present. In a previous study of DM mid-thoracic spinal cord using IHC, HSP70 was upregulated in ependymal cells, but not the white matter or grey matter. GSDs with DM were not studied, and the dogs were reported to be at the end stage of DM, so it is possible that this captured a different period of time compared to the animals in the present study, and there could be breed differences. The authors suggested that HSP70 in the spinal cord had a role in inflammatory processes in DM (Lovett *et al.*, 2014).

BiP and HSP90 proteins were significantly upregulated in the DM thoracic cord compared to controls when unpaired t-tests were used suggesting these chaperones contributed to the refolding of misfolded proteins (SOD1 and others). As *BiP* mRNA did not appear to increase, it is possible that BiP protein was starting to accumulate through interactions with misfolded proteins, but signalling for upregulation may not have been initiated yet. It has been shown in ALS that upregulation of BiP is not consistently found in patients with early-stage ALS (or pre-symptomatically). Further, it has been surmised that upregulation of BiP does not occur until the later stages of the UPR (Prell, Lautenschläger and Grosskreutz, 2013). This refolding may have started in the cervical cord of DM cases as a borderline significant difference in HSP90ß was seen. Calnexin also showed an upwards trend in DM cases in the thoracic region, but this did not reach significance.

6.5.6.2 The ubiquitin proteasome system and the unfolded protein response

In the present study, E2 was significantly upregulated in the thoracic cord of DM samples compared to controls while PMSA1 was not significantly different. It could be surmised that ubiquitination is upregulated in the DM spinal cord to label misfolded and dysfunctional proteins, as indicated by the changes in HSPs and the statistically significant increase in ubiquitin in the WB of samples. The latter has also been shown in other studies (Ogawa *et al.*, 2011; Ogawa *et al.*, 2014). The lack of statistical difference in PMSA1 indicates levels of this proteasomal enzyme were normal, however it could indicate that upregulation to cope with the increased ubiquitinated protein load was not initiated.

As previously discussed in Section 1.4, several DM studies have found the UPR can be activated in DM cases and they have used PDI, CHOP (Chang *et al.*, 2019) and BiP (Yokota *et al.*, 2018) to confirm this. In the current study, an upwards trend in PDI was observed in the DM thoracic cord compared to controls, however it did not reach significance with the stringent nonparametric test. The less stringent unpaired t-test showed the change was significant and further suggests there would be a benefit in investigating this protein further. There was a clear change in PDI and induction of ER stress in the study by Chang *et al.*, (2019), but in the current study, ER stress did not appear to be induced. GSDs were not used in the study by Chang *et al.*, (2019) and dogs were at various stages of DM but grouped together. Nevertheless, it could indicate breed and/or disease stage differences.

6.5.6.3 Autophagy

Previously, it has been suggested that the fusion of the autophagosome to the lysosome is deficient in DM as evidenced by an increase in p62 accumulations (Ogawa *et al.*, 2015). The proteomics dataset was interrogated for markers of autophagy including p62 and LC3, but they were not reliably identified in the TMT proteomics dataset. LC3BI and LC3BII were identified in the samples using biochemistry, however WBs were not clear enough to make firm conclusions, but they may be used to derive hypotheses to be tested as similar findings have been reported in other DM studies (Ogawa *et al.*, 2015). There was a statistically significant increase in the LC3BII/LC3BI ratio in the DM thoracic spinal cord and similar trend has been observed in a previous DM study, but white matter and grey matter were separated. Only the white matter displayed significance, and this was a result of increased autophagy due to the significant axon and myelin degradation in the white matter (Ogawa *et al.*, 2015). In the current study, the ratio is likely to reflect an increase in autophagy secondary to myelin/axon degradation, although further studies separating the cell types would be required. Other findings by Ogawa *et al.*, (2015) suggested deficient autophagy may lead to the accumulation of LC3BII positive autophagosomes in DM. A significant increase was seen in the current study for LC3BII in the thoracic DM cord potentially indicating a build-up of autophagosomes. Further, in the cervical cord, LC3BI was significantly increased in DM cases but LC3BII was not indicating autophagy was likely upregulated, but still functional at the earlier stage of the disease. Employment of a visual technique such as electron microscopy would be valuable to test this theory in future studies.

In addition to the other functions mentioned in Section 1.4, ANXA1 upregulation has been linked to autophagy activity (Kang *et al.*, 2011; Xi, Ju and Wang, 2020). It was postulated by Kang *et al.*, (2011) that this may aid in the recycling of nutrients as AXNA1 is upregulated in times of nutrient starvation. In the current study, ANXA1 showed an upwards trend in both spinal cord regions of DM dogs, with statistical significance in the thoracic cord (cervical p= 0.064; thoracic p= 0.0002). It could be suggested that cells induced autophagy to clear misfolded proteins and to gain the components needed to produce correctly folded proteins. As the trend was seen in both regions, it could be suggested that autophagy had been upregulated to cope with the axon and myelin degradation occurring. ANXA1 upregulation can also trigger apoptosis and it can ensure that apoptotic cells are recognised by phagocytes including microglia in the CNS (Sheikh and Solito, 2018). ANXA1 can regulate NO when the inflammatory response is triggered to prevent the release of iNOS (Sheikh and Solito, 2018). As iNOS has been suggested to be upregulated in the DM spinal cord (Ogawa *et al.*, 2011), it is also possible that ANXA1 was increased to reduce the production of iNOS in an attempt to reduce the reactive oxygen species (ROS) present. These findings highlight further specific analysis should be carried out to investigate ANXA1's role in DM.

Findings suggest that autophagy should be considered within the context of the different cell types in the CNS. For example, in neurones, autophagosomes are often generated in the axon while most lysosomes reside in the cell body. Amphisome formation has been linked to the transport of autophagosomes to the cell body to allow for fusion with lysosomes. Disruption to amphisome formation could therefore prevent fusion of autophagosomes and lysosomes and lead to accumulation of autophagosomes in the axon which could also have an impact on macroautophagy and organelle specific forms of autophagy including mitophagy (autophagy of mitochondria) (Cai and Ganesan, 2022). The endosome and general intracellular transport will be discussed later (Sections 6.5.7 and 6.5.8). In oligodendrocytes on the other hand, autophagy may be an important pathway to degrade membrane and cytoplasm components in the long-lived cells. Inhibition of autophagy in oligodendrocytes of a mouse model showed a delayed onset of neurodegeneration. MBP, PLP, MOG and MAG can be found in LC3 positive vesicles including autophagosomes, autolysosomes and amphisomes, implying that autophagy is used for myelin protein turnover. When autophagy is inhibited in oligodendrocytes, this can lead to changes in myelin structure and neurodegeneration, but only after a period of time and not during development. Changes to myelin sheath morphology can result in the presence of axonal spheroids, indicating the presence of axon degeneration. There is a fine balance between the degradation and formation of myelin that must be retained for proper CNS functioning (Aber *et al.*, 2022).

6.5.6.4 Apoptosis and programmed cell death

CTSD is a lysosomal proteolytic enzyme, but it can translocate to the cytoplasm when needed, for example, during oxidative stress, or to the extracellular space. A previous study using ALS mutant SOD1 mice found significant increases in CTSD in the spinal cord of ALS mice by biochemistry and found a disruption to the normally punctate appearance of the protein in neuronal lysosomes by IHC. The authors suggested that these enzymes could contribute to widespread degeneration seen in MNs in ALS (Wootz *et al.*, 2006). Further, CTSD has been linked to apoptosis (Deiss *et al.*, 1996). The increase in CTSD in both regions of the DM spinal cord may indicate that the protein was transported to the cytoplasm and caused aberrant degradation of proteins. This could be explained by the significant axon and myelin degradation observed in the DM cases and could also indicate that apoptosis was induced (Deiss *et al.*, 1996). Inclusion of a TUNEL assay for example would be of value to test for the presence of apoptosis within the spinal cord.

6.5.7 EV protein investigation

EVs isolated from the CNS of SOD1 models and ALS patients have been used to understand the neurodegenerative changes in the disease and potential propagation of pathology. In the current study, flotillin-1 was the main marker for EVs in cell culture experiments and therefore investigated *ex vivo*. The protein was identified by WB, but it was not detected in the proteomics dataset. With WB, flotillin-1 was statistically similar between groups in the cervical region but was significantly reduced in the thoracic region of DM dogs compared to controls. Subcellular fractionation was not performed and since flotillin-1 is associated with lipid rafts in the plasma membrane of cells, it was not possible to differentiate EV or membranous populations. Further, in the proteomics dataset, three additional EV markers, CD9, CD81 and ALIX were assessed and found to be statistically similar between both groups in both spinal cord regions. Combined, these results suggest the reduction in flotillin-1 potentially reflects a reduction in plasma membrane associated lipid rafts, which are found in all CNS cells (Moll *et al.*, 2021), possibly as a consequence of degeneration of axons and myelin in the DM spinal cord. An example of this suggested mechanism can be found in McGonigal *et al.*, (2021) where disruption to the plasma membrane due to a deficiency in gangliosides (glycosphingolipid subtype) caused changes to lipid rafts as indicated by a shift of flotillin-1 out of the raft associated fractions. This was studied in transgenic mice with a neurodegenerative phenotype and reduced lifespan (McGonigal *et al.*, 2021). In a proteomic study of lipid rafts extracted from the spinal cords of transgenic mouse SOD1-ALS models, many proteins of neuronal and glial origin were found to be differentially expressed between the model and controls. Mutant SOD1 was found in the lipid raft fraction and it was suggested that mutant SOD1 could therefore affect intracellular signalling, cell to cell interactions and other lipid raft associated functions (Zhai *et al.*, 2009).

Only one unique peptide was found for CD81 so caution should be exercised when drawing conclusions at the current stage. It was potentially higher in the DM thoracic region compared to the cervical region, but this difference was not reciprocated in controls. A previous study using a murine SOD1 ALS model found flotillin-1 and CD81 were enriched in vesicles associated with mutant SOD1 within neurones. They suggested this indicated early formation of EVs which would be secreted, resulting in spread of SOD1 to other cells (Salvany *et al.*, 2022), therefore this protein may be of interest in future studies. ANXA1 is also associated with EVs and is believed to have anti-inflammatory roles in this form (Sheikh and Solito, 2018). A study to investigate EV formation should be based on Salvany *et al.*, (2022) where EV associated proteins are marked with fluorescent or coloured labels in immunocytochemistry or IHC respectively allowing localisation of proteins. To assess EVs in the extracellular space, EVs should be isolated from tissue, similar to that described in Silverman *et al.*, (2019) and then studied with various proteomic and biochemical techniques.

6.5.8 Proteomics suggest cellular metabolism changes in DM

Neuronal axons and oligodendrocytes have a mutual dependency on each other to meet metabolic demands for normal axonal functioning and myelination. For this reason, oligodendrocytes/myelin and neurones are particularly sensitive to changes in energy metabolism (Traiffort *et al.*, 2021). Glycolysis is an important metabolic process where glucose is broken down into pyruvate. In aerobic conditions, pyruvate enters mitochondria where it fuels the tricarboxylic acid cycle and undergoes oxidative phosphorylation, producing adenosine triphosphate (ATP). In anaerobic conditions, pyruvate is catalysed to lactate by LDH (Yao *et al.*, 2023). Lactate is found in the CNS when aerobic respiration is present and may be utilised by the CNS during stressful conditions for energy by the alteration of LDH isoform ratios (Ross *et al.*, 2010). Additionally, lactate is a signalling molecule in the body, including in the CNS (Yao *et al.*, 2023) and glia and neurones can share lactate (Ross *et al.*, 2010). It is likely that neurones meet their high energy demands by metabolising substrates from glia, including lactate, and glucose (Vandoorne, De Bock and Van Den Bosch, 2018).

LDHA deficiency in astrocytes results in less lactate being produced and may affect energy availability for neuronal functions. In stressful conditions, lactate is upregulated and is thought to protect neurones from sustaining damage, however chronic stimulation of these pathways may lead to defects in sustaining the lactate production. Disruption to oligodendrocyte production of lactate has also been associated with neuronal disruption (Yao *et al.*, 2023). Lactate can move in a gradient dependent manner into neurones but when neurones use lactate and other substrates from glia, ROS are produced (Vandoorne, De Bock and Van Den Bosch, 2018). Oxidative phosphorylation also results in the production of superoxide ROS, the substrate for SOD1 and SOD2 (Smith, Shaw and De Vos, 2019). These ROS upregulate lipid generation and the lipids can be transported back to glia and used as energy sources. If the interaction between neurones and glia is impeded, neurodegeneration can occur. When neurones are subject to stress due to energy deficits, the use of glial derived substrates can lead to an influx of ROS which can compromise cells by putting them at risk of oxidative stress (Vandoorne, De Bock and Van Den Bosch, 2018). Oxidative damage to DNA, proteins and lipids can occur and cause various cellular disturbances including excitotoxicity, protein aggregation, ER stress and death. SOD1 can present with oxidative damage, and this can encourage misfolding and aggregation of the protein (Smith, Shaw and De Vos, 2019). If cellular stress is not rectified, cells can die (Vandoorne, De Bock and Van Den Bosch, 2018).

The increase in LDHA but not LDHB in the current study suggests there was an upregulation in the conversion of pyruvate to lactate in the DM spinal cord which further suggests there was an increase in anaerobic respiration and/or compromised conditions such as stress. Generally, a reduction in aerobic respiration and increase in anaerobic respiration is associated with defective mitochondria and is characteristic of aging (Ross *et al.*, 2010), but something may exacerbate it in DM. As LDHB was unchanged, it suggests the conversion of lactate back to pyruvate in neurones was not affected. In a study by Zhai *et al.*, (2009), LDHB was found to be downregulated in the lipid raft fraction isolated from a SOD1-ALS mouse model, so it was surmised that metabolic support from astrocytes was disrupted in the model.

In the GO analysis of proteins, many pathways relating to calcium (Ca^{2+}) homeostasis were significantly upregulated in DM thoracic segments compared to controls. Ca^{2+} intracellular signalling within neurones is perturbed in many neurodegenerative diseases including ALS (Vollrath *et al.*, 2014). Neurones are a cell type that are particularly vulnerable to Ca^{2+} induced toxicity due to the high prevalence of Ca^{2+} permeable ion coupled receptors and low quantity of Ca^{2+} buffering proteins which are important for normal function (Leal and Gomes, 2015). Mild changes to Ca^{2+} levels in neurones can lead to long term cellular damage (Vollrath *et al.*, 2014). As previously described in Section 0, changes to lipid rafts can affect intracellular Ca^{2+} as they regulate many Ca^{2+} channels (Vollrath *et al.*, 2014). In ALS where SOD1 mutations are present, intracellular Ca^{2+} overload has been found to affect MNs and buffering proteins appear to show reduced expression in the axons of MNs in ALS patients. As Ca^{2+} binding proteins are reduced in MNs overall compared to other cell types, mitochondria potentially have a greater responsibility for buffering the Ca^{2+} ions. Increased intracellular Ca^{2+} can lead to mitochondria becoming overloaded with Ca^{2+} which can cause ROS production and oxidative stress which can eventually lead to cell death (Leal and Gomes, 2015).

Mutant SOD1 has been found to accumulate in the mitochondrial intermembrane space in ALS studies and this accumulation can affect mitochondrial function by interfering with oxidative phosphorylation and the mutants have been found to bind to apoptosis related proteins associated with the mitochondria including Bcl2. Additionally, mitochondrial SOD1 accumulation can negatively affect Ca^{2+} homeostasis, and the interaction between the ER and mitochondria (discussed in Section 0). Intracellular saturation with Ca^{2+} can also cause SOD1 to aggregate when it is in the immature (apo-SOD1) state (Leal and Gomes, 2015). Disruption to Ca^{2+} homeostasis can also affect general proteostasis. When Ca^{2+} is preferentially channelled to the mitochondria, Ca^{2+} can become depleted in the ER which can affect protein folding and proteasomal degradation. As in other circumstances, this can lead to ER stress and apoptosis if not rectified. Ca^{2+} dysregulation can also impact a MN’s ability to mediate excitotoxicity caused by glutamate ions and can induce Ca^{2+} dependent apoptosis as cytoplasmic Ca^{2+} increases (Leal and Gomes, 2015).

6.6 Conclusions

In this study, samples were collected from GSDs at an early stage of DM where pelvic limb paraparesis was observed and the thoracic region of the cord had the most histopathological changes compared to the cervical region. Proteomics data identified several changes that reflect the heterogeneity of the cellular population in the spinal cord and provided some indication of their response to pathological changes associated with the disease (summarised in Table 6-4).

Myelin disruption and astrocyte activation appeared to occur in the less effected cervical region and became more apparent in the thoracic region where more proteins associated with these lesions were differentially expressed. Clear changes to neurones were absent in the cervical region but appeared in the thoracic cord where protein changes potentially reflected axon degeneration.

Evidence was provided suggesting that certain phases of the UPS and autophagy pathways may be disrupted early in DM which may lead to the accumulation of proteins and eventual apoptosis. In the cervical region, there were changes to few proteins associated with the UPS (ubiquitin) and autophagy (LC3BI and cathepsin D) but in the thoracic region, many more proteins indicative of changes to protein processing pathways were observed (Table 6-4). The data suggest there were changes to protein processing and that induction of ER stress the UPR were potentially imminent in the thoracic region of the cord. The study also showed there were potential changes to structural components in cells of the thoracic cord, but not the cervical cord, at least in terms of the actin cytoskeleton and the plasma membrane/lipid rafts. These changes could further impede on normal cellular and protein processing functions within cells of the spinal cord. Proteomics and biochemistry highlighted that changes to cellular metabolism and oxidative homeostasis may play roles in DM. The changes in LDHA levels within both regions of the spinal cord potentially indicate a reliance on using glial derived metabolites for energy by neurones to meet normal energy demands. Furthermore, there were changes to Ca^{2+} regulation which may reflect changes in Ca^{2+} associated proteins, lipids and/or mitochondrial disfunction. All these changes are associated with ROS generation and given that SOD1 activity appeared to be disrupted in DM, this could suggest there was insufficient ROS clearance from cells.

Table 6-4: Proteins significantly different in spinal cord regions of DM dogs.

Marker	*Cervical*		*Thoracic*	
	Protein	Expr.	Protein	Expr.
Neuronal	N/A	-	NSE, NfL, NfM, NfH, Tau	↓
Myelin	PLP, MBP X1	↓	PLP, MBP X4, MAG, CNP	↓
			MBP X1	↑
Astrocyte	Vimentin, EAAT1	↑	GFAP, vimentin, EAAT1	↑
Protein processing	CTSD, Ubiquitin, LC3BI	↑	BiP, HSP90ß, E2, ubiquitin, CTSD, ANXA1, LC3BII	↑
Lipid/ metabolism	LDHA	↑	LDHA, apoE	↑
Structural	N/A	-	ß-actin	↑
			Flotillin-1	↓

Proteins presented in the table were significantly different between control and DM cases within each spinal segment. Whether protein expression was up (blue) or down (red) regulated in the DM spinal cord is indicated by “Expr.”.

7 General discussion and future direction

This PhD project aimed to use a multistrand approach to investigate the initiation and progression of DM. It was hypothesised that the *Sod*1 mutation causes misfolding of the SOD1 protein which can disrupt various protein processing pathways within cells of the spinal cord. This may drive changes to protein (including SOD1) and lipid processing which could have consequences for EV production, cell metabolism and structure. Ultimately, these changes have a detrimental impact on CNS homeostasis resulting in axonal degeneration and demyelination, culminating in paresis and eventual paralysis in affected dogs. The combination of clinical signs, histopathology and genetics make DM an alluring naturally occurring large animal model for human ALS (Story *et al.*, 2020).

In vitro and *ex vivo* samples were derived and examined with a range of biochemical and proteomic techniques to test the hypothesis. *In vitro* cell culture systems were used to investigate the dynamics of protein processing and EV production while the *ex vivo* study was used to examine the proteome of dogs with DM compared to controls. DM dogs in this study were euthanised when they became non-ambulatory and histopathological assessment was carried out to confirm the presence of lesions associated with the disease. All dogs were genotyped using an in-house assay; all controls were *Sod1:c.118G* (WT) homozygotes and all DM cases were *Sod1:c.118A* homozygotes.

7.1 Discussion and updated hypotheses

7.1.1 Summary of CNS findings

The impact of the *Sod*1 mutation on the behaviour of the SOD1 protein has not been clearly defined for DM or ALS as it appears to have a diverse range of roles in disease pathogenesis and progression (Crisp *et al.*, 2013; Nakamae *et al.*, 2015). *In vitro* cell culture findings presented in this thesis show that disruption to the typical cellular protein processing pathways autophagy and the ubiquitin proteasome system can have significant implications for SOD1 processing within cells and the compartmentalisation of the protein into extracellular vesicles.

The alternative mechanisms set in motion after these pathways are disrupted appear to be influenced by the conformation of SOD1, with cells expressing the DM associated E40K mutant SOD1 being more likely to show higher levels of SOD1 aggregation. The key observations in this study were based on the assessment of SOD1 and pathway associated proteins, but markers for key signalling components in the cell membrane, including flotillin-1, led to the speculation that lipid rafts may be disrupted by *Sod*1 mutations.

Findings from the proteasome inhibition experiments seem to be the most likely to parallel the changes seen in *ex vivo* spinal cord experiments. The main similarity is the proposal that the organisation of membranous components such as lipid rafts may be disrupted as suggested by changes in cellular flotillin-1 and EV formation and secretion. Further assessment of UPS associated proteins within spinal cord samples suggested there is decreased efficiency in the UPS within the DM thoracic spinal cord and coupled with findings in other studies, discussed in Sections 0 and 6.5.6.2, could be one of the initiating factors of DM. The autophagy inhibition and ER stress induction experiments may represent changes seen at different stages of DM progression. The proposed hypotheses developed from findings in this thesis are as follows and are summarised in Figure 7-1.

Age related changes to the UPS may lead to accumulation of mutant SOD1 within the cytoplasm and mitochondria of neurones. Accumulation of mutant SOD1 within the mitochondria may cause Ca^{2+} dysregulation and disruption to oxidative phosphorylation resulting in reduced ATP generation, increased ROS production and changes to ER folding capabilities. Deficient SOD1 activity could lead to the accumulation of ROS within neurones which may trigger further protein misfolding and oxidative distress. Reduced ATP production in neurones may result in an increased demand for metabolism substrates, specifically lactate, from glia so pyruvate can be used to eventually generate ATP. UPS deficiency could cause lipid raft disorganisation which may contribute to Ca^{2+} dysregulation, negatively affecting the endosomal pathway and its function. Deficiency of the UPS could result in upregulation of heat shock protein production and the autophagy pathway to assist with protein clearance, however due to changes in the endosomal pathway, autophagosomes in the axon may not be transported to lysosomes in the cell body leading to autophagosome accumulation. As a result of disruption to the UPS, autophagy and ATP production, lysosomal enzymes may be upregulated by cells in attempt to produce substrates for ATP generation, but these enzymes may cause aberrant degradation of proteins within the cytoplasm. Alternative clearance mechanisms including the LC3-dependent EV loading and secretion (LDELS) pathway may be upregulated to reduce the protein load in neurones but may also contribute to the spread of misfolded SOD1 to other neurones and glia within the CNS.

7.1.2 Potential implications for specific cell types

SOD1 is ubiquitously expressed (Green *et al.*, 2002) but there is mounting evidence in DM and ALS that the protein may have different impacts on cellular functions depending on the cell type affected in the CNS. For this reason, the potential implications of *Sod*1 mutations on cellular function will be hypothesised within the context of each major CNS cell type.

Oligodendrocytes may contribute to the provision of lactate to neurones for energy generation, but this also produces ROS within the glia cells (Vandoorne, De Bock and Van Den Bosch, 2018). Endogenous mutant SOD1 and misfolded SOD1 taken in from neurones may be enzymatically deficient in oligodendrocytes preventing the clearance of ROS. Accumulation of ROS may further exacerbate SOD1 misfolding which may induce the HSP response and the UPS. ROS and misfolded SOD1 may reduce mitochondrial function leading to ATP deficiencies which may affect the efficiency of the proteasome and Ca^{2+} dysregulation. Defective protein turnover may cause disorganisation of myelin which may reduce the ability of myelin to exchange metabolites and substrates with neurones. In addition, lipid organisation may become unstable and contribute to the cellular defects previously explained in neurones including autophagy and endosome dysfunction. As demyelination occurs, this potentially contributes to ATP deficiencies in neurones.

Astrocytes may be recruited to areas of neuronal degeneration and demyelination for several reasons: astrocytes may uptake lipids associated with apolipoprotein E to facilitate regeneration of lipid membranes (Hesse *et al.*,

2000) and astrocytes may become the main contributors of lactate to neurones (Vandoorne, De Bock and Van Den Bosch, 2018). Degeneration of oligodendrocytes may increase glutamate within the extracellular space meaning astrocytes initially upregulate EAAT receptors to protect neurones from excitotoxicity (Duan *et al.*, 1999). Chronic energy demands on astrocytes by MNs may lead to an accumulation of ROS within the glia which could then follow the same path as previously described for oligodendrocytes and MNs. Disruption in the cell membrane compartments of astrocytes could affect the distribution of EAATs which may have detrimental effects of expression of the transporters and induce excitotoxicity in MNs (Butchbach *et al.*, 2004). Eventual widespread protein misfolding and reduction in metabolic support from glia may lead to ER stress and apoptosis of MNs. Microglia have been shown to have a role in DM (Ogawa *et al.*, 2014; Toedebusch *et al.*, 2018), however they could not be assessed efficiently in this project, so specifics will not be commented on. It was however clear that throughout the DM disease progress, there were many potential triggers for microglia recruitment.

Neurones have high energy demands (Vandoorne, De Bock and Van Den Bosch, 2018) and their ability to generate/utilise energy may be disrupted by the *Sod*1 mutation. Oligodendrocytes may be called upon first for energy substrates, but this may cause ROS which may disrupt myelin organisation. This could lead to astrocytes being recruited to provide energy substrates. Energy demands, ROS and mutated SOD1 may affect the UPS early leading to recruitment of other protein processing pathways including autophagy.

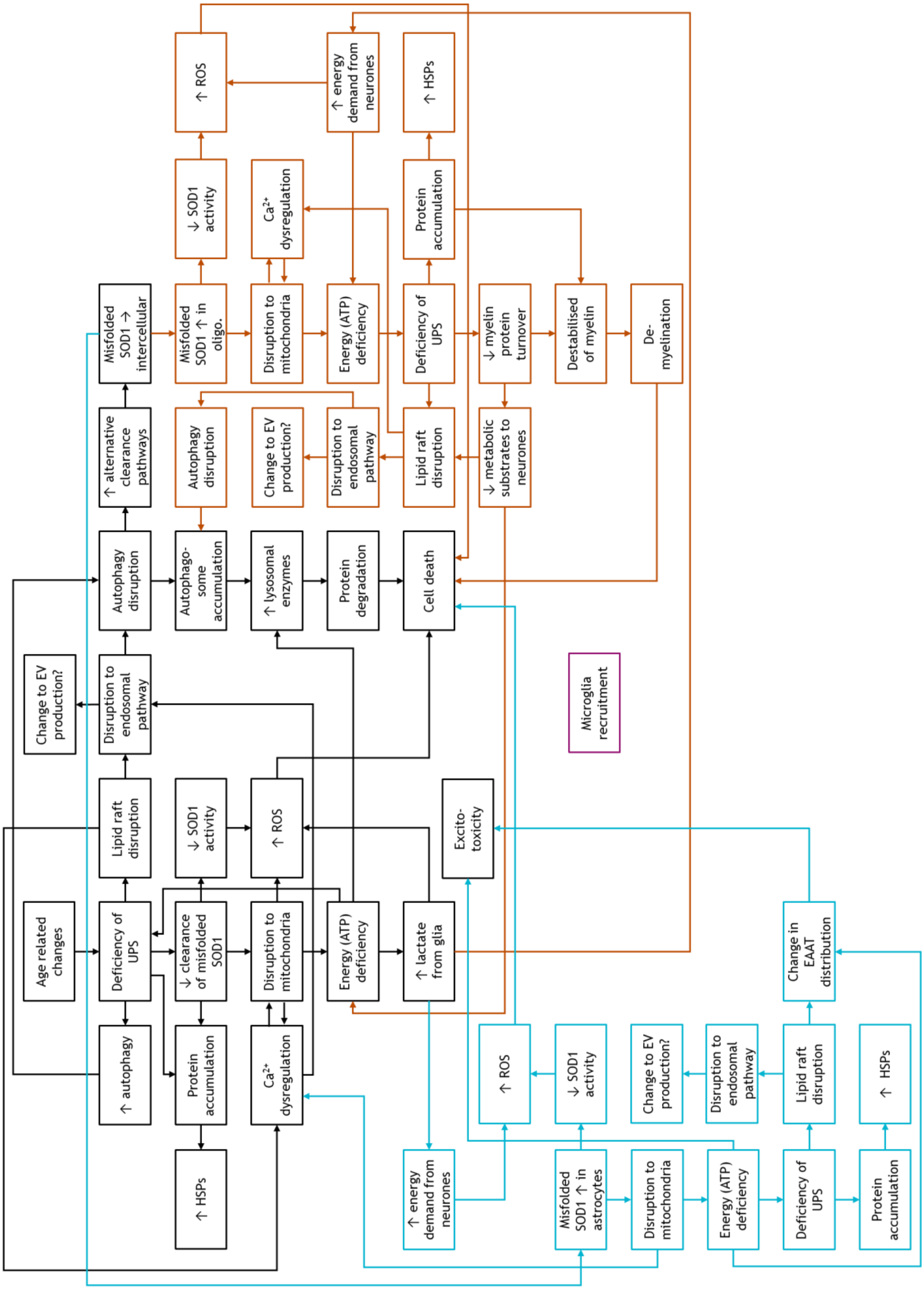
↑ ROS
↑ energy demand from neurones
↑ HSPs
↓ SOD1 activity
Ca^{2+} dysregulation
Protein accumulation
Misfolded SOD1 → intercellular
Misfolded SOD1 ↑ in oligo.
Disruption to mitochondria
Energy (ATP) deficiency
Deficiency of UPS
↓ myelin protein turnover
Destabilised of myelin
De-myelination
↑ alternative clearance pathways
Autophagy disruption
Change to EV production?
Disruption to endosomal pathway
Lipid raft disruption
↓ metabolic substrates to neurones
Autophagy disruption
Autophago-some accumulation
↑ lysosomal enzymes
Protein degradation
Cell death
Change to EV production?
Disruption to endosomal pathway
Microglia recruitment
Lipid raft disruption
↓ SOD1 activity
↑ ROS
Excito-toxicity
Age related changes
Deficiency of UPS
↓ clearance of misfolded SOD1
Disruption to mitochondria
Energy (ATP) deficiency
↑ lactate from glia
Change in EAAT distribution
↑ autophagy
Protein accumulation
Ca^{2+} dysregulation
↑ ROS
↓ SOD1 activity
Change to EV production?
Disruption to endosomal pathway
Lipid raft disruption
↑ HSPs
↑ HSPs
↑ energy demand from neurones
Misfolded SOD1 ↑ in astrocytes
Disruption to mitochondria
Energy (ATP) deficiency
Deficiency of UPS
Protein accumulation

Figure 7-1: Suggested schematic for updated hypotheses. Presented in the schematic are the possible interactions between pathological mechanisms in DM as suggested by results from the current *in vitro* and *ex vivo* experiments which are discussed in the main text. Black boxes and lines represent changes in neurones, brown boxes and lines represent changes in oligodendrocytes, aqua boxes and lines represent changes in astrocytes and the purple box represents the presence of microglial recruitment. Microglia were not clearly assessed in this thesis so have not been included in the flowchart, however there is evidence that various proteins were upregulated that can influence microglial recruitment.

7.1.3 Suggested hypothesis for regional differences in the spinal cord

It may be possible to compare the differentially expressed proteins in the cervical and thoracic spinal cord regions (Table 6-4) to postulate how DM progresses as changes to the cervical region may be indicative of the pre-symptomatic stage, while changes in the thoracic region are indicative of symptomatic stages. Further, based on the clinical signs of dogs before euthanasia, this can help to determine what stage of symptomatic disease they are at. In this study, it was reported that a degree of movement in the pelvic limbs was present, but DM dogs were non-ambulatory, indicating they were at an early stage of symptomatic disease. The thoracic region of the spinal cord is reliant on high levels of energy (Coates and Wininger, 2010). As suggested by the increased expression of LDHA and reduction in NSE, ATP production may be affected early in the DM disease process which may make the thoracic region particularly vulnerable to the changes induced by the misfolded SOD1 protein. As the disease progresses and pelvic limbs become compromised, this may put more energy demand on the cervical region of the cord due to increased use of the cervical limbs. This, accompanied by increased mutant SOD1 in the CSF may be the trigger for cervical limb pathology and subsequent clinical signs.

EVs were not assessed directly in the tissue but it is possible that the different CNS cell types may contribute different amounts of EVs at different stages of the disease or they may occur at the same time (Silverman *et al.*, 2019). *In vitro* studies highlighted that disruption to different protein processing pathways can have different effects on the production of EVs and their composition. Additionally, *in vitro* studies did not rule out the possibility that EVs could act as vehicles to disseminate mutated SOD1 to other cells. There is clearly the need for future experiments that consolidate these hypotheses and a multistrand, collaborative approach will be required, however this study has positively contributed to the DM field. Many proteins have been highlighted that have the potential to be developed into biomarkers for the disease and they may allow identification of mechanisms that could be therapeutic targets in the future.

7.2 Limitations and future work

This project was partly forged by the COVID-19 pandemic and the impact this had on the project is summarised in Appendix 8.1. Regardless of this event, it would not have been possible to pursue every avenue of interest, but they will be discussed in this section.

7.2.1 *In vitro* and *ex vivo* sample sizes

The number of replicates used in cell culture experiments were determined by the time and resources needed to complete each replicate and the type of experiment being conducted. For optimisation experiments for example, replicate numbers were usually made up to three however experiments investigating the impact of treatments on EV production were generally made up to five to try and improve statistical rigor. In *ex vivo* studies, the number of samples used was dictated by the number of referrals of DM to the UoGSAH and availability of non-neurological controls. To ensure proteomics could be included in this thesis, we had to settle with the number of samples available (four affected and five unaffected) at the time, however the recruitment of DM cases and controls is still ongoing for future studies. As proteomics of the canine DM spinal cord is novel and in-depth studies of the disease are limited, this study generated vast amounts of data that will be useful for formulating future hypotheses. Ideally, statistical power analyses should be performed before collection of samples to determine the optimum number of replicates required to assess if any changes/differences between groups observed are due to normal biological variation, or the effect of treatments or disease for example.

7.2.2 Development of primary cell cultures and expansion of the *in vitro* model

An avenue that was going to be pursued in this project was the generation of DM primary cell culture using fibroblasts derived from skin samples and mesenchymal stem cells (MSCs) derived from bone marrow. Unfortunately, contamination was present in the first attempt of fibroblast culture, but steps were taken to prevent this leading to successful culture in 2023 of DM fibroblasts. Primary culture of DM bone marrow MSCs was successfully started by Mohammad Ghasemzadeh Hasankolaei in 2022.

The generation of primary cultures will be useful in further understanding how the *Sod*1 mutation affects cellular processes as the mutated protein will be endogenous to cells and mitigate the need for transfection with large fusion proteins. This provides the opportunity to carry out similar studies described in this thesis with treatments and allow for analysis of proteins, RNA and EVs. Furthermore, as previously discussed (Section 4.5.5.2), primary cells can be differentiated into specific cell types, for example, MSCs can be differentiated into neurone-like and glia-like cells (Kim *et al.*, 2002; Tohill *et al.*, 2004) which allows the investigation of the non-cell autonomous nature of DM.

7.2.2.1 Assessment of SOD1 structure and function

Large fusion proteins can alter the biochemical properties of the protein of interest (Draper *et al.*, 2020) which may impact protein processing pathways and protein behaviour. The presence of endogenous proteins in primary cell cultures removes this complication which will be particularly beneficial in the evaluation of SOD1 activity in DM. In some instances, it may be beneficial to include fusion proteins and the current study showed that the SOD1-EGFP constructs were a valuable tool to investigate the influence of disease mechanisms on SOD1 protein and activity. Alternatively, smaller constructs could be generated using the FLAG-tag to minimise biochemical changes induced by large proteins. FLAG-tagged SOD1 has been successfully developed and used for the investigation of DM previously (Nakamae *et al.*, 2015; Tanaka *et al.*, 2021; Yokota *et al.*, 2018).

It is believed only certain SOD1 species present in cells aggregate and that there is a progression from soluble SOD1 oligomers to insoluble SOD1 aggregates/fibrils in DM (Draper *et al.*, 2020; Kimura *et al.*, 2020; Tiwari and Hayward, 2005). Primary cell cultures would also help to establish which stimuli may contribute to these phenotypes and allow for investigation of SOD1 aggregate lifecycles. Further, *in vivo* it has been shown that an element of damage may need to occur in CNS cells (MNs and/or glia) in order for mutant SOD1 to have the pathological effects observed in ALS (Gomes *et al.*, 2007), so primary cultures will allow this to be investigated in a controlled environment.

7.2.2.2 Additional characterisation and purification of EVs

The MISEV guidelines recommend the use of two different methods to characterise EVs isolated from culture or tissues (Théry *et al.*, 2018). In this thesis, Western blotting was used as the main method to characterise EVs. Nanoparticle tracking analysis (NTA) and electron microscopy (EM) was also investigated but equipment and time restrictions made this difficult to finish before publication of this thesis. Before submission to a journal, at least one of these methods will be completed on a selection of EV samples to assess the population of EVs being isolated from media and subsequently assessed, and to give an indication of the purity of the EV fraction.

7.2.2.3 Dissecting the EV population

Multiple cell lines can be cultured together, and this would be of value in the investigation of EVs. As suggested in Section 4.5.5.2, transwell inserts with filter membranes can be used to separate cell types but allow EVs to be shared between cells (Hanspal *et al.*, 2017). Throughout this thesis, the human neuroblastoma derived cell line SK-N-SH was used for their neurone like qualities. Similar experiments could be carried out with cell lines derived from other cell types including primary cell cultures (differentiated or not) and the immortal murine cell lines MN-like NSC34 and oligodendrocyte 158N. This would not only allow the comparison of protein processing pathways between cell lines, but also facilitate experiments that investigate the contribution of various cell types to the EV population. The population of EVs can be better understood when the size of each particle is measured. The size and shape of EVs, in addition to the biochemical composition, may indicate which EV subtypes are present in the population (Théry *et al.*, 2018). Additionally, changes to the size, shape and concentration of EVs can be indicative of alterations to the EV pathways within parent cells (Xu, Camfield and Gorski, 2018). There are different ways to analyse the size and shape of EVs and they have their own advantages and disadvantages. EM for example can determine size and morphology of EVs, but EVs must be fixed and a relatively small population is measured. Another method is NTA which provides information on the size of particles based on the light scattering pattern. Images and videos of the particles can be obtained, and the concentration of each population in the sample is also noted (Théry *et al.*, 2018). The list of techniques to study EVs is not exhaustive and is discussed further in Théry *et al.*, (2018). One of the main restrictions for the EV *in vitro* studies in this project was the volume of transfected EVs isolated for analysis. With the current scale, it was difficult to perform multiple methods from one preparation. In the future, the transfection process could be scaled up so larger volumes of EVs could be isolated for omics studies, larger scale conditioned medium experiments, biochemistry and characterisation.

7.2.2.4 Investigation of lipid rafts *in vitro*

One of the key speculations that has arisen from the work in this thesis is the potential involvement of cell membrane disruption in disease pathogenesis. As previously discussed, lipid rafts are membrane microdomains that have various functions in cell signalling, cell-cell interactions and the endosomal pathway (Zhai *et al.*, 2009) and have been implicated in neurodegenerative diseases (McGonigal *et al.*, 2021). To investigate lipid rafts, proteins in samples need to be partitioned into detergent soluble and insoluble fractions. The insoluble fraction is where lipid rafts are found and further sucrose density centrifugation of the fraction allows for investigation of protein and lipid constituents associated with lipid rafts. A method for investigation of these structures in murine CNS is described in McGonigal *et al.*, (2021) and could be adapted for cell culture.

7.2.3 Further assessment of biological samples

7.2.3.1 Omics technologies

In the current study, proteomics was thoroughly investigated. Using multiple omics technologies gives a fuller picture of biological function and disease pathogenesis (Tan *et al.*, 2016), so other omics should be included to expand on the current findings. Transcriptomics is used to investigate all RNA transcripts in a sample and allows for direct assessment on gene expression. Coding mRNAs become proteins while noncoding RNAs can have a range of functions. Investigation of RNA allows for assessment of gene regulation which can give insights into how different cells, tissues and diseases work (Lowe *et al.*, 2017). The metabolome is the result of gene expression but is influenced by a range of other factors meaning it is a good indicator of the true physiological status and biological phenotype. Tan *et al.,* (2016) described this eloquently: “genes determine what may happen and metabolites define what happened”. Metabolites include small molecule compounds of sugars, amino acids, organic acids, lipids and more (Yang *et al.*, 2019). The lipidome is made up of tens of thousands to hundreds of thousands of lipids and is a subdivision of the metabolome. Lipids have many functions including roles in cell structure, signalling and energy storage. The up or downregulation of lipids can indicate the metabolic status of cells and can suggest cell enzyme activity or levels may be disrupted in different situations or diseases and possibly contribute to the identification of pathological mechanisms and determination of disease stage (Addepalli and Mullangi, 2020; Han, 2016). Different metabolic pathways can interact with each other, and it is important to integrate the investigation of the lipidome with other biomes including the metabolome, proteome and genome (Han, 2016). Metabolites are able to represent changes that happen at a specific time point more reliably than other omics as metabolites can change in seconds or minutes rather than minutes or hours like the transcriptome or proteome for example (Tan *et al.*, 2016).

Metabolites and lipids were extracted from spinal cord tissues (by MM with LEB assistance), processed at GP (Shellie Walsh, Clement Regnault, Phillip Whitfield and Gavin Blackburn) and will be thoroughly analysed for a follow up publication as details are beyond the scope of this thesis. These studies will be valuable in examining the changes to lipids, energy sources and other metabolites which will help to determine if the hypotheses generated after the *in vitro* and *ex vivo* studies are true or not. Metabolomics and lipidomics should provide an insight into the membranous components of cells including EVs and lipid rafts but further processing of tissue samples is required to separate EVs and lipid rafts from other cellular constituents. Samples can be further interrogated by membrane fractionation to investigate lipid rafts specifically as described in McGonigal *et al.*, (2021) and summarised earlier in this chapter.

7.2.3.2 Investigating EVs from biological samples

EVs can be extracted from spinal cord tissue and this has been attempted in the DM field by Pfeiffer *et al.*, (2023), but has had limited success due to low yields. Extraction of EVs from the ALS spinal cord has been successful to investigate the role of EVs as propagators of SOD1 pathology and better understand the non-cell autonomous nature of the disease. EVs extracted from tissue or biofluids can be transferred to cell cultures and animal models to assess the effect EVs have on different cell types and systems (Silverman *et al.*, 2019). Tissue derived EVs can be investigated using the biochemical and proteomic techniques described throughout this thesis. To further investigate the interaction between EVs and proteins of interest, co-immunoprecipitation experiments can be carried out as described in McLaughlin *et al.*, (2002). Appropriate antibodies could be used to represent EVs, for example flotillin-1, and the protein of interest including SOD1.

EVs can be isolated from CSF, serum and plasma. EVs are generally found at low concentrations in the CSF as the fluid contains a large quantity of secreted proteins, but several studies in the human field have been able to isolate enough EVs for omics analysis (Otake, Kamiguchi and Hirozane, 2019; Thompson *et al.*, 2020). EVs isolated from plasma and serum are more readily accessible and a study of serum derived exosomes from control and DM dogs by Pfeiffer *et al.*, (2023) found that two marker proteins, TDP-43 (and phosphorylated derivates) and SOD1 for ALS and DM respectively, were significantly upregulated in the exosome fraction from DM cases.

7.2.3.3 Labelling of proteins *in situ*

The proteins of interest identified throughout this thesis could also be investigated in tissues using IHC and immunocytochemistry. This allows assessment of specific proteins *in situ* and can validate the hypotheses generated. This is particularly valuable when assessing SOD1 distribution and aggregation within tissues (Ogawa *et al.*, 2011), however biochemical techniques such as filter trap assays can also be used to quantitively assess aggregation (Crisp *et al.*, 2013). Antibodies raised against human WT and canine E40K mutant SOD1 have been used in DM studies to investigate the distribution of SOD1 within spinal cords (Awano *et al.*, 2009; Kohyama *et al.*, 2017; Nakamae *et al.*, 2015; Nakata *et al.*, 2021; Ogawa *et al.*, 2011). Both have their advantages; human WT SOD1 antibodies can identify WT and mutant SOD1 in canine tissue while the canine E40K specific antibody allows investigation of the mutant protein specifically. Both are of value for better understanding the pathological processes in DM. IHC is also a valuable tool for investigating specific cell types in spinal cord sections and for the findings presented here, this would be important for labelling astrocytes and microglia (Ogawa *et al.*, 2011). Furthermore, markers associated with cell clearance and toxicity pathways can be labelled in tissues and multiple markers can be investigated within the same section allowing for inspection of any interactions between proteins. Studies of this form have been conducted in DM to investigate the interaction between SOD1 and the main clearance pathways autophagy (Ogawa *et al.*, 2015) and the UPS (Ogawa *et al.*, 2011) for example.

Imaging techniques can be used to investigate the interaction between different cell types. For example, neuronal Caspr and neurofascin interact with oligodendrocyte contactin-1 at the paranodes of myelinated axons and act as a point of contact between the two cell types. In some ALS studies using mutant SOD1 mice, Caspr can be disrupted and abnormally distributed before symptom onset (Maglemose *et al.*, 2017). As axon degeneration and demyelination are hallmarks of DM (and ALS), it may be worth investigating how the three proteins interact with each other in the disease to determine if there are any perturbations to the connection between axon and myelin at the paranode. While the abundance of Caspr, neurofascin and contactin-1 proteins in this study were not significantly different, the interaction between these proteins was not assessed. Immunostaining the proteins in axons and myelin would allow visualisation and the opportunity to measure their distribution within and around the paranodes (McGonigal *et al.*, 2021).

7.2.3.4 Investigation of SOD1 post translational modifications

Post translational modifications (PTMs) can affect the functional properties of proteins they are added to (Hedl *et al.*, 2019) and this was briefly introduced (Section 6.1.1) and discussed for flotillin-1 in relation to SUMOylation and palmitoylation (Section 5.5.2) and SOD1 in relation to oxidation (Section 6.5.8) in this thesis. PTMs associated with SOD1 were not investigated in the current study however PTMs in human and murine studies of SOD1, often related to fALS associated mutant protein, have shown that various PTMs can influence aggregation or location of SOD1 in addition to aiding normal function. Some phosphorylation sites on SOD1 have roles in regulation of normal dismutase activity while other sites have been shown to improve the stability of some fALS mutant SOD1. Additionally, some phosphorylation sites can negatively impact the structure of SOD1 leading to structural changes. Other PTMs that can have positive and negative effects on SOD1 structure are acetylation, SUMOylation and glycation. Further palmitoylation has been linked to fALS mutant SOD1 more regularly than WT-SOD1 and is thought to influence the localisation of SOD1 in cells (Banks and Andersen, 2019). Further proteomic assessment of tissues geared towards understanding the PTMs of SOD1 within DM may help to understand any modifications happening *in vivo* that could influence SOD1 aggregation and general protein processing.

7.3 Conclusions and the impact of this study

Finally, to address the specific aims and hypotheses laid out in Section 1.6, the following conclusions can be made as a result of the data presented in this thesis:

- Alteration of cell clearance and toxicity pathways can alter the processing of WT- and DM-SOD1 within cells and in association with EVs, and the *Sod*1 mutation plays a role in the recruitment of alternative protein processing pathways in neuroblastoma derived cultured cells.
- Alteration of cell clearance and toxicity pathways can increase the aggregation of WT- and DM-SOD1, but the *Sod*1 mutation can

detrimentally impact the processing of misfolded proteins in neuroblastoma derived cultured cells.

- WT- and DM-SOD1 associated with the EV fraction from cultured SK-N-SH cells can be spread to other cell cultures.
- Markers for cell clearance and toxicity pathways were altered in DM thoracic spinal cord segments and changes were accompanied by variations to CNS cell specific markers compared to controls reflecting induction of axon degeneration and demyelination.
- Overall soluble SOD1 did not appear to be affected in the DM spinal cord compared to controls, however there was an upregulation in the conversion of soluble SOD1 monomers to soluble SOD1 oligomers in the DM thoracic spinal cord potentially preceding the development of insoluble SOD1 aggregates.
- Some cell clearance and toxicity pathway markers and markers of specific CNS cells were different in the DM cervical spinal cord region in addition to the changes seen in the thoracic cord, potentially reflecting early pathological changes in the DM disease course.

DM has been shown to share many similarities with human ALS with respect to clinical signs, histopathology, genetics and other pathological mechanisms as described frequently throughout this thesis. The findings described here continued to justify the translational capabilities of DM and ALS which will help to improve diagnostic and treatment options in the future for both species.

8 Appendices

8.1 COVID-19 impact statement

The COVID-19 pandemic had a marked impact on this project because of lockdowns and COVID-19 mitigations. Several adaptations were made to the study as the situation evolved.

Access to the tissue culture facilities was prohibited for many months due to the first UK lockdown. When access was granted again, we were hesitant to start long-term cell culture experiments as there was still uncertainty about access if another lockdown was to occur. Instead, it was decided that LEB would help in another project that did not require tissue culture facilities and this resulted in being included in a publication (McGonigal *et al.*, 2021). Contribution to this project helped to optimise the WB technique described in this thesis. When the COVID-19 situation was clearer, cell culture studies resumed. Adaptations were made to the original plan regarding cell culture including the removal of the aim to generate FLAG-tagged SOD1 plasmids and there was a reduction in the number of cell lines used. Eventually the decision was made to extend the allocated time for cell culture studies to ensure they were completed to a standard that provided meaningful results. Additional methods of EV characterisation were explored including electron microscopy and nanoparticle tracking analysis as discussed in Section 4.5.1. These methods relied on collaboration with other researchers, either for access to equipment or for processing of samples. Unfortunately, due to constraints imposed by COVID-19 and technical issues, these methods were not further pursued. This was also the case for further confocal microscopy which was considered for high quality images of the EV transfer experiments.

Neurology referrals to the UoGSAH were reduced during the COVID-19 period so there is a chance that fewer potential DM cases could be recruited to the study. To try and increase the visibility of the study, a poster/flyer was made by LEB that was distributed by CES to the Police Scotland Canine Unit and clinics. A website was also made by LEB but was not published by the end of the PhD period. Additionally, access to post-mortem and pathology facilities was limited by the pandemic, meaning it was more difficult to recruit control cases due to occupancy limits in the post-mortem room and staff schedules. To mitigate the effect of limited DM cases, MM set up a collaboration with a world leading DM researcher in the USA who has a repository of DM samples, however, there were logistical issues and subsequent time constraints, so we had to go with the few samples we had at the time.

Another integral aim that was removed from the study was the establishment of potential serum biomarkers of DM. This was the result of a reduction in cases and a reduction in time available. To make up for any shortcomings in cell culture or case recruitment, substantial proteomic, lipidomic and metabolomic studies were introduced so large data sets could be retrieved from a small number of samples in a relatively short space of time. These have since produced copious amounts of valuable data that could not be fully processed in the current thesis but will be in a follow up publication.

8.2 Supplementary materials and methods

8.2.1 Cell culture

Cells were broken out for culture by thawing them at 37°C, then they were transferred into a collecting tube containing NGM. The resuspended cells were centrifuged at 800 *xg* for 5 minutes at RT. The SN was discarded, and the pellet resuspended in 1 ml warm NGM before being added to a vented culture flask containing NGM.

When the confluence of cells was less than 80%, NGM was replaced. When cells were more than 80% confluent, the cells were split. All solutions used in cell culture were incubated at 37°C to minimise inducing cold stress. NGM was removed and cells were washed twice with PBS. To separate the cells from the bottom of the flask, Trypsin-EDTA (Gibco, UK) was added before the flask was incubated at 37°C for approximately 1 minute. The flask was tapped on each side to dislodge cells from the bottom of the flask. When most cells were floating in the trypsin-EDTA, the reaction was stopped by adding NGM, then the contents were collected for centrifugation at 800 *xg* for 5 minutes at RT. The SN was discarded, the pellet resuspended in NGM then cells were transferred to another vented culture flask and incubated in humidified conditions at 37°C, 5% CO_2.

To freeze cells, confluent flasks were washed, trypsinised and centrifuged as before. The pellet was resuspended in DMEM containing 10% FBS and 10% dimethyl sulfoxide (DMSO; Sigma-Aldrich, UK). The suspension was divided into 1 ml aliquots and stored at -70°C before being moved to liquid nitrogen for long term storage.

8.2.1.1 Poly-L-lysine treated coverslips

Poly-L-lysine coated coverslips were used for visualising cells in experiments. Autoclaved 13 mm cover slips were placed into each well of a 4-well plate then 300 µl of the working poly-L-lysine solution (Table 8-1) was added to each well. Plates were incubated at RT in a flow hood for 1 hour, washed 3 times with sterile water then dried out at RT.

Table 8-1: Poly-L-lysine working solution.

Chemical	Volume
Poly-L-lysine stock solution (Sigma Aldrich)	200 µl
Sodium borate buffer (pH 8.5)	60 ml

Volume required for treating 50, 13 mm coverslips.

8.2.1.2 Seeding density calculations

Trypan blue stains non-viable cells as the disrupted membrane allows the dye to enter the cell, resulting in the clear observation of viable cells for cell counting (Sigma-Aldrich, 2022). An aliquot of the resuspended pellet was added to trypan blue (1:1; Gibco, UK) then a Neubauer chamber was filled. The number of cells within 3 separate large squares (containing 16 smaller squares) spread between both sides of the chamber were counted. The average cell count was multiplied by 2 (dilution factor) then multiplied by 1000 (one large square/set of 16 squares contains 1x10^{-4} ml) to calculate the number of cells/ml. The seeding density was then calculated and the volume from the original cell suspension was added to each well.

8.2.1.3 *Sod*1-EGFP Plasmid design

Table 8-2: Primers pairs for the amplification of WT and DM *Sod*1 plasmids.

Primer direction	**Primer sequence**
Forward	XhoI 5′-CTC GAG ATG GAG ATG AAG GCC GTG TGC GTG-3′
Reverse	HindIII 5′-AAG CTT TTA TTG GGC GAT CCC AAT GAC ACC –3′

8.2.1.4 Reagent ratios for transfection using Lipofectamine™ 3000

Table 8-3: Example transfection reagent quantities per well.

	Tube A (per 13 mm well)	**Tube B (per 13 mm well)**	**Tube A (per 346 mm well)**	**Tube B (per 346 mm well)**
Opti-MEM	25 µl	25 µl	50 µl	50 µl
Lipofectamine™	1 µl	-	2 µl	-
P3000	-	1 µl	-	2 µl
Plasmid	-	1 µl	-	2 µl

The quantity of each reagent required per well for transfection is show above for 4-well plates (13 mm) and 6-well plates (346 mm).

8.2.2 Nucleic acid analysis

8.2.2.1 DNA ladder working solution

Table 8-4: 100 bp DNA ladder working solution.

Reagent	Volume per lane (μl)
6X loading buffer (New England BioLabs, US)	1
100 bp DNA ladder (Promega, US)	3
MQ water	2

Listed in the table are the reagents required for the DNA ladder and their quantities per lane.

8.2.3 Protein analysis

8.2.3.1 Lysis buffer

Table 8-5: Lysis buffer composition.

Chemical/reagent	Final concentration	Function
10% Triton™ X-100	1%	Non-ionic detergent
500mM HEPES solution	50 mM	Buffer to stabilise pH
250mM sodium orthovanadate	1 mM	Phosphatase inhibitor
250mM sodium pyrophosphate	1 mM	Phosphatase inhibitor
Protease Inhibitor Cocktail 100X*	1X	Inhibits serine, cysteine and acid proteases and aminopeptidases.
Phenylmethylsulfonyl fluoride (PMSF)	1 mM	Inhibits serine and thiol proteases

Triton, HEPES, sodium orthovanadate, sodium pyrophosphate and Protease Inhibitor Cocktail (Sigma-Aldrich, UK) were combined and made to 10 ml with MQ water. Aliquots were stored at -20°C. After thawing an aliquot, PMSF was added just before the lysis buffer was to be used.

8.2.3.2 Sample denaturation buffer

Table 8-6: Sample denaturation buffer.

Chemical	Concentration (at 1X)
Tris-HCl (pH 6.8)	62.5 mM
Glycerol	10%
LDS	1%
Bromophenol blue	0.005%
DTT	50 mM

Tris-HCl, Glycerol, LDS and bromophenol blue are contained within 4X laemmli sample buffer (Bio-Rad Laboratories). LDS is a detergent used to denature proteins. Glycerol increases the density of the sample so that it goes to the bottom of the well when loading and bromophenol blue is used help visualise the sample when loading. During gel electrophoresis, the bromophenol blue runs in front of the proteins in the sample so their position on the gel is clear. DTT is added as a reducing agent to disrupt disulphide bonds within and between proteins.

8.2.3.3 2X Loading buffer for native gel samples

Table 8-7: 2X loading buffer for native gel samples.

Chemical	Final concentration
Tris-HCl (pH 6.8)	0.125 M
Glycerol	20 %
Bromophenol blue	Speck

A 5 ml stock solution was made then aliquoted and frozen at -20°C for use in future experiments. Glycerol was added to the Tris-HCl (pH 6.8) before being vortexed until the solution was homogenous. A small speck of Bromophenol blue was added until the solution was a transparent blue colour, similar to laemmli sample buffer.

8.2.3.4 Coomassie Blue staining solutions

Table 8-8: Coomassie blue stain and de-stain.

	Chemical	Final concentration
Coomassie Blue stain	Coomassie brilliant blue	0.125% (w/v)
	Methanol	50% (v/v)
	Acetic acid	10% (v/v)
De-stain	Methanol	40% (v/v)
	Acetic acid	10% (v/v)

Coomassie brilliant blue was dissolved in MQ before adding methanol, then acetic acid. Methanol and acetic acid were added to water for de-stain.

8.2.3.5 Silver stain solutions

Table 8-9: Silver stain solutions.

Solution	Chemical	Volume (ml) per 1 mm thick gel	MQ water (ml)
Fixing solution	Methanol	100	90
	Acetic acid	20	
Sensitising solution	Methanol	100	105
	Sensitiser (contains glutaraldehyde)	5	
Staining solution	Stainer A (contains silver nitrate)	5	90
	Stainer B (contains ammonium hydroxide and sodium hydroxide)	5	
Developing solution	Developer (contains formaldehyde and citric acid)	5	95

All solutions, excluding methanol, acetic acid and MQ water were provided in the SilverXpress™ silver staining kit (Invitrogen, UK).

8.2.3.6 Native acrylamide gel composition

Table 8-10: Acrylamide native gel recipe.

	Chemical	Volume for 1 gel
10% acrylamide (resolving gel)	MQ water	3.7 ml
	1.5 M Tris-HCl (pH 8.8)	2.5 ml
	30% acrylamide solution	3.4 ml
	10% ammonium persulphate (APS)	50 µl
	Tetramethylethylenediamine (TEMED)	5 µl
4% acrylamide (stacking gel)	MQ water	3.1 ml
	0.5 M Tris-HCl (pH 6.8)	1.3 ml
	30% acrylamide solution	0.7 ml
	10% APS	25 µl
	TEMED	3 µl

10% resolving gel: Tris-HCl (pH 8.8), acrylamide solution, APS and TEMED were added to MQ water in the listed order while being stirred. The resolving gel mixture was poured into the gel mould then refrigerated overnight to allow the gel to set. 4% stacking gel: Tris-HCl (pH 6.8), acrylamide solution, APS and TEMED were added to MQ water in the listed order while being stirred. This stacking gel mixture was layered on top of the resolving gel and allowed to set at RT.

8.2.3.7 100 mM Phosphate buffer (pH 7.8)

Table 8-11: 100 mM phosphate buffer.

Chemical	Volume (ml)
0.25 M potassium phosphate monobasic (KH_2PO_4)	4
0.25 M potassium phosphate dibasic (K_2HPO_4)	36

8.2.3.8 Riboflavin mixture

Table 8-12: Riboflavin mixture recipe.

Chemical	Volume
28 mM riboflavin	100 µl
100 mM phosphate buffer (pH 7.8)	29.9 ml
TEMED	400 µl

Riboflavin was made in phosphate buffer and stored in the dark until it was to be used. Just before being applied to the gel, TEMED was added.

8.2.3.9 10X Tris-buffered saline with Tween 20 (T-TBS)

Table 8-13: 10X T-TBS stock.

Chemical	Quantity in 1 l
Tris-base	60.2 g
Sodium chloride (NaCl)	87.6 g
Tween 20	10 ml

All chemicals were dissolved in MQ water. 1 M hydrochloric acid (HCl) was added to make the pH 7.4. The solution was made up to 1 l with MQ water. For 1X T-TBS, 100 ml 10X T-TBS was diluted in 900 ml MQ water.

8.2.3.10 Antibody validation and Western blot profiles

All antibodies used on SK-N-SH cells were reported to show reactivity with human samples in the manufacturer’s information. Reactivity of antibodies with canine samples was not always reported in the manufacturer’s information, therefore further literature searches were carried out to establish if other studies have used them in canine tissues. The approximate molecular weight and percentage similarity was determined using literature available and protein BLASTs. This information is summarised in Table 8-14.

Table 8-14: Antibody validation information for use with canine tissue.

Primary antibody	Approx. expected molecular weight (kDa)	% similarity	Canine reactivity reported in manufacturer's information?	If no, canine reactivity reported in literature?
Mouse monoclonal anti-actin (Sigma-Aldrich, UK; #A5441)	42	93	Yes	-
Rabbit polyclonal anti-CuZnSOD (Enzo Life Sciences, US; #ADI-SOD1-100)	20	81	No	Qi *et al*., 2019; Nakamae *et al*., 2015
Mouse monoclonal anti-flotillin-1 (BD Transduction Laboratories, USA; #610821)	48	97	No	Reference not found
Rabbit polyclonal anti-LC3 (Cell Signalling Technology, US; #2775)	14/16	99	No	Reference not found
Rabbit polyclonal anti-ubiquitin (DAKO, US; #Z0458)	Range	97-100	No	Ogawa *et al*., 2014
Rabbit polyclonal anti-glial fibrillary acidic protein (DAKO, US; #Z0334)	50	92	Yes	-
Rabbit polyclonal anti-lactate dehydrogenase (Abcam, UK; #ab130923)	36	63	No	Reference not found
Mouse monoclonal anti-human neurone specific enolase (Agilent Dako, US; #M087301-2)	46	99	No	Martin *et al*., 2022
Rabbit polyclonal anti-proteolipid protein (gifted by Prof. N.P. Groome)	20/26	100	N/A	Reference not found
Mouse monoclonal anti-vimentin (Sigma-Adrich, UK; #V6630)	58	98	Yes	-

Protein BLAST searches were carried out to compare antibody sequences (specific amino acid sequence or whole protein sequence) with canine (*Canis lupus familiaris* or *Canis lupus dingo*) protein sequences. "Non redundant protein sequences" and "UniProt/SwissProt" databases were used. The approximate expected molecular weight of each protein was provided by the antibody manufacturer except for PLP. The PLP antibody was derived as described in Nussbaum *et al*., (1985) and molecular weights of PLP/DM20 were recorded from McLaughlin *et al*., (2002). Where canine reactivity was not noted in the manufacturer's information, a literature search was carried out for reference of the antibody catalogue numbers in canine studies. In some cases, specific references were not found. The ubiquitin antibody had 9 matches within the canine protein sequence and they ranged from 97-100% similarity.

Representative full length Western blots are presented in Figure 8-1 for SK-N-SH cells and canine spinal cord where appropriate. Of note, some antibodies including anti-GFAP and LC3, may have cross reacted with other proteins because they had similar sequences. On these occasions, it was important to take the molecular weight into consideration.

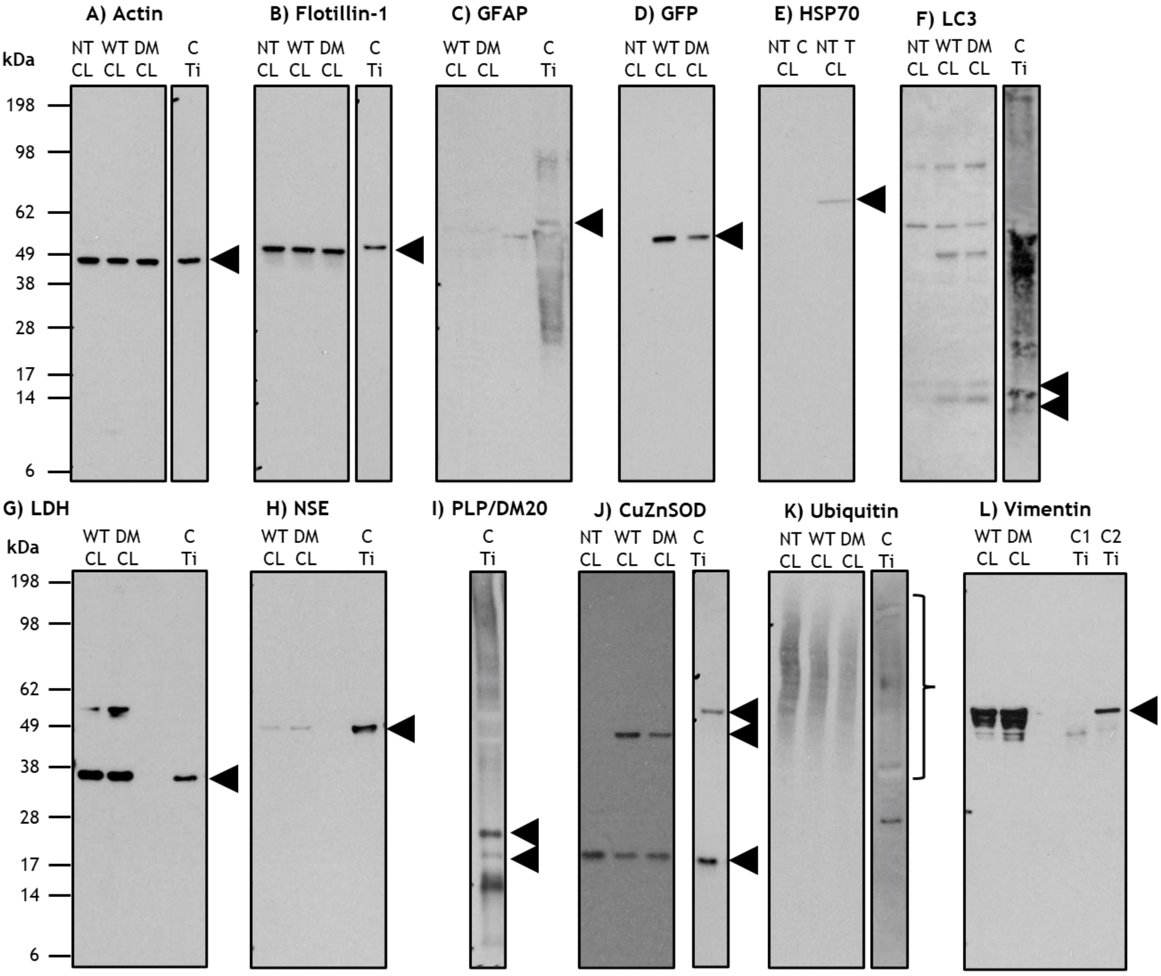
A) Actin
B) Flotillin-1
C) GFAP
D) GFP
E) HSP70
F) LC3
kDa
NT CL
WT CL
DM CL
C Ti
NT C CL
NT T CL
198
98
62
49
38
28
17
14
6
G) LDH
H) NSE
I) PLP/DM20
J) CuZnSOD
K) Ubiquitin
L) Vimentin
C1 Ti
C2 Ti

Figure 8-1: WB profiles for antibodies used in this study. Blots were probed with various antibodies in this study and the profiles are shown in this figure for NT, WT- and DM-SOD1-EGFP transfected CLs and control tissue samples. **A)** actin (42 kDa), **B)** flotillin-1 (47 kDa), **C)** GFAP (50 kDa), **D)** GFP (SOD1 fusion proteins ~49 kDa), **E)** HSP70 (70 kDa), **F)** LC3 (~17 kDa), **G)** LDH (~37 kDa), **H)** NSE (47 kDa), **I)** PLP/DM20 (PLP ~26 kDa; DM20 20 kDa), **J)** CuZnSOD (endogenous SOD1 monomer ~16 kDa; fusion SOD1 ~49 kDa; endogenous SOD1 oligomer ~50 kDa), **K)** ubiquitin, **L)** vimentin (54 kDa). For HSP70 (**E**), only NT CLs with (T) or without (C) MG132 were probed. For tissue blots, WT- and DM-SOD1-EGFP transfected control CLs (with DMSO) used. Arrows indicate specific proteins and all other bands are non-specific.

8.2.4 Image processing with ImageJ

8.2.4.1 Protein and nucleic acid analysis

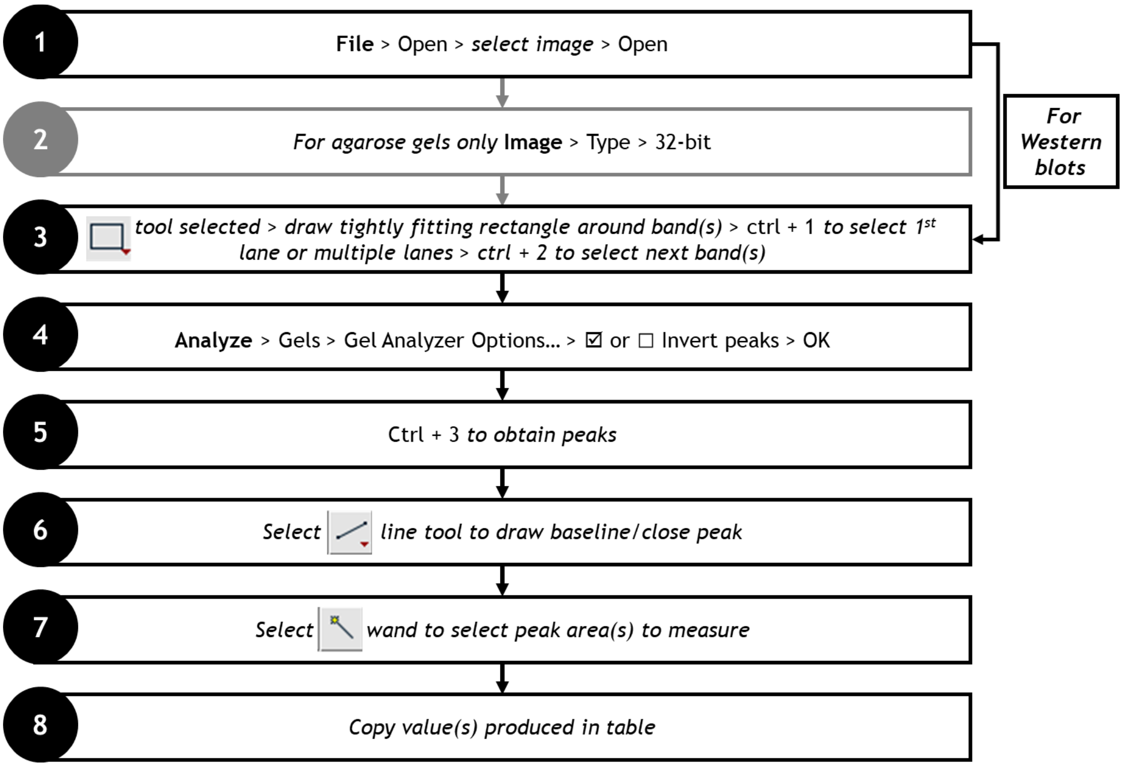
1
File > Open > select image > Open
For Western blots
2
For agarose gels only Image > Type > 32-bit
3
tool selected > draw tightly fitting rectangle around band(s) > ctrl + 1 to select 1st lane or multiple lanes > ctrl + 2 to select next band(s)
4
Analyze > Gels > Gel Analyzer Options… > ☑ or ☐ Invert peaks > OK
5
Ctrl + 3 to obtain peaks
6
Select line tool to draw baseline/close peak
7
Select wand to select peak area(s) to measure
8
Copy value(s) produced in table

Figure 8-2: Quantifying proteins and nucleic acids using ImageJ. Detailed in the flowchart above are the steps involved in quantifying protein from WBs or nucleic acids from agarose gels. Words in bold indicate the tab used from the ImageJ toolbar. The image was opened (step 1) then converted to 32-bit if image of agarose gel (step 2) so that there was more contrast between the white bands and the black background. If quantifying WBs, this step was skipped. In step 3, the protein or nucleic acid band or bands to be quantified were selected using the box tool, then *Ctrl + 1* was pressed to select the first lane or total area to be quantified. This step can also be carried out by going to **Analyze** > Gels > Select First Lane. If lanes were being selected one by one, each lane following the first one was added by Ctrl + 2 or **Analyze** > Gels > Select Next Lane. When all lanes were selected, step 4 was followed to select “invert peaks” for WBs or deselect this for agarose gels. Ctrl + 3, or Analyze > Gels > Plot Lanes was actioned to convert each band into corresponding peaks (step 5) then the line tool was used to separate the bands from background and to adjust the baseline if needed (step 6). The wand tool was used to quantify the pixel density under each peak (step 7) and the values generated in the table were copied and recorded.

8.2.4.2 Creating a coloured image with one picture

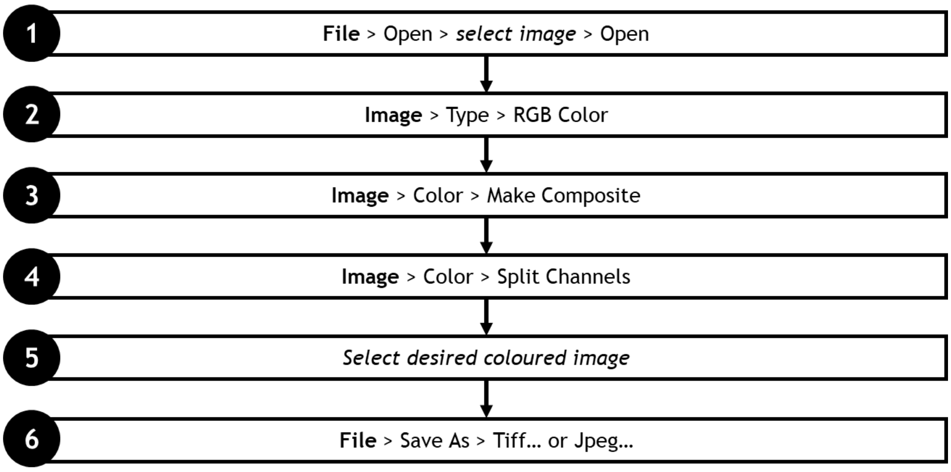

1. **File** > Open > *select image* > Open
2. **Image** > Type > RGB Color
3. **Image** > Color > Make Composite
4. **Image** > Color > Split Channels
5. *Select desired coloured image*
6. **File** > Save As > Tiff… or Jpeg…

Figure 8-3: Creating a coloured image with ImageJ using one filter. Detailed in the flowchart above are the steps involved in creating a coloured image using images captured with one filter. Words in bold indicate the tab used from the ImageJ toolbar. All images were greyscale when captured at the microscope, so it was important to ensure the colour of the cells under the microscope was noted in the image title. For example, an image of DAPI stained nuclei would contain “blue” (or similar) in the title. Once the images with the different filters were captured from the same field, they were opened in ImageJ (step 1, needs to be repeated for each image using a different filter). The next step (2) involved conversion of the 8- or 16-bit image to RGB colour. A composite image was made by following step 3, then the channels were split (step 4) to produce three images coloured red, blue and green. The appropriate colour for the filter was selected (step 5) then the image was saved as a Jpeg or Tiff file, depending on downstream requirements.

8.2.4.3 Creating a coloured image with multiple pictures

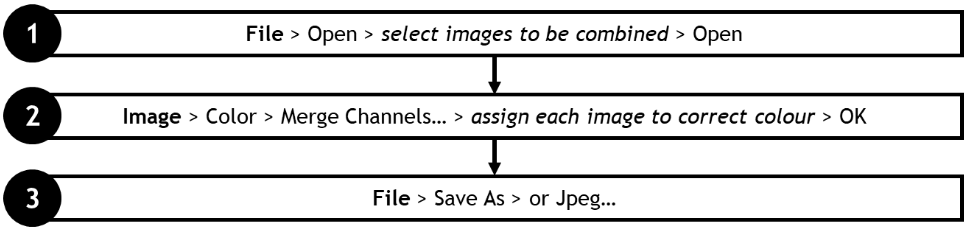

1. **File** > Open > *select images to be combined* > Open
2. **Image** > Color > Merge Channels… > *assign each image to correct colour* > OK
3. **File** > Save As > or Jpeg…

Figure 8-4: Creating a coloured image in ImageJ using multiple filters. Detailed in the flowchart above are the steps involved in creating a coloured, composite image using images captured with different coloured filters. Words in bold indicate the tab used from the ImageJ toolbar. All images were greyscale when captured at the microscope, so it is important to ensure the colour of the cells under the microscope is noted in the image title. Once the images with the different filters were captured from the same field, they were opened in ImageJ (step 1) then they were compiled in one image using step 2. In step 2, a pop-up opens and each image to be combined has to be assigned to the colour it was originally captured in, for example, if the cells were stained with DAPI, this image would be assigned to blue and GFP labelled images green. This created a composite image with different parts labelled the appropriate colour. This was saved as a Jpeg file.

8.2.4.4 Manual cell counting with ImageJ

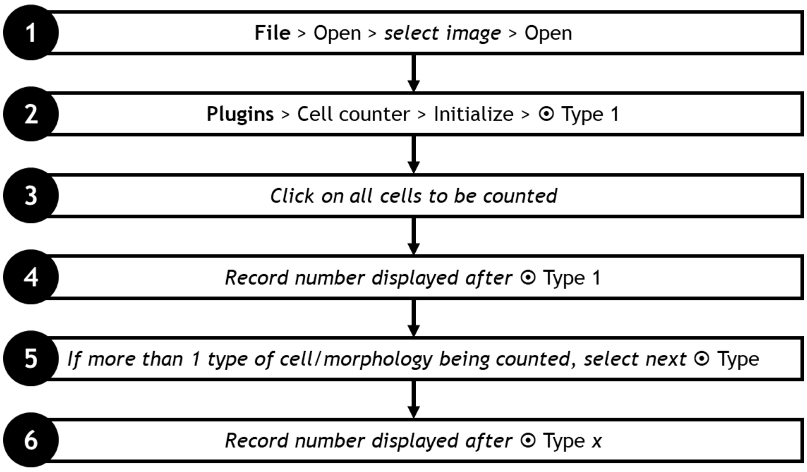
1 **File** > Open > *select image* > Open
2 **Plugins** > Cell counter > Initialize > ⊙ Type 1
3 *Click on all cells to be counted*
4 *Record number displayed after* ⊙ Type 1
5 *If more than 1 type of cell/morphology being counted, select next* ⊙ Type
6 *Record number displayed after* ⊙ Type *x*

Figure 8-5: Manually counting cells using ImageJ. For manual cell counting, the Cell Counter plugin (De Vos, 2001) in ImageJ was installed. Words in bold indicate tabs in the ImageJ toolbar. The image was opened (step 1) along with the Cell counter plugin (step 2). After initialising the image, the Type 1 counter was selected and all cells were clicked (step 3). If aggregates were counted, the next "Type" was selected (step 5) and steps 3 and 4 repeated. The number on the counter next to each "Type" was recorded (step 4).

8.2.4.5 Automatic cell counting workflow

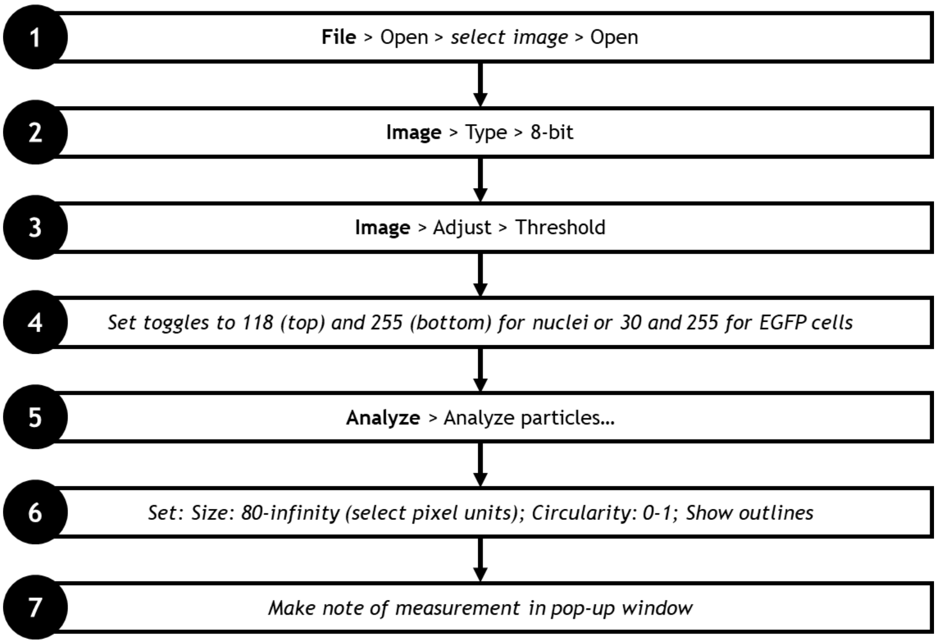
1 **File** > Open > *select image* > Open
2 **Image** > Type > 8-bit
3 **Image** > Adjust > Threshold
4 *Set toggles to 118 (top) and 255 (bottom) for nuclei or 30 and 255 for EGFP cells*
5 **Analyze** > Analyze particles...
6 *Set: Size: 80-infinity (select pixel units); Circularity: 0-1; Show outlines*
7 *Make note of measurement in pop-up window*

Figure 8-6: Counting cells automatically with Image J. Words in bold indicate tabs in the Image J toolbar. The image containing cells to be counted was opened (step 1) then the image was converted to 8-bit (step 2). The threshold was set to capture as many nuclei or cells as possible (step 3 and 4). The cells were counted using the Analyze particles feature on image J (step 5). The size and shape of cells to be counted was set by adjusting the size and circularity (step 6). The number of cells counted by Image J were displayed in a pop-up and recorded in a spreadsheet.

8.2.5 Case collection and processing

8.2.5.1 DM information recruitment poster

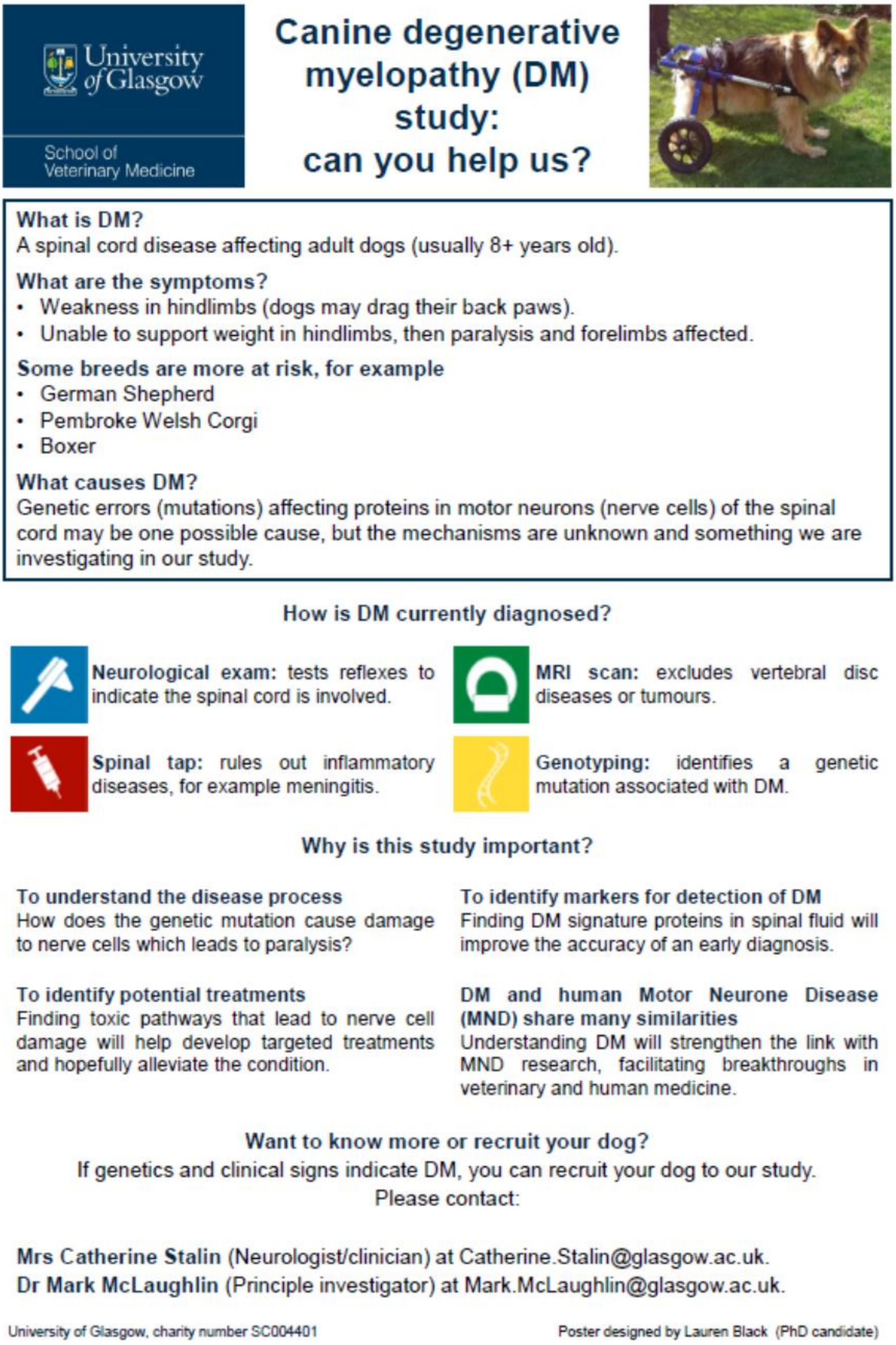

University of Glasgow

School of Veterinary Medicine

Canine degenerative myelopathy (DM) study: can you help us?

What is DM?

A spinal cord disease affecting adult dogs (usually 8+ years old).

What are the symptoms?

- Weakness in hindlimbs (dogs may drag their back paws).
- Unable to support weight in hindlimbs, then paralysis and forelimbs affected.

Some breeds are more at risk, for example

- German Shepherd
- Pembroke Welsh Corgi
- Boxer

What causes DM?

Genetic errors (mutations) affecting proteins in motor neurons (nerve cells) of the spinal cord may be one possible cause, but the mechanisms are unknown and something we are investigating in our study.

How is DM currently diagnosed?

Neurological exam: tests reflexes to indicate the spinal cord is involved.

MRI scan: excludes vertebral disc diseases or tumours.

Spinal tap: rules out inflammatory diseases, for example meningitis.

Genotyping: identifies a genetic mutation associated with DM.

Why is this study important?

To understand the disease process

How does the genetic mutation cause damage to nerve cells which leads to paralysis?

To identify potential treatments

Finding toxic pathways that lead to nerve cell damage will help develop targeted treatments and hopefully alleviate the condition.

To identify markers for detection of DM

Finding DM signature proteins in spinal fluid will improve the accuracy of an early diagnosis.

DM and human Motor Neurone Disease (MND) share many similarities

Understanding DM will strengthen the link with MND research, facilitating breakthroughs in veterinary and human medicine.

Want to know more or recruit your dog?

If genetics and clinical signs indicate DM, you can recruit your dog to our study.
Please contact:

Mrs Catherine Stalin (Neurologist/clinician) at Catherine.Stalin@glasgow.ac.uk.
Dr Mark McLaughlin (Principle investigator) at Mark.McLaughlin@glasgow.ac.uk.

University of Glasgow, charity number SC004401

Poster designed by Lauren Black (PhD candidate)

8.2.5.2 Client consent form and participant information

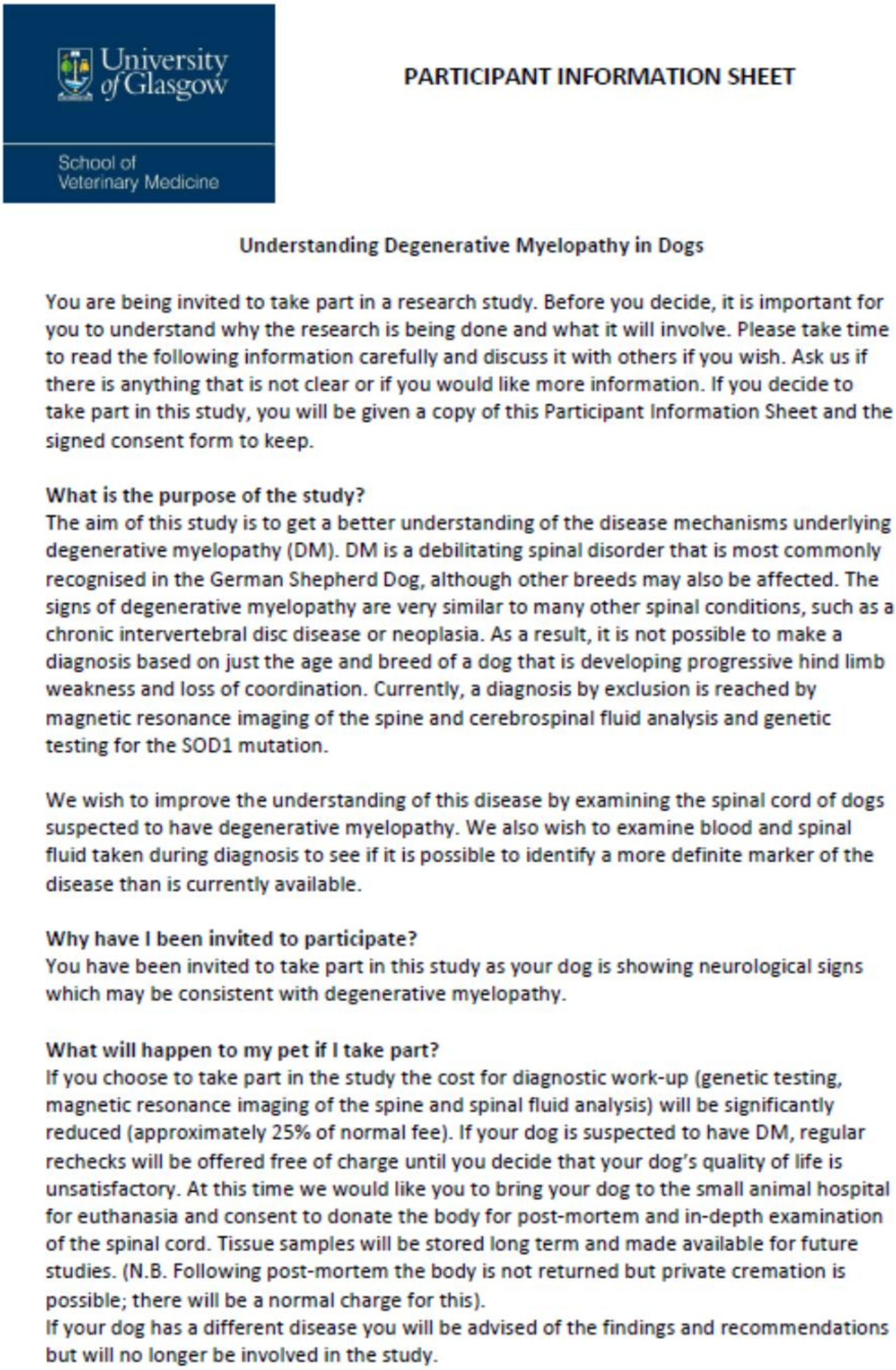

University of Glasgow

School of Veterinary Medicine

PARTICIPANT INFORMATION SHEET

Understanding Degenerative Myelopathy in Dogs

You are being invited to take part in a research study. Before you decide, it is important for you to understand why the research is being done and what it will involve. Please take time to read the following information carefully and discuss it with others if you wish. Ask us if there is anything that is not clear or if you would like more information. If you decide to take part in this study, you will be given a copy of this Participant Information Sheet and the signed consent form to keep.

What is the purpose of the study?
The aim of this study is to get a better understanding of the disease mechanisms underlying degenerative myelopathy (DM). DM is a debilitating spinal disorder that is most commonly recognised in the German Shepherd Dog, although other breeds may also be affected. The signs of degenerative myelopathy are very similar to many other spinal conditions, such as a chronic intervertebral disc disease or neoplasia. As a result, it is not possible to make a diagnosis based on just the age and breed of a dog that is developing progressive hind limb weakness and loss of coordination. Currently, a diagnosis by exclusion is reached by magnetic resonance imaging of the spine and cerebrospinal fluid analysis and genetic testing for the SOD1 mutation.

We wish to improve the understanding of this disease by examining the spinal cord of dogs suspected to have degenerative myelopathy. We also wish to examine blood and spinal fluid taken during diagnosis to see if it is possible to identify a more definite marker of the disease than is currently available.

Why have I been invited to participate?
You have been invited to take part in this study as your dog is showing neurological signs which may be consistent with degenerative myelopathy.

What will happen to my pet if I take part?
If you choose to take part in the study the cost for diagnostic work-up (genetic testing, magnetic resonance imaging of the spine and spinal fluid analysis) will be significantly reduced (approximately 25% of normal fee). If your dog is suspected to have DM, regular rechecks will be offered free of charge until you decide that your dog's quality of life is unsatisfactory. At this time we would like you to bring your dog to the small animal hospital for euthanasia and consent to donate the body for post-mortem and in-depth examination of the spinal cord. Tissue samples will be stored long term and made available for future studies. (N.B. Following post-mortem the body is not returned but private cremation is possible; there will be a normal charge for this).
If your dog has a different disease you will be advised of the findings and recommendations but will no longer be involved in the study.

What are the possible disadvantages and risks of taking part?
Not all owners are willing to submit their pet for post mortem examination so this may not be a study in which you wish to participate. Also it is necessary that euthanasia and post mortem are performed at the vet school which may difficult if you live at a distance.

What are the possible benefits of taking part?
Initial investigations will be charged at a significantly reduced price. All re-checks will be free of charge. Information from this study may help us to understand this disease better and hopefully lead to future treatments.

What if I no longer wish to participate in the study?
You have a right to withdraw from the study at any point without incurring additional financial costs for the diagnostic work-up.

Will my taking part in this study be kept confidential?
Clinical information which include client details will only by accessed by clinicians involved in the study or by other members of the study. Biological samples will be pseudo-anonymised for storage (it will be stored under a number which can be linked back to the clinical notes in case anything needs to be verified e.g. MRI images). These samples may be shared with other DM research projects. All research data will be retained for at least 10 years and may be shared with similar projects but remain anonymised and will not contain any personal data. On publication of research findings, all information relating to the case will be anonymous.

What will happen to the results of the research study?
Results will be published in neurology and veterinary peer-reviewed journals

This study has been funded by the Vet Fund and reviewed by the University of Glasgow School of Veterinary Medicine ethics committee. If you have further queries please contact Catherine.stalin@glasgow.ac.uk

Consent to participate in the study on canine degenerative myelopathy

I have read the information above and agree to the cost of ……………………………
for general anaesthetic, magnetic resonance imaging of the spine, blood tests for genetic screening and sampling of cerebrospinal fluid.

I am aware that by having tests at a reduced cost that there is an expectation for me to bring my dog to the vet school for euthanasia and post mortem when my dog no longer has a satisfactory quality of life.

I consent to samples being kept and case notes used for the purpose of this study.

Signed……………………………………………………………………

8.3 Supplementary results

8.3.1 Analysis of cell culture derived RNA

8.3.1.1 RNA integrity gels from DTT and CQ experiments

Extracted RNA from control and DTT treated samples was stored for around 2 years at -20°C but despite the long-term storage, RNA was still intact with values ranging from 45.0 to 241.7 ng/µl and 260/280 ratios around 2 (range= 1.79 to 2.05). DTT treated samples had lower RNA quantities compared to untreated controls and this was most likely because there were fewer cells after treatment. This reduction was also visible when RNA was run in a non-denaturing 1.5% agarose gel, but all RNA had retained integrity (Figure 8-7). RNA derived from control and CQ treated samples ranged from 120.3 to 646.0 ng/µl and 260/280 ratios were around 2 (range= 1.84-1.98). CQ treated samples had lower quantities of RNA compared to untreated controls, but the quality was similar. This was potentially the result of reduced cells in the treated groups. When RNA was separated by electrophoresis, bands corresponding to various RNA species were clearly intact, indicating the RNA had retained integrity (Figure 8-7).

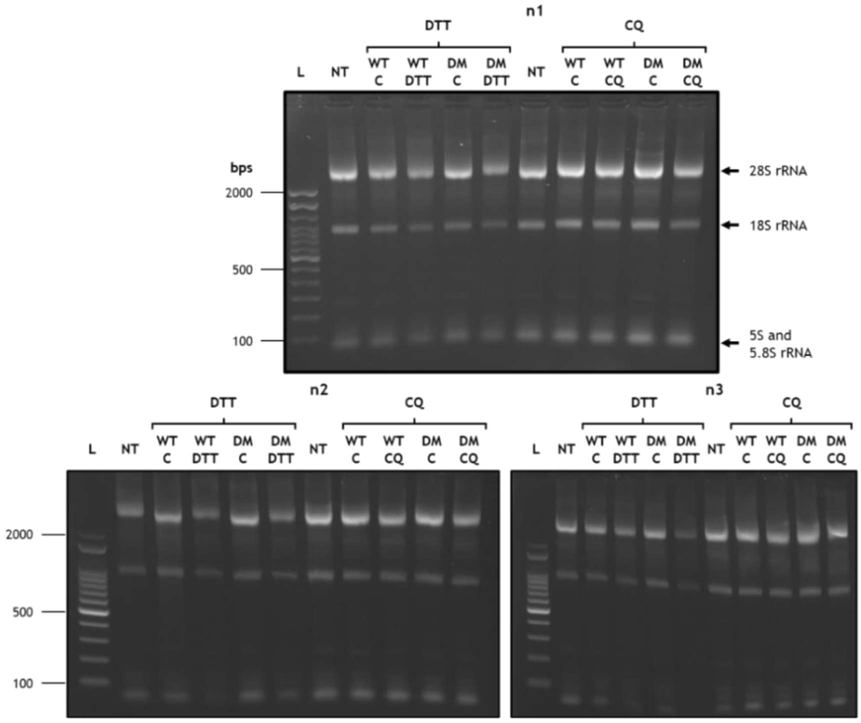
n1
DTT
CQ
L
NT
WT C
WT DTT
DM C
DM DTT
NT
WT C
WT CQ
DM C
DM CQ
bps
2000
500
100
28S rRNA
18S rRNA
5S and 5.8S rRNA
n2
DTT
CQ
L
NT
WT C
WT DTT
DM C
DM DTT
NT
WT C
WT CQ
DM C
DM CQ
2000
500
100
n3
DTT
CQ
L
NT
WT C
WT DTT
DM C
DM DTT
NT
WT C
WT CQ
DM C
DM CQ

Figure 8-7: RNA integrity gels for DTT and CQ studies. The 100 bp DNA ladder (L) is shown on the left. *NT samples were not produced from the DTT experiments, so a different NT control was included from the CQ study for each preparation. The labelled bands are 28S, 18S, 5.8S and 5S ribosomal RNA (rRNA). Also in the area indicated as 5S and 5.8S rRNA is transfer RNA (tRNA). Other bands that are not labelled represent messenger RNA (mRNA)(Farrell, 2017). DTT treated samples had less RNA present and this accounts for the slight reduction in band intensity in the gel.

8.3.1.2 RNA integrity gels from MG132 experiments

After RNA extraction, the integrity of RNA from control and MG132 treated samples was assessed. RNA quantities ranged from 75.0 to 571.9 ng/µl and 260/280 ratios were around 2 (range= 1.83-2.01). MG132 treated samples had lower quantities of RNA than control samples and this was visible when samples were separated in a gel. This was likely to reflect a reduction in cell density in treated cells. The expected bands corresponding to the various RNA species were present in all samples (Figure 8-8).

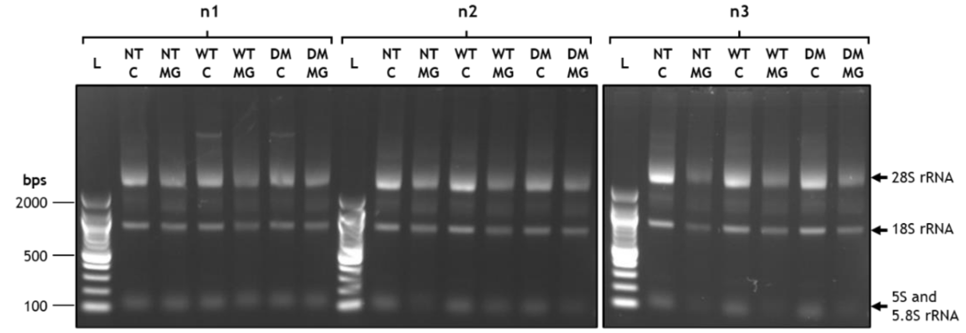

Figure 8-8: RNA integrity gel for control and MG132 treated cells. RNA was separated in a 1.5% agarose gel to assess integrity. The 100 bp DNA ladder (L) is shown on the left. The visible bands for each sample represent different RNA species. The labelled bands are 28S, 18S, 5.8S and 5S rRNA. Also in the area indicated as 5S and 5.8S rRNA is tRNA. Other bands that are not labelled represent mRNA (Farrell, 2017).

8.3.1.3 RT-PCR primer characterisation for *in vitro* derived samples

Primer characterisation showed *ATF3*, *BiP*, *GAPDH* and *XBP1* primers were compatible with the SK-N-SH derived samples but overall, *Cyc*, *Bcl2* and *CHOP* primers were not (Figure 8-9). *GAPDH* was successful as a housekeeping primer as it gave bands of the same size and intensity for each sample (Figure 8-9A). *Cyc* was trialled as a housekeeping primer, however levels were not consistent in SK-N-SH derived cDNA (Figure 8-9B), so it was not used further.

ATF3 was found in SK-N-SH cells at low levels, so it was included for investigation in case it was upregulated in times of ER stress (Figure 8-9C). *BiP* is associated with ubiquitination of proteins for degradation by the proteasome. *BiP* cDNA was absent in the NT control sample but present in both WT- and DM-SOD1-EGFP transfected controls (Figure 8-9E), suggesting the presence of the fusion proteins led to increased ubiquitination. Total *XBP1* (*XBP1t*) was present in all samples (Figure 8-9G) which can be expected as it is the splicing event of this transcription factor that is associated with stress, although levels of *XBP1t* can be elevated when stress is induced. At this level of investigation, the primer was deemed acceptable for further investigation.

The apoptosis markers *Bcl2* (Figure 8-9D) and *CHOP* (Figure 8-9F) had variable success when used with SK-N-SH cells. *Bcl2* was visible in all samples but was lowest in the SK-N-SH samples (NT, WT- and DM-SOD1-EGFP transfected) while *CHOP* was only present in the murine *rsh* sample. The *rsh* sample was found previously to have various stress markers present (McLaughlin *et al.*, 2007) while no stress was known to be induced in SK-N-SH controls. Low levels of *Bcl2* are found during homeostasis (Liu, Liu and Yang, 2019) so *Bcl2* was used for further investigation initially, however signals were inconsistent, so this primer was removed in the interest of time. The absence of *CHOP* in SK-N-SH samples suggested the primer was not compatible with human derived SK-N-SH cells, so it was not used further.

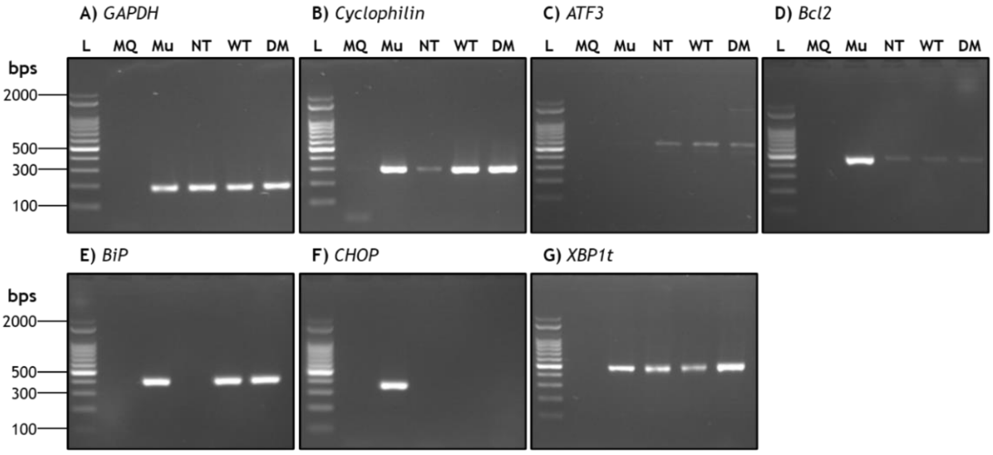

Figure 8-9: Characterisation of primers for RT-PCR. RNA was separated in a 2% agarose gel to assess primers. The 100 bp DNA ladder (L) is shown on the left of each image. Samples used were MQ water, murine *rsh* cDNA (Mu) and SK-N-SH NT, WT- and DM-SOD1-EGFP transfected control cDNA from one CQ experiment. Housekeeping primers trialled were *GAPDH* (**A**; ~195 bps) and *Cyc* (**B**; ~300 bps). Stress primers trialled were **C)** *ATF3*(~532 bps), **D)** *Bcl2* (~446 bps), **E)** *BiP* (~398 bps); **F)** *CHOP* (~356 bps) and **G)** *XBP1t* (~450 bps).

8.3.2 Analysis of tissue derived RNA

Integrity of RNA isolated from spinal cord tissues was good as rRNA was clearly present in all samples (Figure 8-10A). The intensity of some bands varied between samples, potentially because there was carry over of the loading buffer, increasing the total volume. Other work in MM's laboratory using canine derived cDNA showed *GAPDH* was not consistent as a housekeeping primer, so *Cyc* was used for characterisation of primers. *Cyc* was uniform across samples and band intensity was satisfactory (8-10B). For *ATF3*, *BiP* and *XBP1t* primers, there was evidence of cDNA present in canine samples, however compared to human and murine samples, levels were much lower (8-10C-E), so the PCR conditions were adjusted to improve cDNA retrieval.

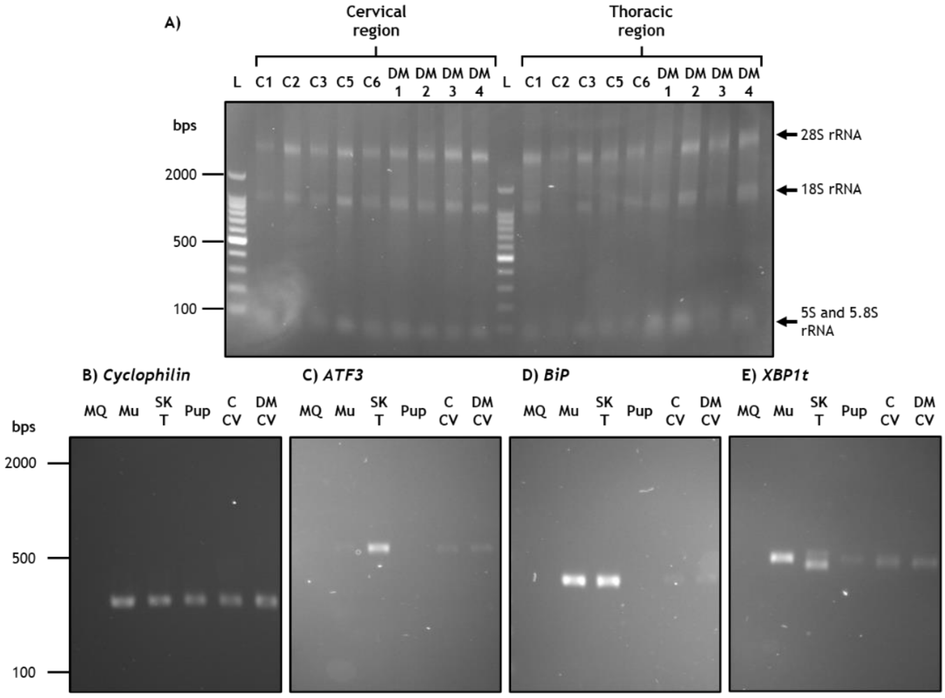
A)
Cervical region
Thoracic region
L C1 C2 C3 C5 C6 DM 1 DM 2 DM 3 DM 4 L C1 C2 C3 C5 C6 DM 1 DM 2 DM 3 DM 4
bps
2000
500
100
28S rRNA
18S rRNA
5S and 5.8S rRNA
B) Cyclophilin
C) ATF3
D) BiP
E) XBP1t
MQ Mu SK T Pup C CV DM CV
bps
2000
500
100

Figure 8-10: Spinal cord RNA integrity gels and characterisation of primers. A) RNA from control and DM spinal cords. cDNA from *rsh* mouse (Mu), DTT treated SK-N-SH cells (SK T), puppy brain (Pup) and pooled control and DM cervical spinal cord probed for **B)** *Cyc*; **C)** *ATF3*; **D)** *BiP* and **E)** *XBP1t*.

8.3.3 Analysis of proteins derived from cell culture

8.3.3.1 Ponceau S stained EV blots from Chapter 4

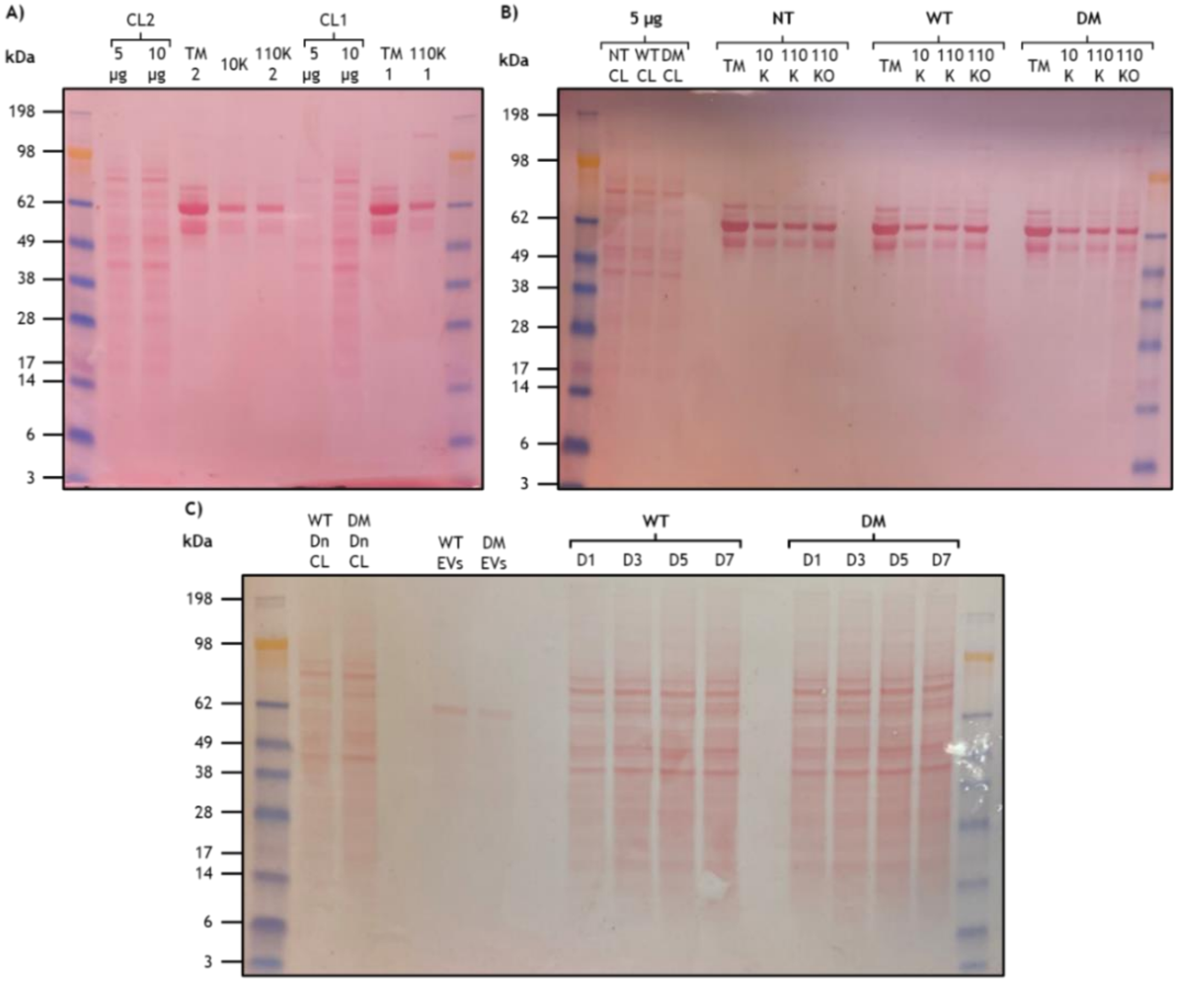
A)
kDa
CL2
5 µg
10 µg
TM 2
10K
110K 2
CL1
5 µg
10 µg
TM 1
110K 1
198
98
62
49
38
28
17
14
6
3
B)
kDa
5 µg
NT CL
WT CL
DM CL
NT
TM
10 K
110 K
110 KO
WT
TM
10 K
110 K
110 KO
DM
TM
10 K
110 K
110 KO
198
98
62
49
38
28
17
14
6
3
C)
kDa
WT Dn CL
DM Dn CL
WT EVs
DM EVs
WT
D1
D3
D5
D7
DM
D1
D3
D5
D7
198
98
62
49
38
28
17
14
6
3

Figure 8-11: Ponceau S staining of representative EV blots from Chapter 4. A) Stained blot from the initial investigation of two ultracentrifugation steps with NT cells. **B)** Stained blot from investigation of two ultracentrifugation steps with NT and transfected cells. “KO” is short for 110K only. **C)** Stained blot from initial EV transfer experiment.

8.3.3.2 Ponceau S stained EV blots from Chapter 5

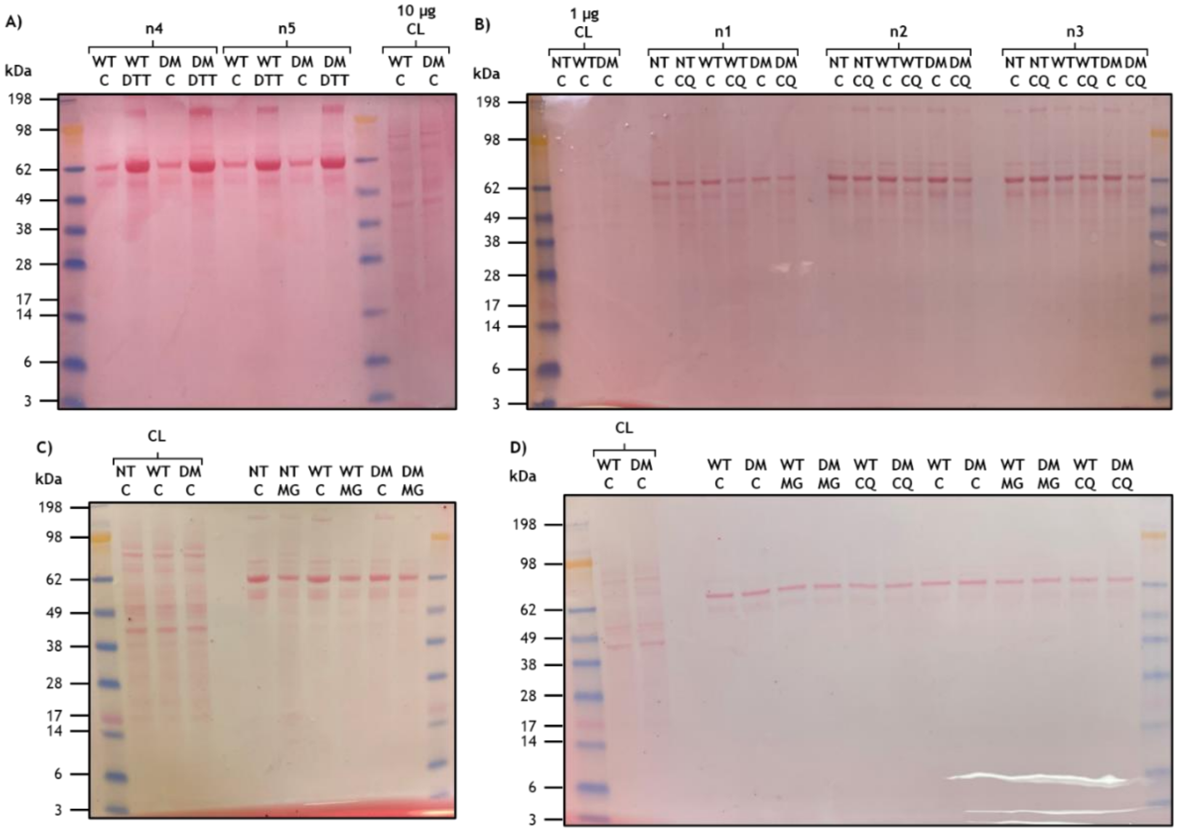
A)
n4
n5
10 µg CL
WT C
WT DTT
DM C
DM DTT
WT C
WT DTT
DM C
DM DTT
WT C
DM C
kDa
198
98
62
49
38
28
17
14
6
3
B)
1 µg CL
NT C
WT C
DM C
n1
n2
n3
NT C
NT CQ
WT C
WT CQ
DM C
DM CQ
kDa
198
98
62
49
38
28
17
14
6
3
C)
CL
NT C
WT C
DM C
NT C
NT MG
WT C
WT MG
DM C
DM MG
kDa
198
98
62
49
38
28
17
14
6
3
D)
CL
WT C
DM C
WT C
DM C
WT MG
DM MG
WT CQ
DM CQ
WT C
DM C
WT MG
DM MG
WT CQ
DM CQ
kDa
198
98
62
49
38
28
17
14
6
3

Figure 8-12: Ponceau S staining of representative EV blots for Chapter 5. A) Stained EV blot from the DTT study with CL controls. The blot contained samples from preparations four and five. **B)** Stained EV blot from CQ study with CL controls. The blot contained samples from preparations one, two and three. **C)** Stained EV blot from MG132 study with CL controls. The blot contained samples from preparation one. **D)** Stained EV blot from study with three centrifugation steps with MG312 and CQ treatments. CL controls were also loaded. The blot contained samples from preparation one.

8.3.3.3 DTT total protein gels

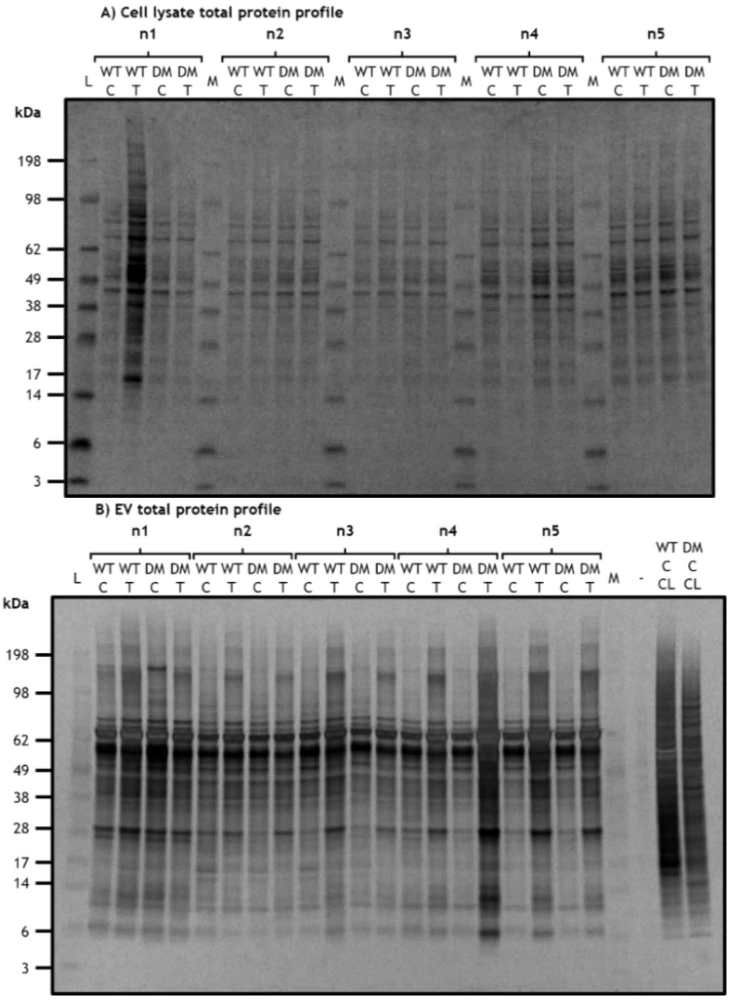
A) Cell lysate total protein profile
n1
n2
n3
n4
n5
L
WT WT DM DM
C T C T
M
kDa
198
98
62
49
38
28
17
14
6
3
B) EV total protein profile
n1
n2
n3
n4
n5
L
WT WT DM DM
C T C T
M
-
WT DM
C C
CL CL
kDa
198
98
62
49
38
28
17
14
6
3

Figure 8-13: All total protein profiles from DTT studies. A) shows the total protein profile of CLs from cells transfected with pWT- and pDM-SOD1-EGFP, with (T) or without (C) DTT treatment. All five preparations are shown in the one gel stained with Coomassie Blue. **B)** is the total protein profile for all five preparations of EVs using Silver staining. EVs are from cells that were transfected with pWT-SOD1-EGFP or pDM-SOD1-EGFP and either not treated or treated with DTT. The last two lanes represent control WT- and DM-SOD1-EGFP CLs.

8.3.3.4 CQ total protein gels

A) CL total protein profile

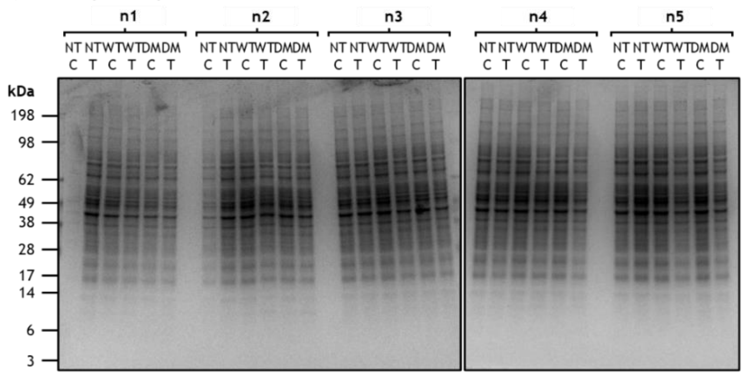
n1
n2
n3
n4
n5
NT NT WT WT DM DM
C T C T C T
kDa
198
98
62
49
38
28
17
14
6
3

B) EV total protein profile

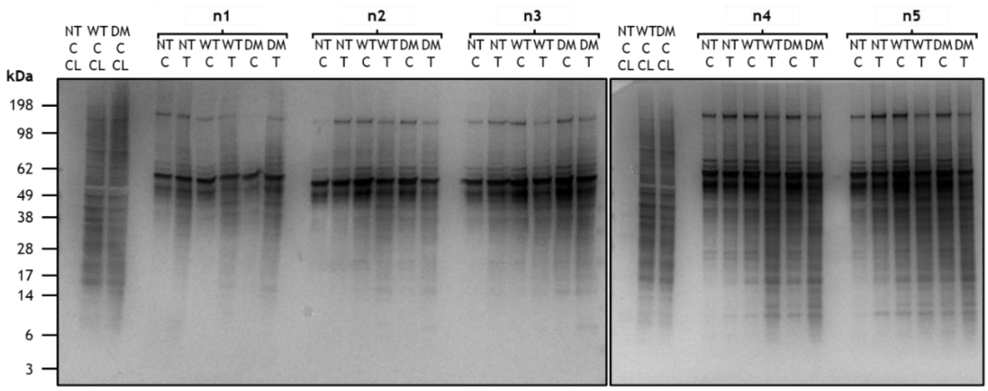
NT WT DM
C C C
CL CL CL
n1
n2
n3
n4
n5
NT NT WT WT DM DM
C T C T C T
kDa
198
98
62
49
38
28
17
14
6
3

Figure 8-14: All total protein profiles from the CQ study. A) shows the total protein profile in CLs from all five preparations using Coomassie Blue staining. Cells were either non-transfected or transfected with WT- or DM-SOD1-EGFP. Some cells were not treated with CQ (C) while others were treated with CQ (T). **B)** is the total protein profile for EVs from each of the five preparations using silver staining. The first three lanes of each well had CL controls from NT, WT- and DM-SOD1-EGFP transfected control cells. Missing lanes in the NT CLs in CL gels and EV control lanes were due to contamination of lysates with TRIzol™ during protein/RNA extraction from culture plates.

8.3.3.5 MG132 total protein gels

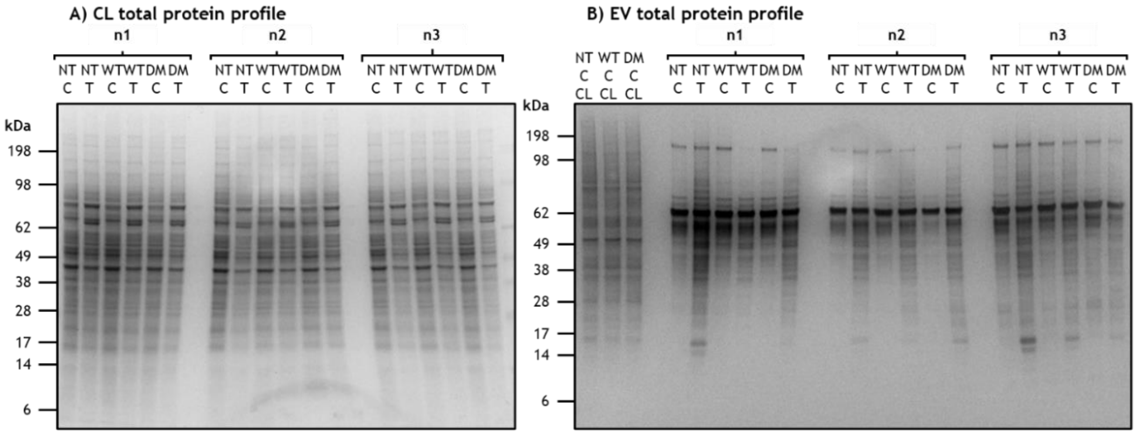
A) CL total protein profile
n1
n2
n3
NT NT WT WT DM DM
C T C T C T
kDa
198
98
62
49
38
28
17
14
6
B) EV total protein profile
NT WT DM
C C C
CL CL CL
n1
n2
n3
NT NT WT WT DM DM
C T C T C T
kDa
198
98
62
49
38
28
17
14
6

Figure 8-15: All total protein profiles from the MG132 study. A) total protein profile in control and MG132 treated CLs from all three preparations using Coomassie Blue staining. **B)** total protein profile for EVs from each of the three preparations using silver staining. The first three lanes were CL controls from NT, WT- and DM-SOD1-EGFP transfected control cells.

8.3.3.6 Full WBs for DTT samples

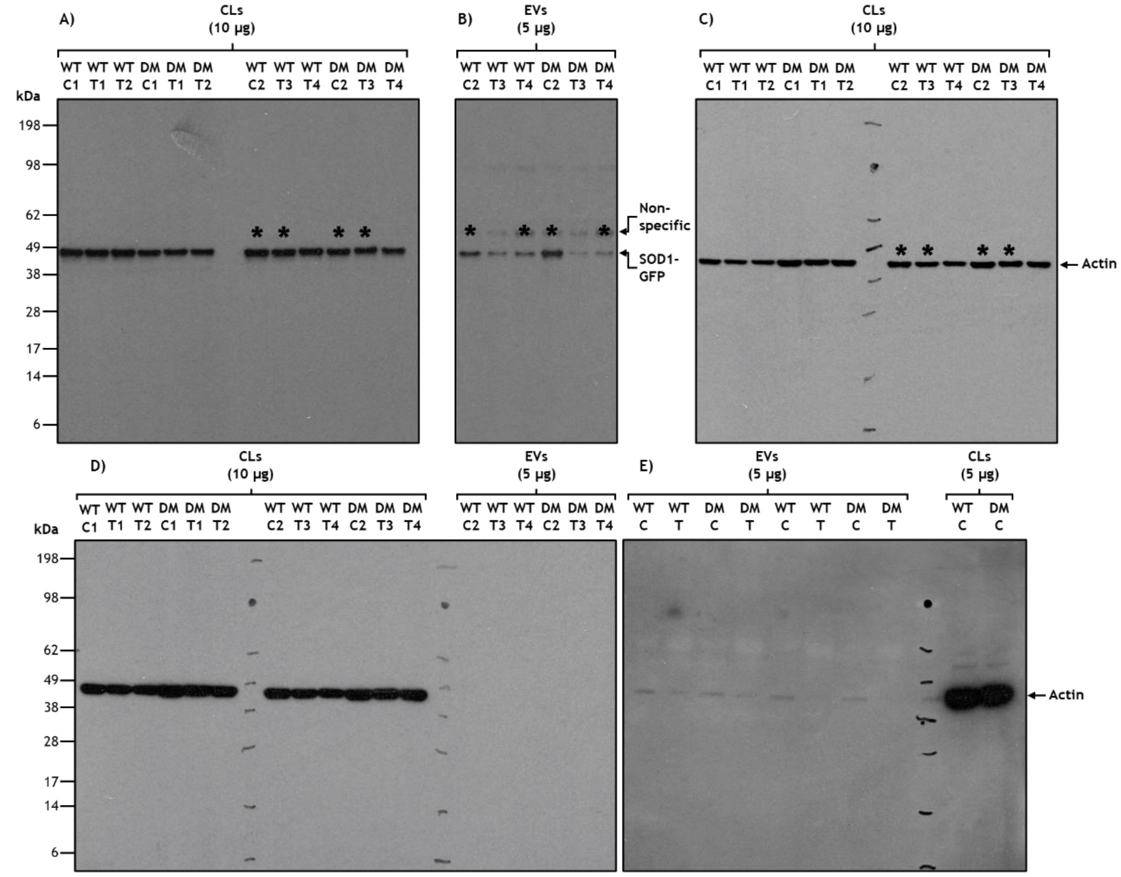
A)
CLs
(10 µg)
WT WT WT DM DM DM WT WT WT DM DM DM
C1 T1 T2 C1 T1 T2 C2 T3 T4 C2 T3 T4
B)
EVs
(5 µg)
WT WT WT DM DM DM
C2 T3 T4 C2 T3 T4
C)
CLs
(10 µg)
WT WT WT DM DM DM WT WT WT DM DM DM
C1 T1 T2 C1 T1 T2 C2 T3 T4 C2 T3 T4
kDa
198
98
62
49
38
28
17
14
6
Non-specific
SOD1-GFP
Actin
D)
CLs
(10 µg)
WT WT WT DM DM DM WT WT WT DM DM DM
C1 T1 T2 C1 T1 T2 C2 T3 T4 C2 T3 T4
EVs
(5 µg)
WT WT WT DM DM DM
C2 T3 T4 C2 T3 T4
E)
EVs
(5 µg)
WT WT DM DM WT WT DM DM
C T C T C T C T
CLs
(5 µg)
WT DM
C C
kDa
198
98
62
49
38
28
17
14
6
Actin

Figure 8-16: Full WBs for DTT studies. A) All CLs in WB for DTT preparation 1 (n1) probed for GFP. **B)** All EVs in WB for DTT n1 probed for GFP. **C)** All CLs in WB for DTT n1 probed for actin (short exposure). Bands used in the figure are indicated by an asterisk. **D)** All CLs and EVs in WB for DTT n1 probed for actin (long exposure). **E)** All EVs and CL control in WB for DTT n4 and n5 probed for actin.

8.3.3.7 Full WBs for CQ EV samples

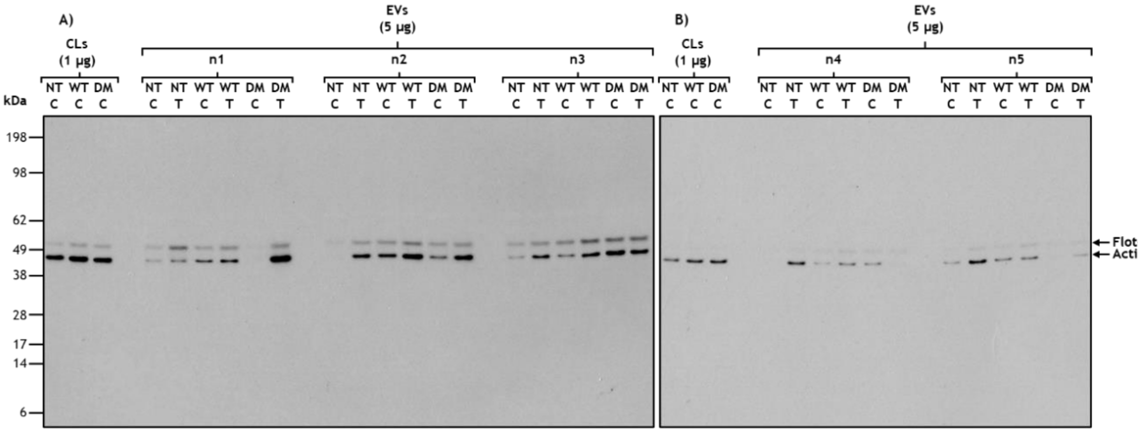
A)
CLs
(1 µg)
EVs
(5 µg)
n1
n2
n3
B)
CLs
(1 µg)
EVs
(5 µg)
n4
n5
NT WT DM
C C C
NT NT WT WT DM DM
C T C T C T
kDa
198
98
62
49
38
28
17
14
6
← Flot-1
← Actin

Figure 8-17: Full WBs used for CQ EVs. All EVs (5 µg) in WBs for CQ samples probed for actin accompanied by NT, WT- and DM-SOD1-EGFP transfected CL controls at 1 µg. A) n1-3, **B)** All EVs (5 µg) in WB n4-n5. Additional band is flotillin-1 (flot-1) as blots were originally probed with anti-flotillin-1.

8.3.3.8 Full WBs for MG132 EV samples

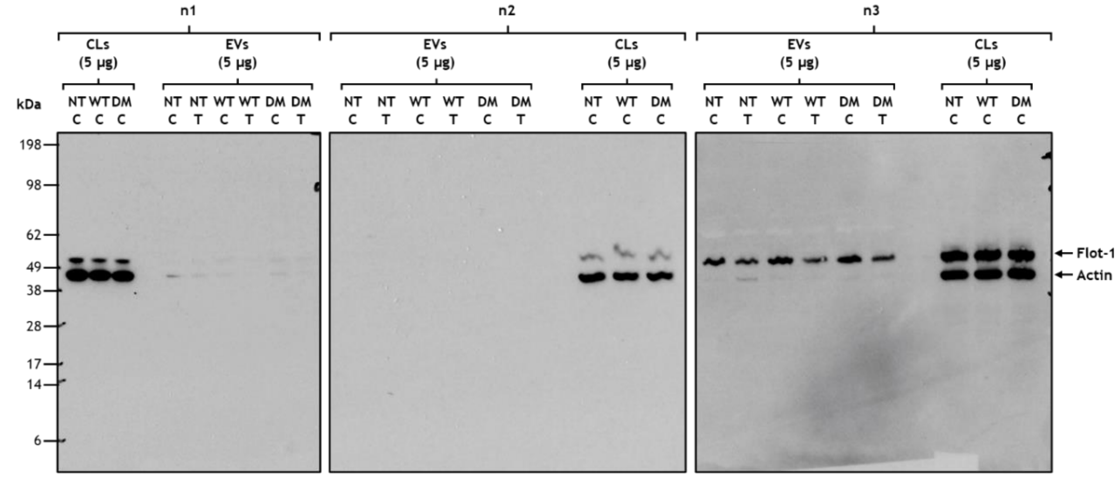
n1
n2
n3
CLs
(5 µg)
EVs
(5 µg)
NT WT DM
C C C
NT NT WT WT DM DM
C T C T C T
kDa
198
98
62
49
38
28
17
14
6
← Flot-1
← Actin

Figure 8-18: Full WBs used for MG132 EVs. A) All EVs (5 µg) in WB for MG132 n1-n3 probed for actin accompanied by NT, WT- and DM-SOD1-EGFP transfected CL controls at 5 µg. An additional band is present for flotillin-1 (flot-1) as all blots were originally probed with anti-flotillin-1, then anti-actin antibodies.

8.3.3.9 Full WBs for three step centrifugation experiment

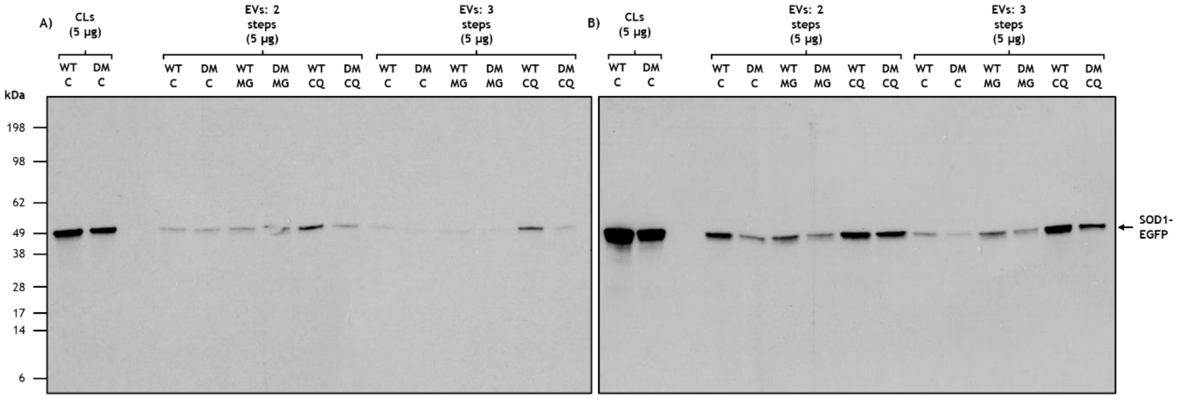

Figure 8-19: Full WBs for EVs from multiple steps. WBs containing CLs and EVs from the 10,000 xg and 110,858 xg centrifugation steps from n2 (**A**) and n3 (**B**) were probed with anti-GFP.

8.3.4 Analysis of proteins from tissue derived samples

8.3.4.1 Optimisation of protein extraction from tissues

Protein extraction was based on methods described in Hesse *et al.,* (2019) and Nelvagal et al., (2020). The protein extraction method was trialled using 2, 50 mg aliquots of C3 cervical powdered cord. Powdered tissue was suspended in 500 µl or 1 ml of chilled extraction buffer (2% SDS and 100 mM Tris-HCl) and blanks of the same volumes were made with the extraction buffer alone. A 5 mm diameter stainless-steel ball was added to each sample then tubes were loaded into a ball mill (Retsch Mixer Mill MM 400, Germany) and tissues homogenised at 30 Hz for 2 minutes at RT. Samples were centrifuged at 380 *xg* for 3 minutes at 4°C then 100 µl and 300 µl of the 500 µl starting volume SN and 200 µl and 600 µl of the 1 ml starting volume SN were transferred to fresh tubes. Another aliquot of the homogenised samples and 500 µl blank was made for protein assay. The 100 µl and 200 µl aliquots were left without protease inhibitors and the 300 µl and 600 µl aliquots had 3 µl and 6 µl of Protease inhibitor cocktail (Sigma Aldrich, USA) added respectively. Absence of protease inhibitors was to minimise interference with downstream trypsinisation required for proteomics. Samples were incubated on ice and centrifuged as previously described. The SN was separated from the pellet and the latter was resuspended in 100 µl extraction buffer. A protein assay was carried out on the homogenate, SN and pellet fractions (Section 2.4.3).

Protein recovered from extraction buffer blanks was minimal (0.09 mg/ml) and was likely not 0 mg/ml due to the white colour present in the extraction buffer from SDS. Total homogenate protein recovery was roughly double in the cord homogenised in 500 µl buffer compared to the cord homogenised in 1 ml (Figure 8-20A). This was expected as the latter sample was more dilute. Protein recovery was higher in the SN from all samples compared to the respective pellets and grouped together, there was significantly more protein in the SN group compared to the pellet group ($p \leq 0.01$). This shows most protein had been collected in the SN and little was left behind in the pellet fraction; on average 23.4% of total protein was found in the pellet. The protein recovered in the SN fraction was roughly the same as the quantity recovered in the total homogenate; the mean protein recovery in the SN fraction was 15% higher than the protein recovered in the total homogenate (p= 0.2083; ratio paired t-test) showing minimal protein was lost in the remainder of the protein extraction. SN samples resuspended in buffer with protease inhibitor cocktail (300 µl and 600 µl) had a slightly higher protein concentration than total homogenate samples and SN without inhibitors (100 µl and 200 µl) indicating some proteins were prevented from being broken down by endogenous enzymes in the presence of the inhibitors. SN samples from the tissue homogenised in 500 µl extraction buffer also had higher protein concentrations than those suspended in 1 ml extraction buffer. For investigative studies, tissues were resuspended in 1 ml of extraction buffer so there was more sample available for downstream analysis and it was easier to handle during the extraction process where froth was formed. As there did not appear to be a significant difference between samples resuspended with or without protease inhibitors, the same protocol was adopted for further studies so there was minimal risk of inhibitors affecting downstream proteomics, and a larger pool of proteins could be analysed for biochemistry.

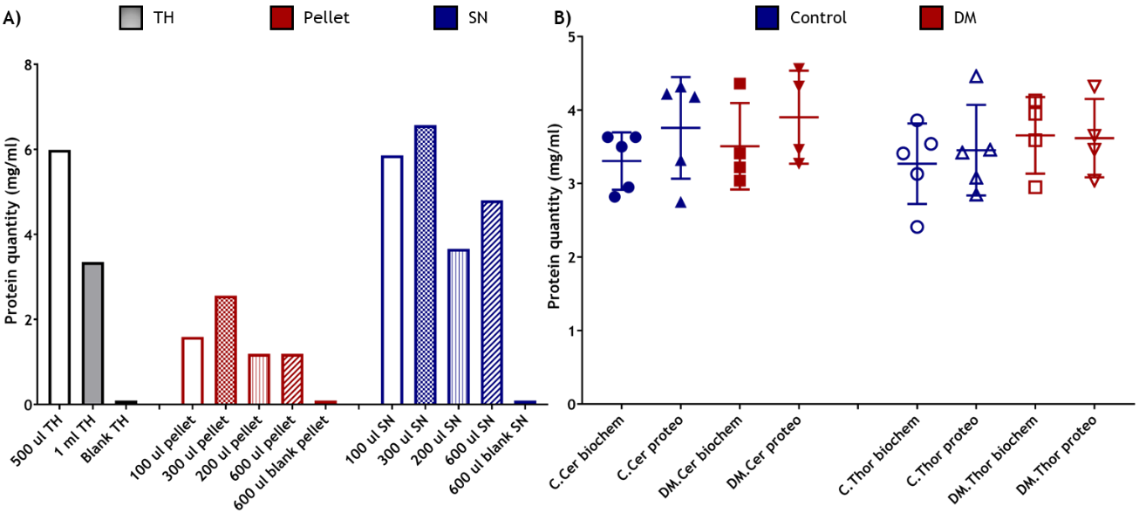

Figure 8-20: Optimisation of the protein extraction method from tissue. A) Shown in the graph are the protein values (mg/ml) for samples at various stages of protein extraction during the trial run. The proteins recovered from the pellet and SN fractions were compared using a paired t-test (*n*= 4) and showed there was significantly more protein in the SN fraction compared to the pellet (*p*= 0.0029). The presence or absence of protease inhibitors was also compared to ensure there was no significant degradation of protein in the absence of inhibitors but as *n*= 2 for each group, statistics were not available. Inhibitors were absent from the 100 µl and 200 µl samples and present in the 300 µl and 600 µl samples. **B)** Shown in the graph are the protein values (mg/ml) for samples collected from cervical and thoracic spinal cord segments in the investigative study. SN collected after the high-speed centrifugation step were assayed with BCA for protein quantity. The samples used for protein biochemistry contained protease inhibitors however the samples for proteomics did not have these inhibitors. The mg/ml of protein for each sample was calculated and plotted on the graph. Control and DM cervical and thoracic segment protein values were combined for ordinary one-way ANOVA analysis with Bonferroni's multiple comparison test. There were no statistically significant differences between groups.

The quantity of protein recovered from the tissues to be investigated by biochemistry and proteomics was compared to ensure the pool of proteins was similar between analyses. An ordinary one-way ANOVA with Bonferroni's multiple comparisons test showed there were no statistical differences in protein concentration between spinal cord segment, extraction conditions (with or without protease inhibitors; Figure 8-20B) or case type.

8.3.4.2 Ponceau S staining of nitrocellulose membranes (tissue)

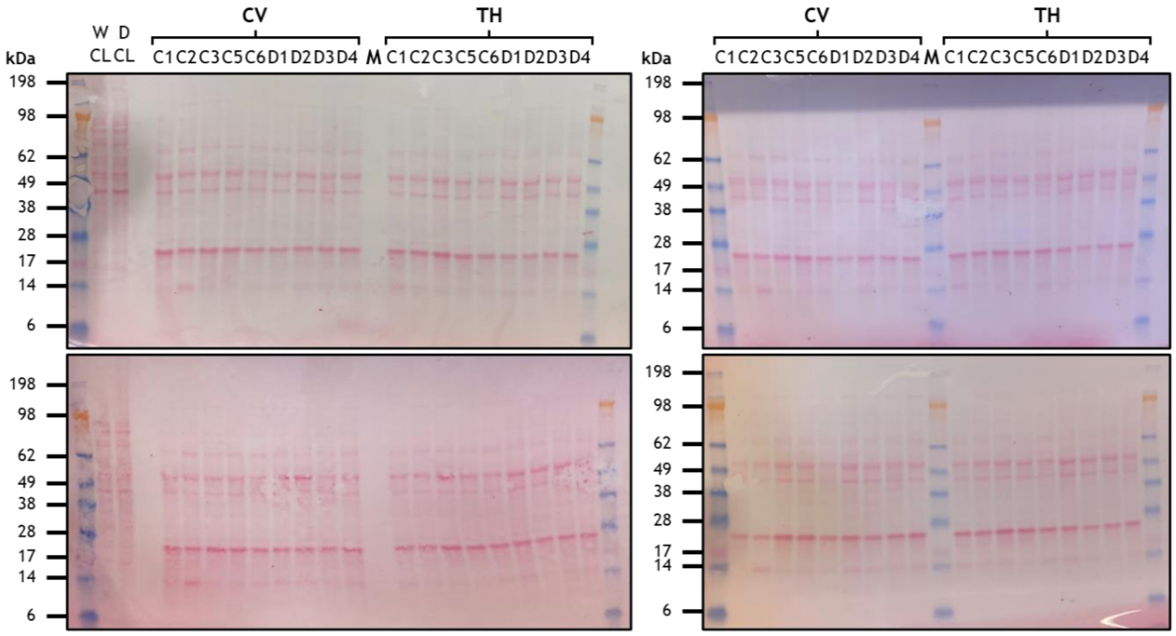
CV
TH
W CL
D CL
C1 C2 C3 C5 C6 D1 D2 D3 D4
M
C1 C2 C3 C5 C6 D1 D2 D3 D4
kDa
198
98
62
49
38
28
17
14
6

Figure 8-21: Ponceau S staining of tissue blots from Chapter 6. To ensure equal loading, nitrocellulose membranes were stained with Ponceau S before being probed with antibodies.

8.3.4.3 Full tissue WBs

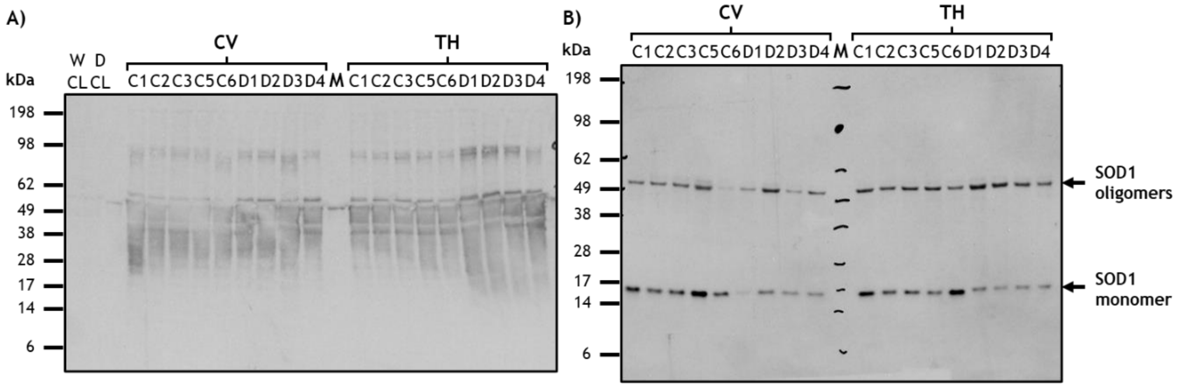
A)
CV
TH
W CL
D CL
C1 C2 C3 C5 C6 D1 D2 D3 D4
M
C1 C2 C3 C5 C6 D1 D2 D3 D4
kDa
198
98
62
49
38
28
17
14
6
B)
SOD1 oligomers
SOD1 monomer

Figure 8-22: Full WBs for tissue samples. A) full WB for tissues probed with anti-GFAP. **B)** full WB for tissues probed with anti-CuZnSOD.

8.3.4.4 BLAST results for MBP isoforms

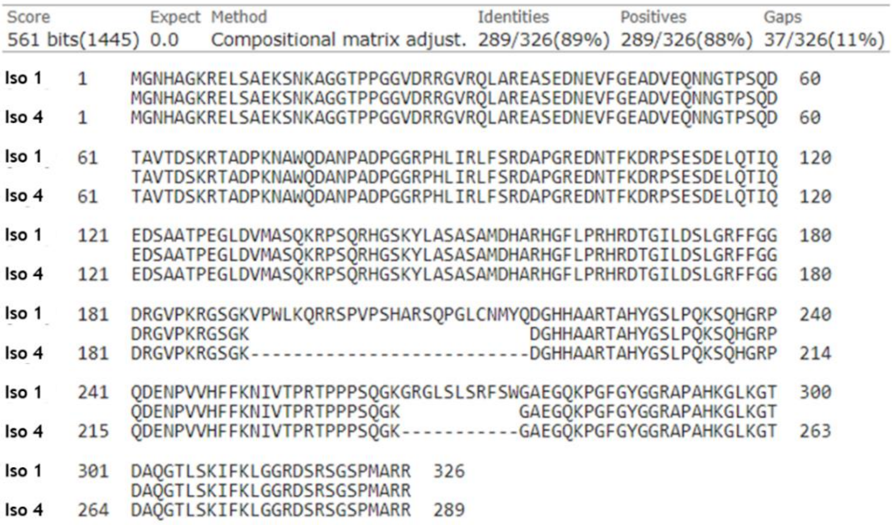

```
Score             Expect  Method                          Identities      Positives       Gaps
561 bits(1445)    0.0     Compositional matrix adjust.    289/326(89%)    289/326(88%)    37/326(11%)

Iso 1  1    MGNHAGKRELSAEKSNKAGGTPPGGVDRRGVRQLAREASEDNEVFGEADVEQNNGTPSQD  60
            MGNHAGKRELSAEKSNKAGGTPPGGVDRRGVRQLAREASEDNEVFGEADVEQNNGTPSQD
Iso 4  1    MGNHAGKRELSAEKSNKAGGTPPGGVDRRGVRQLAREASEDNEVFGEADVEQNNGTPSQD  60

Iso 1  61   TAVTDSKRTADPKNAWQDANPADPGGRPHLIRLFSRDAPGREDNTFKDRPSESDELQTIQ  120
            TAVTDSKRTADPKNAWQDANPADPGGRPHLIRLFSRDAPGREDNTFKDRPSESDELQTIQ
Iso 4  61   TAVTDSKRTADPKNAWQDANPADPGGRPHLIRLFSRDAPGREDNTFKDRPSESDELQTIQ  120

Iso 1  121  EDSAATPEGLDVMASQKRPSQRHGSKYLASASAMDHARHGFLPRHRDTGILDSLGRFFGG  180
            EDSAATPEGLDVMASQKRPSQRHGSKYLASASAMDHARHGFLPRHRDTGILDSLGRFFGG
Iso 4  121  EDSAATPEGLDVMASQKRPSQRHGSKYLASASAMDHARHGFLPRHRDTGILDSLGRFFGG  180

Iso 1  181  DRGVPKRGSGKVPWLKQRRSPVPSHARSQPGLCNMYQDGHHAARTAHYGSLPQKSQHGRP  240
            DRGVPKRGSGK                          DGHHAARTAHYGSLPQKSQHGRP
Iso 4  181  DRGVPKRGSGK--------------------------DGHHAARTAHYGSLPQKSQHGRP  214

Iso 1  241  QDENPVVHFFKNIVTPRTPPPSQGKGRGLSLSRFSWGAEGQKPGFGYGGRAPAHKGLKGT  300
            QDENPVVHFFKNIVTPRTPPPSQGK           GAEGQKPGFGYGGRAPAHKGLKGT
Iso 4  215  QDENPVVHFFKNIVTPRTPPPSQGK-----------GAEGQKPGFGYGGRAPAHKGLKGT  263

Iso 1  301  DAQGTLSKIFKLGGRDSRSGSPMARR  326
            DAQGTLSKIFKLGGRDSRSGSPMARR
Iso 4  264  DAQGTLSKIFKLGGRDSRSGSPMARR  289
```

Figure 8-23: BLAST results for MBP isoform 1 and 4. The percent identity between MBP isoform 1 and 4 is approximately 88%.

8.3.4.5 BLAST results for LDHA and LDHB

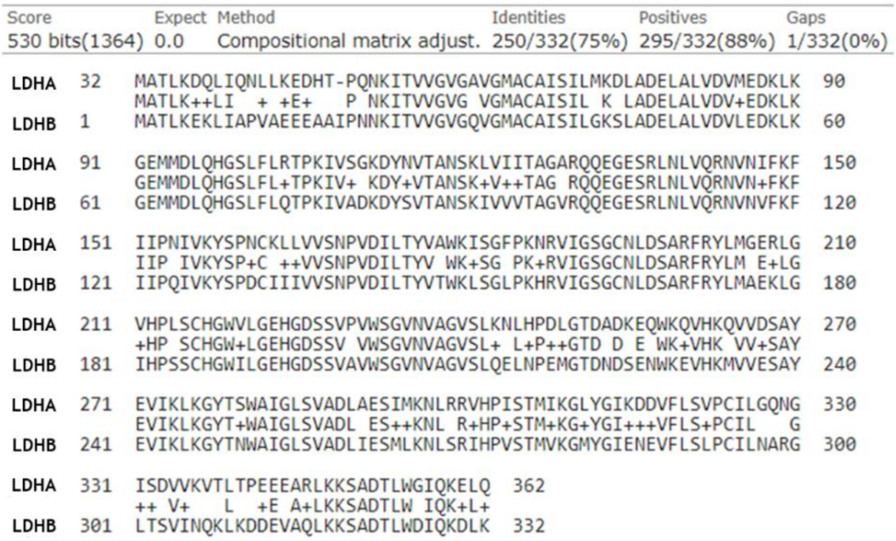

```
Score             Expect  Method                          Identities      Positives       Gaps
530 bits(1364)    0.0     Compositional matrix adjust.    250/332(75%)    295/332(88%)    1/332(0%)

LDHA  32   MATLKDQLIQNLLKEDHT-PQNKITVVGVGAVGMACAISILMKDLADELALVDVMEDKLK  90
           MATLK++LI  + +E+   P NKITVVGVG VGMACAISIL K LADELALVDV+EDKLK
LDHB  1    MATLKEKLIAPVAEEEAAIPNNKITVVGVGQVGMACAISILGKSLADELALVDVLEDKLK  60

LDHA  91   GEMMDLQHGSLFLRTPKIVSGKDYNVTANSKLVIITAGARQQEGESRLNLVQRNVNIFKF  150
           GEMMDLQHGSLFL+TPKIV+ KDY+VTANSK+V++TAG RQQEGESRLNLVQRNVN+FKF
LDHB  61   GEMMDLQHGSLFLQTPKIVADKDYSVTANSKIVVVTAGVRQQEGESRLNLVQRNVNVFKF  120

LDHA  151  IIPNIVKYSPNCKLLVVSNPVDILTYVAWKISGFPKNRVIGSGCNLDSARFRYLMGERLG  210
           IIP IVKYSP+C ++VVSNPVDILTYV WK+SG PK+RVIGSGCNLDSARFRYLM E+LG
LDHB  121  IIPQIVKYSPDCIIIVVSNPVDILTYVTWKLSGLPKHRVIGSGCNLDSARFRYLMAEKLG  180

LDHA  211  VHPLSCHGWVLGEHGDSSVPVWSGVNVAGVSLKNLHPDLGTDADKEQWKQVHKQVVDSAY  270
           +HP SCHGW+LGEHGDSSV VWSGVNVAGVSL+ L+P++GTD D E WK+VHK VV+SAY
LDHB  181  IHPSSCHGWILGEHGDSSVAVWSGVNVAGVSLQELNPEMGTDNDSENWKEVHKMVVESAY  240

LDHA  271  EVIKLKGYTSWAIGLSVADLAESIMKNLRRVHPISTMIKGLYGIKDDVFLSVPCILGQNG  330
           EVIKLKGYT+WAIGLSVADL ES++KNL R+HP+STM+KG+YGI+++VFLS+PCIL   G
LDHB  241  EVIKLKGYTNWAIGLSVADLIESMLKNLSRIHPVSTMVKGMYGIENEVFLSLPCILNARG  300

LDHA  331  ISDVVKVTLTPEEEARLKKSADTLWGIQKELQ  362
           ++ V+   L  +E A+LKKSADTLW IQK+L+
LDHB  301  LTSVINQKLKDDEVAQLKKSADTLWDIQKDLK  332
```

Figure 8-24: BLAST results for LDHA and LDHB. The accession numbers for the LDHA and LDHB isoforms found in the proteomics dataset were compared with a BLAST. The protein sequences were 75% similar.

List of references

Aber, E. R., Griffey, C. J., Davies, T., Li, A. M., Yang, Y. J., Croce, K. R., Goldman, J. E., Grutzendler, J., Canman, J. C. and Yamamoto, A. (2022) 'Oligodendroglial macroautophagy is essential for myelin sheath turnover to prevent neurodegeneration and death', *Cell Rep,* 41(3), pp. 111480.

Abramowitz, M. and Davidson, M. W. (2020) *Introduction to Fluorescence*: Olympus Corporation. Available at: https://www.olympus-lifescience.com/en/microscope-resource/primer/lightandcolor/fluorointroduction/ (Accessed: July 2020).

Addepalli, R. V. and Mullangi, R. (2020) 'A concise review on lipidomics analysis in biological samples', *ADMET & DMPK,* 9(1), pp. 1-22.

Agnello, L., Colletti, T., Lo Sasso, B., Vidali, M., Spataro, R., Gambino, C. M., Giglio, R. V., Piccoli, T., Bivona, G., La Bella, V. and Ciaccio, M. (2021) 'Tau protein as a diagnostic and prognostic biomarker in amyotrophic lateral sclerosis', *Eur J Neurol,* 28(6), pp. 1868-1875.

Alberts, B., Johnson, A., Lewis, J., Raff, M., Roberts, K. and Walter, P. (2002) 'Transport from the ER through the Golgi Apparatus', in *Molecular Biology of the Cell* [Online]. Version. Available at: https://www.ncbi.nlm.nih.gov/books/NBK26941/ (Accessed: 2023).

ALSoD, A. L. S. o. D. (2023) *Gene summary for SOD1.* Available at: https://alsod.ac.uk/output/gene.php/SOD1 2023).

Averill, D. R., Jr. (1973) 'Degenerative myelopathy in the aging German Shepherd dog: clinical and pathologic findings', *J Am Vet Med Assoc,* 162(12), pp. 1045-51.

Awano, T., Johnson, G. S., Wade, C. M., Katz, M. L., Johnson, G. C., Taylor, J. F., Perloski, M., Biagi, T., Baranowska, I., Long, S., March, P. A., Olby, N. J., Shelton, G. D., Khan, S., O'Brien, D. P., Lindblad-Toh, K. and Coates, J. R. (2009) 'Genome-wide association analysis reveals a SOD1 mutation in canine degenerative myelopathy that resembles amyotrophic lateral sclerosis', *Proc Natl Acad Sci U S A,* 106(8), pp. 2794-9.

Banks, C. J. and Andersen, J. L. (2019) 'Mechanisms of SOD1 regulation by post-translational modifications', *Redox Biol,* 26, pp. 101270.

Baron, O., Boudi, A., Dias, C., Schilling, M., Nölle, A., Vizcay-Barrena, G., Rattray, I., Jungbluth, H., Scheper, W., Fleck, R. A., Bates, G. P. and Fanto, M. (2017) 'Stall in Canonical Autophagy-Lysosome Pathways Prompts Nucleophagy-Based Nuclear Breakdown in Neurodegeneration', *Curr Biol,* 27(23), pp. 3626-3642.e6.

Baron, O. and Fanto, M. (2018) 'Karyoptosis: A novel type of cell death caused by chronic autophagy inhibition', *Autophagy,* 14(4), pp. 722-723.

Berdyński, M., Miszta, P., Safranow, K., Andersen, P. M., Morita, M., Filipek, S., Żekanowski, C. and Kuźma-Kozakiewicz, M. (2022) 'SOD1 mutations associated with amyotrophic lateral sclerosis analysis of variant severity', *Sci Rep,* 12(1), pp. 103.

Biedler, J. L., Helson, L. and Spengler, B. A. (1973) 'Morphology and growth, tumorigenicity, and cytogenetics of human neuroblastoma cells in continuous culture', *Cancer Res,* 33(11), pp. 2643-52.

Bonifacino, T., Zerbo, R. A., Balbi, M., Torazza, C., Frumento, G., Fedele, E., Bonanno, G. and Milanese, M. (2021) 'Nearly 30 Years of Animal Models to Study Amyotrophic Lateral Sclerosis: A Historical Overview and Future Perspectives', *Int J Mol Sci,* 22(22).

Bozzo, F., Mirra, A. and Carri, M. T. (2017) 'Oxidative stress and mitochondrial damage in the pathogenesis of ALS: New perspectives', *Neurosci Lett,* 636, pp. 3-8.

Braund, K. G. and Vandevelde, M. (1978) 'German Shepherd dog myelopathy--a morphologic and morphometric study', *Am J Vet Res,* 39(8), pp. 1309-15.

Brennan, K., Martin, K., FitzGerald, S. P., O'Sullivan, J., Wu, Y., Blanco, A., Richardson, C. and Mc Gee, M. M. (2020) 'A comparison of methods for the isolation and separation of extracellular vesicles from protein and lipid particles in human serum', *Sci Rep,* 10(1), pp. 1039.

Broeckx, B. J., Coopman, F., Verhoeven, G. E., Van Haeringen, W., van de Goor, L., Bosmans, T., Gielen, I., Saunders, J. H., Soetaert, S. S., Van Bree, H., Van Neste, C., Van Nieuwerburgh, F., Van Ryssen, B., Verelst, E., Van Steendam, K. and Deforce, D. (2013) 'The prevalence of nine genetic disorders in a dog population from Belgium, the Netherlands and Germany', *PLoS One,* 8(9), pp. e74811.

Butchbach, M. E., Tian, G., Guo, H. and Lin, C. L. (2004) 'Association of excitatory amino acid transporters, especially EAAT2, with cholesterol-rich lipid raft microdomains: importance for excitatory amino acid transporter localization and function', *J Biol Chem,* 279(33), pp. 34388-96.

Cai, Q. and Ganesan, D. (2022) 'Regulation of neuronal autophagy and the implications in neurodegenerative diseases', *Neurobiol Dis,* 162, pp. 105582.

Campagnoni, A. T. and Skoff, R. P. (2001) 'The pathobiology of myelin mutants reveal novel biological functions of the MBP and PLP genes', *Brain Pathol,* 11(1), pp. 74-91.

Chang, H. S., Kamishina, H., Mizukami, K., Momoi, Y., Katayama, M., Rahman, M. M., Uddin, M. M., Yabuki, A., Kohyama, M. and Yamato, O. (2013) 'Genotyping assays for the canine degenerative myelopathy-associated c.118G>A (p.E40K) mutation of the SOD1 gene using conventional and real-time PCR methods: a high prevalence in the Pembroke Welsh Corgi breed in Japan', *J Vet Med Sci,* 75(6), pp. 795-8.

Chang, R. C., Parakh, S., Coates, J. R., Long, S. and Atkin, J. D. (2019) 'Protein disulphide isomerase is associated with mutant SOD1 in canine degenerative myelopathy', *Neuroreport,* 30(1), pp. 8-13.

Chen, Y., Xia, K., Chen, L. and Fan, D. (2019) 'Increased Interleukin-6 Levels in the Astrocyte-Derived Exosomes of Sporadic Amyotrophic Lateral Sclerosis Patients', *Front Neurosci,* 13, pp. 574.

Cheroni, C., Marino, M., Tortarolo, M., Veglianese, P., De Biasi, S., Fontana, E., Zuccarello, L. V., Maynard, C. J., Dantuma, N. P. and Bendotti, C. (2009) 'Functional alterations of the ubiquitin-proteasome system in motor neurons of a mouse model of familial amyotrophic lateral sclerosis', *Hum Mol Genet,* 18(1), pp. 82-96.

Choi, M. E., Price, D. R., Ryter, S. W. and Choi, A. M. K. (2019) 'Necroptosis: a crucial pathogenic mediator of human disease', *JCI Insight,* 4(15).

Coates, J. R., March, P. A., Oglesbee, M., Ruaux, C. G., Olby, N. J., Berghaus, R. D., O'Brien, D. P., Keating, J. H., Johnson, G. S. and Williams, D. A. (2007) 'Clinical characterization of a familial degenerative myelopathy in Pembroke Welsh Corgi dogs', *J Vet Intern Med,* 21(6), pp. 1323-31.

Coates, J. R. and Wininger, F. A. (2010) 'Canine degenerative myelopathy', *Vet Clin North Am Small Anim Pract,* 40(5), pp. 929-50.

Corti, S., Donadoni, C., Ronchi, D., Bordoni, A., Fortunato, F., Santoro, D., Del Bo, R., Lucchini, V., Crugnola, V., Papadimitriou, D., Salani, S., Moggio, M., Bresolin, N. and Comi, G. P. (2009) 'Amyotrophic lateral sclerosis linked to a novel SOD1 mutation with muscle mitochondrial dysfunction', *J Neurol Sci,* 276(1-2), pp. 170-4.

Crisp, M. J., Beckett, J., Coates, J. R. and Miller, T. M. (2013) 'Canine degenerative myelopathy: biochemical characterization of superoxide dismutase 1 in the first naturally occurring non-human amyotrophic lateral sclerosis model', *Exp Neurol,* 248, pp. 1-9.

De Vos, K. (2001) *Cell Counter*. Available at: https://imagej.nih.gov/ij/plugins/cell-counter.html 2019-2023).

De Vos, K. (2001-2021) *Cell Counter (ImageJ plugin)*. Maryland, USA: National Institutes of Health. Available at: https://imagej.nih.gov/ij/plugins/cell-counter.html 2019).

Deiss, L. P., Galinka, H., Berissi, H., Cohen, O. and Kimchi, A. (1996) 'Cathepsin D protease mediates programmed cell death induced by interferon-gamma, Fas/APO-1 and TNF-alpha', *Embo j,* 15(15), pp. 3861-70.

Draper, A. C. E., Wilson, Z., Maile, C., Faccenda, D., Campanella, M. and Piercy, R. J. (2020) 'Species-specific consequences of an E40K missense mutation in superoxide dismutase 1 (SOD1)', *Faseb j,* 34(1), pp. 458-473.

Duan, S., Anderson, C. M., Stein, B. A. and Swanson, R. A. (1999) 'Glutamate induces rapid upregulation of astrocyte glutamate transport and cell-surface expression of GLAST', *J Neurosci,* 19(23), pp. 10193-200.

Ejlerskov, P., Rasmussen, I., Nielsen, T. T., Bergström, A. L., Tohyama, Y., Jensen, P. H. and Vilhardt, F. (2013) 'Tubulin polymerization-promoting protein (TPPP/p25α) promotes unconventional secretion of α-synuclein through exophagy by impairing autophagosome-lysosome fusion', *J Biol Chem,* 288(24), pp. 17313-35.

Elmore, S. (2007) 'Apoptosis: a review of programmed cell death', *Toxicol Pathol,* 35(4), pp. 495-516.

European Collection of Authenticated Cell Cultures (ECACC) (2020) *Passage numbers explained*: Public Health England. Available at: https://www.phe-culturecollections.org.uk/media/114565/m219_passage-numbers-explained.pdf (Accessed: June 2020).

Farrell, R. E. (2017) 'Chapter 6 - Quality Control for RNA Preparations', in Farrell, R.E. (ed.) *RNA Methodologies (Fifth Edition)*: Academic Press, pp. 167-185.

Fernández-Fernández, M. R., Gragera, M., Ochoa-Ibarrola, L., Quintana-Gallardo, L. and Valpuesta, J. M. (2017) 'Hsp70 - a master regulator in protein degradation', *FEBS Lett,* 591(17), pp. 2648-2660.

Gal, J., Ström, A. L., Kwinter, D. M., Kilty, R., Zhang, J., Shi, P., Fu, W., Wooten, M. W. and Zhu, H. (2009) 'Sequestosome 1/p62 links familial ALS mutant SOD1 to LC3 via an ubiquitin-independent mechanism', *J Neurochem,* 111(4), pp. 1062-73.

GE Healthcare Bio-Sciences AB (2018) *Western Blotting: Principles and Methods*: GE Heathcare. Available at: https://cdn.gelifesciences.com/dmm3bwsv3/AssetStream.aspx?mediaformatid=10061&destinationid=10016&assetid=15994 (Accessed: July 2020).

Gene Ontology Consortium (2006) 'The Gene Ontology (GO) project in 2006', *Nucleic Acids Res,* 34(Database issue), pp. D322-6.

Gois, A. M., Mendonça, D. M. F., Freire, M. A. M. and Santos, J. R. (2020) 'IN VITRO AND IN VIVO MODELS OF AMYOTROPHIC LATERAL SCLEROSIS: AN UPDATED OVERVIEW', *Brain Res Bull,* 159, pp. 32-43.

Golubczyk, D., Malysz-Cymborska, I., Kalkowski, L., Janowski, M., Coates, J. R., Wojtkiewicz, J., Maksymowicz, W. and Walczak, P. (2019) 'The Role of Glia in Canine Degenerative Myelopathy: Relevance to Human Amyotrophic Lateral Sclerosis', *Mol Neurobiol,* 56(8), pp. 5740-5748.

Gomes, C., Keller, S., Altevogt, P. and Costa, J. (2007) 'Evidence for secretion of Cu,Zn superoxide dismutase via exosomes from a cell model of amyotrophic lateral sclerosis', *Neurosci Lett,* 428(1), pp. 43-6.

Green, S. L., Tolwani, R. J., Varma, S., Quignon, P., Galibert, F. and Cork, L. C. (2002) 'Structure, chromosomal location, and analysis of the canine Cu/Zn superoxide dismutase (SOD1) gene', *J Hered,* 93(2), pp. 119-24.

Griffiths, I. (1982) 'Spinal disease in the dog', *In Pract,* 4(2), pp. 44-52.

Griffiths, I. R. and Duncan, I. D. (1975) 'Chronic degenerative radiculomyelopathy in the dog', *J Small Anim Pract,* 16(8), pp. 461-71.

Guo, N. and Peng, Z. (2013) 'MG132, a proteasome inhibitor, induces apoptosis in tumor cells', *Asia Pac J Clin Oncol,* 9(1), pp. 6-11.

Han, X. (2016) 'Lipidomics for studying metabolism', *Nat Rev Endocrinol,* 12(11), pp. 668-679.

Hanspal, M. A., Dobson, C. M., Yerbury, J. J. and Kumita, J. R. (2017) 'The relevance of contact-independent cell-to-cell transfer of TDP-43 and SOD1 in amyotrophic lateral sclerosis', *Biochim Biophys Acta Mol Basis Dis,* 1863(11), pp. 2762-2771.

Haraszti, R. A., Didiot, M. C., Sapp, E., Leszyk, J., Shaffer, S. A., Rockwell, H. E., Gao, F., Narain, N. R., DiFiglia, M., Kiebish, M. A., Aronin, N. and Khvorova, A. (2016) 'High-resolution proteomic and lipidomic analysis of exosomes and microvesicles from different cell sources', *J Extracell Vesicles,* 5, pp. 32570.

Hashimoto, K., Watanabe, S., Akutsu, M., Muraki, N., Kamishina, H., Furukawa, Y. and Yamanaka, K. (2023) 'Intrinsic structural vulnerability in the hydrophobic core induces species-specific aggregation of canine SOD1 with degenerative myelopathy-linked E40K mutation', *J Biol Chem,* 299(6), pp. 104798.

Hayashi, N., Doi, H., Kurata, Y., Kagawa, H., Atobe, Y., Funakoshi, K., Tada, M., Katsumoto, A., Tanaka, K., Kunii, M., Nakamura, H., Takahashi, K., Takeuchi, H., Koyano, S., Kimura, Y., Hirano, H. and Tanaka, F. (2019) 'Proteomic analysis of exosome-enriched fractions derived from cerebrospinal fluid of amyotrophic lateral sclerosis patients', *Neurosci Res.*

Hedl, T. J., San Gil, R., Cheng, F., Rayner, S. L., Davidson, J. M., De Luca, A., Villalva, M. D., Ecroyd, H., Walker, A. K. and Lee, A. (2019) 'Proteomics Approaches for Biomarker and Drug Target Discovery in ALS and FTD', *Front Neurosci,* 13, pp. 548.

Hesse, C., Larsson, H., Fredman, P., Minthon, L., Andreasen, N., Davidsson, P. and Blennow, K. (2000) 'Measurement of apolipoprotein E (apoE) in cerebrospinal fluid', *Neurochem Res,* 25(4), pp. 511-7.

Hesse, R., Hurtado, M. L., Jackson, R. J., Eaton, S. L., Herrmann, A. G., Colom-Cadena, M., Tzioras, M., King, D., Rose, J., Tulloch, J., McKenzie, C. A., Smith, C., Henstridge, C. M., Lamont, D., Wishart, T. M. and Spires-Jones, T. L. (2019) 'Comparative profiling of the synaptic proteome from Alzheimer's disease patients with focus on the APOE genotype', *Acta Neuropathol Commun,* 7(1), pp. 214.

Hessvik, N. P. and Llorente, A. (2018) 'Current knowledge on exosome biogenesis and release', *Cell Mol Life Sci,* 75(2), pp. 193-208.

Hetz, C. (2012) 'The unfolded protein response: controlling cell fate decisions under ER stress and beyond', *Nat Rev Mol Cell Biol,* 13(2), pp. 89-102.

Hinman, J. D., Chen, C. D., Oh, S. Y., Hollander, W. and Abraham, C. R. (2008) 'Age-dependent accumulation of ubiquitinated 2',3'-cyclic nucleotide 3'-phosphodiesterase in myelin lipid rafts', *Glia,* 56(1), pp. 118-33.

Holder, A. L., Price, J. A., Adams, J. P., Volk, H. A. and Catchpole, B. (2014) 'A retrospective study of the prevalence of the canine degenerative myelopathy associated superoxide dismutase 1 mutation (SOD1:c.118G > A) in a referral population of German Shepherd dogs from the UK', *Canine Genet Epidemiol,* 1, pp. 10.

Hosaka, T., Yamashita, T., Tamaoka, A. and Kwak, S. (2019) 'Extracellular RNAs as Biomarkers of Sporadic Amyotrophic Lateral Sclerosis and Other Neurodegenerative Diseases', *Int J Mol Sci,* 20(13).

Huang da, W., Sherman, B. T. and Lempicki, R. A. (2009a) 'Bioinformatics enrichment tools: paths toward the comprehensive functional analysis of large gene lists', *Nucleic Acids Res,* 37(1), pp. 1-13.

Huang da, W., Sherman, B. T. and Lempicki, R. A. (2009b) 'Systematic and integrative analysis of large gene lists using DAVID bioinformatics resources', *Nat Protoc,* 4(1), pp. 44-57.

Isgrò, M. A., Bottoni, P. and Scatena, R. (2015) 'Neuron-Specific Enolase as a Biomarker: Biochemical and Clinical Aspects', *Adv Exp Med Biol,* 867, pp. 125-43.

Ivansson, E. L., Megquier, K., Kozyrev, S. V., Muren, E., Korberg, I. B., Swofford, R., Koltookian, M., Tonomura, N., Zeng, R., Kolicheski, A. L., Hansen, L., Katz, M. L., Johnson, G. C., Johnson, G. S., Coates, J. R. and Lindblad-Toh, K. (2016) 'Variants within the SP110 nuclear body protein modify risk of canine degenerative myelopathy', *Proc Natl Acad Sci U S A,* 113(22), pp. E3091-100.

Jahangiri, B., Saei, A. K., Obi, P. O., Asghari, N., Lorzadeh, S., Hekmatirad, S., Rahmati, M., Velayatipour, F., Asghari, M. H., Saleem, A. and Moosavi, M. A. (2022) 'Exosomes, autophagy and ER stress pathways in human diseases: Cross-regulation and therapeutic approaches', *Biochim Biophys Acta Mol Basis Dis,* 1868(10), pp. 166484.

Jang, D., Kwon, H., Choi, M., Lee, J. and Pak, Y. (2019) 'Sumoylation of Flotillin-1 promotes EMT in metastatic prostate cancer by suppressing Snail degradation', *Oncogene,* 38(17), pp. 3248-3260.

Johnston, P. E., Barrie, J. A., McCulloch, M. C., Anderson, T. J. and Griffiths, I. R. (2000) 'Central nervous system pathology in 25 dogs with chronic degenerative radiculomyelopathy', *Vet Rec,* 146(22), pp. 629-33.

Jurga, A. M., Paleczna, M., Kadluczka, J. and Kuter, K. Z. (2021) 'Beyond the GFAP-Astrocyte Protein Markers in the Brain', *Biomolecules,* 11(9).

Kabeya, Y., Mizushima, N., Ueno, T., Yamamoto, A., Kirisako, T., Noda, T., Kominami, E., Ohsumi, Y. and Yoshimori, T. (2000) 'LC3, a mammalian homologue of yeast Apg8p, is localized in autophagosome membranes after processing', *Embo j,* 19(21), pp. 5720-8.

Kanehisa, M. and Goto, S. (2000) 'KEGG: kyoto encyclopedia of genes and genomes', *Nucleic Acids Res,* 28(1), pp. 27-30.

Kang, J. H., Li, M., Chen, X. and Yin, X. M. (2011) 'Proteomics analysis of starved cells revealed Annexin A1 as an important regulator of autophagic degradation', *Biochem Biophys Res Commun,* 407(3), pp. 581-6.

Kiernan, M. C., Vucic, S., Cheah, B. C., Turner, M. R., Eisen, A., Hardiman, O., Burrell, J. R. and Zoing, M. C. (2011) 'Amyotrophic lateral sclerosis', *Lancet,* 377(9769), pp. 942-55.

Kim, B. J., Seo, J. H., Bubien, J. K. and Oh, Y. S. (2002) 'Differentiation of adult bone marrow stem cells into neuroprogenitor cells in vitro', *Neuroreport,* 13(9), pp. 1185-8.

Kimura, S., Kamatari, Y. O., Kuwahara, Y., Hara, H., Yamato, O., Maeda, S., Kamishina, H. and Honda, R. (2020) 'Canine SOD1 harboring E40K or T18S mutations promotes protein aggregation without reducing the global structural stability', *PeerJ,* 8, pp. e9512.

Kobatake, Y., Nakata, K., Sakai, H., Sasaki, J., Yamato, O., Takashima, S., Nishii, N., Maeda, S., Islam, M. S. and Kamishina, H. (2021) 'The Long-Term Clinical Course of Canine Degenerative Myelopathy and Therapeutic Potential of Curcumin', *Vet Sci,* 8(9).

Kohyama, M., Kitagawa, M., Kamishina, H., Kobatake, Y., Yabuki, A., Sawa, M., Kakita, S. and Yamato, O. (2017) 'Degenerative myelopathy in the Collie breed: a retrospective immunohistochemical analysis of superoxide dismutase 1 in an affected Rough Collie, and a molecular epidemiological survey of the SOD1: c.118G>A mutation in Japan', *J Vet Med Sci,* 79(2), pp. 375-379.

Ku, H. C. and Cheng, C. F. (2020) 'Master Regulator Activating Transcription Factor 3 (ATF3) in Metabolic Homeostasis and Cancer', *Front Endocrinol (Lausanne),* 11, pp. 556.

Laskowska, E., Kuczyńska-Wiśnik, D. and Lipińska, B. (2019) 'Proteomic analysis of protein homeostasis and aggregation', *J Proteomics,* 198, pp. 98-112.

Leal, S. S. and Gomes, C. M. (2015) 'Calcium dysregulation links ALS defective proteins and motor neuron selective vulnerability', *Front Cell Neurosci,* 9, pp. 225.

Lee, M., Ban, J. J., Kim, K. Y., Jeon, G. S., Im, W., Sung, J. J. and Kim, M. (2016) 'Adipose-derived stem cell exosomes alleviate pathology of amyotrophic lateral sclerosis in vitro', *Biochem Biophys Res Commun,* 479(3), pp. 434-439.

Leidal, A. M. and Debnath, J. (2020) 'LC3-dependent extracellular vesicle loading and secretion (LDELS)', *Autophagy,* 16(6), pp. 1162-1163.

Leighton, D. J., Newton, J., Stephenson, L. J., Colville, S., Davenport, R., Gorrie, G., Morrison, I., Swingler, R., Chandran, S. and Pal, S. (2019) 'Changing epidemiology of motor neurone disease in Scotland', *J Neurol,* 266(4), pp. 817-825.

Liu, J., Liu, W. and Yang, H. (2019) 'Balancing Apoptosis and Autophagy for Parkinson's Disease Therapy: Targeting BCL-2', *ACS Chem Neurosci,* 10(2), pp. 792-802.

Longinetti, E. and Fang, F. (2019) 'Epidemiology of amyotrophic lateral sclerosis: an update of recent literature', *Curr Opin Neurol,* 32(5), pp. 771-776.

Lovett, M. C., Coates, J. R., Shu, Y., Oglesbee, M. J., Fenner, W. and Moore, S. A. (2014) 'Quantitative assessment of hsp70, IL-1beta and TNF-alpha in the spinal cord of dogs with E40K SOD1-associated degenerative myelopathy', *Vet J,* 200(2), pp. 312-7.

Lowe, R., Shirley, N., Bleackley, M., Dolan, S. and Shafee, T. (2017) 'Transcriptomics technologies', *PLoS Comput Biol,* 13(5), pp. e1005457.

Maglemose, R., Hedegaard, A., Lehnhoff, J., Dimintiyanova, K. P., Moldovan, M., Grøndahl, L. and Meehan, C. F. (2017) 'Potassium channel abnormalities are consistent with early axon degeneration of motor axons in the G127X SOD1 mouse model of amyotrophic lateral sclerosis', *Exp Neurol,* 292, pp. 154-167.

Maki, S., Islam, M. S., Itoh, T., Nurimoto, M., Yabuki, A., Furusawa, Y., Kamishina, H., Kobatake, Y., Rakib, T. M., Tacharina, M. R. and Yamato, O. (2022) 'Molecular Epidemiological Survey for Degenerative Myelopathy in German Shepherd Dogs in Japan: Allele Frequency and Clinical Progression Rate', *Animals (Basel),* 12(13).

March, P. A., Coates, J. R., Abyad, R. J., Williams, D. A., O'Brien, D. P., Olby, N. J., Keating, J. H. and Oglesbee, M. (2009) 'Degenerative myelopathy in 18 Pembroke Welsh Corgi dogs', *Vet Pathol,* 46(2), pp. 241-50.

Martín, L., Pumarola, M., Altuzarra, R., Espinosa, J. and Ortega, M. (2022) 'First Case of a Cerebrocortical Ganglioglioma in a Dog', *Vet Sci,* 9(10).

McGonigal, R., Barrie, J. A., Yao, D., Black, L. E., McLaughlin, M. and Willison, H. J. (2021) 'Neuronally expressed a-series gangliosides are sufficient to prevent the lethal age-dependent phenotype in GM3-only expressing mice', *J Neurochem,* 158(2), pp. 217-232.

McLaughlin, M., Hunter, D. J. B., Thomson, C. E., Yool, D., Kirkham, D., Freer, A. A. and Griffiths, I. R. (2002) 'Evidence for possible interactions between PLP and DM20 within the myelin sheath', *Glia,* 39(1), pp. 31-36.

McLaughlin, M., Karim, S. A., Montague, P., Barrie, J. A., Kirkham, D., Griffiths, I. R. and Edgar, J. M. (2007) 'Genetic background influences UPR but not PLP processing in the rumpshaker model of PMD/SPG2', *Neurochem Res,* 32(2), pp. 167-76.

Miller, A. D. (2013) 'Dural ossification (ossifying pachymeningitis)', *J Am Vet Med Assoc,* 242(9), pp. 1211.

Miller, A. D., Barber, R., Porter, B. F., Peters, R. M., Kent, M., Platt, S. R. and Schatzberg, S. J. (2009) 'Degenerative myelopathy in two Boxer dogs', *Vet Pathol,* 46(4), pp. 684-7.

Miller, R. G., Mitchell, J. D. and Moore, D. H. (2012) 'Riluzole for amyotrophic lateral sclerosis (ALS)/motor neuron disease (MND)', *Cochrane Database Syst Rev,* 2012(3), pp. Cd001447.

Moll, T., Marshall, J. N. G., Soni, N., Zhang, S., Cooper-Knock, J. and Shaw, P. J. (2021) 'Membrane lipid raft homeostasis is directly linked to neurodegeneration', *Essays Biochem,* 65(7), pp. 999-1011.

Momen-Heravi, F. (2017) 'Isolation of Extracellular Vesicles by Ultracentrifugation', *Methods Mol Biol,* 1660, pp. 25-32.

Morgan, B. R., Coates, J. R., Johnson, G. C., Bujnak, A. C. and Katz, M. L. (2013) 'Characterization of intercostal muscle pathology in canine degenerative myelopathy: a disease model for amyotrophic lateral sclerosis', *J Neurosci Res,* 91(12), pp. 1639-50.

Morgan, B. R., Coates, J. R., Johnson, G. C., Shelton, G. D. and Katz, M. L. (2014) 'Characterization of thoracic motor and sensory neurons and spinal nerve roots in canine degenerative myelopathy, a potential disease model of amyotrophic lateral sclerosis', *J Neurosci Res,* 92(4), pp. 531-41.

Morrice, J. R., Gregory-Evans, C. Y. and Shaw, C. A. (2017) 'Necroptosis in amyotrophic lateral sclerosis and other neurological disorders', *Biochim Biophys Acta Mol Basis Dis,* 1863(2), pp. 347-353.

Nakamae, S., Kobatake, Y., Suzuki, R., Tsukui, T., Kato, S., Yamato, O., Sakai, H., Urushitani, M., Maeda, S. and Kamishina, H. (2015) 'Accumulation and aggregate formation of mutant superoxide dismutase 1 in canine degenerative myelopathy', *Neuroscience,* 303, pp. 229-40.

Nakata, K., Namiki, M., Kobatake, Y., Nishida, H., Sakai, H., Yamato, O., Urushitani, M., Maeda, S. and Kamishina, H. (2021) 'Up-regulated spinal microRNAs induce aggregation of superoxide dismutase 1 protein in canine degenerative myelopathy', *Res Vet Sci,* 135, pp. 479-485.

Nardone, R., Holler, Y., Taylor, A. C., Lochner, P., Tezzon, F., Golaszewski, S., Brigo, F. and Trinka, E. (2016) 'Canine degenerative myelopathy: a model of human amyotrophic lateral sclerosis', *Zoology (Jena),* 119(1), pp. 64-73.

Nelvagal, H. R., Hurtado, M. L., Eaton, S. L., Kline, R. A., Lamont, D. J., Sands, M. S., Wishart, T. M. and Cooper, J. D. (2020) 'Comparative proteomic profiling reveals mechanisms for early spinal cord vulnerability in CLN1 disease', *Sci Rep,* 10(1), pp. 15157.

Nussbaum, J. L., Roussel, G., Wünsch, E. and Jollès, P. (1985) 'Site-specific antibodies to rat myelin proteolipids directed against the C-terminal hexapeptide', *J Neurol Sci,* 68(1), pp. 89-100.

Ogawa, M., Uchida, K., Park, E. S., Kamishina, H., Sasaki, J., Chang, H. S., Yamato, O. and Nakayama, H. (2011) 'Immunohistochemical observation of canine degenerative myelopathy in two Pembroke Welsh Corgi dogs', *J Vet Med Sci,* 73(10), pp. 1275-9.

Ogawa, M., Uchida, K., Yamato, O., Inaba, M., Uddin, M. M. and Nakayama, H. (2014) 'Neuronal loss and decreased GLT-1 expression observed in the spinal cord of Pembroke Welsh Corgi dogs with canine degenerative myelopathy', *Vet Pathol,* 51(3), pp. 591-602.

Ogawa, M., Uchida, K., Yamato, O., Mizukami, K., Chambers, J. K. and Nakayama, H. (2015) 'Expression of Autophagy-Related Proteins in the Spinal Cord of Pembroke Welsh Corgi Dogs With Canine Degenerative Myelopathy', *Vet Pathol,* 52(6), pp. 1099-107.

Oji, T., Kamishina, H., Cheeseman, J. A. and Clemmons, R. M. (2007) 'Measurement of myelin basic protein in the cerebrospinal fluid of dogs with degenerative myelopathy', *Vet Clin Pathol,* 36(3), pp. 281-4.

Onesto, E., Rusmini, P., Crippa, V., Ferri, N., Zito, A., Galbiati, M. and Poletti, A. (2011) 'Muscle cells and motoneurons differentially remove mutant SOD1 causing familial amyotrophic lateral sclerosis', *J Neurochem,* 118(2), pp. 266-80.

Oslowski, C. M. and Urano, F. (2011) 'Measuring ER stress and the unfolded protein response using mammalian tissue culture system', *Methods Enzymol,* 490, pp. 71-92.

Otake, K., Kamiguchi, H. and Hirozane, Y. (2019) 'Identification of biomarkers for amyotrophic lateral sclerosis by comprehensive analysis of exosomal mRNAs in human cerebrospinal fluid', *BMC Med Genomics,* 12(1), pp. 7.

Oyake, K., Kobatake, Y., Shibata, S., Sakai, H., Saito, M., Yamato, O., Kushida, K., Maeda, S. and Kamishina, H. (2016) 'Changes in respiratory function in Pembroke Welsh Corgi dogs with degenerative myelopathy', *J Vet Med Sci,* 78(8), pp. 1323-7.

Pan, S. and Chan, J. R. (2017) 'Regulation and dysregulation of axon infrastructure by myelinating glia', *J Cell Biol,* 216(12), pp. 3903-3916.

Panek, W. K., Gruen, M. E., Murdoch, D. M., Marek, R. D., Stachel, A. F., Mowat, F. M., Saker, K. E. and Olby, N. J. (2020) 'Plasma Neurofilament Light Chain as a Translational Biomarker of Aging and Neurodegeneration in Dogs', *Mol Neurobiol,* 57(7), pp. 3143-3149.

Pfeiffer, P., Coates, J. R., Esqueda, Y. M., Kennedy, A., Getchell, K., McLenon, M., Kosa, E. and Agbas, A. (2023) 'Exosomal TAR DNA binding protein 43 profile in canine model of amyotrophic lateral sclerosis: a preliminary study in developing blood-based biomarker for neurodegenerative diseases', *Ann Med,* 55(1), pp. 34-41.

Prell, T., Lautenschläger, J. and Grosskreutz, J. (2013) 'Calcium-dependent protein folding in amyotrophic lateral sclerosis', *Cell Calcium,* 54(2), pp. 132-43.

Price, P. J. (2017) 'Best practices for media selection for mammalian cells', *In Vitro Cell Dev Biol Anim,* 53(8), pp. 673-681.

Qi, Y., McLaughlin, M., Anderson, T. J. and Montague, P. (2016) *Characterisation of Superoxide Dismutase 1 Protein in canine degenerative myelopathy.* MSc(R), University of Glasgow, Glasgow.

Qi, Y., Montague, P., Loney, C., Campbell, C., Shafie, I. N. F., Anderson, T. J. and McLaughlin, M. (2019) 'In vitro evidence consistent with an interaction between wild-type and mutant SOD1 protein associated with canine degenerative myelopathy', *Eur J Neurosci,* 50(12), pp. 3896-3905.

Rakhit, R. and Chakrabartty, A. (2006) 'Structure, folding, and misfolding of Cu,Zn superoxide dismutase in amyotrophic lateral sclerosis', *Biochim Biophys Acta,* 1762(11-12), pp. 1025-37.

Rasband, W. S. (1997) *ImageJ.* Maryland, USA: U. S. National Institute for Health. Available at: https://imagej.nih.gov/ij/ 2019-2023).

Ravits, J., Appel, S., Baloh, R. H., Barohn, R., Brooks, B. R., Elman, L., Floeter, M. K., Henderson, C., Lomen-Hoerth, C., Macklis, J. D., McCluskey, L., Mitsumoto, H., Przedborski, S., Rothstein, J., Trojanowski, J. Q., van den Berg, L. H. and Ringel, S. (2013) 'Deciphering amyotrophic lateral sclerosis: what phenotype, neuropathology and genetics are telling us about pathogenesis', *Amyotroph Lateral Scler Frontotemporal Degener,* 14 Suppl 1(0 1), pp. 5-18.

Renna, M., Jimenez-Sanchez, M., Sarkar, S. and Rubinsztein, D. C. (2010) 'Chemical inducers of autophagy that enhance the clearance of mutant proteins in neurodegenerative diseases', *J Biol Chem,* 285(15), pp. 11061-7.

Ross, J. M., Öberg, J., Brené, S., Coppotelli, G., Terzioglu, M., Pernold, K., Goiny, M., Sitnikov, R., Kehr, J., Trifunovic, A., Larsson, N. G., Hoffer, B. J. and Olson, L. (2010) 'High brain lactate is a hallmark of aging and caused by a shift in the lactate dehydrogenase A/B ratio', *Proc Natl Acad Sci U S A,* 107(46), pp. 20087-92.

Saccon, R. A., Bunton-Stasyshyn, R. K., Fisher, E. M. and Fratta, P. (2013) 'Is SOD1 loss of function involved in amyotrophic lateral sclerosis?', *Brain,* 136(Pt 8), pp. 2342-58.

Salvany, S., Casanovas, A., Piedrafita, L., Gras, S., Calderó, J. and Esquerda, J. E. (2022) 'Accumulation of misfolded SOD1 outlines distinct patterns of motor neuron pathology and death during disease progression in a SOD1(G93A) mouse model of amyotrophic lateral sclerosis', *Brain Pathol,* 32(6), pp. e13078.

Sapoń, K., Mańka, R., Janas, T. and Janas, T. (2023) 'The role of lipid rafts in vesicle formation', *J Cell Sci,* 136(9).

Sasaki, S., Shibata, N., Komori, T. and Iwata, M. (2000) 'iNOS and nitrotyrosine immunoreactivity in amyotrophic lateral sclerosis', *Neurosci Lett,* 291(1), pp. 44-8.

Schrezenmeier, E. and Dörner, T. (2020) 'Mechanisms of action of hydroxychloroquine and chloroquine: implications for rheumatology', *Nat Rev Rheumatol,* 16(3), pp. 155-166.

Sha, Z., Schnell, H. M., Ruoff, K. and Goldberg, A. (2018) 'Rapid induction of p62 and GABARAPL1 upon proteasome inhibition promotes survival before autophagy activation', *J Cell Biol,* 217(5), pp. 1757-1776.

Shaffer, L. G., Ramirez, C. J., Phelps, P., Aviram, M., Walczak, M., Bar-Gal, G. K. and Ballif, B. C. (2017) 'An International Genetic Survey of Breed-Specific Diseases in Working Dogs from the United States, Israel, and Poland', *Cytogenet Genome Res,* 153(4), pp. 198-204.

Shafie, I. N., McLaughlin, M., Burchmore, R., Lim, M. A., Montague, P., Johnston, P. E., Penderis, J. and Anderson, T. J. (2014) 'The chaperone protein clusterin may serve as a cerebrospinal fluid biomarker for chronic spinal cord disorders in the dog', *Cell Stress Chaperones,* 19(3), pp. 311-20.

Shafie, I. N. F., Anderson, T. J. and McLaughlin, M. (2013) *The establishment of potential cerebrospinal fluid biomarkers for canine degenerative myelopathy.* PhD, University of Glasgow, Enlighten [Online] Available at: https://theses.gla.ac.uk/4292/ (Accessed: March 2020).

Sheikh, M. H. and Solito, E. (2018) 'Annexin A1: Uncovering the Many Talents of an Old Protein', *Int J Mol Sci,* 19(4).

Shelton, G. D., Johnson, G. C., O'Brien, D. P., Katz, M. L., Pesayco, J. P., Chang, B. J., Mizisin, A. P. and Coates, J. R. (2012) 'Degenerative myelopathy associated with a missense mutation in the superoxide dismutase 1 (SOD1) gene progresses to peripheral neuropathy in Pembroke Welsh corgis and boxers', *J Neurol Sci,* 318(1-2), pp. 55-64.

Sigma (1998) *Ponceau S Staining Solution*: Sigma-Aldrich. Available at: https://www.sigmaaldrich.com/content/dam/sigma-aldrich/docs/Sigma-Aldrich/Product_Information_Sheet/p7170pis.pdf (Accessed: July 2020).

Sigma-Aldrich (2022) *Trypan Blue solution*: Merck. Available at: https://www.sigmaaldrich.com/GB/en/product/sigma/t8154?gclid=EAIaIQobChMI-fqXua7e9QIVmK3tCh25RgKHEAAYASAAEgKY5PD_BwE (Accessed: February 2022).

Silverman, J. M., Christy, D., Shyu, C. C., Moon, K. M., Fernando, S., Gidden, Z., Cowan, C. M., Ban, Y., Stacey, R. G., Grad, L. I., McAlary, L., Mackenzie, I. R., Foster, L. J. and Cashman, N. R. (2019) 'CNS-derived extracellular vesicles from superoxide dismutase 1 (SOD1)(G93A) ALS mice originate from astrocytes and neurons and carry misfolded SOD1', *J Biol Chem,* 294(10), pp. 3744-3759.

Smith, E. F., Shaw, P. J. and De Vos, K. J. (2019) 'The role of mitochondria in amyotrophic lateral sclerosis', *Neurosci Lett,* 710, pp. 132933.

Story, B. D., Miller, M. E., Bradbury, A. M., Million, E. D., Duan, D., Taghian, T., Faissler, D., Fernau, D., Beecy, S. J. and Gray-Edwards, H. L. (2020) 'Canine Models of Inherited Musculoskeletal and Neurodegenerative Diseases', *Front Vet Sci,* 7, pp. 80.

Sugita, H. and Irimajiri, M. (2016) 'A Survey of Veterinarians’ Attitudes toward Euthanasia of Companion Animals in Japan', *Anthrozoös,* 29(2), pp. 297-310.

Tan, S. Z., Begley, P., Mullard, G., Hollywood, K. A. and Bishop, P. N. (2016) 'Introduction to metabolomics and its applications in ophthalmology', *Eye (Lond),* 30(6), pp. 773-83.

Tanaka, N., Kimura, S., Kamatari, Y. O., Nakata, K., Kobatake, Y., Inden, M., Yamato, O., Urushitani, M., Maeda, S. and Kamishina, H. (2021) 'In vitro evidence of propagation of superoxide dismutase-1 protein aggregation in canine degenerative myelopathy', *Vet J,* 274, pp. 105710.

Thavarajah, R., Mudimbaimannar, V. K., Elizabeth, J., Rao, U. K. and Ranganathan, K. (2012) 'Chemical and physical basics of routine formaldehyde fixation', *J Oral Maxillofac Pathol,* 16(3), pp. 400-5.

Thermo Fisher Scientific Inc. 2010. NanoDrop 1000 Spectrophotometer V3.8 User’s Manual. Thermo Fisher Scientific Inc.

Thompson, A. G., Gray, E., Mäger, I., Thézénas, M. L., Charles, P. D., Talbot, K., Fischer, R., Kessler, B. M., Wood, M. and Turner, M. R. (2020) 'CSF extracellular vesicle proteomics demonstrates altered protein homeostasis in amyotrophic lateral sclerosis', *Clin Proteomics,* 17, pp. 31.

Théry, C., Witwer, K. W., Aikawa, E., Alcaraz, M. J., Anderson, J. D., Andriantsitohaina, R., Antoniou, A., Arab, T., Archer, F., Atkin-Smith, G. K., Ayre, D. C., Bach, J. M., Bachurski, D., Baharvand, H., Balaj, L., Baldacchino, S., Bauer, N. N., Baxter, A. A., Bebawy, M., ... and Zuba-Surma, E. K. (2018) 'Minimal information for studies of extracellular vesicles 2018 (MISEV2018): a position statement of the International Society for Extracellular Vesicles and update of the MISEV2014 guidelines', *J Extracell Vesicles,* 7(1), pp. 1535750.

Tiwari, A. and Hayward, L. J. (2005) 'Mutant SOD1 instability: implications for toxicity in amyotrophic lateral sclerosis', *Neurodegener Dis,* 2(3-4), pp. 115-27.

Toedebusch, C. M., Bachrach, M. D., Garcia, V. B., Johnson, G. C., Katz, M. L., Shaw, G., Coates, J. R. and Garcia, M. L. (2017) 'Cerebrospinal Fluid Levels of Phosphorylated Neurofilament Heavy as a Diagnostic Marker of Canine Degenerative Myelopathy', *J Vet Intern Med,* 31(2), pp. 513-520.

Toedebusch, C. M., Snyder, J. C., Jones, M. R., Garcia, V. B., Johnson, G. C., Villalon, E. L., Coates, J. R. and Garcia, M. L. (2018) 'Arginase-1 expressing microglia in close proximity to motor neurons were increased early in disease progression in canine degenerative myelopathy, a model of amyotrophic lateral sclerosis', *Mol Cell Neurosci,* 88, pp. 148-157.

Tohill, M., Mantovani, C., Wiberg, M. and Terenghi, G. (2004) 'Rat bone marrow mesenchymal stem cells express glial markers and stimulate nerve regeneration', *Neurosci Lett,* 362(3), pp. 200-3.

Traiffort, E., Morisset-Lopez, S., Moussaed, M. and Zahaf, A. (2021) 'Defective Oligodendroglial Lineage and Demyelination in Amyotrophic Lateral Sclerosis', *Int J Mol Sci,* 22(7).

Urushitani, M., Sik, A., Sakurai, T., Nukina, N., Takahashi, R. and Julien, J. P. (2006) 'Chromogranin-mediated secretion of mutant superoxide dismutase proteins linked to amyotrophic lateral sclerosis', *Nat Neurosci,* 9(1), pp. 108-18.

van Blitterswijk, M., van Es, M. A., Hennekam, E. A., Dooijes, D., van Rheenen, W., Medic, J., Bourque, P. R., Schelhaas, H. J., van der Kooi, A. J., de Visser, M., de Bakker, P. I., Veldink, J. H. and van den Berg, L. H. (2012) 'Evidence for an oligogenic basis of amyotrophic lateral sclerosis', *Hum Mol Genet,* 21(17), pp. 3776-84.

Van Damme, P., Robberecht, W. and Van Den Bosch, L. (2017) 'Modelling amyotrophic lateral sclerosis: progress and possibilities', *Dis Model Mech,* 10(5), pp. 537-549.

Vandoorne, T., De Bock, K. and Van Den Bosch, L. (2018) 'Energy metabolism in ALS: an underappreciated opportunity?', *Acta Neuropathol,* 135(4), pp. 489-509.

Vollrath, J. T., Sechi, A., Dreser, A., Katona, I., Wiemuth, D., Vervoorts, J., Dohmen, M., Chandrasekar, A., Prause, J., Brauers, E., Jesse, C. M., Weis, J. and Goswami, A. (2014) 'Loss of function of the ALS protein SigR1 leads to ER pathology associated with defective autophagy and lipid raft disturbances', *Cell Death Dis,* 5(6), pp. e1290.

Wakayama, K., Kimura, S., Kobatake, Y., Kamishina, H., Nishii, N., Takashima, S., Honda, R. and Kamatari, Y. O. (2022) 'Molecular Mechanisms of Aggregation of Canine SOD1 E40K Amyloidogenic Mutant Protein', *Molecules,* 28(1).

Waxman, F. J., Clemmons, R. M., Johnson, G., Evermann, J. F., Johnson, M. I., Roberts, C. and Hinrichs, D. J. (1980) 'Progressive myelopathy in older German shepherd dogs. I. Depressed response to thymus-dependent mitogens', *J Immunol,* 124(3), pp. 1209-15.

Weydert, C. J. and Cullen, J. J. (2010) 'Measurement of superoxide dismutase, catalase and glutathione peroxidase in cultured cells and tissue', *Nat Protoc,* 5(1), pp. 51-66.

Wininger, F. A., Zeng, R., Johnson, G. S., Katz, M. L., Johnson, G. C., Bush, W. W., Jarboe, J. M. and Coates, J. R. (2011) 'Degenerative myelopathy in a Bernese Mountain Dog with a novel SOD1 missense mutation', *J Vet Intern Med,* 25(5), pp. 1166-70.

Wootz, H., Weber, E., Korhonen, L. and Lindholm, D. (2006) 'Altered distribution and levels of cathepsinD and cystatins in amyotrophic lateral sclerosis transgenic mice: possible roles in motor neuron survival', *Neuroscience,* 143(2), pp. 419-30.

Xi, Y., Ju, R. and Wang, Y. (2020) 'Roles of Annexin A protein family in autophagy regulation and therapy', *Biomed Pharmacother,* 130, pp. 110591.

Xu, J., Camfield, R. and Gorski, S. M. (2018) 'The interplay between exosomes and autophagy - partners in crime', *J Cell Sci,* 131(15).

Yang, Q., Zhang, A.-h., Miao, J.-h., Sun, H., Han, Y., Yan, G.-l., Wu, F.-f. and Wang, X.-j. (2019) 'Metabolomics biotechnology, applications, and future trends: a systematic review', *RSC Advances,* 9(64), pp. 37245-37257.

Yao, S., Xu, M. D., Wang, Y., Zhao, S. T., Wang, J., Chen, G. F., Chen, W. B., Liu, J., Huang, G. B., Sun, W. J., Zhang, Y. Y., Hou, H. L., Li, L. and Sun, X. D. (2023) 'Astrocytic lactate dehydrogenase A regulates neuronal excitability and depressive-like behaviors through lactate homeostasis in mice', *Nat Commun,* 14(1), pp. 729.

Ye, J. and Liu, X. (2022) 'Interactions between endoplasmic reticulum stress and extracellular vesicles in multiple diseases', *Front Immunol,* 13, pp. 955419.

Yokota, S., Kobatake, Y., Noda, Y., Nakata, K., Yamato, O., Hara, H., Sakai, H., Nishida, H., Maeda, S. and Kamishina, H. (2018) 'Activation of the unfolded protein response in canine degenerative myelopathy', *Neurosci Lett,* 687, pp. 216-222.

Zamboni, C., Zamarian, V., Stefanello, D., Ferrari, R., Auletta, L., Milanesi, S., Mauri, S., Grieco, V., Ceciliani, F. and Lecchi, C. (2022) 'Plasma small extracellular vesicles from dogs affected by cutaneous mast cell tumors deliver high levels of miR-21-5p', *Front Vet Sci,* 9, pp. 1083174.

Zelko, I. N., Mariani, T. J. and Folz, R. J. (2002) 'Superoxide dismutase multigene family: a comparison of the CuZn-SOD (SOD1), Mn-SOD (SOD2), and EC-SOD (SOD3) gene structures, evolution, and expression', *Free Radic Biol Med,* 33(3), pp. 337-49.

Zeng, R., Coates, J. R., Johnson, G. C., Hansen, L., Awano, T., Kolicheski, A., Ivansson, E., Perloski, M., Lindblad-Toh, K., O'Brien, D. P., Guo, J., Katz, M. L. and Johnson, G. S. (2014) 'Breed distribution of SOD1 alleles previously associated with canine degenerative myelopathy', *J Vet Intern Med,* 28(2), pp. 515-21.

Zhai, J., Ström, A. L., Kilty, R., Venkatakrishnan, P., White, J., Everson, W. V., Smart, E. J. and Zhu, H. (2009) 'Proteomic characterization of lipid raft proteins in amyotrophic lateral sclerosis mouse spinal cord', *Febs j,* 276(12), pp. 3308-23.